Design, Synthesis, and Evaluation of Supramolecular Polymer Structures for Signaling Gas Delivery

Ryan Joseph Carrazzone

Dissertation submitted to the faculty of Virginia Polytechnic Institute and State University in partial fulfillment of the requirements for the degree of

Doctor of Philosophy
In
Macromolecular Science and Engineering

J.B. Matson, Chair
L.A. Madsen
R.M. Davis
M.D. Schulz
R. Tong

June 9, 2021
Blacksburg, VA

Keywords: hydrogen sulfide (H_2S), sulfur dioxide (SO_2), polymer micelles, drug delivery, reversible addition-fragmentation chain transfer (RAFT) polymerization

Copyright 2021

Abstract: Design, Synthesis, and Evaluation of Supramolecular Polymer Structures for Signaling Gas Delivery

Ryan Joseph Carrazzone

ABSTRACT

In the early 2000s, hydrogen sulfide (H_2S) was added to the family of molecules known as gasotransmitters, a class of endogenously produced and freely diffusing biological signaling molecules. Since this discovery, biologists and chemists have sought to understand the physiological roles of H_2S and to elucidate the potential benefits of exogenous H_2S delivery. As a result, many synthetic small molecule donor compounds have been created to deliver H_2S in response to various biologically relevant stimuli. Furthermore, macromolecular and supramolecular H_2S donor systems have been created to protect donors in the biological milieu, extend release kinetics, or control H_2S release conditions. Thus, H_2S-donating nanostructures with precisely tuned release rates provide invaluable tools for further investigating the biological roles and therapeutic potential of H_2S.

This work describes two polymer micelle systems for the controlled delivery of H_2S. The first system is based on H_2S-releasing polymer amphiphiles with varying degrees of a plasticizing comonomer incorporated into the core-forming block. The glass transition temperature of the core-forming block varied predictably with incorporation of the plasticizing comonomer. Accordingly, the half-life of H_2S release decreased from 4.2 h to 0.18 h with increasing core-forming block mobility. The second system is based on H_2S releasing polymer amphiphiles with varying degrees of crosslinking in the core-forming block. The crosslinked system was designed to achieve control over H_2S release rate with minimal dilution of donor in the core-forming block. The half-life of

H_2S release increased from 117 min to 210 min with increasing crosslink density in the core-forming block, further demonstrating that H_2S release rates can be precisely controlled by tuning micelle core mobility.

Beyond control over H_2S release rate, further study of the biological roles of H_2S requires donor systems with precisely triggered release. To this end, this dissertation also discusses efforts to investigate fundamental micelle–unimer relationships. This section includes an evaluation of the impact of core-forming block mobility on micelle–unimer coexistence utilizing a model polymer amphiphile system. Unimer populations correlated with glass transition temperatures of the core-forming block, suggesting the need to consider micelle core mobility when discussing polymer chain phase behavior of amphiphilic block copolymers. Finally, this work discloses new methods for the radical polymerization of poly(olefin sulfones) with control over molecular weight. POSs are a unique class of polymers with great potential for stimuli-responsive depolymerization to generate sulfur dioxide (SO_2), a signaling gas related to H_2S.

Abstract Public: Utilizing Polymer Chemistry to Develop Advanced Hydrogen Sulfide Donors

Ryan Joseph Carrazzone

GENERAL AUDIENCE ABSTRACT

Hydrogen sulfide (H_2S) is commonly known for its pungent odor and toxicity. Despite this negative stigma, H_2S has been revealed as a vital signaling molecule in both plants and animals. This discovery has prompted the coordination of biologists and chemists in an effort to better understand the roles of H_2S in the body. Driven by this motive, great interest has centered around the development of finely tuned molecules designed to generate H_2S in the body, termed H_2S donors. A variety of synthetic H_2S donors have been reported with various conditions enabling release. Building on this work, the development of polymeric H_2S donors with tunable release rates will enable investigation into the complex behavior of H_2S in the body.

The first half of this dissertation focuses on the design and synthesis of two polymeric H_2S donor systems for the controlled release of H_2S. These systems take advantage of sequestering the H_2S donating species inside a polymeric nanostructure in water called a micelle. Because H_2S release requires a triggering molecule to enter the polymeric nanostructure, release rate can be tuned by modifying the mobility of the structure. The first system discussed demonstrates this concept by increasing the flexibility of the micelle core. As expected, H_2S release rates increased with increasing flexibility. The second system discussed advances this idea by limiting mobility within the micelle core, rather than increasing flexibility. Accordingly, H_2S release rates decreased with decreasing mobility within the micelle core.

The latter half of this dissertation broadly explores the development of polymeric signaling gas delivery vehicles with triggered release conditions. We first investigate the impact of polymer chain flexibility on the formation of micelles in water. Polymer chain flexibility significantly impacted the balance between micelles and unassembled polymer chains in solution, suggesting the need to consider this characteristic when designing donor systems for precise release conditions. Lastly, we discuss the development of controlled polymerization techniques for poly(olefin sulfones). We envision that poly(olefin sulfones) will be a useful class of polymers in the design of donor systems relying on triggered depolymerization for release of the signaling gas sulfur dioxide.

Dedication

This dissertation is dedicated to my parents, Kevin and Kathleen Carrazzone.

Acknowledgements

I would firstly like to thank my Ph.D. advisor, Prof John Matson. When I joined the Matson lab in the Fall of 2016, I had ambitions of becoming proficient in the design and synthesis of polymer systems. Prof. Matson has been a vital part of my growth as a chemist, acting as both an invaluable resource and a steadying presence throughout my graduate school career. I will always be grateful for his guidance and wisdom, especially considering he always makes time to speak with his students when they need to talk about chemistry, life, or anything in between.

I would also like to thank my committee members, Prof. Louis Madsen, Prof. Richey Davis, Prof. Michael Schulz, and Prof. Rong Tong. I have received great advice concerning my projects from each of them individually, and I will always appreciate their willingness to discuss science. I have had the pleasure of collaborating with Prof. Madsen on a project combining the expertise of both our lab and theirs. Throughout our time working together, Prof. Madsen always treated me with the respect of a colleague and valued my opinion. Prof. Davis was a valuable asset when I was learning to characterize polymer nanostructures in solution, and often took the time to answer my questions. Prof. Schulz was a pleasure to discuss organic synthesis with, and was a friendly face to talk to at the 2019 Gordon Research Seminar for Polymers. Dr. Tong gave great feedback on my projects, always challenging me to look at them from a different perspective. I feel honored to have been guided by such a talented group of scientists and have no doubt that their mentorship was a huge proponent in my growth as a polymer chemist.

I would also like to thank Prof. Thomas Smith, my undergraduate research advisor when I was at Rochester Institute of Technology. Prof. Smith taught me how to conduct research and operate safely in a laboratory setting. He also started me down the path of learning polymer chemistry, inspiring me to further my education in the field. I will always appreciate being taught

the “old school” laboratory techniques, like pulling your own capillary tubes or performing polymerizations in sealed ampoules.

Of course, I must thank my family for their unfaltering belief in me throughout my studies. Though my mother and father never pursued higher education, they always encouraged me to continue learning. My father is the voice of reason in my life, always there to give me advice when I am unsure of how to approach something. I thank him for instilling his strong work ethic and confident attitude in me. To my mother, thank you for always calming me down no matter how stressed or overwhelmed I was. The reassurance of knowing that you were only ever one phone call away was a calming thought throughout my graduate school career.

During my time in the Matson lab, I have had the pleasure of working with several talented colleagues who have provided me with invaluable mentorship. Dr. Jeff Foster was my first mentor in graduate school. Jeff taught me the ropes of the Matson lab, from things like synthetic techniques to how to tell a story with your data. I am thankful for him helping to get me started off on the right foot in graduate school. Dr. Kyle Arrington was a great resource to learn about materials chemistry. Without his guidance, techniques like DSC and TGA would have been much more frustrating to pick up. Dr. Chadwick Powell was great for discussing organic synthesis or ideas for new projects. I often looked forward to the nights we would go out for some drinks and talk science. He was also a great flag football quarterback and led our team to some well-deserved wins.

Dr. Kuljeet Kaur quickly became one of my closest friends in the Matson lab. She was always willing to talk about science, or general problems in life, and could be counted on for support. I will always remember the many hours we spent working together to write a review article in 6 weeks. Kearsley Dillon is both a dear friend and a wonderfully talented chemist.

Whether we were outside enjoying the weather, or inside watching some football, I always enjoyed your company. While our friendship started in the Matson lab, I'm sure it will extend well beyond the time we both leave. Samantha Scannelli, I cannot say enough about how important you have been during my time in graduate school. Thank you for being my support system, the one person who I could confide in when I felt like giving up. You are a kindhearted person and a bright scientist. And I would also like to thank Anna Steele. Though we did not overlap for very long in the Matson lab, it was a pleasure teaching you what I know. I'm sure that your strong work ethic and creative mind will bring you much success during your time in graduate school.

Lastly, I would like to thank my friends outside of graduate school. Having a close-knit group of friends was vital to maintaining my sanity during the trials and tribulations of graduate research. Stacy Carlos, thank you for always being around to talk and play some video games when I needed to de-stress. Dylan Zottarelli, thanks for the frequent discussions of life, games, and the best shows to watch. Jayde Ngo, thanks for being my own personal life coach, and making sure I kept my work-life balance in check. There are too many others to name them all, but I am grateful to all the friends who have helped me along the way.

Table of Contents

Attribution xiii

Chapter 1: The Benefits of Macromolecular/Supramolecular Approaches in H_2S delivery: A Review of Polymeric and Self-Assembled Donors 1

1.1. Authors 1

1.2. Abstract 1

1.3. Introduction 2

1.4. Advantages of Macromolecular Systems 5

1.5. Macromolecular Systems with Covalently Bound H_2S Donors 5

1.5.1. H_2S Releasing Linear Polymers 7

1.5.2. Polymeric Micelles for H_2S Delivery 10

1.5.3. Polymeric Liposomes 17

1.5.4. Polymeric Micro/Nanoparticles 18

1.5.5. Complex Self-Assembled and Crosslinked Materials 21

1.5.6. De-polymerizable H_2S-Donating Systems 26

1.6. Macromolecular Systems with Physically Entrapped H_2S Donors 28

1.6.1. Hydrogels 30

1.6.2. Electrospun Fibers 30

1.6.3. De-polymerizable H_2S-Donating Systems 33

1.7. Key Challenges and Future Perspectives 35

1.8. Acknowledgements 39

1.9. References 39

Chapter 2: Tuning H_2S Release by Controlling Mobility in a Micelle Core 50

2.1. Authors 50

2.2. Abstract 50

2.3. Introduction 51

2.4. Results and Discussion 54

2.4.1. Influence of Electronics on H_2S Release from Statistical Block Copolymers 54

2.4.2. Micelle Swelling using EtOH 57

2.4.3. Tuning the Glass Transition Temperature of the H_2S-Releasing Block 59

2.4.4. Effect of Core Mobility on Diffusion 64

2.4.5. Effect of Core Mobility on H_2S Release 66

2.5. Conclusions 68

2.6. Acknowledgements 69
2.7. References 69
2.8. Experimental 72
2.9. Experimental References.....116
Chapter 3: Tuning Small Molecule Release from Polymer Micelles: The Effect of Crosslinking in the Hydrophobic Block 117
3.1. Authors 117
3.2. Abstract 117
3.3. Introduction 118
3.4. Results and Discussion.....121
3.4.1. Synthesis of Micelles with Crosslinks in the Hydrophobic Core 121
3.4.2. Installation of SATO H_2S Donors into Micelle Cores 129
3.4.3. Impact of Crosslinking Percentage of the Hydrophobic Block on H_2S Release Rate131
3.5. Conclusions 134
3.6. Acknowledgements 134
3.7. References 135
3.8. Experimental 140
3.9. Supporting Information 147
3.10. Supporting Information References 166
Chapter 4: Strong Variation of Micelle-Unimer Coexistence as a Function of Core Chain Mobility.....167
4.1. Authors 167
4.2. Abstract 167
4.3. Introduction 168
4.4. Results and Discussion.....170
4.5. Conclusions 182
4.6. Acknowledgements 183
4.7. References 183
4.8. Experimental 188
4.9. Experimental References.....231
Chapter 5: Development of Controlled Polymerization Methods for the Preparation of Poly(Olefin Sulfones) 233
5.1. Authors 233

5.2. Abstract 233
5.3. Introduction 234
5.4. Results and Discussion 236
5.4.1. Determining a Polymerization Method for Controlled Synthesis of POSs 236
5.4.2. Evaluating Photoiniferter Polymerization in the Controlled Synthesis of POSs 238
5.4.3. Utilizing photo-RAFT Polymerization in the Controlled Synthesis of POSs 245
5.5. Conclusions and Future Work 251
5.6. References 252
5.7. Experimental 255
5.8. Experimental References 262
Chapter 6: Conclusions and Future Perspectives 263

Attribution

This work was completed with the help of several colleagues. A brief description of the contributions from each person is included below:

Chapter 1: Ryan J. Carrazzone (graduate student, Macromolecular Science and Engineering, Virginia Tech) performed the writing and editing for portions of this chapter. Kuljeet Kaur (graduate student, Department of Chemistry, Virginia Tech) also performed the writing and editing for portions of this chapter. John B. Matson (Ph.D., Department of Chemistry, Virginia Tech) is the advisor and committee chair who provided guidance, writing, and editing for this chapter.

Chapter 2: Ryan J. Carrazzone (graduate student, Macromolecular Science and Engineering, Virginia Tech) performed the writing, editing, synthesis, and experimental work for portions of this chapter. Jeffrey C. Foster (graduate student, Department of Chemistry, Virginia Tech) also performed the writing, editing, synthesis, and experimental work for portions of this chapter. Nathan J. Spear (undergraduate student, Department of Chemistry, Virginia Tech) performed the synthesis for portions of this chapter. Scott C. Radsinski (graduate student, Department of Chemistry, Virginia Tech) provided synthetic guidance for this chapter. Kyle J. Arrington (graduate student, Department of Chemistry, Virginia Tech) assisted with DSC analysis for this chapter. John B. Matson (Ph.D., Department of Chemistry, Virginia Tech) is the advisor and committee chair who provided guidance, writing, and editing for this chapter.

Chapter 3: Ryan J. Carrazzone (graduate student, Macromolecular Science and Engineering, Virginia Tech) performed the writing, editing, synthesis, and experimental work for most of this chapter. Jeffrey C. Foster (graduate student, Department of Chemistry, Virginia Tech) provided editing and synthetic guidance for this chapter. Zhao Li (graduate student, Department of

Chemistry, Virginia Tech) provided TEM images for portions of this chapter. John B. Matson (Ph.D., Department of Chemistry, Virginia Tech) is the advisor and committee chair who provided guidance, writing, and editing for this chapter.

Chapter 4: Ryan J. Carrazzone (graduate student, Macromolecular Science and Engineering, Virginia Tech) performed the writing, editing, synthesis, and experimental work for most of this chapter. Xiuli Li (graduate student, Department of Chemistry, Virginia Tech) performed the experimental work, data analysis, and editing for portions of this chapter. Jeffrey C. Foster (graduate student, Department of Chemistry, Virginia Tech) provided editing and synthetic guidance for this chapter. Candace E. Wall (M.S., Department of Chemistry, Virginia Tech) and Alan R. Esker (Ph.D., Department of Chemistry, Virginia Tech) performed contact angle measurements and provided experimental guidance for portions of this chapter. Louis A. Madsen (Ph.D., Department of Chemistry, Virginia Tech) provided guiding, writing, and editing for this chapter. John B. Matson (Ph.D., Department of Chemistry, Virginia Tech) is the advisor and committee chairs who also provided guidance, writing, and editing for this chapter.

Chapter 5: Ryan J. Carrazzone (graduate student, Macromolecular Science and Engineering, Virginia Tech) performed the writing, editing, synthesis, and experimental work for most of this chapter. Anna Steele (graduate student, Department of Chemistry, Virginia Tech) performed the synthesis and experimental work for portions of this chapter. Kearsley M. Dillon (graduate student, Department of Chemistry, Virginia Tech) provided synthetic and experimental guidance for portions of this chapter. John B. Matson (Ph.D., Department of Chemistry, Virginia Tech) is the advisor and committee chair who provided guidance, writing, and editing for this chapter.

Chapter 1: The Benefits of Macromolecular/Supramolecular Approaches in H_2S delivery: A Review of Polymeric and Self-Assembled Donors

Reprinted (adapted) with permission from: Carrazzone R. J. et al. *Antioxid. Redox Signal.* **2020** *33*, 79-95. Copyright 2020 Mary Ann Liebert Inc. https://doi.org/10.1089/ars.2019.7864

1.1 Authors:

Ryan J. Carrazzone, [§,†,‡] Kuljeet Kaur, [§,‡] John B. Matson*[§,‡]

[§]Department of Chemistry, Virginia Tech, Blacksburg, Virginia 24060, United States

[†]Macromolecules Innovation Institute, Virginia Tech, Blacksburg, Virginia 24060, United States

[‡]Virginia Tech Center for Drug Discovery, Virginia Tech, Blacksburg, Virginia 24060, United States

1.2 Abstract:

***Significance*:** Cell homeostasis and redox balance are regulated in part by hydrogen sulfide (H_2S), a gaseous signaling molecule known as a gasotransmitter. Given its biological roles, H_2S has promising therapeutic potential, but controlled delivery of this reactive and hazardous gas is challenging due to its promiscuity, rapid diffusivity, and toxicity at high doses. Macromolecular and supramolecular drug delivery systems are vital for the effective delivery of many active pharmaceutical ingredients, and H_2S stands to benefit greatly from the tunable physical, chemical, and pharmacokinetic properties of polymeric and/or self-assembled drug delivery systems.

***Recent Advances*:** Several types of H_2S-releasing macro- and supramolecular materials have been developed in the past five years, and the field is expanding quickly. Slow-releasing polymers,

polymer assemblies, polymer nano- and microparticles, and self-assembled hydrogels have enabled triggered, sustained, and/or localized H_2S delivery, and many of these materials are more potent in biological assays than analogous small molecule H_2S donors.

***Critical Issues*:** H_2S plays a role in a number of (patho)physiological processes, including redox balance, ion channel regulation, modulation of inducible nitric oxide synthase, angiogenesis, blood pressure regulation, and more. Chemical tools designed to 1) deliver H_2S to study these processes, and 2) exploit H_2S signaling pathways for treatment of diseases require control over the timing, rate, duration, and location of release.

***Future Directions*:** Development of new materials approaches for H_2S delivery that enable long-term, triggered, localized, and/or targeted delivery of the gas will enable greater understanding of this vital signaling molecule and eventually expedite its clinical application.

1.3 Introduction:

Next-generation approaches to disease treatment will rely on the precise and controlled delivery of active pharmaceutical ingredients (APIs) such as drugs, peptides, enzymes, and vaccines, among others.[1-3] To this end, drug delivery systems provide numerous benefits, including a wide range of administration techniques, increased efficacy and longer circulation times relative to pure APIs, and the potential for advanced delivery conditions (e.g., targeting, triggered response). Often researchers transport, contain, and/or protect therapeutic agents using synthetic polymers due to their ease of synthesis and wide versatility.[4] In fact, many pharmaceuticals on the market use macromolecular/supramolecular delivery approaches including microparticle depots (e.g., Lupron, Vivitrol), liposomal formulations (e.g., Doxil), nanoparticles (e.g., Abraxane), and

implantable systems (e.g., Vitrasert).[5-9] The development of polymeric drug delivery systems is well studied, with many thorough reviews existing in the literature.[10-15] Despite several decades of work in this field, there remains a clinical need to continue to develop drug delivery systems.

Signaling gases, known as gasotransmitters,[16-18] stand to benefit from drug delivery approaches even more than conventional small molecule drugs, proteins, and other APIs due to their potency and fast action. Gasotransmitters are biological signaling molecules which fulfill several well-defined criteria, the most important being enzymatic regulation of their production/metabolism and their independence from specific membrane receptors.[19-20] There exist three known gasotransmitters: Nitric oxide (NO), carbon monoxide (CO), and hydrogen sulfide (H_2S). Each is produced and regulated endogenously, and each has specific physiological functions and targets. There exist therapeutics on the market and/or in clinical trials for formulations of each gasotransmitter, either in the form of the gas itself or as small molecules that release or generate the gas in vivo.[21-23] Unlike other chemical messengers, gasotransmitter signaling is not limited by exocytosis-mediated release, receptor-binding, vesicular storage, and/or elaborate removal processes from the site of action.[18] Instead, cells quickly turn on or off gasotransmitter production to regulate autocrine or paracrine signaling, and these gases diffuse rapidly through biological membranes. Their short *in vivo* half-lives match their rapid production, allowing NO, CO, and H_2S to work together to regulate cell behavior nearly instantaneously.[24] Due to their gaseous nature, fast diffusivity, and high reactivity, gasotransmitters are challenging to administer therapeutically but may offer substantial benefits if delivered at a desired site of action in a controlled manner.

H_2S, the most recent addition to the list of gasotransmitters,[19,25-26] has attracted attention due to its various biological roles, including cardioprotection,[27-29] vasodilation,[30-32] angiogenesis,[33-35] anti-inflammation,[36-37] neurotransmission,[38-40] and others. It is produced

endogenously by the enzymes CSE, CBS, and 3-MST, which are present in organs and systems throughout the body. Physiological concentrations of H_2S are highly regulated by distinct biosynthetic processes, which contribute toward homeostasis of the organism. The appreciable roles of H_2S in physiological and pathophysiological processes have led researchers to develop methods to deliver H_2S to study its physiological pathways and therapeutic potential.[41-43] Indeed, small molecules that release H_2S *in vivo* (so-called H_2S donors) provide evidence for the beneficial effects of exogenous delivery of H_2S.[44-47] However, as is true for other gasotransmitters, H_2S is toxic at high concentrations, it has a short half-life, and it has no specific receptor but many targets. Coupled with its propensity to oxidize, these factors make sustained release and precise dosage control vital for H_2S delivery, even more so than in delivery of traditional therapeutics.[48]

Delivery of H_2S can take several forms. Direct inhalation presents the most straightforward method for exogenous H_2S administration, delivering the gas without any byproducts or carriers. The inhalation method can deliver the required H_2S dosage by modulating gas partial pressure over time. Researchers have successfully employed inhalation to systemically deliver H_2S in mice, initiating a state of suspended animation or slower metabolism.[49] Despite its advantages, inhaled delivery of H_2S is not likely to reach a clinical setting due to the malodorous nature of the gas and its lack of targeting. Stringent safety regulations concerning storage of this flammable and corrosive gas also hinder inhaled delivery. Inorganic sulfide salts (NaHS, Na_2S, and CaS) are common alternatives to gaseous H_2S delivery, providing instantaneous access to H_2S in its pure form while avoiding the need to handle the gas directly. Sulfide salts are currently the most widely employed delivery strategy in biological and preclinical studies investigating the *in vitro* and *in vivo* role of H_2S. Despite their availability and easy administration, sulfide salts have several drawbacks. In particular, the burst H_2S release profile from aqueous sulfide salt solutions stands

in stark contrast to sustained, tightly regulated enzymatic H_2S production. To address these drawbacks, chemists and pharmacologists have designed synthetic H_2S donors over the past decade with control over the release kinetics, dosage, and location of release. Recent reviews cover the many types of existing small molecule H_2S donors.[50-53] However, designing a synthetic H_2S donor is not trivial and requires careful consideration of stability, water solubility, H_2S release rate, trigger specificity, and toxicity of the donor itself as well as any byproducts generated after H_2S release. Thus, despite great progress in the development of H_2S donors, advanced delivery methods are still needed.

Due to the benefits of drug delivery systems, and the inherent challenges in effectively delivering H_2S, there has been a strong interest in macromolecular and supramolecular H_2S donors.[48,54-55] Here we provide an overview of the development and current state of macromolecular/supramolecular H_2S donor systems. In particular, we focus on the distinct advantages that polymeric and self-assembled delivery systems provide over small molecule H_2S donors, and we illustrate how these advantages may enable a greater understanding of H_2S (patho)physiology and potentially translate to clinical applications of H_2S therapy.

1.4 Advantages of Macromolecular Systems:

Macromolecular/supramolecular drug delivery systems can modulate the chemical, physical, and pharmacokinetic properties of an API without drastically changing the chemical nature of the payload. Through this control over these key properties, many of the challenges associated with delivering therapeutics can be addressed. For example, a large number of potential therapeutic agents are inherently hydrophobic. This presents a problem with solubility in biological systems, ultimately leading to low bioavailability and drug efficacy. Incorporating the hydrophobic

drug into a water-soluble polymeric drug delivery system facilitates delivery in aqueous environments.[56-57] Furthermore, the incorporated hydrophobic drug adopts the pharmacokinetic properties of the polymer/supramolecular structure; therefore, changes that alter these properties (i.e., changes to polymer composition, morphology, or functionality) may enable sustained or timed release of the payload.[13,58] Additionally, the polymer/supramolecular scaffold shields the entrapped API from the surrounding environment, leading to reduced cytotoxicity in situations where a burst release of the drug might be hazardous or toxic.[59] The shielding structure also provides a large area for attachment of targeting functionalities, which may enable triggered or localized release of the payload.[60-61] Altogether, it is clear that integrating small molecule therapeutics into macromolecular/supramolecular systems provides advantages for biological delivery.

The two major strategies for preparing macromolecular drug delivery systems include covalent linkage and physical entrapment. In the covalent linkage approach, APIs are chemically linked to polymer scaffolds. The linkage method often depends on the specific chemical nature of the API, making this approach specific to a given drug. In the physical entrapment approach, APIs are sequestered in polymeric nanostructures without the formation of covalent bonds. While this approach often leads to lower loading rates than covalent linking, the lack of chemical modification enables its use with a wider range of APIs. For example, poly(lactide-*co*-glycolide) (PLGA) has been used to deliver a wide range of APIs by physical entrapment.[62-65] While these preparation methods differ in their implementation, they both succeed in changing the chemical, physical, and pharmacokinetic properties of small molecule drugs, proteins, and other APIs.

1.5 Macromolecular Systems with Covalently Bound H_2S Donors:

Chemically linking APIs to a polymer scaffold, despite the need for linker chemistry

specific to each API, provides several advantages over physical entrapment. For example, a physically entrapped API is prone to leaching, a process in which the drug escapes from the polymer scaffold in an undesirable fashion (i.e., too quickly or before reaching the desired site of release). Covalent linkage of drug to the polymer scaffold minimizes leeching and maintains the desired release profile and/or pharmacokinetics. Additionally, chemical incorporation of the API can be used to influence the physical properties of the polymer itself. For example, conjugation of a hydrophobic drug to a hydrophilic polymer can result in amphiphilic behavior, which provides a method for modifying the morphology of the system that is unique to covalently linked donors. Finally, covalent linkers can be designed to release the drugs under specific conditions, such as a change in pH or the presence of a particular enzyme. As a result of these advantages of covalently linked drug delivery systems over physically entrapped systems, a variety of chemically linked H_2S releasing polymers have been developed.

1.5.1 H_2S Releasing Linear Polymers:

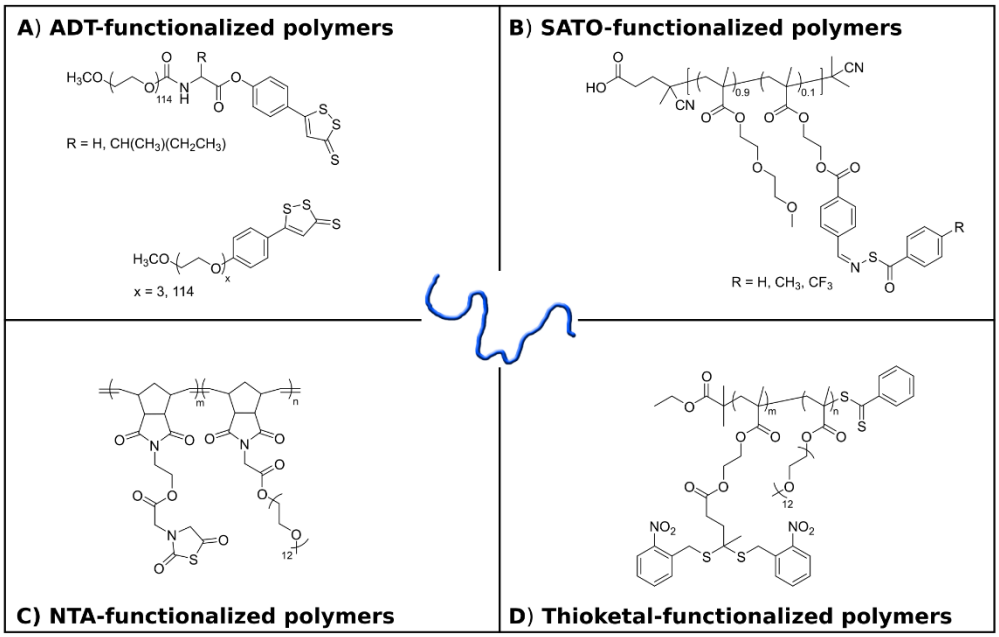

Figure 1-1. Chemical structures of H_2S-releasing linear polymers: A) ADT-functionalized PEG-based polymers. **B)** SATO-functionalized copolymer. **C)** NTA-functionalized statistical copolymer. **D)** Thioketal-functionalized copolymer. PEG, poly(ethylene glycol); ADT, 5-(4-hydroxyphenyl)-3H-1,2-dithiole-3-thione; SATO, *S*-aroylthiooxime; NTA, *N*-thiocarboxyanhydride.

Covalent attachment of an H_2S donating motif to a linear polymer provides a simple strategy for design of a macromolecular donor. To this end, a variety of systems utilizing small molecule H_2S donors attached to linear polymers have been developed. A popular H_2S donor that can be easily attached to polymers is 5-(4-hydroxyphenyl)-3*H*-1,2-dithiole-3-thione (ADT-OH). ADT-OH is the active metabolite in anethole trithione (a bile-secretion stimulating drug used in the treatment of dry mouth) and may have bioactivity aside from releasing H_2S[66]; beyond this, its mechanism of release is not clear, nor are the factors that affect its rate of release. Despite these issues, it has been conjugated onto several polymer systems, the first of which was reported by

Hasegawa et al. in 2014 (Fig. 1-1A).[67] In this work, ADT-OH was conjugated to the chain end of poly(ethylene glycol) (PEG), producing PEG-ADT. Conjugation to the polymer provided improved solubility of the drug, significantly reducing toxicity *in vitro* in RAW-Blue macrophages. Interestingly, the authors demonstrated that PEG-ADT conjugates became less cytotoxic with more hydrolytically stable linkages, underlining the importance of covalently attaching ADT-OH to the polymer. The PEG-ADT conjugates entered cells through endocytosis, while small molecule ADT-OH diffused across the cell membrane into the cytoplasm. The authors attribute the difference in cytotoxicity between small molecule and polymeric donors to a difference in intracellular distribution due to these unique pathways of cellular entry. Furthermore, the slower release of H_2S from PEG-ADT relative to ADT-OH resulted in a significantly enhanced potentiating effect on lipopolysaccharide-induced inflammation.

Also in 2014, our group developed macromolecular H_2S-donating polymers with each repeating unit functionalized with *S*-aroylthiooximes (SATOs) through a post-polymerization modification of pendant aldehyde groups (Fig. 1-1B).[68] SATOs, reported by our group earlier in 2014, release H_2S upon addition of a thiol. H_2S release rate from SATOs could be tuned by changing substituents on the aroyl ring.[69] The SATO-conjugated polymers retained control of H_2S release through electronics of the aroyl structure, allowing for the preparation of several polymers with varying H_2S release kinetics. A statistical copolymer, in which polymer repeat units are randomly distributed, containing SATO pendant groups as well as oligo(ethylene glycol) (OEG) pendant groups enhanced the water solubility of these hydrophobic donors.

In 2016, we developed a different H_2S-donating polymer system using *N*-thiocarboxyanhydrides (NTAs) as the H_2S-releasing groups (Fig. 1-1C).[70] Nucleophilic addition of an amine to the carbonyl neighboring the unsubstituted CH_2 unit caused ring-opening of the

NTA and released carbonyl sulfide (COS), which is rapidly converted into H_2S enzymatically by carbonic anhydrase.[71] We synthesized NTA-functionalized and OEG-functionalized norbornene derivatives for use in ring-opening metathesis polymerization (ROMP). ROMP provided a polymerization method devoid of nucleophiles potentially capable of opening the NTA ring, and copolymerization with the OEG-functionalized norbornene derivative imparted good water solubility to the copolymer. Conjugation of NTA motifs to the polymer resulted in prolonged H_2S release, with a 3-fold increase in release half-life relative to the small molecule NTA. This change in release profile may be a result of steric crowding around the NTA, retarding nucleophilic addition, which again showcases the protective effect of polymer systems on sensitive prodrugs.

Recently Li et al. reported an H_2S-donating polymer system based on conjugation of 2-nitrobenzenemethanethiol to pendant ketones on a polymethacrylate backbone, creating a photodegradable thioketal linkage (Fig. 1-1D).[72] Upon UV irradiation, the thioketal linkage degraded to release H_2S and 1,2-nitrobenzaldehyde, while also regenerating the parent polymer. Copolymerization of a ketone functionalized methacrylate with an OEG-functionalized methacrylate produced a highly water-soluble graft copolymer with a molecular weight close to the renal excretion threshold (40 kg/mol), the size below which clearance by the kidneys is rapid.[73] The rate of H_2S release from the copolymer correlated positively with the intensity of UV irradiation, with no release observed in the absence of irradiation. Additionally, the gem-dithiol functionalized polymer and its byproducts showed no cytotoxicity below 25 µM in NIH3T3 cells.

1.5.2 Polymeric Micelles for H_2S Delivery:

Polymer micelles, a common drug delivery system made from amphiphilic block copolymers, are known for their drug loading capability and long circulation times in the

bloodstream.[74] In such systems, amphiphilic block copolymers, polymers in which long runs of repeat units are discretely partitioned but chemically linked, self-assemble in water to form micelles due to the differential solubility of the component blocks. Polymer micelles form core-shell architectures in aqueous environments, with hydrophobic blocks forming the core and hydrophilic blocks composing the surrounding shell. As a result, micellar systems can carry various hydrophobic drug molecules within their cores, either through covalent attachment or via physical encapsulation, thereby behaving as efficient drug delivery vehicles. Furthermore, the size range (typically 10–100 nm) of polymer micelles is critical in determining their biodistribution, as larger micelles may exceed the renal excretion threshold and accumulate in sites of interest through the enhanced permeability and retention (EPR) effect.[75] Additionally, micellar carriers improve aqueous solubility and prolong the circulation times of encapsulated hydrophobic small molecule APIs in the bloodstream.

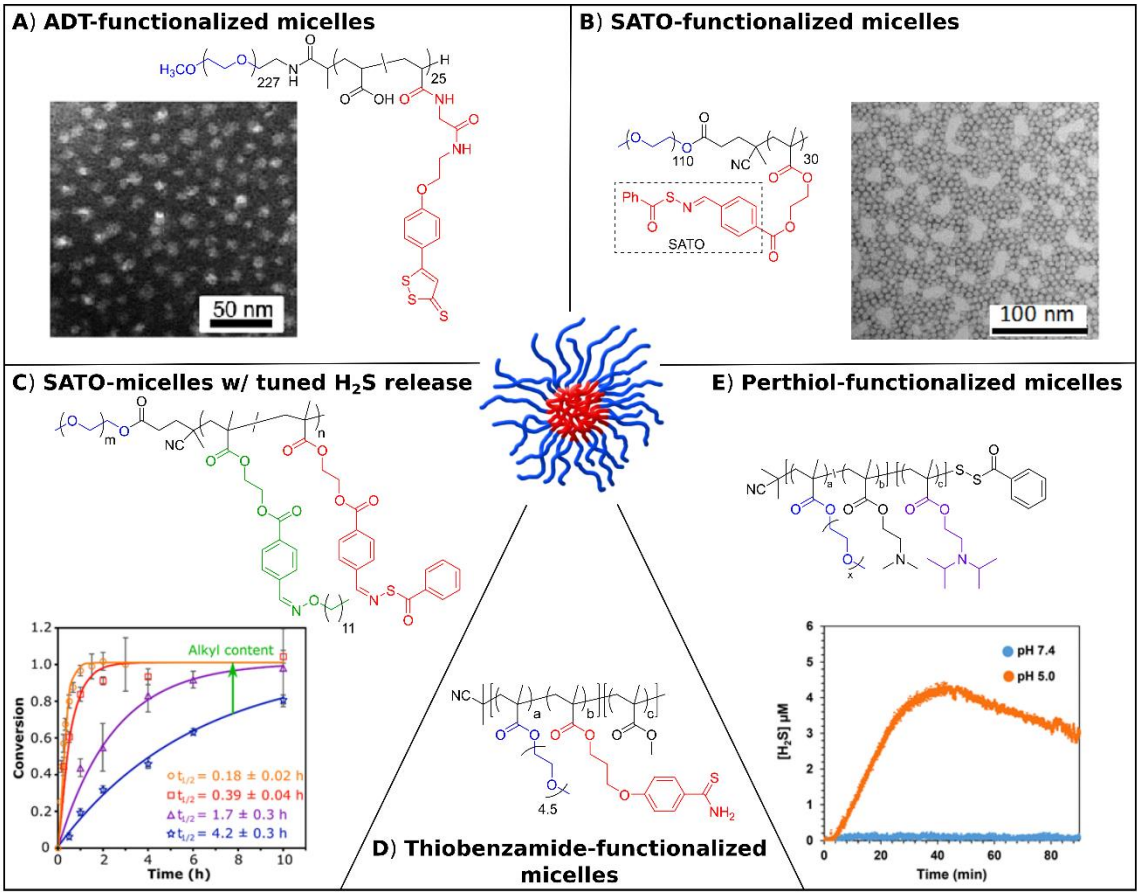

Figure 1-2. H_2S-releasing micelles from amphiphilic block copolymers: A) PEG-*b*-PADT block copolymer consisting of PEG and ADT-functionalized blocks and TEM image of block copolymer micelles. **B)** SATO-functionalized block copolymer with PEG as a hydrophilic block and TEM image of block copolymer micelles. **C)** Structure of SATO-functionalized block copolymers consisting of a PEG hydrophilic block and alkyl-*co*-SATO-functionalized blocks as hydrophobic blocks. A graphical representation of H_2S release kinetics of the micelles depicting decrease in H_2S release half-lives with increasing amounts of alkyl component. **D)** Structure of thiobenzamide-functionalized block copolymer. **E)** Structure of PEG-based block copolymer with persulfide end group and a graph of H_2S release at two pH values. TEM, transmission electron

microscopy; PEG, polyethylene glycol; PADT, poly(5-(4-hydroxyphenyl)-3H-1,2-dithiole-3-thione); SATO, *S*-aroylthiooxime.

Among the earliest examples of H_2S releasing polymer micelles, Hasegawa et al. expanded upon their previous work with linear H_2S-donating polymers to create ADT-containing polymer micelles (Fig. 1-2A).[76] In this work, ADT was conjugated to poly(acrylic acid) that was polymerized through reversible addition-fragmentation chain-transfer (RAFT) polymerization, a radical polymerization technique capable of producing polymers with controllable molecular weights and end-group fidelity, using a PEGylated chain transfer agent (CTA) to yield an amphiphilic block copolymer. Here PEG was the hydrophilic block and ADT-functionalized poly(acrylic acid) was the hydrophobic block (PADT). Analysis by dynamic light scattering (DLS) and transmission electron microscopy revealed formation of spherical micelles in water, with an average hydrodynamic radius of 36 nm. Although only small amounts were released, the H_2S release profiles observed for these PEG-*b*-PDAT polymer micelles were similar to those for linear PEG-ADT, indicating that micellization did not hinder H_2S release from the encapsulated ADT-OH moieties. As reported for PEG-ADT linear polymers, PEG-*b*-PADT micelles showed less cytotoxicity than small molecule ADT-OH *in vitro*. Interestingly, PEG-*b*-PADT micelles enhanced the pro-inflammatory response in gardiquimode-stimulated murine macrophages, whereas ADT-OH slightly decreased the pro-inflammatory response under similar conditions. The observed difference is likely due to the altered cellular internalization of ADT micelles relative to ADT-OH, similar to that observed for ADT-PEG polymers. This study showed the ability of micellar systems to attenuate certain toxic effects of H_2S donors by shielding them and controlling their entry into cells.

In 2017, we reported an H_2S-releasing polymer micelle system to address the rapid clearance rate associated with linear polymers and access better pharmacokinetics (Fig. 1-2B).[77] In this work, 2-(4-formylbenzoyloxy)ethyl methacrylate (FBEMA) monomer was polymerized via RAFT using a PEGylated CTA to give an amphiphilic block copolymer bearing pendant SATO in the hydrophobic block. Uniform spherical micelles were then prepared with an average core diameter of 21 ± 2 nm as measured via TEM and hydrodynamic diameter of 38 ± 4 nm as measured by DLS. Confinement of SATO moieties in the hydrophobic core of micelles resulted in a significant increase in the H_2S release half-life, with micelles releasing 9-fold more slowly than a small molecule analog. We attributed this drastic difference in release rate to restricted diffusion of the hydrophilic Cys trigger into the hydrophobic micelle cores, retarding H_2S release compared with molecularly dissolved small molecules and linear polymers. This finding highlights the potential for tuned release rate of H_2S through control of polymer properties. Furthermore, the polymer micelles were more effective relative to common small molecule H_2S donors (Na_2S, a small molecule SATO, and GYY4137) in decreasing viability of HCT116 colon carcinoma cells. These results reveal the importance of H_2S release rate on biological activity and further underline the potential of polymeric H_2S donors.

Expanding upon the previous study, in 2019 we developed a method for systematically tuning H_2S release rate from SATO-conjugated micelles (Fig. 1-2C).[78] PEG-*b*-pFBEMA block copolymers, prepared in a similar fashion to the previous work, were conjugated with functionalized SATO derivatives. We hypothesized that controlling the rate of Cys diffusion into the micelle core would control the H_2S release rate. H_2S release experiments on micelles swollen in water with varying amounts of ethanol provided evidence to support this claim, where the H_2S release rate became increasingly faster with greater degrees of micelle swelling. We further

hypothesized that H_2S release from SATO-conjugated micelles could be systematically tuned by controlling the chain mobility of the micelle core. To this end, we co-functionalized PEG-*b*-FBEMA block copolymers with varying amounts of SATO and an alkyl plasticizing agent, which we expected would increase the mobility of polymer chains. As expected, the resulting series of block copolymers showed a trend in hydrophobic block T_g, the temperature above which long-range polymer backbone movement can occur, correlating with the mass ratio of SATO versus alkyl group. Additionally, the H_2S release rate varied over 20-fold throughout the series, with the lowest T_g hydrophobic block resulting in a release half-life similar to that of small molecule SATOs. Overall, this work highlighted the structural tunability of polymeric micelles and demonstrated precise control over H_2S release from a polymeric system without chemically modifying the donor.

Another thiobenzamide-functionalized macromolecular H_2S-releasing system was reported by Davis et al. in 2016 (Fig. 1-2D).[79] Two amphiphilic polymethacrylates were synthesized by co-polymerizing 3-(4-cyanophenoxy)propyl methacrylate (CPPMA), oligo(ethylene glycol) monomethyl ether methacrylate (OEGMA), and methyl methacrylate using RAFT polymerization. Pendant thioamides were generated in-situ via thionation of benzonitrile pendant groups present on the CPPMA block in a post-polymerization modification. The final polymers, [POEGMA-*co*-PTHA]-*b*-PMMA and PEOGMA-*b*-[PTHA-*co*-PMMA] both formed micelles in aqueous buffered solutions. Faster H_2S release from [POEGMA-*co*-PTHA]-*b*-PMMA versus PEOGMA-*b*-[PTHA-*co*-PMMA] micelles was attributed to the placement of the H_2S-releasing thioamide units in the hydrophilic corona of the micelle in the former system versus within the hydrophobic core for the latter system. The differences observed in the H_2S release profiles of the two micellar systems highlights the shielding effect of micellization in slowing

down the hydrolysis of donors encapsulated within the core. Furthermore, the H_2S delivered from slow-releasing PEOGMA-*b*-[PTHA-*co*-PMMA] polymer micelles gradually increased levels of cytosolic extracellular signal–regulated kinases and plasma membrane-localized protein kinase C activity in HEK293 cells.

In 2017, Quinn et. al. reported on H_2S releasing micelles from perthioester-containing polymer constructs synthesized via RAFT polymerization with facile end-group modification (Fig. 1-2E).[80] The benzyl dithioester chain end was first functionalized with pyridyl disulfide groups and subsequently reacted with thiobenzoic acid to yield polymers with benzoyl-capped perthiol ω-chain ends. The final perthioester-functionalized polymer P[OEGMA]-S-S-(C=O)Ph underwent nucleophilic attack by cysteine to release a free perthiol, which subsequently liberated H_2S. The polymer remained stable in buffered aqueous solutions without thiol. As an extension of this concept, the authors prepared an amphiphilic block copolymer by polymerizing butyl methacrylate as a hydrophobic block to yield P[OEGMA-*b*-BMA]-S-S-(C=O)Ph. This polymer readily formed micelles when dispersed in PBS (pH = 7.4) and showed significantly slower H_2S release relative to the homopolymers. Furthermore, a pH-responsive amphiphilic block copolymer was synthesized by copolymerizing *N*,*N*-(dimethylamino) ethyl methacrylate (DMAEMA) and *N*,*N*-(diisopropylamino) ethyl methacrylate (DIPMA) to generate P[OEGMA-*co*-DMAEMA-*b*-DIPMA]-S-S-(C=O)Ph. Cys-triggered H_2S release from these pH-responsive micelles significantly accelerated under acidic conditions. This phenomenon was attributed to increased hydrophilicity of the DIPMA block under acidic conditions, leading to micelle disassembly and increased exposure to cysteine; this work demonstrated the potential for triggered release of gasotransmitters through careful design of a polymeric drug delivery system.

1.5.3 Polymeric Liposomes:

Related to micelles, liposomes represent another nanostructure accessible from surfactants or amphiphilic block copolymers. The structure of liposomes resembles that of a lipid bilayer as found in cell membranes—the amphiphilic constituents of liposomes arrange in parallel to form a bilayer with hydrophilic units forming the lining of the bilayer and hydrophobic tails forming the core. As a result, liposomes can encapsulate hydrophobic drugs in the bilayer core and hydrophilic drugs in the aqueous inner compartment. Additionally, manipulation of membrane properties allows for controlled release of bilayer-encapsulated drugs and/or penetration of triggering molecules into the hydrophilic core.

In 2017, Quinn et. al. reported on a liposomal H_2S-donating macro- and supramolecular system utilizing PEG-cholesterol (PEG-Chol) conjugates with trisulfide linkages.[81] Organic polysulfides, which are biologically active components in various natural products, release H_2S upon thiol exchange reactions.[82-84] The authors hypothesized that incorporation of the trisulfide linker into the PEG-Chol conjugate would allow for thiol-triggered H_2S release, and the resultant disruption of the liposomal membrane might induce release of a hydrophilic payload trapped inside the liposome. Thiol-triggered release of H_2S from micelles formed by the trisulfide-linked conjugates was confirmed using SF4, an H_2S selective fluorescent probe. In contrast, no H_2S release was observed from micelles that included disulfide or amide linkages in place of the trisulfide. The PEG-Chol conjugates were then incorporated into pre-formed liposomes using the cholesterol group to anchor the conjugates into the bilayer. H_2S release from these liposomes was evaluated through amperometry using an H_2S-selective micro-sensor. Trisulfide conjugates incorporated into liposomes showed a reduced peaking concentration of H_2S relative to micelles. The authors attributed this decrease in total H_2S release to partial inaccessibility of trisulfides in

the bilayer membrane, which suggests a potential for tuning release from liposomes through control of membrane properties.

1.5.4 Polymeric Micro/Nanoparticles:

Nanoparticles range in diameter from a few to a few hundred nanometers, making them suitable for injection directly into the bloodstream. This allows for free circulation throughout the vasculature, targeting to specific tissues, and long-term systemic release of APIs for long-circulating nanoparticles. Polymer nanoparticles differ from polymer micelles in that they are typically made using specific processing methods such as nanoprecipitation, a phase separation process rather than a self-assembly process. Conversely, microparticles range in diameter from 1-100 μm and are therefore restricted in migrating from their site of injection. As a result, microparticles are more useful for applications requiring long-term localized release through injection or implantation at a desired site (e.g., muscle tissue, peritoneum). Due to their much smaller surface area to volume ratio compared with nanoparticles, microparticles degrade more slowly and release their cargo more slowly. Combined with their retention in tissue, these features make microparticles suitable for long-term delivery of APIs.

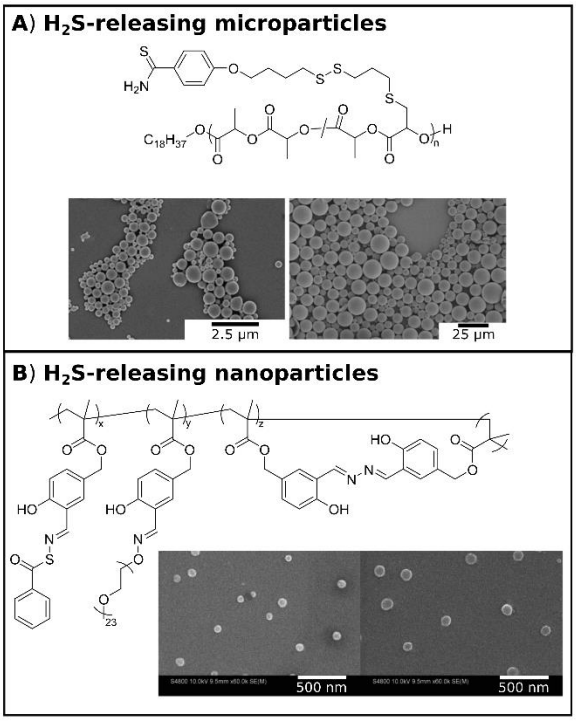

Figure 1-3. Chemical structure and TEM images of H_2S-releasing nano- and microparticles: A) Structure of thiobenzamides-containing polylactide block copolymer and SEM images of polymer microparticles. **B)** Statistical copolymer consisting of SATO-, PEG-, and AIEgen-functionalized polymethacrylate and SEM images of polymer nanoparticles. SEM, scanning electron microscopy; SATO, *S*-aroylthiooxime; PEG, polyethylene glycol; AIEgen, aggregation induced emission fluorophore.

In 2015, Bowden et al. reported a polymeric H_2S-donating microparticle system consisting of a polylactide backbone decorated with thiobenzamide groups.[85] Ring-opening copolymerization of l-lactide and a 4-hydroxythiobenzamide-functionalized lactide monomer afforded polymers with varying thiobenzamide loading along the backbone. Two sets of spherical microparticles were generated with average diameters of 12 ± 4 and 0.5 ± 0.1 µm (Fig. 1-3A). Degradation studies of

the microparticles revealed 10% weight loss after four weeks at pH 7.4, suggesting the potential for prolonged H_2S delivery. However, the authors could not quantitatively measure H_2S levels due to low thiobenzamide loadings in the microparticles, slow microparticle degradation, and rapid loss of H_2S from aqueous solutions. The need for better analytical methods to assess H_2S delivery over sustained periods is addressed in the Key Challenges and Future Perspectives section below. Despite this limitation, microparticle systems offer the potential for localized H_2S delivery in the range of weeks to months, which could be useful in a number of indications where low endogenous H_2S levels need long-term supplementation.

In related work focusing on nanoparticles instead of microparticles, Lin and co-workers recently described self-fluorescing, H_2S-releasing nanoparticles containing SATOs and aggregation-induced emission fluorophores (AIEgens).[86] RAFT polymerization of 3-formyl-4-hydroxybenzyl methacrylate (FHMA) yielded poly(FHMA) or pFHMA decorated with salicylaldehyde (ortho-hydroxybenzaldehyde) units as reactive handles, which were functionalized in three different ways (Fig. 1-3B). A small percentage of aldehyde units were functionalized with aminooxy PEG to impart water solubility to the polymer, while others were crosslinked with hydrazine to form salicylalhydrazine as an AIEgen. Crosslinking with hydrazine was carried out at a high dilution to promote intra-chain crosslinking of aldehyde units, yielding a water-soluble, AIE-active polymer nanoparticle. Finally, the remaining salicylaldehyde units were converted into SATO groups, yielding H_2S-releasing, AIE-active nanoparticles. The crosslinked polymers were then dispersed in water with vigorous stirring, and nanoparticles were in the range of 100 nm, as confirmed by SEM and DLS. Cellular internalization of the polymeric nanoparticles was observed by confocal laser scanning microscopy, highlighting the self-fluorescence characteristics of the nanoparticles. This was the first example of H_2S releasing nanoparticles that

could also be traced within the living systems. This work provides insight into the multi-functional capabilities of polymeric drug delivery systems and exhibits the potential for in vivo H_2S quantification directly at the targeted sites.

1.5.5 Complex Self-Assembled and Crosslinked Materials:

Hydrogels are three dimensional networks of entangled covalent or supramolecular polymers that trap a substantial amount of water. In the field of drug delivery, hydrogels are studied widely due to their resemblance to soft tissue in terms of morphology and mechanical properties combined with their ability to sequester and release APIs. Hydrogels can be broadly categorized as physically or chemically crosslinked gels depending on the type of network crosslinking. Physically crosslinked hydrogels retain their 3D structures through reversible, non-covalent supramolecular interactions, whereas covalent bonds link individual chains in chemically crosslinked hydrogels. Hydrogels can be particularly advantageous for delivering H_2S in a localized manner. While macromolecular assemblies like micelles and nanoparticles may deliver H_2S to the targeted tissues through systemic administration, hydrogels can be injected or implanted at the site of interest and deliver H_2S locally.

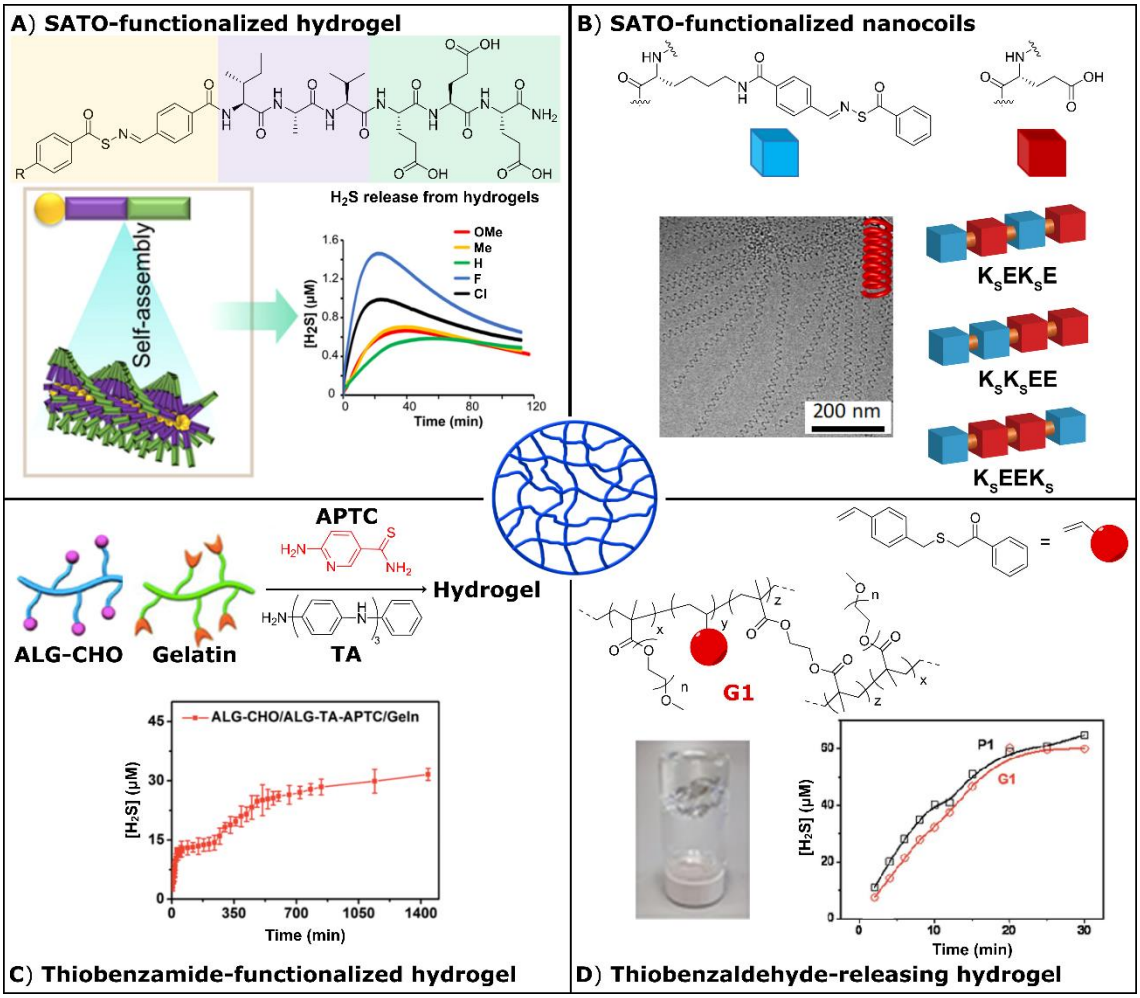

Figure 1-4. H_2S-releasing hydrogels with covalently bound H_2S donors: A) Structure of SATO-functionalized peptide with SATO unit screened in yellow, β-sheet region in purple, and charged region in green. Cartoon illustration shows self-assembly of SATO-peptide into one-dimensional nanostructures. H_2S release profiles of SATO hydrogels with varying SATO substituents show that peaking times and concentrations depend on R group. **B)** Structure of SATO-modified lysine and glutamic acid is represented as blue and red cubes respectively. Three different sequences of constitutionally isomeric peptides consisting of two lysine and two glutamic acid units each. Cryo-TEM image shows nanocoils formed by peptide K_sEEK_s. **C)** Schematic representation showing formation of multi-component hydrogel from partially oxidized alginate,

which is functionalized with TA and APTC and subsequently crosslinked with gelatin to form a hydrogel. The H_2S release profile from the final hydrogel shows gradual release extending over hours. **D)** Structure of thiobenzamide precursor and PEGMA polymer functionalized with thiobenzamide. A hydrogel was obtained by crosslinking PEGMA polymer with EDGMA. Graph of H_2S release from hydrogel G1 and polymer solution P1, showing similar release profiles. SATO, *S*-aroylthiooxime; TEM, transmission electron microscopy; APTC, 2-aminopyridine-5-thiocarboxamide; TA, tetraaniline; PEGMA, poly(ethylene glycol) methyl ether methacrylate; EDGMA, ethylene glycol dimethacrylate.

In 2015, our group reported a supramolecular, peptide-based H_2S-releasing hydrogel system containing a covalently bound SATO donor.[87] The 6-mer peptide sequence included a β-sheet-rich region (where peptide chains are arranged parallel/anti-parallel to each other and are stabilized by a network of intermolecular H-bonds), a hydrophilic region containing three glutamic acid residues, and the N-terminus functionalized with a SATO group. Driven by hydrophobic interactions and stabilized by hydrogen-bonding in the β-sheet rich region, the SATO-functionalized peptides self-assembled into nanofibers in aqueous solutions. At concentrations as low as 1 wt%, a robust hydrogel formed upon charge screening through the addition of $CaCl_2$. Due to shielding of the SATO groups in the nanofiber core, extended release was observed, with measurable H_2S levels beyond 15 h. More recently we conducted deeper investigations into these peptide-based materials by varying substituents on and around the SATO group (Fig. 1-4A).[88-89] Specifically, we found that R group substitution on the aroyl ring of the SATO unit affected the internal structure of the self-assembled nanofibers, which in turn regulated gel stiffness. H_2S release rates from the hydrogels depended on a complex balance between substituent electronic

effects and internal nanofiber morphology, but extended release profiles were observed for all hydrogels. These H_2S-releasing, peptide-based hydrogels may be ideal for localized H_2S delivery because the peptide components of the gels can be degraded into benign metabolites.

Recently we reported a self-assembled H_2S-releasing system based on constitutionally isomeric peptides.[90] A series of three tetrapeptides were designed with two lysine (K) and two glutamic (E) acid units varying in their placement along the peptide backbone (Fig. 1-4B). The lysine residues were modified with SATO groups, yielding three peptides, K_sEEK_s, K_sEK_sE, and K_sK_sEE (K_s = SATO-modified lysine). Peptide K_sEEK_s self-assembled into an unusual nanocoil morphology, whereas the other two peptides formed conventional twisted nanoribbons. Interestingly, H_2S release from the nanocoils was slower than release from the nanoribbons, which we attributed to slower diffusion of cysteine into nanocoils relative to nanoribbons. Furthermore, nanocoils were more effective compared to small molecule H_2S donors (GYY4137 and Na_2S) as well as nanoribbons in rescuing H9C2 cardiomyocytes from doxorubicin toxicity, likely due to the significant differences in H_2S release rates amongst the donors. This work demonstrated the influence of morphology on donor release profiles, and provided evidence for the increased efficacy of prolonged-release donors relative to burst-release. Comparisons in biological studies between comparable H_2S donors with different release rates will be vital for determining the optimal rate in various settings. Tuning nanostructures through supramolecular approaches may offer a method to modify release rate without changing H_2S donor chemistry or released byproducts, allowing for clear comparisons between H_2S donors with variable release half-lives.

Recently, Liang and co-researchers reported a smart, H_2S-releasing hydrogel for potential treatment of myocardial infarction.[91] The researchers synthesized a macromolecular H_2S donor by grafting 2-aminopyridine-5-thiocarboxamide (APTC), a thiol triggered H_2S donor, onto partially

oxidized alginate (Alg-CHO). The macromolecular donor was further functionalized by tetraaniline (TA) to impart conductivity to the final Alg-APTC-TA construct, which was crosslinked with gelatin to form an H_2S-releasing conductive hydrogel (Fig. 1-4C). The hydrogel showed strong adhesion to tissue due to presence of aldehyde groups on the hydrogel surface, which can react with nucleophilic amines in tissue proteins. The authors observed a significant increase in H_2S release half-life of small molecule APTC from 3 to 270 min by encapsulating it within the hydrogel, and the hydrogel showed extended H_2S release exceeding 24 h. The hydrogel was evaluated in mice hearts, exhibiting positive effects on function and remodeling of the left ventricle by significantly reducing cardiac fibrosis and ventricle wall thickening. This multifunctional hydrogel system underscores the importance of localized H_2S delivery for conditions like myocardial infarction and further demonstrates the potential for self-assembled systems to achieve these advanced drug delivery goals.

A light-responsive hydrogel was reported by Connal and co-workers in 2017.[92] They synthesized light sensitive thiobenzaldehyde precursors that released thioaldehydes upon irradiation. The released thioaldehydes further reacted with amines to form imines, releasing H_2S as a byproduct. The small molecule thiobenzaldehyde precursors released a small amount of H_2S upon irradiation followed by enhancement in H_2S release rate upon addition of amines. The authors then synthesized a vinyl monomer incorporating the thiobenzaldeyhyde precursor group, which was copolymerized with polyethylene glycol methacrylate (PEGMA) to form water soluble, light-sensitive, H_2S-releasing polymers, and further crosslinked with ethylene glycol dimethacrylate (EGDMA) to provide light-sensitive H_2S releasing hydrogels (Fig. 1-4D). Slow H_2S release rates were observed from the hydrogels and linear polymers relative to the small molecule donor. To

that end, the hydrogel was tested as a surface for cell-culture to study H_2S delivery *in vitro* and showed successful growth of cells on the gel surface and subsequent H_2S delivery.

1.5.6 De-polymerizable H_2S-Donating Systems:

An area of macromolecular drug delivery strategies that holds great potential but is in its infancy is depolymerizable systems. In such systems, therapeutic agents are covalently attached to or physically entrapped in polymers which can systematically depolymerize (also called self-immolation) upon application of a specific stimulus.[93-94] These strategies are appealing because they enable methods for triggered release of payloads and avoid the potentially long biological clearance times of polymer byproducts associated with conventional macromolecular drug delivery systems.

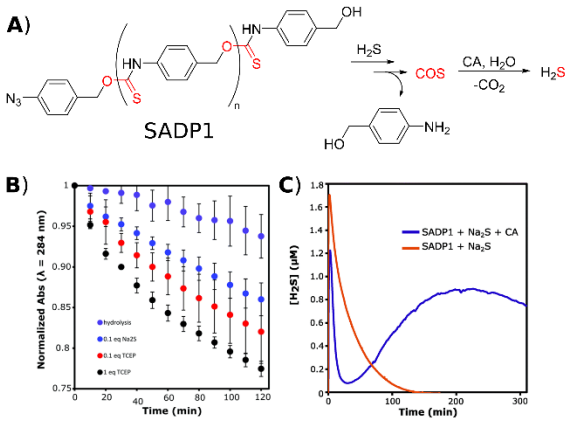

Figure 1-5. Depolymerizable H_2S-releasing polymers: A) Schematic illustration of H_2S-triggered depolymerization of SADP1 polymer. Reduction of the azide end group initiates de-polymerization of SADP1 polymer, generating COS, which is rapidly converted into H_2S by the enzyme CA. **B)** Graph of depolymerization kinetics measured via UV-Vis spectroscopy comparing

various triggers. **C)** Graph of H_2S release curves from SADP1 polymer with Na_2S as trigger. No H_2S release from the polymer was observed in the absence of enzyme CA. SADP1, self-amplified depolymerizable polymer; COS, carbonyl sulfide; CA, carbonic anhydrase.

In 2019, we developed a depolymerizable COS/H_2S donor based on oligo(thiourethanes).[95] A class of benzyl thiocarbamates developed by Pluth are COS/H_2S donors that can be triggered by a variety of stimuli.[96-97] Operating through a 1,6-elimination mechanism, cleavage of a protecting group initiates the reaction, generating the COS product that can be converted into H_2S by carbonic anhydrase. Inspired by this work, our group synthesized an aryl isothiocyanate monomer for use in a polyaddition reaction to form an oligothiourethane. This monomer was polymerized and end-capped with 4-azidobenzylalcohol to achieve an aryl azide end-capped oligothiourethane termed self-amplified depolymerizable polymer 1 (SADP1, Fig. 1-5A). Previous work suggested the potential for reduction of the aryl azide to the corresponding aryl amine upon reaction with two equivalents of H_2S, which provided a pathway for self-amplified depolymerization.[98] The molecular weight was limited to 1,600 g/mol due to the low thermodynamic driving force for the polymerization, but depolymerization triggered by reducing agents revealed a decrease in polymer peaks and the appearance of peaks representative of 4-aminobenzylalcohol by UV-Vis spectroscopy (Fig. 1-5B). The H_2S release profile of the oligothiourethane was observed by an H_2S-selective electrochemical probe (Fig. 1-5C). In the absence of carbonic anhydrase, addition of Na_2S to a SADP1 solution showed only a spike in H_2S concentration from the initial Na_2S addition. However, the experiment performed in the presence of carbonic anhydrase produced a sudden spike followed by a gradual increase in H_2S concentration over several hours. The gradual increase after the initial spike was a result of slow generation of COS through the depolymerization

mechanism, which was then converted into H_2S by carbonic anhydrase. In this way, the system self-amplified H_2S production, where two equivalents of H_2S reduced the azide end-group to trigger the depolymerization, generating several more equivalents of H_2S, which then went on to trigger more depolymerization, producing more H_2S. This work hints at the possibilities of depolymerizable polymers as carriers for delivery of "caged" small molecules such as H_2S, with potential to tune the triggering stimulus, the rate of H_2S production, and the released byproducts.

1.6 Macromolecular Systems with Physically Entrapped H_2S Donors:

Physical entrapment of APIs within macromolecular or supramolecular materials is experimentally simpler than covalent binding of APIs to the scaffold. Consisting at a minimum of only a polymer and the drug to be delivered, no linker chemistry needs to be developed, so chemical designs are less elaborate. Additionally, a wide range of APIs can be sequestered in the same polymer matrix, and multiple APIs can be entrapped if desired. On the macroscale, physical entrapment tends to affect the physical properties of the polymer matrix less than covalent attachment, so physical, morphological, and biological properties of the matrix can be determined and optimized independent of the API. A number of delivery systems have been developed based on physically entrapping H_2S donors.

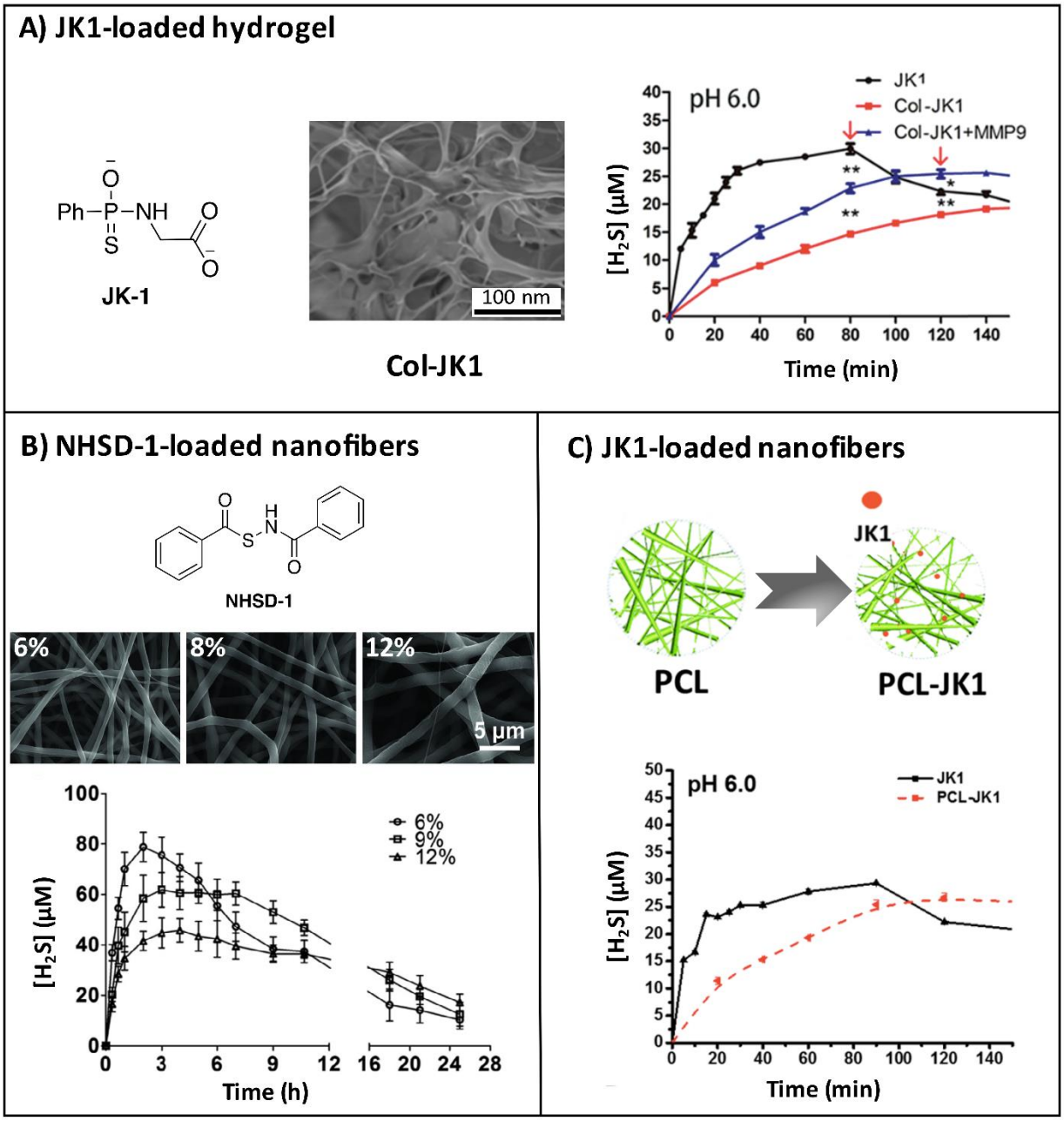

Figure 1-6. Hydrogels and nanofibers with physically entrapped H_2S donors: A) Chemical structure of pH sensitive JK1 donor and SEM images of Col-JK1 hydrogel. Graph of H_2S release comparing hydrogels and small molecule JK1 donor. **B)** Chemical structure of NHSD-1 donor and SEM images of fibers with varying PCL concentrations. Graph of H_2S release profile from fibers. **C)** Illustration showing JK1 donor embedded within PCL fibers and concentration vs. time graph

showing H_2S release profile. SEM, scanning electron microscopy; Col-JK1, collagen JK1; PCL, poly(caprolactone); NSHD-1, N-mercapto-based H_2S donor.

1.6.1 Hydrogels:

In 2019, Xiao et al. reported a dual pH- and enzyme-responsive H_2S-releasing hydrogel based on collagen for the potential treatment of indivertible disc degeneration (IDD).[99] A pH-sensitive small molecule H_2S donor, JK1, was encapsulated within the porous network of the collagen hydrogel to generate Col-JK1 gel (Fig. 1-6A). Col-JK1 could be slowly degraded by MMP9, an enzyme that is overexpressed under IDD conditions. Degradation of the collagen gel led to release of JK1 into the low pH environment of the inflamed tissue, where it underwent intramolecular cyclization to release H_2S. H_2S release from Col-JK1 was slower compared to the small molecule donor alone and was accelerated in the presence of MMP9. Furthermore, Col-JK1 successfully inhibited apoptosis in nucleus pulposus cells and prevented degradation of extracellular matrix (ECM), indicating its potential for IDD treatment. Encapsulating the donor within the collagen hydrogel not only increased its retention time in the IDD lesion and prolonged the H_2S release time, but it also created an enzyme-responsive, on-demand release system. However, H_2S release from Col-JK1 gel in the absence of MMP9 was still substantial, highlighting the need for continued development of enzyme-responsive systems that release H_2S only in the presence of the desired enzyme.

1.6.2 Electrospun Fibers:

A simple method to prepare drug-releasing polymers with control over release rates,

mechanical properties, and matrix degradability is electrospinning. Electrospinning is a process of generating nano/microfibers by spraying a continuous stream of polymer solution and stretching it under high voltage. Electrospun fibers, like polymeric and self-assembled hydrogels, resemble the ECM in morphology and mechanical properties and therefore find use as materials for tissue engineering and regenerative medicine. Electrospun fibers, however, are much larger in diameter than peptide-based nanofibers or polymer chains (in the range of ~1 µm versus 1-10 nm). The large diameter allows the fibrous network to physically entrap and stabilize drugs and other bioactive molecules with high drug loading capacity. Chemical structure and morphology affect polymer degradation kinetics, as does fiber diameter, giving researchers several methods to alter drug release profiles. With its tunability and versatility, the inexpensive technique of electrospinning is a natural fit for H_2S releasing materials, where control of release rate is vital.

Wang and co-workers reported the first electrospun H_2S-releasing microfibers in 2015 based on a biodegradable polycaprolactone (PCL) polymer matrix.[100] A solution of PCL at different concentrations (6%, 8%, and 12%) and a thiol activated H_2S-donor (NSHD1) were subjected to electrospinning to yield microfibers with diameters ranging from 0.5 to 1.5 µm (Fig. 1-6B). An increase in microfiber diameter was observed with increasing PCL concentration. SEM revealed smooth microfiber surfaces indicative of uniform distribution of NSHD-1 within the fibers, and FTIR spectroscopy confirmed NSHD-1 encapsulation. H_2S release half-lives for the microfibers were longer than NSHD-1 alone, with measurable H_2S levels extending past 24 h. Release rate depended on fiber thickness, with thicker fibers releasing more slowly than thinner ones. Additionally, these electrospun, H_2S-releasing microfibers protected H9C2 cardiomyocytes subjected to oxidative stress by addition of H_2O_2. They also enhanced proliferation of 3T3 fibroblasts, which is potentially useful for wound healing.

A few years later, the same group applied H_2S-releasing PCL nanofibers, with diameters near 300 nm, in the development of a nanofibrous coating for wound healing.[101] The fabrication and characterization of the nanofibers was similar to PCL-NSHD-1 nanofibers, but the pH-responsive H_2S donor JK1 was included instead. H_2S release from PCL-JK1 fibers was higher at pH 6 relative to physiological pH, and was significantly slower than small molecule JK1 donor alone, with measurable H_2S levels past 2 h (Fig. 1-6C). One-time application of PCL-JK1 nanofibrous scaffolds to full-thickness cutaneous wound models in mice showed successful wound regeneration over 20 d with healing rates significantly higher than PCL fibers alone. It is not clear how the release profile changed *in vivo* compared with the release over a few hours *in vitro*, but it likely released H_2S for a much longer period based on the results from the *in vivo* studies.

In 2018 Melino and co-workers reported electrospun microfibrous polylactic acid (PLA) membranes containing garlic-derived organosulfur compounds (OSCs) fabricated using two different approaches.[102] In the first approach, garlic oil-soluble extract (GaOS) was directly coated onto the electrospun microfibers (~700 nm in diameter) to yield GaOS-coated PLA fiber membranes (PFM+GaOS). In the second approach, GaOS or diallyl disulfide (DADS) was encapsulated within the PFMs during the electrospinning process to generate GaOSPFM or DADSPFM fibers, respectively. Both doped fibers released substantially less H_2S than the coated fibers. H_2S release experiments were conducted in pH 8 buffer at 37 °C, and although the authors did not conduct a typical release experiment to measure cumulative or real-time H_2S concentrations over time, the electrospun mats clearly protected the extracts in the dry state for several days. Studies on cardiac mesenchymal stem cells showed that the fiber mats protected the cells from oxidative stress.

1.6.3 Nanoemulsions and Liposomes:

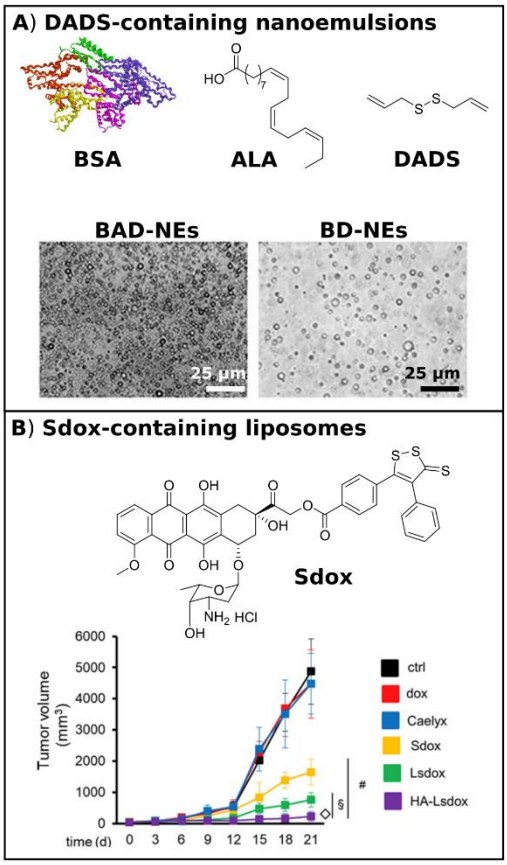

Figure 1-7. Nanoemulsions and liposomes with physically entrapped H_2S donors: A) Structures of BSA, ALA, and DADS. Optical micrographs depicting spherical particles for H_2S-releasing nanoemulsions with ALA (BAD-NEs) and without ALA (BD-NEs). **B)** Chemical structure of Dox modified with an H_2S donor. BSA, bovine serum albumin; ALA, α-linoleic acid; DADS, diallyl disulfide; Dox, doxorubicin.

Nanoemulsions and liposomes physically loaded with H_2S donors have similar therapeutic potential to polymer micelles described above. They can protect encapsulated APIs to improve stability, increase circulation times, and accumulate at sites of interest (e.g., tumors). These types

of formulations are generally prepared through simple and scaleable processes such as nanoprecipitation. Careful process control allows for tunable and uniform droplet sizes. The facile preparation and wide range of formulation possibilities are ideal for the development of various macromolecular H_2S donor systems.

In 2016, Melino et al. reported on an H_2S-releasing protein nanoemulsion formulation utilizing DADS, α-linoleic acid (88), and bovine serum albumin (BSA) (Fig. 1-7A).[104] DADS is found in various natural extracts and releases small amounts of H_2S upon reaction with a thiol. Similarly, ALA promotes cardiovascular health, reduces the risk of cardiovascular attacks, and exhibits chemoprotective effects.[106-107] The therapeutic applications of both DADS and ALA are limited by low aqueous solubility and stability. The authors suggested that a nanoemulsion formulation of both compounds may improve their bioavailability, thus increasing their therapeutic potential. Protein nanoemulsions of BSA-ALA-DADS (BAD-NEs) and BSA-DADS (BD-NEs) were prepared by sonication, with average diameters in the range of a few hundred nm. Interestingly, in thiol-containing buffer, BAD-NEs, which contained all three components, released more total H_2S per unit of DADS relative to both BD-NEs, which lacked the ALA lipid component, and DADS alone. The authors attributed this result to both increased stability of DADS in the nanoemulsion and the antioxidant properties of ALA. Incubation of BAD-NE nanoemulsions with supercoiled plasmid DNA in an oxidative environment revealed superior antioxidant properties relative to ALA and DADS alone, as well as their binary mixture. Furthermore, BAD-NEs significantly decreased cell viability in MCF-7 mammary adenocarcinoma and HuT 78 T-cell lymphoma cells, suggesting their potential as an anti-cancer therapeutic.

In 2019, Arpicco, Riganti and coworkers reported on liposomal formulations of doxorubicin (Dox) conjugated to an H_2S-donor (Sdox).[108] The Sdox compounds, reported by the authors in previous work,[109-111] showed reduced cardiotoxic effects compared with free Dox while retaining their efficacy against human bone osteosarcoma cells (characterized for their resistance to Dox). The authors suggested that encapsulation of Sdox in liposomes conjugated with hyaluronic acid (HA) might promote targeting to osteosarcoma cells due to their expression of the HA-receptor CD44. Liposomal Sdox (Lsdox) and hyaluronated liposomal Sdox (HA-Lsdox) were prepared through hydration of drug-lipid films, and successful insertion of Sdox into the liposomal membrane was confirmed by differential scanning calorimetry. HA-Lsdox showed a higher accumulation in CD44-expressing cells *in vitro* relative to Dox, Sdox, Lsdox, and Caelyx®, a commercial liposomal Dox formulation (Fig. 1-7B). Additionally, HA-Lsdox induced higher cell damage, apoptosis, and lower cell viability relative to the other formulations *in vitro*. *In vivo* studies revealed that HA-Lsdox greatly outperformed Sdox and the other liposomal Dox formulations with respect to inhibition of K7M2 tumor growth. This work highlights the potential for supramolecular donor systems in clinical applications of H_2S therapy. Sdox is an advanced form of Dox that may reduce side effects of this common chemotherapy drug, but this work shows that drug delivery vehicles are still needed for Sdox to maximize its anti-cancer effects while limiting cardiotoxicity.

1.7 Key Challenges and Future Perspectives:

In recent years it has become clear that H_2S, along with the other known gasotransmitters NO and CO, are molecules of supreme importance in mammalian physiology. Our understanding of the biological significance and therapeutic potential of H_2S continues to expand, and there exists

a need for a wide variety of strategies to deliver the gas at the desired location in the body, at the intended time, for the appropriate duration, and with the chosen rate of release. Due to its reactivity and short half-life, controlled delivery becomes even more important for H_2S than conventional small molecule drugs, which are typically selected from a variety of possible structures with considerations toward their pharmacokinetics and target specificity. Small molecule H_2S donors remain vital in this endeavor, but H_2S-releasing macro- and supramolecular materials offer additional possibilities for regulating these key drug delivery parameters.

Polymers functionalized with H_2S donors were the first macromolecular materials developed for H_2S delivery, with initial reports in 2014. This strategy provides a straightforward method for extending the duration of H_2S release and potentially altering its biodistribution and pharmacokinetics compared with small molecule donors. However, the polymer itself in this strategy typically brings limited if any additional control over release compared with small molecule analogs. Additionally, the fate of the polymeric byproduct(s) must be considered in these delivery systems. If the polymer is small enough, it may be renally excreted; otherwise it may accumulate if it is not biodegradable. Depolymerizable H_2S-releasing polymers, first reported in 2019, may hold advantages over functionalized non-degradable or slowly degradable polymers, including the potential for a specific trigger to initiate depolymerization.

Compared with soluble homopolymers and copolymers, H_2S-releasing block copolymers that form assemblies, such as micelles and liposomes, enhance release control. The hydrophilic block can protect H_2S donors linked to or sequestered in the hydrophobic domain of a micelle or liposome, and micelle core mobility can regulate release rate. Beyond these advantages, micelles, liposomes, and other self-assembled structures have been studied extensively as drug delivery vehicles, so H_2S-releasing components can be included in existing platforms. H_2S-releasing

micelles with targeting groups on their peripheries hold potential for site-specific H_2S delivery through systemic injection. Furthermore, polymer assemblies enable H_2S delivery across biological membranes such as the blood brain barrier, which may provide a unique method for studying the biological effects of H_2S on neuromodulation.[112]

Localized H_2S delivery may prove invaluable in studying the effects of H_2S on specific organs because systemic drug delivery vehicles never have perfect targeting capacity. Hydrogels, either with covalently attached H_2S donor motifs or sequestered donors, lead the way in localized H_2S delivery. Hydrogels can be made from crosslinked water-soluble polymers (chemically crosslinked hydrogels) or from self-assembling small molecules such as peptides (physically crosslinked hydrogels). Both can be implanted (or injected from a needle in the case of shear-thinning hydrogels, which disassemble in response to shear stress during injection and reassemble in vivo after injection) at a site of interest to deliver H_2S locally. Increased capacity to control the H_2S release rate, hydrogel stiffness, and degradability of the hydrogel carrier material will further enhance the utility of H_2S-releasing hydrogels. The potential to functionalize hydrogels with additional bioactive units offers exciting possibilities in influencing cellular behavior and promoting healing. H_2S-releasing microspheres and electospun scaffolds, which may offer longer release periods than hydrogels, may also enable a number of biological studies and applications where long-term delivery (i.e., weeks to months) is desired. Both platforms, several types of which have thoroughly characterized degradation rates and mechanisms, are also well-suited to pairing H_2S with other small molecule drugs where synergistic effects could be observed.

Many challenges remain in this field. While triggerable, small-molecule H_2S donors have many advantages over sulfide salts, they are inherently unstable compounds that must be handled with care to avoid triggering release prematurely. This need for careful handling and storage

extends to H_2S-releasing materials, and it can limit storage times and shipment methods. The instability of H_2S donors also limits delivery of H_2S to active delivery, where exogenous H_2S is administered *in response* to a specific condition. In contrast, proactive delivery strategies involve materials containing *latent* APIs that respond only to a biological trigger to release their payload. Development of proactive H_2S-releasing materials with precisely triggered release mechanisms are needed to continue moving the field forward.

Beyond stimuli-responsive delivery strategies, materials that release H_2S over the course of weeks to months are needed. Most extended biological studies on the effects of H_2S treatment in slow processes, for example chronic wound healing, are conducted using daily dosing of donor compounds. This dosing schedule results in fluctuations in H_2S levels in circulation and/or at the treatment site. Delivery from materials, such as hydrogels, microparticles, electrospun scaffolds, or polymer films, has the potential to stabilize H_2S levels through sustained release. Furthermore, long-releasing H_2S donors may enable treatment of chronic disease, such as high blood pressure, through H_2S therapy. Indeed, delivery from various materials is used widely to decrease dosing frequency and extend release times in many common pharmaceuticals.[113-114] Sustained delivery of H_2S from materials has great therapeutic potential, but analytical challenges must be addressed in order to properly characterize H_2S release profiles from these materials, both *in vitro* and *in vivo*. Methods for determining H_2S release profiles, such as the methylene blue method, fluorescent sensing methods, and electrochemical probes, are well suited for measuring release times on the order of minutes to hours, but each has limitations beyond this time period. Reliable and sensitive methods for long-term measurement of H_2S concentrations are needed.

Addressing these challenges in H_2S-releasing materials may provide insight into H_2S biology and physiology and answer questions regarding potential H_2S therapies. For example, will

targeted and or localized delivery reduce the dose needed compared with systemic injection? Another question is how release rates affect therapeutic outcomes. Ongoing work in our lab and other labs is beginning to show that sustained H_2S concentrations at low levels are more effective than instantaneous H_2S donors or very long-acting donors. These results are consistent with a bell-shaped exposure-response curve, in which H_2S exerts its maximum beneficial biological effect at intermediate concentrations. More efforts to compare similar donors with varying rates of H_2S release are needed to verify these early results, and the outcomes of these experiments will inform clinical possibilities for H_2S therapy. Compared with other drugs, the field of H_2S-releasing materials is in its infancy; drug delivery methods have been used clinically for decades and continue to be developed for other APIs. In the coming years, we expect to see materials capable of controlling many aspects of H_2S delivery, revealing (patho)physiological insights and moving toward clinical applications.

1.8 Acknowledgements:

We are grateful to the National Science Foundation (DMR-1454754) and the National Institutes of Health (R01GM123508) for support of our work in this area.

1.9 References:

1. Suk, J. S.; Xu, Q. G.; Kim, N.; Hanes, J.; Ensign, L. M., *Adv Drug Deliv Rev* **2016**, *99*, 28-51.

2. Bulbake, U.; Doppalapudi, S.; Kommineni, N.; Khan, W., *Pharmaceutics* **2017**, *9* (2), 33.

3. Hu, Q. Q.; Li, H.; Wang, L. H.; Gu, H. Z.; Fan, C. H., *Chem. Rev.* **2019**, *119* (10), 6459-6506.

4. Ekladious, I.; Colson, Y. L.; Grinstaff, M. W., *Nat. Rev. Drug Discov.* **2019**, *18* (4), 273-294.

5. Dlugi, A. M.; Miller, J. D.; Knittle, J., *Fertil. Steril.* **1990**, *54* (3), 419-427.

6. Gordon, M. S.; Kinlock, T. W.; Vocci, F. J.; Fitzgerald, T. T.; Memisoglu, A.; Silverman, B., *J. Subst. Abus. Treat.* **2015**, *59*, 52-58.

7. Barenholz, Y., *J Control Release* **2012**, *160* (2), 117-134.

8. Ferrari, M., *Nat. Rev. Cancer* **2005**, *5* (3), 161-171.

9. Sanborn, G. E.; Anand, R.; Torti, R. E.; Nightingale, S. D.; Cal, S. X.; Yates, B.; Ashton, P.; Smith, T., *JAMA Ophthalmol.* **1992**, *110* (2), 188-195.

10. Uhrich, K. E.; Cannizzaro, S. M.; Langer, R. S.; Shakesheff, K. M., *Chem. Rev.* **1999**, *99* (11), 3181-3198.

11. Kataoka, K.; Harada, A.; Nagasaki, Y., *Adv Drug Deliv Rev* **2001**, *47* (1), 113-131.

12. Cho, K.; Wang, X.; Nie, S.; Chen, Z.; Shin, D. M., *Clin. Cancer Res.* **2008**, *14* (5), 1310.

13. Mura, S.; Nicolas, J.; Couvreur, P., *Nat. Mater.* **2013**, *12* (11), 991-1003.

14. Petros, R. A.; DeSimone, J. M., *Nat. Rev. Drug Discov.* **2010**, *9* (8), 615-627.

15. Allen, T. M.; Cullis, P. R., *Adv Drug Deliv Rev* **2013**, *65* (1), 36-48.

16. Wang, R., *FASEB J.* **2002**, *16* (13), 1792-1798.

17. Mustafa, A. K.; Gadalla, M. M.; Snyder, S. H., *Sci. Signal.* **2009**, *2* (68), re2.

18. Wang, R., *Trends Biochem. Sci.* **2014**, *39* (5), 227-232.

19. Wang, R., *Physiol. Rev.* **2012**, *92* (2), 791-896.

20. Wang, R., *Antioxid. Redox Signal.* **2003**, *5* (4), 493-501.

21. Wallace, J. L.; Vaughan, D.; Dicay, M.; MacNaughton, W. K.; de Nucci, G., *Antioxid. Redox Signal.* **2017**, *28* (16), 1533-1540.

22. Ji, X.; Damera, K.; Zheng, Y.; Yu, B.; Otterbein, L. E.; Wang, B., *J. Pharm. Sci.* **2016**, *105* (2), 406-416.

23. Carpenter, A. W.; Schoenfisch, M. H., *Chem. Soc. Rev.* **2012**, *41* (10), 3742-3752.

24. Wang, R., *Proc. Natl. Acad. Sci.* **2012**, *109* (23), 8801.

25. Gadalla, M. M.; Snyder, S. H., *J. Neurochem.* **2010**, *113* (1), 14-26.

26. Abe, K.; Kimura, H., *J. Neurosci.* **1996**, *16* (3), 1066-1071.

27. Rajpal, S.; Katikaneni, P.; Deshotels, M.; Pardue, S.; Glawe, J.; Shen, X.; Akkus, N.; Modi, K.; Bhandari, R.; Dominic, P.; Reddy, P.; Kolluru, G. K.; Kevil, C. G., *Redox Biol.* **2018**, *15*, 480-489.

28. Barr, L. A.; Calvert, J. W., *Circulation* **2014**, *78* (9), 2111-2118.

29. Calvert John, W.; Jha, S.; Gundewar, S.; Elrod John, W.; Ramachandran, A.; Pattillo Christopher, B.; Kevil Christopher, G.; Lefer David, J., *Circ. Res.* **2009**, *105* (4), 365-374.

30. Mustafa Asif, K.; Sikka, G.; Gazi Sadia, K.; Steppan, J.; Jung Sung, M.; Bhunia Anil, K.; Barodka Viachaslau, M.; Gazi Farah, K.; Barrow Roxanne, K.; Wang, R.; Amzel, L. M.; Berkowitz Dan, E.; Snyder Solomon, H., *Circ. Res.* **2011**, *109* (11), 1259-1268.

31. Zhao, W.; Zhang, J.; Lu, Y.; Wang, R., *EMBO J.* **2001**, *20* (21), 6008-6016.

32. Tang, G.; Wu, L.; Liang, W.; Wang, R., *Mol. Pharmacol.* **2005**, *68* (6), 1757.

33. Wang, M.-J.; Cai, W.-J.; Zhu, Y.-C., *Clin. Exp. Pharmacol. Physiol.* **2010**, *37* (7), 764-771.

34. Szabó, C.; Papapetropoulos, A., *Br. J. Pharmacol.* **2011**, *164* (3), 853-865.

35. Szabo, C., *Am. J. Physiol., Cell Physiol.* **2016**, *312* (1), C3-C15.

36. Zhang, H.; Zhi, L.; Moochhala, S.; Moore, P. K.; Bhatia, M., *Am. J. Physiol. Lung Cell Mol. Physiol.* **2007**, *292* (4), L960-L971.

37. Whiteman, M.; Li, L.; Rose, P.; Tan, C.-H.; Parkinson, D. B.; Moore, P. K., *Antioxid. Redox Signal.* **2009**, *12* (10), 1147-1154.

38. Kimura, Y.; Kimura, H., *FASEB J.* **2004**, *18* (10), 1165-1167.

39. Whiteman, M.; Armstrong, J. S.; Chu, S. H.; Jia-Ling, S.; Wong, B.-S.; Cheung, N. S.; Halliwell, B.; Moore, P. K., *J. Neurochem.* **2004**, *90* (3), 765-768.

40. Kimura, Y.; Dargusch, R.; Schubert, D.; Kimura, H., *Antioxid. Redox Signal.* **2006**, *8* (3-4), 661-670.

41. Olson, K. R., *Am. J. Physiol. Regul. Integr. Comp. Physiol.* **2011**, *301* (2), R297-R312.

42. Wallace, J. L.; Wang, R., *Nat. Rev. Drug Discov.* **2015**, *14*, 329.

43. Szabó, C., *Nat. Rev. Drug Discov.* **2007**, *6* (11).

44. Cirino, G.; Vellecco, V.; Bucci, M., *Br. J. Pharmacol.* **2017**, *174* (22), 4021-4031.

45. Li, Z.; Polhemus David, J.; Lefer David, J., *Circ. Res.* **2018**, *123* (5), 590-600.

46. Nagpure, B. V.; Bian, J.-S., Brain, Learning, and Memory: Role of H_2S in Neurodegenerative Diseases. In *Chemistry, Biochemistry and Pharmacology of Hydrogen Sulfide*, Moore, P. K.; Whiteman, M., Eds. Springer International Publishing: Cham, 2015; pp 193-215.

47. Wallace, J.; Buret, A.; Nagy, P.; Muscara, M.; Nucci, G. d., *Ann. Rheum. Dis.* **2019**, *78* (Suppl 2), 522-522.

48. Qian, Y.; Matson, J. B., *Adv Drug Deliv Rev* **2017**, *110-111*, 137-156.

49. Blackstone, E.; Morrison, M.; Roth, M. B., *Science* **2005**, *308* (5721), 518.

50. Xu, S.; Hamsath, A.; Neill, D. L.; Wang, Y.; Yang, C.-t.; Xian, M., *Chem.: Eur. J.* **2019**, *25* (16), 4005-4016.

51. Lau, N.; Pluth, M. D., *Curr. Opin. Chem. Biol.* **2019**, *49*, 1-8.

52. Powell, C. R.; Dillon, K. M.; Matson, J. B., *Biochemical Pharmacology* **2018**, *149*, 110-123.

53. Zheng, Y.; Ji, X.; Ji, K.; Wang, B., *Acta Pharm. Sin. B* **2015**, *5* (5), 367-377.

54. Connal, L. A., *J. Mater. Chem. B* **2018**, *6* (44), 7122-7128.

55. Urquhart, M. C.; Ercole, F.; Whittaker, M. R.; Boyd, B. J.; Davis, T. P.; Quinn, J. F., *Polym. Chem.* **2018**, *9* (35), 4431-4439.

56. Wischke, C.; Schwendeman, S. P., *Int. J. Mol. Sci.* **2008**, *364* (2), 298-327.

57. Wang, H.; Zhao, Y.; Wu, Y.; Hu, Y. L.; Nan, K. H.; Nie, G. J.; Chen, H., *Biomaterials* **2011**, *32* (32), 8281-8290.

58. Jeong, B.; Bae, Y. H.; Lee, D. S.; Kim, S. W., *Nature* **1997**, *388* (6645), 860-862.

59. Gabizon, A.; Shmeeda, H.; Barenholz, Y., *Clin. Pharmacokinet.* **2003**, *42* (5), 419-436.

60. Liu, J.; Bu, W.; Pan, L.; Shi, J., *Angew. Chem. Int. Ed.* **2013**, *52* (16), 4375-4379.

61. Yoo, H. S.; Park, T. G., *J Control Release* **2004**, *96* (2), 273-283.

62. Govender, T.; Stolnik, S.; Garnett, M. C.; Illum, L.; Davis, S. S., *J Control Release* **1999**, *57* (2), 171-185.

63. Sahana, D. K.; Mittal, G.; Bhardwaj, V.; Kumar, M., *J. Pharm. Sci.* **2008**, *97* (4), 1530-1542.

64. Kalaria, D. R.; Sharma, G.; Beniwal, V.; Kumar, M., *Pharm. Res.* **2009**, *26* (3), 492-501.

65. Song, Z. M.; Feng, R. L.; Sun, M.; Guo, C. Y.; Gao, Y.; Li, L. B.; Zhai, G. X., *J. Colloid Interface Sci.* **2011**, *354* (1), 116-123.

66. Hamada, T.; Nakane, T.; Kimura, T.; Arisawa, K.; Yoneda, K.; Yamamoto, T.; Osaki, T., *Am. J. Med. Sci.* **1999**, *318* (3), 146-151.

67. Hasegawa, U.; van der Vlies, A. J., *Bioconjugate Chem.* **2014**, *25* (7), 1290-1300.

68. Foster, J. C.; Matson, J. B., *Macromolecules* **2014**, *47* (15), 5089-5095.

69. Foster, J. C.; Powell, C. R.; Radzinski, S. C.; Matson, J. B., *Org. Lett.* **2014**, *16* (6), 1558-1561.

70. Powell, C. R.; Foster, J. C.; Okyere, B.; Theus, M. H.; Matson, J. B., *J. Am. Chem. Soc.* **2016**, *138* (41), 13477-13480.

71. Steiger, A. K.; Zhao, Y.; Pluth, M. D., *Antioxid. Redox Signal.* **2017**, *28* (16), 1516-1532.

72. Li, Z.; Li, D.; Wang, L.; Lu, C.; Shan, P.; Zou, X.; Li, Z., *Polymer* **2019**, *168*, 16-20.

73. Soo Choi, H.; Liu, W.; Misra, P.; Tanaka, E.; Zimmer, J. P.; Itty Ipe, B.; Bawendi, M. G.; Frangioni, J. V., *Nat. Biotechnol.* **2007**, *25*, 1165.

74. Kataoka, K.; Harada, A.; Nagasaki, Y., *Adv Drug Deliv Rev* **2012**, *64*, 37-48.

75. Maeda, H.; Wu, J.; Sawa, T.; Matsumura, Y.; Hori, K., *J Control Release* **2000**, *65* (1), 271-284.

76. Hasegawa, U.; van der Vlies, A. J., *MedChemComm* **2015**, *6* (2), 273-276.

77. Foster, J. C.; Radzinski, S. C.; Zou, X.; Finkielstein, C. V.; Matson, J. B., *Mol. Pharm.* **2017**, *14* (4), 1300-1306.

78. Foster, J. C.; Carrazzone, R. J.; Spear, N. J.; Radzinski, S. C.; Arrington, K. J.; Matson, J. B., *Macromolecules* **2019**, *52* (3), 1104-1111.

79. Ercole, F.; Mansfeld, F. M.; Kavallaris, M.; Whittaker, M. R.; Quinn, J. F.; Halls, M. L.; Davis, T. P., *Biomacromolecules* **2016**, *17* (1), 371-383.

80. Yu, S. H.; Ercole, F.; Veldhuis, N. A.; Whittaker, M. R.; Davis, T. P.; Quinn, J. F., *Polym. Chem.* **2017**, *8* (41), 6362-6367.

81. Ercole, F.; Whittaker, M. R.; Halls, M. L.; Boyd, B. J.; Davis, T. P.; Quinn, J. F., *Chem. Comm.* **2017**, *53* (57), 8030-8033.

82. Benavides, G. A.; Squadrito, G. L.; Mills, R. W.; Patel, H. D.; Isbell, T. S.; Patel, R. P.; Darley-Usmar, V. M.; Doeller, J. E.; Kraus, D. W., *Proc. Natl. Acad. Sci. U. S. A.* **2007**, *104* (46), 17977-17982.

83. Vo, C. D.; Kilcher, G.; Tirelli, N., *Macromol. Rapid Commun.* **2009**, *30* (4-5), 299-315.

84. Arbach, M.; Santana, T. M.; Moxham, H.; Tinson, R.; Anwar, A.; Groom, M.; Hamilton, C. J., *Biochim. Biophys. Acta-Gen. Subj.* **2019**, *1863* (6), 1050-1058.

85. Long, T. R.; Wongrakpanich, A.; Do, A.-V.; Salem, A. K.; Bowden, N. B., *Polym. Chem.* **2015**, *6* (40), 7188-7195.

86. Lin, L.; Qin, H.; Huang, J.; Liang, H.; Quan, D.; Lu, J., *Polym. Chem.* **2018**, *9* (21), 2942-2950.

87. Carter, J. M.; Qian, Y.; Foster, J. C.; Matson, J. B., *Chem. Comm.* **2015**, *51* (66), 13131-13134.

88. Kaur, K.; Qian, Y.; Gandour, R. D.; Matson, J. B., *J. Org. Chem.* **2018**, *83* (21), 13363-13369.

89. Qian, Y.; Kaur, K.; Foster, J. C.; Matson, J. B., *Biomacromolecules* **2019**, *20* (2), 1077-1086.

90. Wang, Y.; Kaur, K.; Scannelli, S. J.; Bitton, R.; Matson, J. B., *J. Am. Chem. Soc.* **2018**, *140* (44), 14945-14951.

91. Liang, W.; Chen, J.; Li, L.; Li, M.; Wei, X.; Tan, B.; Shang, Y.; Fan, G.; Wang, W.; Liu, W., *ACS Appl. Mater. Interfaces* **2019**, *11* (16), 14619-14629.

92. Xiao, Z.; Bonnard, T.; Shakouri-Motlagh, A.; Wylie, R. A. L.; Collins, J.; White, J.; Heath, D. E.; Hagemeyer, C. E.; Connal, L. A., *Chem.: Eur. J.* **2017**, *23* (47), 11294-11300.

93. Shabat, D., *J. Polym. Sci. A* **2006**, *44* (5), 1569-1578.

94. Peterson, G. I.; Larsen, M. B.; Boydston, A. J., *Macromolecules* **2012**, *45* (18), 7317-7328.

95. Powell, C. R.; Foster, J. C.; Swilley, S. N.; Kaur, K.; Scannelli, S. J.; Troya, D.; Matson, J. B., *Polym. Chem.* **2019**, *10* (23), 2991-2995.

96. Steiger, A. K.; Pardue, S.; Kevil, C. G.; Pluth, M. D., *J. Am. Chem. Soc.* **2016**, *138* (23), 7256-7259.

97. Levinn, C. M.; Steiger, A. K.; Pluth, M. D., *ACS Chem. Biol.* **2019**, *14* (2), 170-175.

98. Henthorn, H. A.; Pluth, M. D., *J. Am. Chem. Soc.* **2015**, *137* (48), 15330-15336.

99. Zheng, Z.; Chen, A.; He, H.; Chen, Y.; Chen, J.; Albashari, A. A.; Li, J.; Yin, J.; He, Z.; Wang, Q.; Wu, J.; Wang, Q.; Kang, J.; Xian, M.; Wang, X.; Xiao, J., *J. Mater. Chem. B* **2019**, *7* (4), 611-618.

100. Feng, S.; Zhao, Y.; Xian, M.; Wang, Q., *Acta Biomater.* **2015**, *27*, 205-213.

101. Wu, J.; Li, Y.; He, C.; Kang, J.; Ye, J.; Xiao, Z.; Zhu, J.; Chen, A.; Feng, S.; Li, X.; Xiao, J.; Xian, M.; Wang, Q., *ACS Appl. Mater. Interfaces* **2016**, *8* (41), 27474-27481.

102. Cacciotti, I.; Ciocci, M.; Di Giovanni, E.; Nanni, F.; Melino, S., *Int. J. Mol. Sci.* **2018**, *19* (8).

103. Talal, J.; Abutbul-Ionita, I.; Schlachet, I.; Danino, D.; Sosnik, A., *Chemistry of Materials* **2017**, *29* (2), 873-885.

104. Matteo Ciocci, E. I., Felicia Carotenuto, Haneen A. Khashoggi, Francesca Nanni, Sonia Melino, *Oncotarget* **2016**, (7), 84338-84358.

105. Cai, Y.-R.; Hu, C.-H., *The Journal of Physical Chemistry B* **2017**, *121* (26), 6359-6366.

106. Bhattacharya, A.; Banu, J.; Rahman, M.; Causey, J.; Fernandes, G., *J. Nutr. Biochem.* **2006**, *17* (12), 789-810.

107. Zhao, G. X.; Etherton, T. D.; Martin, K. R.; West, S. G.; Gillies, P. J.; Kris-Etherton, P. M., *J. Nutr.* **2004**, *134* (11), 2991-2997.

108. Gazzano, E.; Buondonno, I.; Marengo, A.; Rolando, B.; Chegaev, K.; Kopecka, J.; Saponara, S.; Sorge, M.; Hattinger, C. M.; Gasco, A.; Fruttero, R.; Brancaccio, M.; Serra, M.; Stella, B.; Fattal, E.; Arpicco, S.; Riganti, C., *Cancer Lett.* **2019**, *456*, 29-39.

109. Chegaev, K.; Rolando, B.; Cortese, D.; Gazzano, E.; Buondonno, I.; Lazzarato, L.; Fanelli, M.; Hattinger, C. M.; Serra, M.; Riganti, C.; Fruttero, R.; Ghigo, D.; Gasco, A., *J. Med. Chem.* **2016**, *59* (10), 4881-4889.

110. Buondonno, I.; Gazzano, E.; Tavanti, E.; Chegaev, K.; Kopecka, J.; Fanelli, M.; Rolando, B.; Fruttero, R.; Gasco, A.; Hattinger, C.; Serra, M.; Riganti, C., *Cell. Mol. Life Sci.* **2019**, *76* (3), 609-625.

111. Bigagli, E.; Luceri, C.; De Angioletti, M.; Chegaev, K.; D'Ambrosio, M.; Riganti, C.; Gazzano, E.; Saponara, S.; Longini, M.; Luceri, F.; Cinci, L., *Invest. New. Drug.* **2018**, *36* (6), 985-998.

112. Kreuter, J., *Adv Drug Deliv Rev* **2001**, *47* (1), 65-81.

113. Allen, T. M.; Cullis, P. R., *Science* **2004**, *303* (5665), 1818.

114. Duncan, R., *Nat. Rev. Drug Discov.* **2003**, *2* (5), 347-360.

Chapter 2: Tuning H_2S Release by Controlling Mobility in a Micelle Core

Reprinted (adapted) with permission from: Carrazzone, R. J. et al. *Macromolecules* **2019**, *52*, 1104–1111. Copyright 2019 American Chemical Society. https://doi.org/10.1021/acs.macromol.8b02315

2.1 Authors:

Ryan J. Carrazzone, [§,†,‡] Jeffrey C. Foster, [§,‡] Nathan J. Spear, [§,‡] Scott C. Radzinski, [§,‡] Kyle J. Arrington, [§,‡] John B. Matson*[§,‡]

[§]Department of Chemistry, Virginia Tech, Blacksburg, Virginia 24060, United States

[†]Macromolecules Innovation Institute, Virginia Tech, Blacksburg, Virginia 24060, United States

[‡]Virginia Tech Center for Drug Discovery, Virginia Tech, Blacksburg, Virginia 24060, United States

2.2 Abstract:

Drug delivery from polymer micelles has been widely studied, but methods to precisely tune rates of drug release from micelles are limited. Here, the mobility of hydrophobic micelle cores was varied to tune the rate at which a covalently bound drug was released. This concept was applied to cysteine-triggered release of hydrogen sulfide (H_2S), a signaling gas with therapeutic potential. In this system, thiol-triggered H_2S donor molecules were covalently linked to the hydrophobic blocks of self-assembled polymer amphiphiles. Because release of H_2S is triggered by cysteine, diffusion of cysteine into the hydrophobic micelle core was hypothesized to control the rate of release. We confirmed this hypothesis by carrying out release experiments from H_2S-

releasing micelles in varying compositions of EtOH/H_2O. Higher EtOH concentrations caused the micelles to swell, facilitating diffusion in and out of their hydrophobic cores and leading to faster H_2S release from the micelles. To achieve a similar effect without addition of organic solvent, we prepared micelles with varying core mobility via incorporation of a plasticizing co-monomer in the core-forming block. The glass transition temperature (T_g) of the core block could therefore be precisely varied by changing the amount of the plasticizing co-monomer in the polymer. In aqueous solution under identical conditions, the release rate of H_2S varied over 20-fold ($t_{1/2}$ = 0.18 – 4.2 h), with the lowest T_g hydrophobic block resulting in the fastest H_2S release. This method of modulating release kinetics from polymer micelles by tuning core mobility may be applicable to many types of physically encapsulated and covalently linked small molecules in a variety of drug delivery systems.

2.3 Introduction:

Polymeric micelles enhance the activity of conventional therapeutics by improving drug solubility, minimizing off-target effects, providing protection against rapid breakdown, enhancing circulation time (pharmacokinetics), reducing the volume of distribution, and imparting targeting capability such that the therapeutic agent accumulates in the desired tissue(s).[1-3] Most of these enhancements derive from the difference in size of polymer micelles relative to their small molecule encapsulates and from the biocompatibility imparted by their hydrophilic polymer shells.[4] Since the 1990s, numerous polymer assemblies have been developed to deliver assorted payloads, including small molecule anti-cancer drugs,[5-6] contrast/imaging agents,[7-8] proteins,[9] RNA,[10] and DNA,[11] among others.

Despite their numerous advantages, the delivery of drugs by polymeric micelles can be complicated by slow diffusion of triggering agents and/or encapsulated drugs both into and out of the micelle core. For example, Eisenberg and coworkers showed that hydrophobic model drug release from poly(caprolactone)-*b*-poly(ethylene oxide) micelles occurred under diffusion control, with release rates dependent on the structure and concentration of the encapsulated agent.[12] In a similar example, O'Reilly and coworkers demonstrated the inability of a hydrophilic probe to diffuse into the core of poly(triethyleneglycol acrylate)-*b*-poly(*tert*-butyl acrylate) micelles using a FRET experiment.[13] Additionally, Appel and coworkers reported the dependence of the release rate of small molecule dyes from single-chain nanoparticles on core morphology, with low core glass transition temperature (T_g) leading to fast release and higher core T_g exhibiting sustained release.[14] Most recently, Thayumanavan and coworkers established a system in which chain mobility facilitated the release of small molecule encapsulates from the glassy domain of supramolecular assemblies.[15] Diffusion of molecules into micelles is particularly relevant for delivery systems in which the therapeutic is covalently attached to the polymer amphiphile and requires a chemical reaction to elicit drug release. In such systems, the rates of diffusion of small molecules into and out of the micelle core can compete with those of the drug-releasing reaction (i.e., hydrolysis). For example, Cui and coworkers recently demonstrated that supramolecular structure controlled the release of hydrophobic drugs covalently bound to short, self-assembling peptides by restricting access of the triggering molecule to the degradable group linking the drug to the peptide.[16] Similarly, van Esch and coworkers showed that release of a model drug covalently linked to a gelling scaffold via an enzyme-labile linker was limited by the supramolecular structure of the hydrogel.[17] These examples highlight complexities that are often not easily addressed when formulating polymeric micelles and related supramolecular materials for drug delivery.

In our lab, we are interested in materials capable of delivering hydrogen sulfide (H_2S), a field of research garnering much attention recently.[18] An endogenously produced gas that is tightly regulated in vivo, H_2S is extensively involved in cellular signaling and homeostasis.[19] Moreover, the physiological activity of H_2S depends largely on its local concentration; therefore, to effect the desired biological response, H_2S must be delivered selectively (i.e., to the correct tissue), precisely, and on the appropriate timescale.[20-21] H_2S-releasing small molecules and materials have been developed by our lab and others to deliver the gas both in vitro and in vivo,[22-25] but better control over the timing, location, rate, and duration of release are still needed. Using polymer amphiphiles with reaction-triggered H_2S donors covalently bound to the hydrophobic block, we considered here whether the H_2S release rate could be controlled by modulating diffusion of the trigger into the micelles.

In recently published work, we prepared H_2S-releasing polymeric micelles based on block copolymers of poly(ethylene glycol) (PEG) and polymethacrylate.[24] To each constitutional unit of the polymethacrylate hydrophobic block was attached an *S*-aroylthiooxime (SATO) group, which releases H_2S in response to thiols such as cysteine (Scheme S1). We observed that H_2S release from SATO-functionalized micelles occurred over an order of magnitude more slowly than from analogous small molecule SATOs under identical experimental conditions (Table S1). Given that the SATO-functionalized hydrophobic blocks are sequestered within the hydrophobic core of the micelles, the triggering thiol must diffuse into the micelle to induce H_2S release. Therefore, the rate of diffusion of triggering molecules into micelle cores may greatly impact the H_2S release rate from these assemblies. In this contribution, we evaluate the effect of the properties of the polymer amphiphile (i.e., hydrophobic block glass transition temperature) on H_2S release from SATO-functionalized micelles. In addition, we consider how properties of the polymer amphiphile can be

manipulated to tune characteristics of the micelle assemblies including their size and the kinetics of small molecule release. It should be noted that although we focus on triggered release of H_2S, the results discussed here may be applicable to a broad variety of drug-loaded polymer micelles.

2.4 Results and Discussion:

2.4.1 Influence of Electronics on H_2S Release from Statistical and Block Copolymers

We showed in our initial publication on SATOs that the electronics of the SATO structure control the kinetics of thiol-triggered H_2S release (Scheme 2-1).[26] By changing substituents on the aryl thioester unit, the rate of release can be tuned over an order of magnitude for small molecule SATOs, with electron withdrawing substituents accelerating release and electron donating substituents retarding it. In fact, a linear free energy relationship was observed between the rate of the H_2S-releasing reaction and the *para* substituent Hammett constant (σ), allowing for precise chemical control over the release profile.

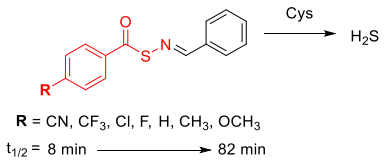

Scheme 2-1. H_2S release from small molecule SATOs.

In further studies, we explored the rate of H_2S release from H_2O-soluble SATO-functionalized copolymers, which was also sensitive to electronic control and followed a similar trend based on substituent electronics.[23] In the present work we initially asked if the rate of H_2S release could be manipulated in the same way for polymer assemblies prepared from SATO-

functionalized block copolymer amphiphiles. Therefore, we prepared a series of three polymer amphiphiles with pendant SATOs that differed in their *para* substituents.

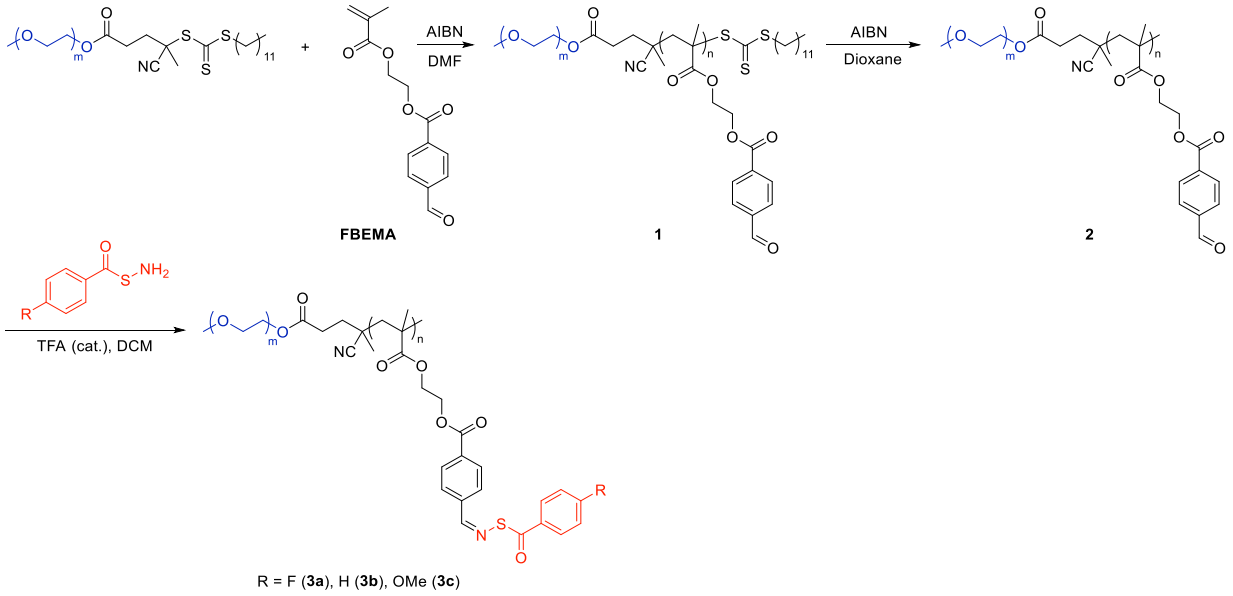

Scheme 2-2. Preparation of SATO-functionalized polymer amphiphiles.

SATO-functionalized polymer amphiphiles were prepared in three steps (Scheme 2-2). First, 2-(4-formylbenzoyloxy)ethyl methacrylate (**FBEMA**) was polymerized via reversible addition–fragmentation chain transfer (RAFT) polymerization using a PEGylated chain transfer agent (macro-CTA; PEG = M_n 5,000 g/mol), yielding block copolymer **1** with a hydrophilic PEG block and a hydrophobic poly(methacrylate) segment bearing pendant aldehyde functionality on each constitutional unit. In the second step, the trithiocarbonate end group was displaced using azobisisobutyronitrile (AIBN) following a reported method,[27] making polymer **2**. Finally, SATO formation was conducted using three different *S*-aroylthiohydroxylamines (SATHAs), which differed in the *para* substituent of the aromatic ring, to prepare SATO-functionalized polymers **3a-c**.

With polymers **3a-c** in hand (molar mass and dispersity(Đ)) values are provided in Table S2), polymer assemblies were prepared by the solvent switch method. Briefly, each polymer was first dissolved in THF; polymer solutions were then rapidly diluted with an equal volume of DI H_2O. The polymer solutions were then transferred to dialysis tubing and dialyzed against DI H_2O for 48 h. Analysis of the three samples by dynamic light scattering (DLS) revealed monomodal size distributions with intensity average diameters of 37 ± 4 nm, 43 ± 2 nm, and 40 ± 3 nm for polymers **3a**, **3b**, and **3c,** respectively (Figure S27). Based on these data, the size of the SATO polymer assemblies did not appear to depend on the *para*-substituent.

H_2S release from SATO-containing micelles was measured using the methylene blue assay, a common method for determining H_2S concentrations.[28] For each experiment, a solution of micelles with 250 μM SATO groups was allowed to react with 1 mM Cys in the presence of $Zn(OAc)_2$ in phosphate buffer (pH = 7). Aliquots were withdrawn periodically and treated with $FeCl_3$ and *N*,*N*-dimethyl-*p*-phenylenediamine, leading to methylene blue formation. Kinetics plots were obtained by measuring the absorbance of methylene blue at 750 nm for each time point until a plateau was reached. In contrast to small molecule SATOs and SATO-functionalized linear polymers, half-lives measured by the methylene blue method for H_2S release from micelles prepared from polymers **3a-c** did not trend with R group electronics (Table S3). These results contradict our previous findings about the effect of substituent electronics on H_2S release rates, warranting further investigation into the origin of this apparent loss of electronic control (Figure 2-1).

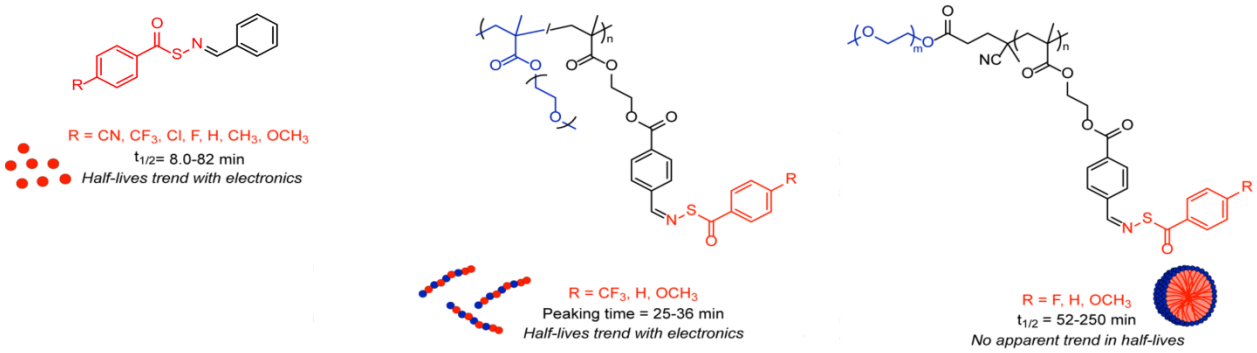

Figure 2-1. Ranges of H_2S release rates from previously studied small molecule SATO and SATO-functionalized statistical copolymers, compared with SATO containing block copolymer micelles.

Based on these data, we concluded that the reaction of Cys with the pendant SATOs of polymers **3a-c** was no longer the rate determining step of H_2S release. In our previous reports, H_2S release studies from small molecule SATOs and SATO statistical copolymers were conducted on single molecules dissolved in aqueous solution. Here, we speculated that the reaction likely occurred inside of the polymer micelles due to the covalent attachment of the SATO groups to the hydrophobic blocks of the polymer amphiphiles. Therefore, we hypothesized that the rate of diffusion of the triggering Cys molecules into the hydrophobic micelle cores might determine the rate of H_2S release from the SATO-functionalized micelles.

2.4.2 Micelle Swelling using EtOH

To evaluate this hypothesis, we conducted H_2S release experiments from micelles made from polymer **3b** with varying amounts of organic solvent (EtOH). We reasoned that EtOH would

swell the micelle cores, facilitating Cys diffusion into the micelles. We also realized that addition of EtOH could influence the rate of the H_2S-releasing reaction in addition to the rate of Cys diffusion. To determine whether EtOH altered the kinetics of H_2S release from SATOs, methylene blue assays were carried out on a small molecule SATO ($C_6H_5COSN{=}CHC_6H_5$) at 0, 10, 20, and 30 v/v% EtOH in phosphate buffer (pH = 7). Half-lives of H_2S release did not vary by more than 8% between the different experimental conditions, and there was no trend between EtOH concentration and half-life (Figure S29 and Table S4); therefore, we concluded that EtOH had no effect on the rate of the H_2S-releasing reaction.

After establishing that EtOH did not affect the rate of H_2S release from small molecule SATOs, we next investigated if EtOH would swell the polymer micelles and accelerate H_2S release kinetics due to increased diffusion of the Cys trigger (Figure 2-2A). Toward this end, DLS of micelles prepared from polymer **3b** was conducted with different amounts of EtOH, showing an increase in the diameter of the micelles from 39 ± 1 nm in DI H_2O to 114 ± 3 nm in 30 v/v% EtOH solution (Figure 2-2B; complete data set in Figure S32). As shown in Figure 2-2C, methylene blue experiments using the same series of EtOH concentrations as the small molecule study revealed a decrease in H_2S release half-lives from 4.2 ± 0.3 h (0 v/v% EtOH) to 1.8 ± 0.5 h (30 v/v% EtOH) (Figure 2-2C; complete data set in Figure S33 and Table S5). Taken together, these data are consistent with our assumption that EtOH could swell the polymer micelles, and that H_2S release would occur more rapidly in solvent-swollen micelles than in micelles that were not swollen. These conclusions support the hypothesis that Cys diffusion into micelles prepared from polymer **3b** affects the rate of H_2S release.

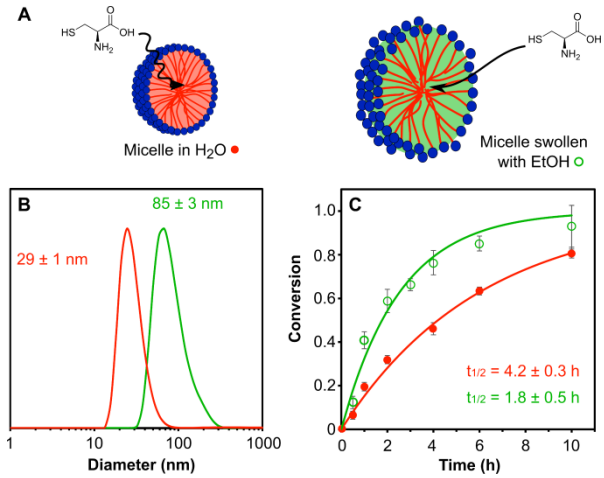

Figure 2-2. A) Schematic illustration of the effect of added EtOH on micelle size and diffusion of Cys into the micelle cores. B) DLS intensity average size distributions of micelles prepared from polymer **3b** in H_2O (red trace) and 30 v/v% EtOH in H_2O (green trace). C) H_2S release kinetics from micelles prepared from polymer **3b** in H_2O (red filled circles and line) and 30 v/v% EtOH in H_2O (green open circles and line). The lines correspond to pseudo-first-order kinetics fits. A SATO concentration of 250 μM was utilized for each experiment, and 1 mM Cys was applied to trigger H_2S release. Release reactions were conducted in EtOH/phosphate buffer (pH = 7.0) mixtures at rt. The error bars represent the standard deviation in conversion of n=3 replicates.

2.4.3 Tuning the Glass Transition Temperature of the H_2S-Releasing Block

Based on the DLS data on the polymer micelles, it is clear that EtOH causes swelling of the micelles, which may play a role in accelerating H_2S release. However, EtOH may also plasticize the micelle core, lowering the glass transition temperature (T_g) of the core block. Solvent swelling of micelle cores has been previously reported[29] and is associated with plasticization of the hydrophobic polymer block.[30] We hypothesized that a reduced T_g might increase the mobility

of the micelle core, also contributing to enhanced diffusion of Cys and accelerated H_2S release kinetics. Therefore, to vary the rate of H_2S release without introducing organic solvents, we envisioned a copolymerization strategy to lower the T_g of the core block.

Copolymerization is an effective method to tune the T_g of a polymer because many copolymers obey statistical estimations of T_g developed by Fox. Using differential scanning calorimetry (DSC), we found that SATO-functionalized poly(FBEMA) has a T_g of 96 °C, while a dodecyl-oxime derivative of poly(FBEMA) has a much lower T_g of 18 °C. Statistical copolymers of the two should therefore have T_g's that are a function of the composition of the polymer in accordance with the Fox equation (Figure 2-3).

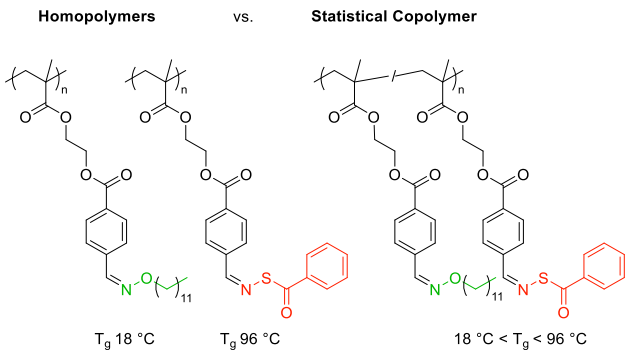

Figure 2-3. Tuning the T_g of the hydrophobic block by introducing a plasticizing co-monomer.

To prepare statistical copolymers functionalized with both SATO and alkyl oxime groups, it was necessary to understand the relative stability of these functional groups. Ideally, copolymers of the desired composition could be obtained simply by altering the ratio of SATHA and hydroxylamine added in a single post-polymerization reaction. Several model reactions were carried out to assess the relative stability of the SATO and oxime groups. Based on ^{1}H NMR spectral evidence, oxime formation dominated the equilibrium between these two functional

groups (see the SI for a more detailed discussion). Therefore, to achieve the desired copolymer composition, poly(FBEMA) was treated with a mixture containing a sub-stoichiometric amount of hydroxylamine and an excess (3 equiv to aldehyde) of SATHA (e.g., to achieve 30 mol% oxime, a polymer with DP 100 would be treated with 30 equiv of hydroxylamine and 300 equiv of SATHA per polymer chain). This strategy, shown in Scheme 2-3, was employed to prepare a series of copolymers where the degree of oxime functionalization was varied from 0-100 mol% (Table 2-1).

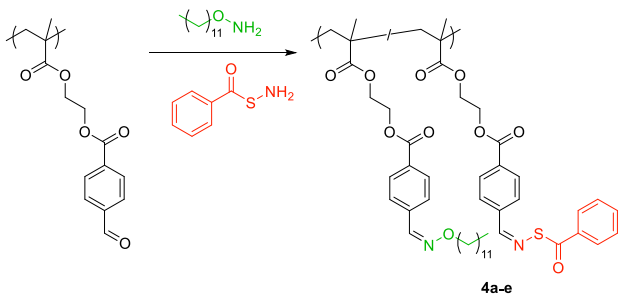

Scheme 2-3. Preparation of alkyl-modified homopolymers.

Table 2-1. Characterization of SATO-*co*-alkyl statistical copolymers.

Polymer	$M_{n,\,SEC}$ (kg mol^{-1})[a]	$M_{n,theo}$ (kg mol^{-1})[b]	$Đ$[a]	Wt. Fraction SATO[c]	T_g (°C)[d]
4a	38	39.7	1.29	1.00	96
4b	39	40.9	1.16	0.72	66
4c	43	42.3	1.21	0.43	49
4d	45	43.6	1.18	0.18	32
4e	44	44.6	1.14	0.00	18

[a]Absolute molar mass measured by SEC with light scattering. [b]Calculated using the molar masses of the two repeating units (SATO and oxime) in the statistical copolymer derived from the

poly(FBEMA) block and mol fractions of each unit obtained via ^{1}H NMR spectroscopy. [c]Weight fraction of SATO comonomer in the statistical copolymer determined from theoretical molar mass values and mol fractions of SATO and oxime units, demonstrated in Equation S1. [d]Measured by DSC with a 20 °C/min heating and cooling ramp; data reported from second heat cycle.

DSC was employed to measure the T_g's of the SATO/oxime statistical copolymers (**4a-e**). As shown in Figure 2-4, the T_g's of the statistical copolymers fit well with predicted values, starting at 18 °C for a homopolymer functionalized with alkyl oximes and increasing to 96 °C for a homopolymer completely functionalized with SATOs.

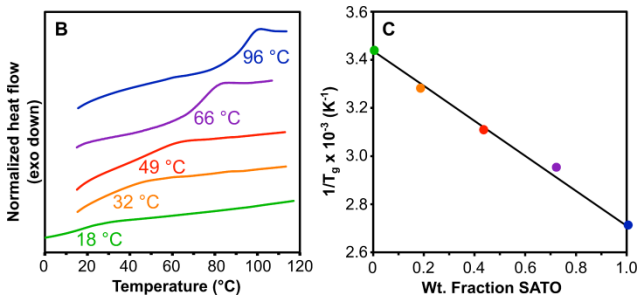

Figure 2-4. DSC analysis of poly(FBEMA) functionalized with different ratios of SATO and oxime. A) DSC of **polymer 4a** (blue trace), **4b** (purple trace), **4c** (red trace), **4d** (orange trace), and **4e** (green trace). B) Plot of $1/T_g$ as a function of weight fraction of SATO-containing repeat unit. The solid black line represents a theoretical fit using the Fox equation and the T_g's of the homopolymers.

Next, a PEG-*b*-poly(FBEMA) block copolymer (polymer **2**) was functionalized with different ratios of SATHA and hydroxylamine, using the strategy described above, to prepare

polymers **5a-e** (Scheme 2-4). Based on the relationship we observed between the weight fraction of the SATO component and T_g for polymers **4a-e** (Figure 2-4B), we supposed that the trend of T_g in weight fraction of the SATO component would likely hold for the block copolymers **5a-e**. However, we were unable to measure T_g values for the block copolymers and we acknowledge that actual T_g values are likely lower than those obtained for statistical copolymers **4a-e** due to the relatively lower molar masses. Our characterization of this series of polymers is provided in Table 2.

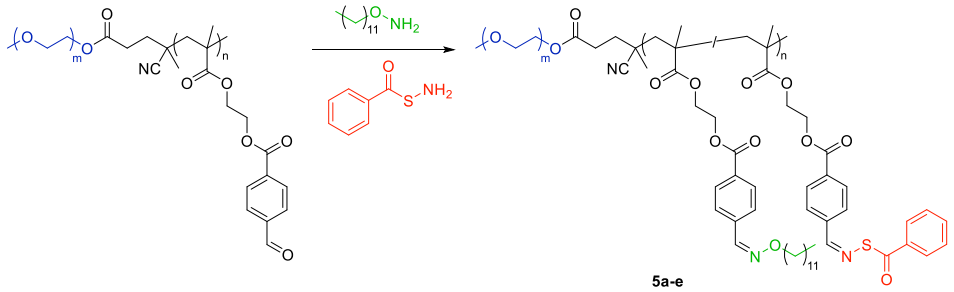

Scheme 2-4. Preparation of PEG-*b*-(SATO-*co*-alkyl) polymer amphiphiles.

Table 2-2. Characterization of PEG-*b*-(SATO-*co*-alkyl) polymer amphiphiles.

Polymer	$M_{n,\,SEC}$ (kg mol^{-1})[a]	$M_{n,theo}$ (kg mol^{-1})[b]	Đ[a]	Wt. Fraction SATO[c]	D_h (nm)[d]
5a	12.4	12.9	1.19	1.00	36 ± 5
5b	13.3	13.2	1.13	0.66	36 ± 1
5c	13.6	13.5	1.14	0.40	36 ± 1
5d	13.8	13.8	1.17	0.09	65 ± 2
5e	14.0	13.9	1.28	0.00	68 ± 5

[a]Absolute molar mass measured by light scattering. [b]Calculated using the molar masses of the two repeating units (SATO and oxime) in the statistical copolymer derived from the poly(FBEMA)

block and mol fractions of each unit obtained via ^{1}H NMR spectroscopy. [c]Weight fraction of SATO comonomer in the statistical copolymer block determined from theoretical molar mass values and mol fractions, demonstrated in equation S1. [d]Intensity average hydrodynamic diameter measured using DLS in DI H_2O at 25 °C with block copolymer concentrations of 1 mg/mL.

As before, polymer assemblies of polymer amphiphiles **5a-e** were prepared using the solvent switch method. The sizes of the resulting polymer assemblies were then characterized by DLS and their solution stability measured using the Nile Red assay. Polymer assembly size did not appear to vary initially as a function of polymer composition, with assemblies prepared from polymers **5a-c** near 36 nm; however, as the alkyl oxime content was raised above 90 wt%, the size of the polymer assemblies increased significantly for polymers **5d** and **5e** (Table 2-2; see Figure S41 for DLS traces). Polymers **5d** and **5e** possess T_g values near rt. It is likely that the hydrophobic cores of the polymer assemblies prepared from these polymers have increased mobility relative to polymers **5a-c**, which are kinetically "frozen" in a glassy state. In contrast, the critical micelle concentrations (CMCs) for assemblies prepared from polymers **5a-e** measured using the Nile Red assay did not vary dramatically as a function of core composition (Table S7).

2.4.4 Effect of Core Mobility on Diffusion

Introduction of the alkyl oxime functionality into the polymer amphiphiles provided an effective strategy to modify the T_g of their hydrophobic blocks. In addition, this change in chemical structure led to differences in the size of polymer assemblies prepared from the alkyl-modified copolymers. Because the presence of EtOH enhanced diffusion of Cys into the micelles, we

hypothesized that the alkyl-modification strategy would have a similar effect on the rate of diffusion of small molecules into and out of polymer assemblies. To quantify diffusion rates, a model study was conducted in which fluorescein was encapsulated in polymer assemblies of polymers **5a**, **5c**, and **5e**. The dye-loaded micelles were placed in dialysis tubes (6-8 kDa MWCO), and the fluorescence intensity of the incubation media was measured over time using fluorescence spectroscopy. The amount of fluorescein released was quantified (Figure 2-5), using a method similar to a previous report.[14] Briefly, the fluorescence intensity at each time point was compared to the equilibrium intensity measured after 48 h. Release rates were extracted from these data using the Ritger-Peppas equation.[31]

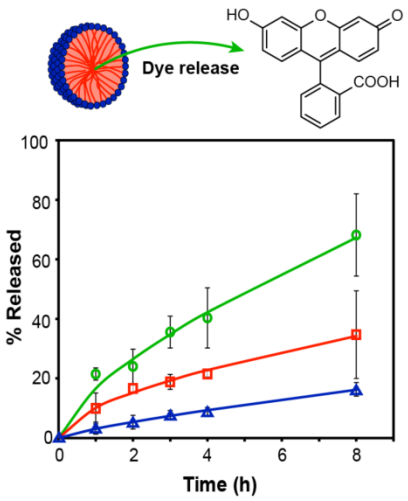

Figure 2-5. Fluorescein release from polymer assemblies **5a** (blue triangles), **5c** (red squares), and **5e** (green circles) at various time points. Release experiments were conducted in phosphate buffer (pH = 7.0) at 25 °C. The colored lines represent fits of the data using the Ritger-Peppas equation. Error bars represent the standard deviation for n=3 replicates.

Micelles prepared from polymer **5a** (highest core T_g) exhibited the slowest release kinetics, with a release rate of 3.1% / h. An intermediate release rate was obtained for polymer assemblies prepared from polymer **5c** (10% / h), while the fastest release rate of 17% / h was measured for assemblies prepared from polymer **5e**. This observed trend in fluorescein release rates is related to the T_g of the block copolymers utilized in the study, with the fastest release rates occurring from the polymer assemblies with the lowest T_g cores. Since release rate in this case only depends on diffusion of fluorescein molecules out of the micelle cores, it is reasonable to assume that the enhanced release kinetics observed for polymer **5e** originate from faster fluorescein diffusion facilitated by increased core mobility and void volume within the polymer assemblies.

2.4.5 Effect of Core Mobility on H_2S Release

Ultimately, we endeavored to modulate the rate of H_2S release from SATO-functionalized micelles. We showed in our earlier study that SATO moieties covalently bound inside the cores of polymer assemblies released H_2S considerably slower than SATO moieties bound to molecularly dissolved (unassembled) polymers.[24] We showed here that this decreased release rate is likely due to slow diffusion of Cys into the glassy core of the polymer micelles. Based on these results, we expected that it would be possible to achieve fast H_2S release by lowering the T_g of the micelle cores by introducing plasticizing alkyl chains to the copolymer structures. To evaluate if this strategy would be useful for modulating H_2S release rates, we conducted methylene blue assays on polymer assemblies prepared from polymers **5a-e**. We prepared micelle samples with identical SATO concentrations (250 μM) and triggered release in all cases with 1 mM Cys to maintain consistent concentrations of the reacting species across all experiments. As shown in Figure 2-6, H_2S release occurred rapidly from assemblies prepared from polymer **5d** (most alkyl content,

lowest T_g) with a half-life of release of 0.18 h. The rate of H_2S release then decreased with increasing T_g, similar to the trend observed for fluorescein release rates measured above. For polymer **5a** (no alkyl content, highest T_g), the release half-life was 4.2 h.

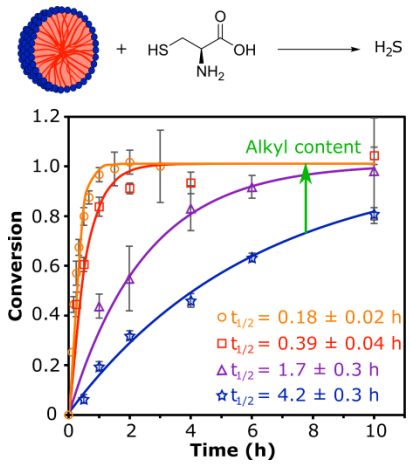

Figure 2-6. Effect of polymer composition and T_g on kinetics of H_2S release from micelles of polymers **5a** (blue stars), **5b** (purple triangles), **5c** (red squares), and **5d** (orange circles). Solid lines represent pseudo-first-order kinetics fits to each data set. A SATO concentration of 250 μM was utilized for each experiment, and 1 mM Cys was applied to trigger H_2S release. Release reactions were conducted in phosphate buffer (pH = 7.0) at rt. The error bars represent the standard deviation in conversion of n=3 replicates.

We attribute the >20-fold difference in rate between the fastest and slowest releasing micelles to increasingly faster diffusion of the triggering Cys molecules into the cores of assemblies with increasingly lower T_g. We also considered that a high rate of unimer exchange for the micelles with plasticized cores could be responsible for the observed rate differences, but previous reports on micelle exchange kinetics indicate that this process is generally much slower than the timescale of H_2S release observed here.[32-33] Our conclusion that core mobility affects Cys

diffusion (and therefore H_2S release kinetics) is supported by the solvent swelling experiments, in which H_2S release occurred more rapidly from swollen, plasticized micelles and was attributed to faster Cys diffusion. Further support comes from the fluorescein release experiments that showed more rapid release of fluorescein for micelles functionalized with the highest content of alkyl oxime (lowest T_g, most mobile). Indeed, at the highest alkyl content (91 wt. %), the rate of H_2S release from the micelles approached the rate of H_2S release from small molecules dissolved in solution, implying that the reaction kinetics have been decoupled from Cys diffusion and again depend on the rate of reaction of Cys with the SATO moieties.

2.5 Conclusions:

The origin of slow release of H_2S from SATO-functionalized micelles was investigated and attributed to limitations in the rate of diffusion of triggering Cys molecules into the micelle cores. Swelling studies with EtOH showed that greater swelling in micelle cores led to faster H_2S release, likely due to faster Cys diffusion. To increase Cys diffusion without adding organic solvent, SATO-containing amphiphilic block copolymers were functionalized with plasticizing alkyl chains to increase micelle core mobility. Incorporation of an alkyl co-monomer was shown to decrease T_g of the hydrophobic block in a systematic fashion. Evidence of enhanced diffusion in lower T_g micelles was provided by release of sequestered fluorescein from micelles prepared from these alkyl-modified block copolymers, with faster release observed from micelles with increased weight fractions of the alkyl comonomer. When triggered with Cys, the half-life of H_2S release could be tuned over more than an order of magnitude, from 0.18 – 4.2 h, by increasing the weight fraction of alkyl comonomer. We attribute this dramatic difference in release rate for block copolymer micelles with high alkyl content to faster diffusion of the triggering Cys molecules into

the micelle cores. Furthermore, we anticipate that this strategy could be broadly applied in other drug delivery systems to precisely modulate drug release kinetics.

2.6 Acknowledgements:

This work was supported by the National Science Foundation (DMR-1454754), the National Institutes of Health (R01GM123508), and the Dreyfus Foundation. NBS was supported by an NSF-funded REU program (1560240). We thank Prof Tim Long and Prof Rick Davis for use of instruments.

2.7 References:

1. Kataoka, K.; Harada, A.; Nagasaki, Y., *Adv. Drug Deliv. Rev.* **2012**, *64*, 37-48.

2. Rösler, A.; Vandermeulen, G. W. M.; Klok, H.-A., *Adv. Drug Deliv. Rev.* **2001**, *53* (1), 95-108.

3. Duncan, R., *Nat. Rev. Drug. Discov.* **2003**, *2* (5), 347-360.

4. Allen, T. M.; Cullis, P. R., *Science* **2004**, *303* (5665), 1818-1822.

5. Nishiyama, N.; Okazaki, S.; Cabral, H.; Miyamoto, M.; Kato, Y.; Sugiyama, Y.; Nishio, K.; Matsumura, Y.; Kataoka, K., *Cancer Res.* **2003**, *63* (24), 8977-8983.

6. Peer, D.; Karp, J. M.; Hong, S.; Farokhzad, O. C.; Margalit, R.; Langer, R., *Nat. Nanotecnol.* **2007**, *2* (12), 751-760.

7. Matson, J. B.; Grubbs, R. H., *J. Am. Chem. Soc.* **2008**, *130* (21), 6731-6733.

8. Robin, M. P.; Mabire, A. B.; Damborsky, J. C.; Thom, E. S.; Winzer-Serhan, U. H.; Raymond, J. E.; O'Reilly, R. K., *J. Am. Chem. Soc.* **2013**, *135* (25), 9518-9524.

9. Lee, Y.; Ishii, T.; Cabral, H.; Kim, H. J.; Seo, J.-H.; Nishiyama, N.; Oshima, H.; Osada, K.; Kataoka, K., *Angew. Chemie. Int. Ed.* **2009**, *121* (29), 5413-5416.

10. Smith, A. E.; Sizovs, A.; Grandinetti, G.; Xue, L.; Reineke, T. M., *Biomacromolecules* **2011**, *12* (8), 3015-3022.

11. Kakizawa, Y.; Kataoka, K., *Adv. Drug Deliv. Rev.* **2002**, *54* (2), 203-222.

12. Lim Soo, P.; Luo, L.; Maysinger, D.; Eisenberg, A., *Langmuir* **2002**, *18* (25), 9996-10004.

13. Robin, M. P.; Osborne, S. A. M.; Pikramenou, Z.; Raymond, J. E.; O'Reilly, R. K., *Macromolecules* **2016**, *49* (2), 653-662.

14. Chan, D.; Yu, A. C.; Appel, E. A., *Biomacromolecules* **2017**, *18* (4), 1434-1439.

15. Molla, M. R.; Rangadurai, P.; Antony, L.; Swaminathan, S.; de Pablo, J. J.; Thayumanavan, S., *Nature Chemistry* **2018**, *10* (6), 659-666.

16. Cheetham, A. G.; Zhang, P.; Lin, Y.-a.; Lock, L. L.; Cui, H., *J. Am. Chem. Soc.* **2013**, *135* (8), 2907-2910.

17. van Bommel, K. J. C.; Stuart, M. C. A.; Feringa, B. L.; van Esch, J., *Org. Biomol. Chem.* **2005**, *3* (16), 2917-2920.

18. Urquhart, M. C.; Ercole, F.; Whittaker, M. R.; Boyd, B. J.; Davis, T. P.; Quinn, J. F., *Polym. Chem.* **2018**, *9* (35), 4431-4439.

19. Wang, R., *Physiol. Rev.* **2012**, *92* (2), 791-896.

20. Zheng, Y.; Yu, B.; De La Cruz, L. K.; Roy Choudhury, M.; Anifowose, A.; Wang, B., *Med. Res. Rev.* **2018**, *38* (1), 57-100.

21. Powell, C. R.; Dillon, K. M.; Matson, J. B., *Biochem. Pharm.* **2018**, *149*, 110-123.

22. Carter, J. M.; Qian, Y.; Foster, J. C.; Matson, J. B., *Chem. Commun.* **2015**, *51* (66), 13131-13134.

23. Foster, J. C.; Matson, J. B., *Macromolecules* **2014**, *47* (15), 5089-5095.

24. Foster, J. C.; Radzinski, S. C.; Zou, X.; Finkielstein, C. V.; Matson, J. B., *Mol. Pharm.* **2017**, *14* (4), 1300-1306.

25. Connal, L. A., *J. Mater. Chem. B* **2018**, *6* (44), 7122-7128.

26. Foster, J. C.; Powell, C. R.; Radzinski, S. C.; Matson, J. B., *Org. Lett.* **2014**, *16* (6), 1558-1561.

27. Chen, M.; Moad, G.; Rizzardo, E., *J. Poly. Sci. Part A: Polym. Chem.* **2009**, *47* (23), 6704-6714.

28. Zhao, Y.; Wang, H.; Xian, M., *J. Am. Chem. Soc.* **2011**, *133*, 15-17.

29. Löbling, T. I.; Ikkala, O.; Gröschel, A. H.; Müller, A. H. E., *ACS Macro Lett.* **2016**, *5* (9), 1044-1048.

30. Evans, C. M.; Henderson, K. J.; Saathoff, J. D.; Shull, K. R.; Torkelson, J. M., *Macromolecules* **2013**, *46* (10), 4131-4140.

31. Ritger, P. L.; Peppas, N. A., *J. Control. Release* **1987**, *5* (1), 37-42.

32. Won, Y.-Y.; Davis, H. T.; Bates, F. S., *Macromolecules* **2003**, *36* (3), 953-955.

33. Lund, R.; Willner, L.; Richter, D.; Dormidontova, E. E., *Macromolecules* **2006**, *39* (13), 4566-4575.

2.8 Experimental:

Materials

All reagents were obtained from commercial vendors and used as received unless otherwise stated. 2,2′-Azobis(2-methylpropionitrile) (AIBN) was recrystallized from methanol prior to use. *S*-Aroylthiohydroxylamine (SATHA) and **SATO1** ((C_6H_5)C=OSN=CH(C_6H_4)COOH were prepared according to previously reported procedures.[1] The monomer 2-(4-formylbenzoyloxy)ethyl methacrylate (FBEMA) was also synthesized as previously reported.[2] Dry solvents were purified by passage through a solvent purification system (MBraun).

Methods

NMR spectra were measured on an Agilent 400 MHz spectrometer. ^{1}H and ^{13}C NMR chemical shifts are reported in ppm relative to internal solvent resonances. Yields refer to chromatographically and spectroscopically pure compounds unless otherwise stated. Size exclusion chromatography (SEC) was carried out in THF at 1 mL/min at 30 °C on two Agilent PLgel 10 µm MIXED-B columns connected in series with a Wyatt Dawn Heleos 2 light scattering detector and a Wyatt Optilab Rex refractive index detector. No calibration standards were used, and d*n*/d*c* values were obtained by assuming 100% mass elution from the columns. UV-Vis absorbance spectra were recorded on a Spectramax M2 plate reader (Molecular Devices) from 800 to 550 nm. Dynamic light scattering (DLS) was conducted using a Malvern Zetasizer Nano

operating at 25 °C. A solution of micelles was prepared at 1 mg/mL and filtered with a 0.2 μm filter prior to scanning. The calculations of the particle size distributions and distribution averages were conducted using CONTIN particle size distribution analysis routines with intensity, volume and number averages. Measurements were made in triplicate and errors reflect standard deviations. In cases where EtOH/H_2O mixtures were used the solvent viscosity and refractive index were set according to literature values[3-4]. Fluorescence spectroscopy was performed on a Varian Cary Eclipse Fluorescence Spectrophotometer. Fluorescence measurements were conducted with λ_{ex} = 460 nm and slit widths of 5 nm for both excitation and emission slits. The emission intensity was then monitored at 540 nm. Differential scanning calorimetry (DSC) studies were carried out on a Q-2000 DSC in aluminum pans operated with a dry nitrogen purge from -50 °C to 140 °C with a heating and cooling rate of 20 °C/min. Results are reported from the second heat cycle and figures are shown as exo down.

Synthesis of Alkyl Hydroxylamine

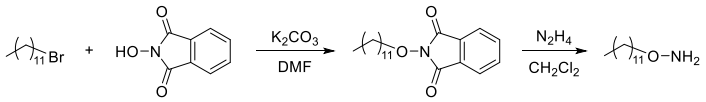

Alkyl hydroxylamine was prepared using a modified literature procedure.[5] A round bottom flask was charged with 1-bromoundecane (10.40 g, 41.7 mmol), hydroxyphthalimide (10.21 g, 62.6 mmol), K_2CO_3 (8.65 g, 62.6 mmol), and DMF (60 mL). The reaction mixture was heated at 80 °C for 48 h. The reaction mixture was then cooled to rt. The reaction mixture was diluted with H_2O (100 mL), and the product was extracted with EtOAc (2 x 100 mL). The combined EtOAc layers were washed with brine (5x), dried over Na_2SO_4, and rotovapped to afford the crude dodecyl phthalimide product as a yellow oil. This was used in the next step without further purification.

Dodecyl phthalimide(14.9 g, 45.0 mmol) was dissolved in CH_2Cl_2 (200 mL) in a round bottom flask. The flask was placed in an ice bath. Hydrazine (40% in H_2O) (17.48 mL, 225 mmol) was added in one portion, and the reaction mixture was allowed to warm to rt and was stirred for 2 h. The reaction mixture was transferred to a separatory funnel and washed consecutively with H_2O, satd. $NaHCO_3$, and brine. The organic layer was dried over Na_2SO_4 and rotovapped to afford the pure product as a colorless oil (5.88 g, 65% yield). ^{1}H NMR ($CDCl_3$, 400 MHz) δ: 5.34 (s, 2H), 3.65 (t, *J* = 8 Hz, 2H), 1.56 (q, *J* = 8 Hz, 2H), 1.28 (m, 18H), 0.88 (t, *J* = 7 Hz, 3H). ^{13}C NMR ($CDCl_3$, 100 MHz) δ: 76.24, 31.90, 29.64, 29.62, 29.58, 29.57, 29.50, 29.33, 28.39, 25.99, 22.67, 14.10.

Synthesis of 4-cyano-4-(dodecylsulfanylthiocarbonyl)sulfanyl pentanoic acid (CTA)

CTA was prepared according to a previously reported procedure:[6] Dodecanethiol (10 mL, 41.7 mmol) was dissolved in hexanes (150 mL) in a round bottom flask. To the flask was added a solution of potassium *tert*-butoxide (4.68 g, 41.7 mmol) in THF (50 mL). The reaction mixture was stirred at rt for 20 min. CS_2 was added (2.7 mL, 44.7 mmol), and the reaction mixture was stirred for an additional 1 h. I_2 was then added in portions until the reaction mixture maintained a persistent dark brown color. The reaction mixture was stirred overnight at rt. The reaction mixture was transferred to a separatory funnel and washed consecutively with 10% $Na_2S_2O_3$, H_2O, and brine. The organic layer was then dried over Na_2SO_4 and rotovapped.

The resulting viscous yellow oil (22.8 g, 41.1 mmol) was redissolved in EtOAc (100 mL) in a round bottom flask. To the flask was added 4,4′-azobis(4-cyanovaleric acid) (11.6 g, 41.4 mmol). The reaction mixture was heated at reflux overnight. Silica gel was poured into the reaction flask, and the silica slurry was rotovapped to dryness. The silica was then dry-loaded onto a silica gel column, eluting with 9:1 hexanes/EtOAc. The product-containing fractions (R_f ~ 0.3 in the

mobile phase) were combined and rotovapped to give the product as a yellow solid (9.50 g, 57% yield). ^{1}H NMR ($CDCl_3$, 400 MHz): δ 3.33 (t, *J* = 4 Hz, 2H), 2.68 (t, *J* = 4 Hz, 2H), 2.54 (m, 1H), 2.39 (m, 1H), 1.88 (s, 3H), 1.69 (q, *J* = 8 Hz, 2H), 1.45-1.19 (m, 18H), 0.88 (t, *J* = 4 Hz, 3H). ^{13}C NMR ($CDCl_3$, 100 MHz): δ 216.88, 177.63, 118.99, 46.30, 37.21, 33.58, 32.03, 29.74, 29.67, 29.66, 29.54, 29.46, 29.19, 29.05, 27.78, 24.96, 22.81, 14.25. HR-MS: $[M + H]^+$ calculated 404.1746; found 404.1749.

Synthesis of macroCTA

MacroCTA was prepared according to a previously reported procedure:[6] A round bottom flask was charged with **CTA** (0.81 g, 2.01 mmol), polyethylene glycol monomethyl ether (M_n = 5,000 g/mol, 2.0 g, 0.400 mmol), 4-dimethylamino pyridine (0.12 g, 0.982 mmol), and anhydrous CH_2Cl_2 (40 mL). *N*,*N*'-Dicyclohexylcarbodiimide (DCC) (0.41 g, 1.99 mmol) was dissolved in 5 mL of anhydrous CH_2Cl_2 in a vial. The DCC solution was added dropwise to the flask containing the other reagents, and the reaction mixture was stirred at rt overnight. The precipitated solids were removed by filtration. The desired product was isolated via precipitation from diethyl ether and was purified by repeated precipitations (2-4) from CH_2Cl_2 into diethyl ether to afford the product as a yellow solid (1.50 g, 69% yield). ^{1}H NMR ($CDCl_3$, 400 MHz): δ 4.24 (t, *J* = 4 Hz, 2H), 3.80 (t, *J* = 4 Hz, 2H), 3.71-3.51 (m, 494H), 3.45 (t, *J* = 4 Hz, 2H), 3.36 (s, 3H), 3.31 (t, *J* = 8 Hz, 2H), 2.64 (t, *J* = 8 Hz, 2H), 2.51 (m, 1H), 2.37 (m, 1H), 1.86 (s, 3H), 1.68 (t, *J* = 8 Hz, 2H), 1.42-1.18 (m, 18H), 0.87 (t, *J* = 4 Hz, 3H).

Synthesis of poly(FBEMA)

PEG-*b*-poly(FBEMA) was prepared according to a previously reported procedure:[2] A typical polymerization procedure is as follows: To an oven-dried Schlenk tube equipped with a

magnetic stir bar was added **CTA** (13 mg, 0.032 mmol), **FBEMA** (1.00 g, 3.81 mmol), and 5 mL of anhydrous DMF. A solution of AIBN was prepared by dissolving 2.61 mg (15.9 μmol) in 1 mL of anhydrous DMF in a vial. 100 μL of this solution was added to the Schlenk tube. The tube was deoxygenated by subjecting the contents to three freeze−pump−thaw cycles. The Schlenk tube was then backfilled with N_2 and submerged in an oil bath maintained at 75 °C. Samples were removed periodically by N_2-purged syringe to monitor molar mass evolution by SEC and conversion by ^{1}H NMR spectroscopy. The polymerization was quenched by submerging the tube into liquid N_2 and exposing the reaction mixture to air. The resulting poly(FBEMA) was isolated via precipitation from diethyl ether. If necessary, further precipitations from CH_2Cl_2 into diethyl ether were preformed to remove residual monomer.

Synthesis of PEG-b-poly(FBEMA)

PEG-*b*-poly(FBEMA) was prepared according to a previously reported procedure:[6] A typical polymerization procedure is as follows: To an oven-dried Schlenk tube equipped with a magnetic stir bar was added macroCTA (127 mg, 25.0 μmol), FBEMA (1.00 g, 3.81 mmol), and 5 mL of anhydrous DMF. A solution of AIBN was prepared by dissolving 4.2 mg (2.54 μmol) in 1 mL of anhydrous DMF in a vial. 100 μL of this solution was added to the Schlenk tube. The tube was deoxygenated by subjecting the contents to three freeze−pump−thaw cycles. The Schlenk tube was then backfilled with N_2 and submerged in an oil bath maintained at 75 °C. Samples were removed periodically by N_2-purged syringe to monitor molar mass evolution by SEC and conversion by ^{1}H NMR spectroscopy. The polymerization was quenched by submerging the tube into liquid N_2 and exposing the reaction mixture to air. The resulting PEG-*b*-poly(FBEMA) was isolated via precipitation from a diethyl ether. If necessary, further precipitations from CH_2Cl_2 into diethyl ether were preformed to remove residual monomer.

Removal of Dithioester End Group

A round-bottom flask was charged with PEG-*b*-poly(FBEMA) (0.50 g, 14.0 µmol), AIBN (47.0 mg, 284 µmol), and 1,4-dioxane (3 mL). The flask was outfitted with a condenser, and the reaction mixture was heated in an oil bath maintained at 80 °C for 1.5 h. The reaction mixture was allowed to cool to rt, and the polymer was recovered via precipitation from diethyl ether.

Addition of SATHA to PEG-b-poly(FBEMA)

A general procedure for the SATO formation reaction is as follows: Following end group removal, PEG-*b*-poly(FBEMA) (100 mg, 3.21 µmol) was dissolved in CH_2Cl_2 (3 mL) in a 1 dram vial. To the vial was added SATHA (147 mg, 962 µmol) in one portion. Approximately 10 µL of trifluoroacetic acid (TFA) was added as a catalyst. The reaction mixture was left to stand at rt for 16 h over molecular sieves. ^{1}H NMR spectroscopy was conducted after this time to determine the conversion of aldehyde to SATO. The modified polymer was recovered via precipitation from diethyl ether.

Thiooxime micelle synthesis

A scintillation vial equipped with a stir bar was charged with polymer (10 mg) and THF (5 mL). Distilled H_2O (5 mL) was rapidly added to the vial, and the solution was allowed to stir for 15 min. The solution was transferred to dialysis tubing (6-8 kD MWCO) and dialyzed against distilled water for 48 h, changing the water every 12 h.

Comparing H_2S release from SATO-containing small molecules, copolymers and micelles

Reactions for kinetic studies were run in quadruplicate, with each reaction vial containing 20 µL of phosphate buffer (1 M in H_2O, pH = 7), SATO solution (either small molecule **SATO1**,

linear copolymer, or micelles to make an overall concentration of SATO groups of 250 μM), 100 μL of $Zn(OAc)_2$ solution (40 mM in H_2O), 20 μL of cysteine solution (100 mM in H_2O), and DI H_2O to 2 mL total volume. Final concentrations were 250 μM SATO functional groups, 2 mM $Zn(OAc)_2$, and 1 mM cysteine. A blank vial was run for each experiment containing DI H_2O instead of SATO solution. At predetermined timepoints, 100 μL aliquots were taken from each vial and diluted with 100 μL of $FeCl_3$ solution (30 mM in 1.2 M HCl) and 100 μL of *p*-phenylene diamine solution (20 mM in 7.2 M HCl). Each aliquot solution remained sealed in a microcentrifuge tube for a minimum of 24 h prior to addition of 250 μL to a 96-well plate. The absorbance for each aliquot was measured at 750 nm using a plate reader.

H_2S Release from small molecule SATO as a function of EtOH concentration

Reactions for kinetic studies were run in quadruplicate, with each reaction vial containing 20 μL of phosphate buffer (1 M in H_2O, pH = 7), 200 μL **SATO1** solution (2.5mM in THF), 400 μL THF, 100 μL of $Zn(OAc)_2$ solution (40 mM in H_2O), 20 μL of cysteine solution (100 mM in H_2O), 0-600 uL of EtOH, and DI H_2O to 2 mL total volume. Final concentrations were 250 μM SATO functional groups, 2 mM $Zn(OAc)_2$, 0-30% EtOH, and 1 mM cysteine. A blank vial was run for each experiment containing DI H_2O instead of SATO solution. At predetermined timepoints, 100 μL aliquots were taken from each vial and diluted with 100 μL of $FeCl_3$ solution (30 mM in 1.2 M HCl) and 100 μL of *p*-phenylene diamine solution (20 mM in 7.2 M HCl). Each aliquot solution remained sealed in a microcentrifuge tube for a minimum of 2 h prior to addition of 250 μL to a 96-well plate. The absorbance for each aliquot was measured at 750 nm using a plate reader.

H_2S Release from micelles as a function of EtOH concentration.

Reactions for kinetic studies were run in quadruplicate, with each reaction vial containing 20 µL of phosphate buffer (1 M in H_2O, pH = 7), micelle solution (final concentration of SATO functional groups 250 µM), 100 µL of $Zn(OAc)_2$ solution (40 mM in H_2O), 20 µL of cysteine solution (100 mM in H_2O), 0-600 µL of EtOH, and DI H_2O to 2 mL total volume. Final concentrations were 250 µM SATO functional groups, 2 mM $Zn(OAc)_2$, 0-30% EtOH, and 1 mM cysteine. A blank vial was run for each experiment containing no micelle solution. At predetermined timepoints, 100 µL aliquots were taken from each vial and diluted with 100 µL of $FeCl_3$ solution (30 mM in 1.2M HCl) and 100 µL of *p*-phenylene diamine solution (20 mM in 7.2M HCl). Each aliquot solution remained sealed in a microcentrifuge tube for a minimum of 24 h prior to addition of 250 µL to a 96-well plate. The absorbance for each aliquot was measured at 750 nm using a plate reader.

Evaluation of Synthesis of SATO-co-Oxime Copolymers

To determine the reactivity of oxime and SATHA nucleophiles towards the pendant aldehydes of poly(FEBMA), a series of NMR tube experiments were conducted. In each, 10 mg of polymer **3** was dissolved in $CDCl_3$ in a vial. To the vial was added a predetermined amount of either SATHA or alkyl oxime, both according to Table S6. 20 µL of TFA and molecular sieves were then added to the vials, and the reactions were allowed to proceed at rt for 16 h. ^{1}H NMR spectroscopy was then utilized to compare the relative incorporation of these nucleophiles via integration of resonances from the oxime, SATO, and/or aldehyde groups. These results are summarized in Table S6.

In addition, a 2-step method was also evaluated wherein poly(FEBMA) was first functionalized with either oxime or SATO groups, isolated via precipitation, and then treated with an excess of the other nucleophile type. NMR spectroscopic analysis was then conducted as

described above. If the oxime was installed first, addition of excess SATHA and catalytic TFA did not alter the proportion of oxime that was present prior to this reaction (ca. 70 mol%). In contrast, oxime addition to a polymer pre-functionalized with SATO groups (ca. 45 mol%) led to a polymer that was completely functionalized with oximes.

Based on these results, we concluded that to achieve a desired sidechain composition, a post-functionalization reaction could be conducted in one step wherein the desired amount of oxime nucleophile would be added in addition to excess SATHA nucleophile. This procedure was employed to prepare polymers **4a-e** and **5a-e**.

Fluorescein release from micelles as a function of alkyl content

PEG-*b*-poly(FBEMA) (1.0 mg, 0.059 µmol) was added to a scintillation vial and dissolved in 0.9 mL of THF. To the vial was added 100 µL of a 1 mg/mL solution of fluorescein in THF, after which 1 mL of H_2O was rapidly added. The solution was stirred for 5 min, then diluted with phosphate buffer (100 mM in H_2O, pH = 7.0) to 10 mL of total volume, transferred to dialysis tubing (MWCO 6-8 kD), and placed in a beaker containing 200 mL of phosphate buffer (100 mM in H_2O, pH =7.0). At predetermined times points, aliquots (2 mL each) were removed from the external dialysate solution and analyzed by fluorescence to quantify fluorescein content.

H_2S Release from micelles as a function of alkyl content

Reactions for kinetic studies were run in quadruplicate, with each reaction vial containing 20 µL of phosphate buffer (1M in H_2O, pH = 7), micelle solution (final concentration of SATO functional groups 250 µM), 100 µL of $Zn(OAc)_2$ solution (40 mM in H_2O), 20 µL of cysteine solution (100 mM in H_2O), and DI H_2O to 2 mL total volume. Final concentrations were 250 µM SATO functional groups, 2 mM $Zn(OAc)_2$, and 1 mM cysteine. A blank vial was run for each

experiment containing no micelle solution. At predetermined timepoints, 100 µL aliquots were taken from each vial and diluted with 100 µL of $FeCl_3$ solution (30 mM in 1.2M HCl) and 100 µL of *p*-phenylene diamine solution (20 mM in 7.2M HCl). Each aliquot solution remained sealed in a microcentrifuge tube for a minimum of 24 h prior to addition of 250 µL to a 96-well plate. The absorbance for each aliquot was measured at 750 nm using a plate reader.

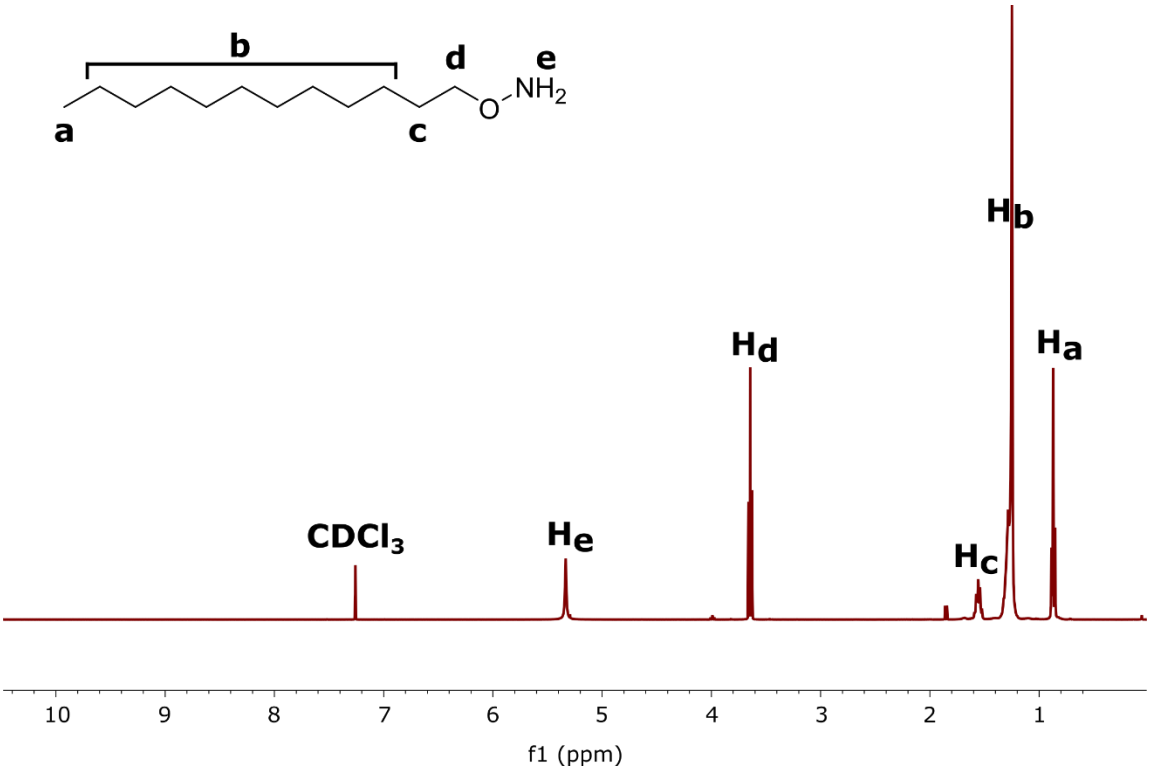

Figure S1. ^{1}H NMR spectrum of dodecyl hydroxylamine.

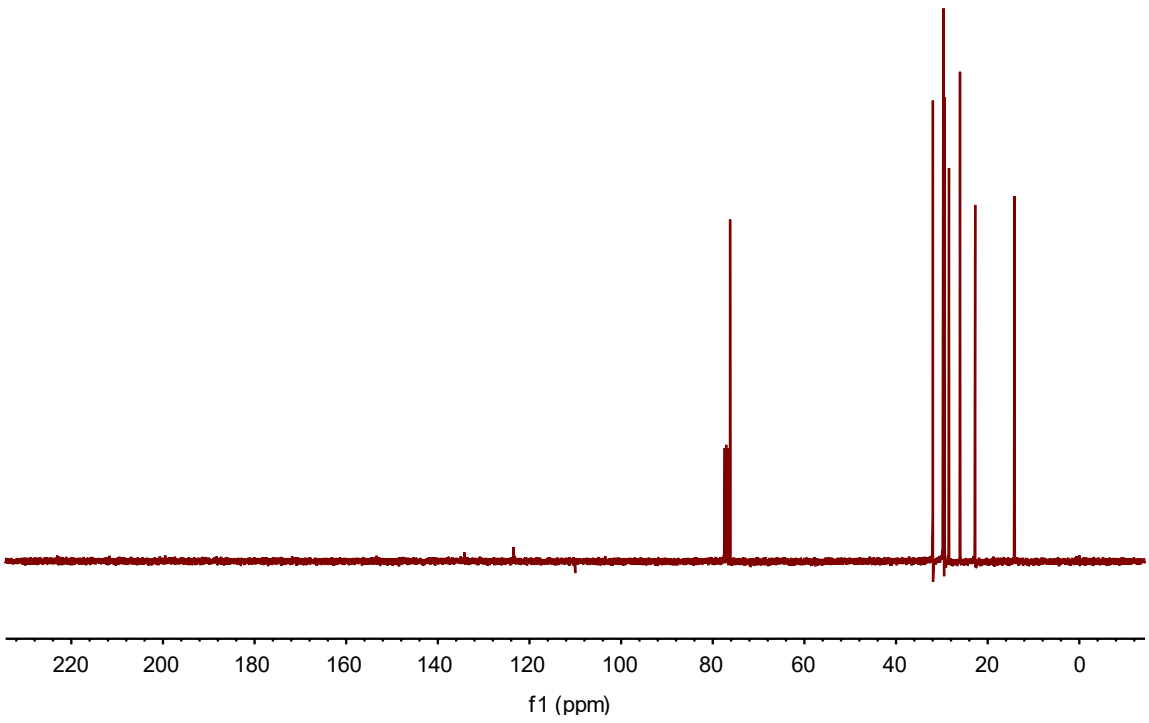

Figure S2. ^{13}C NMR spectrum of dodecyl hydroxylamine.

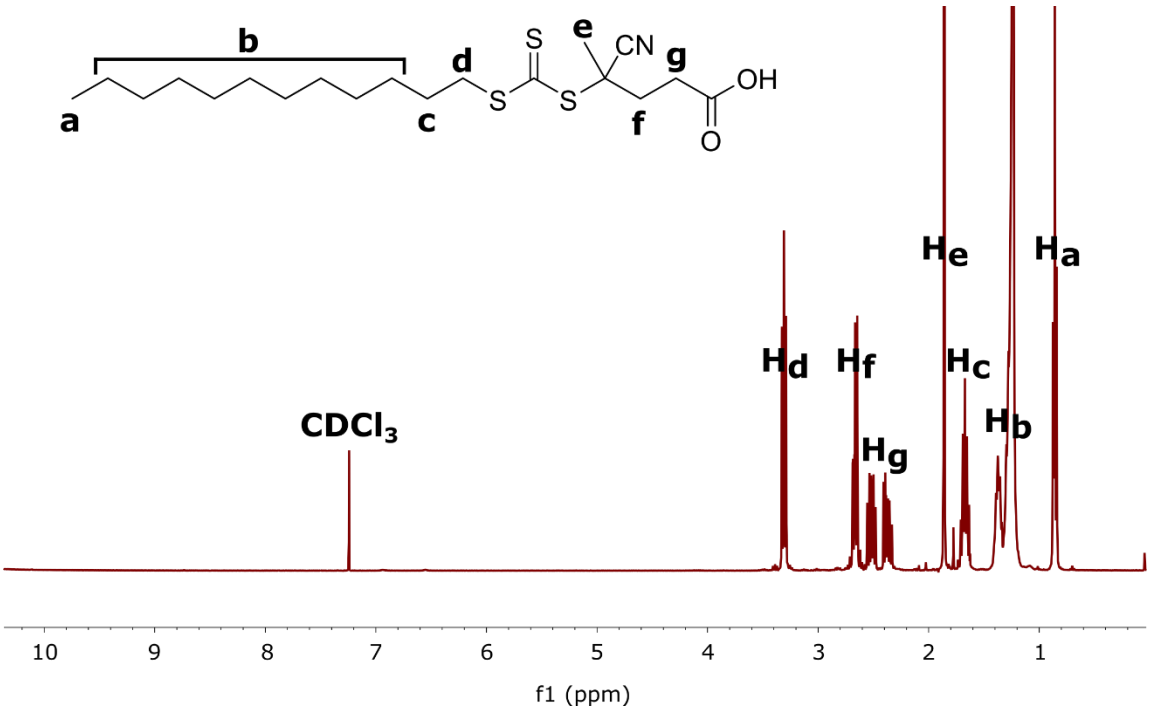

Figure S3. ^{1}H NMR spectrum of **4-cyano-4-(dodecylsulfanylthiocarbonyl)sulfanyl pentanoic acid (CTA)**.

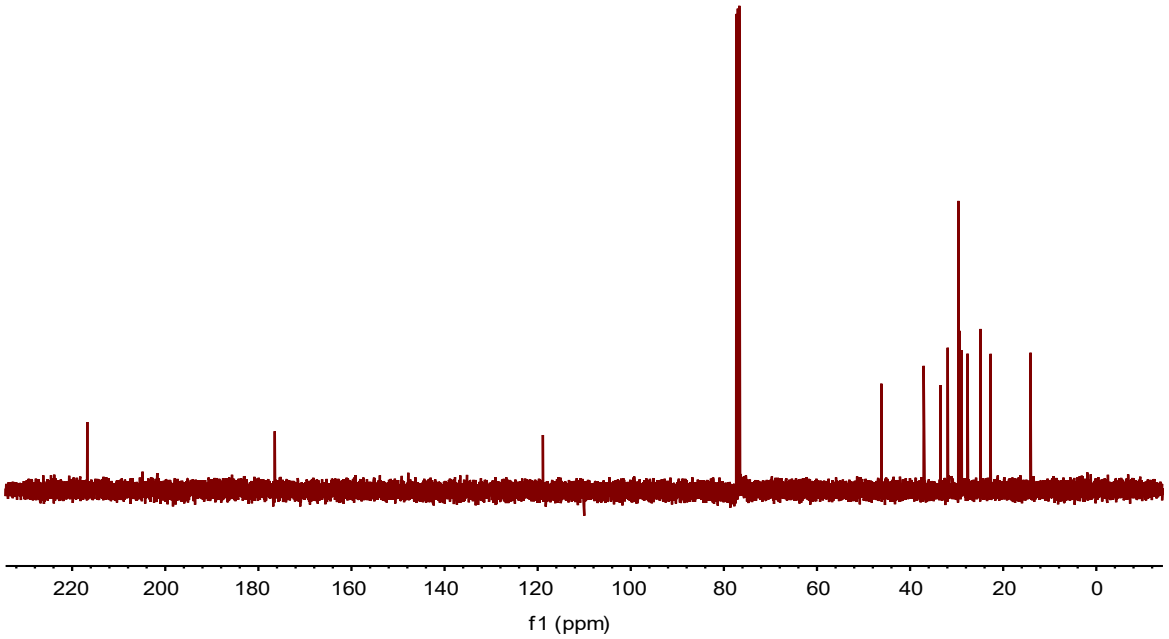

Figure S4. ^{13}C NMR spectrum of **4-cyano-4-(dodecylsulfanylthiocarbonyl)sulfanyl pentanoic acid** (**CTA)**.

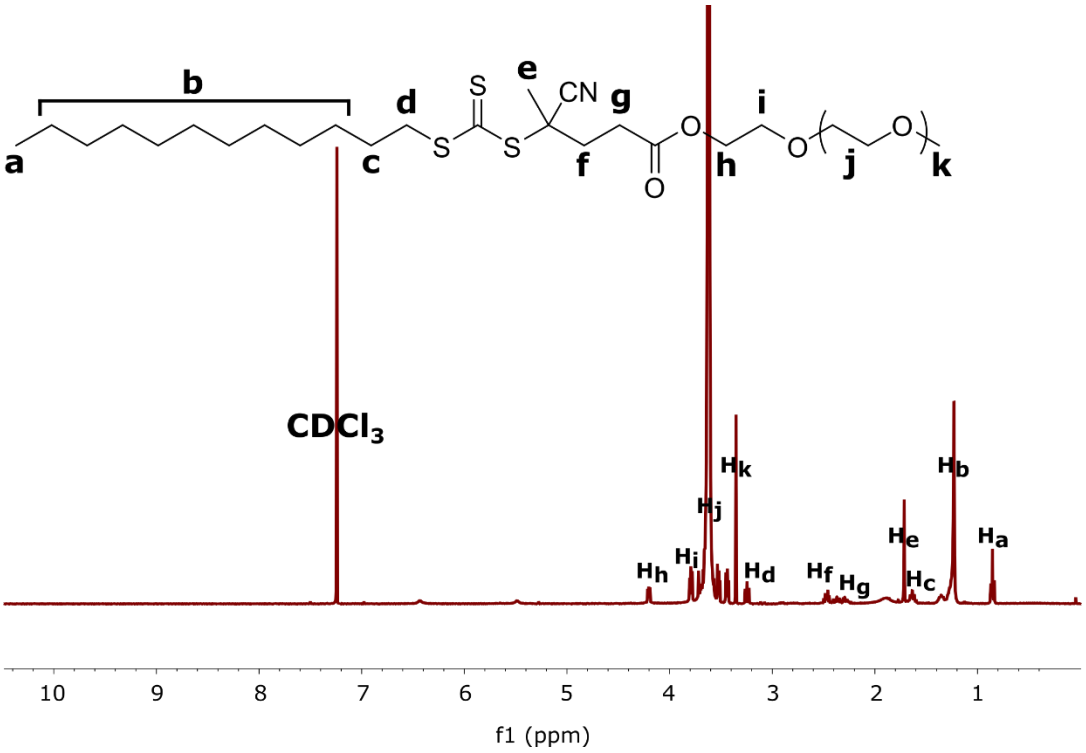

Figure S5. ^{1}H NMR spectrum of **PEG-(4-cyano-4-(dodecylsulfanylthiocarbonyl)sulfanyl pentanoic acid) (macroCTA)**.

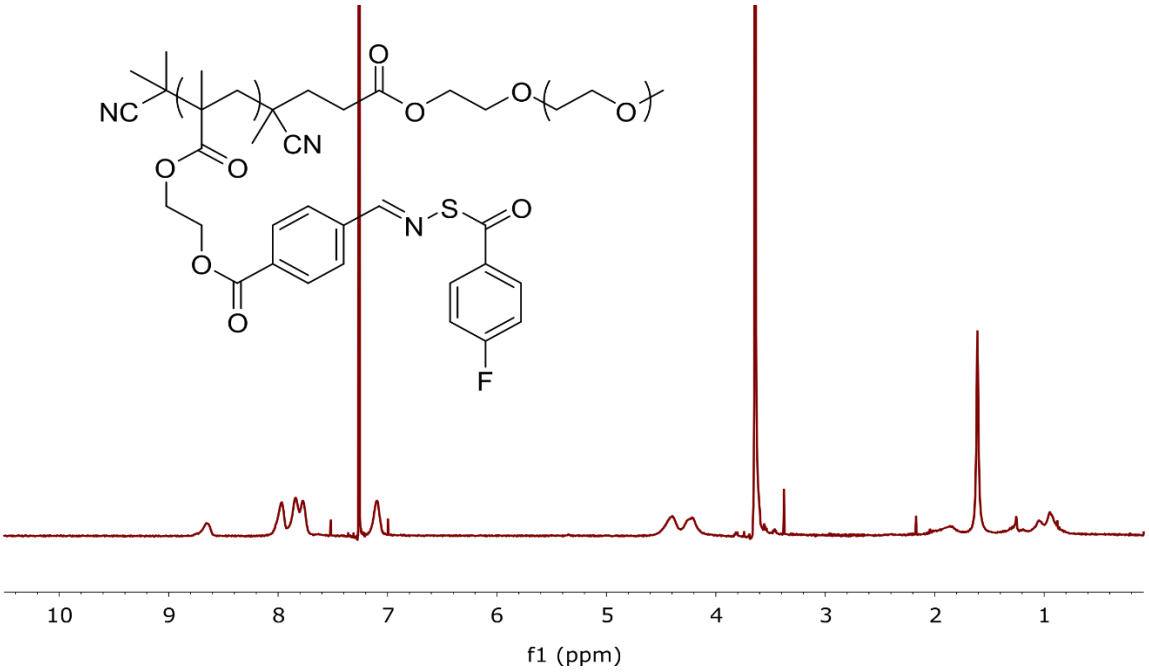

Figure S6. ^{1}H NMR spectrum of **polymer 3a** (PEG-*b*-(SATO-F)).

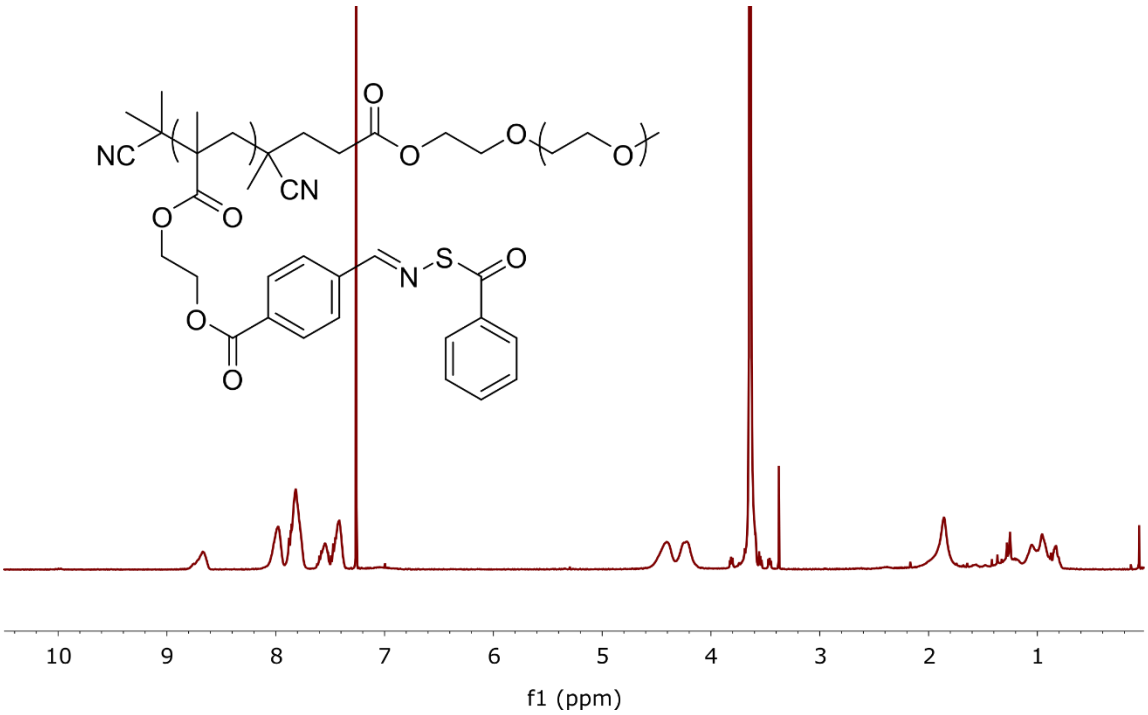

Figure S7. ^{1}H NMR spectrum of **polymer 3b** (PEG-*b*-(SATO).

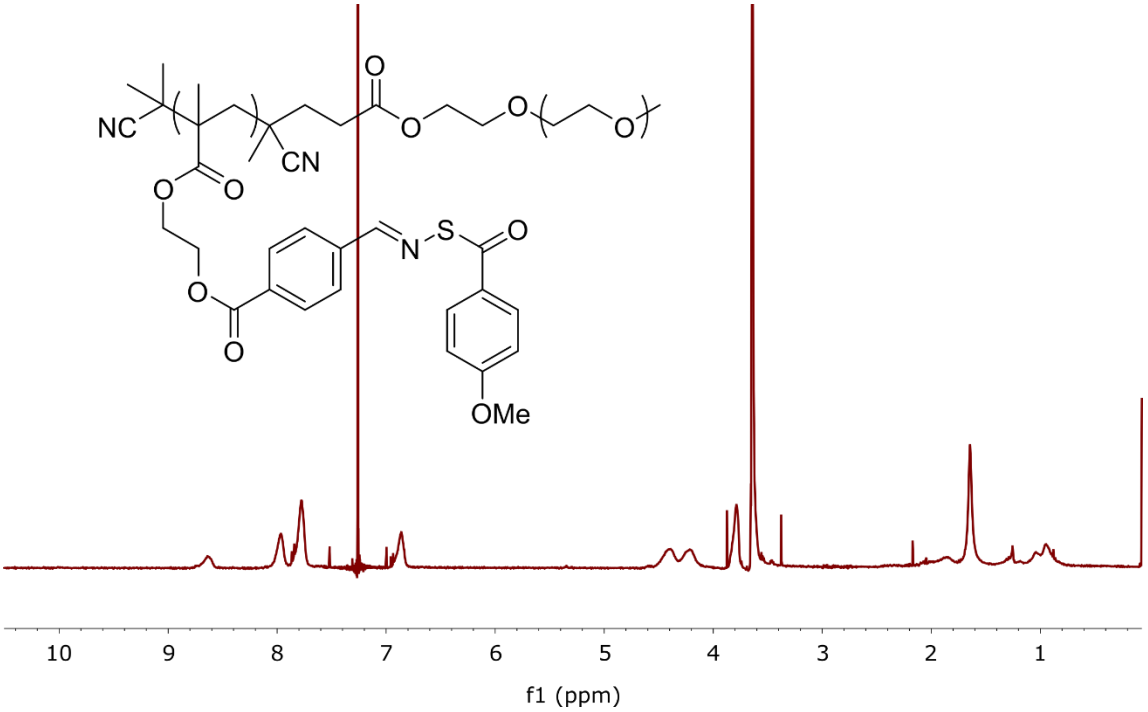

Figure S8. ^{1}H NMR spectrum of **polymer 3c** (PEG-*b*-(SATO-OMe).

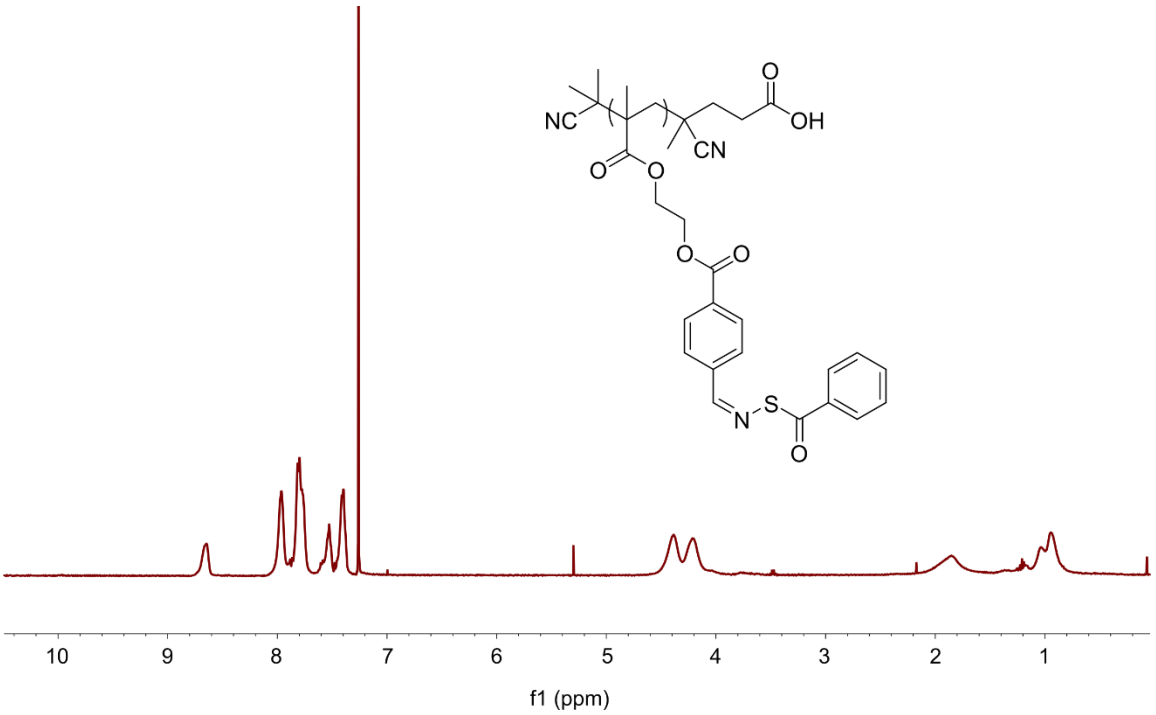

Figure S9. ^{1}H NMR spectrum of **polymer 4a** (poly(SATO)).

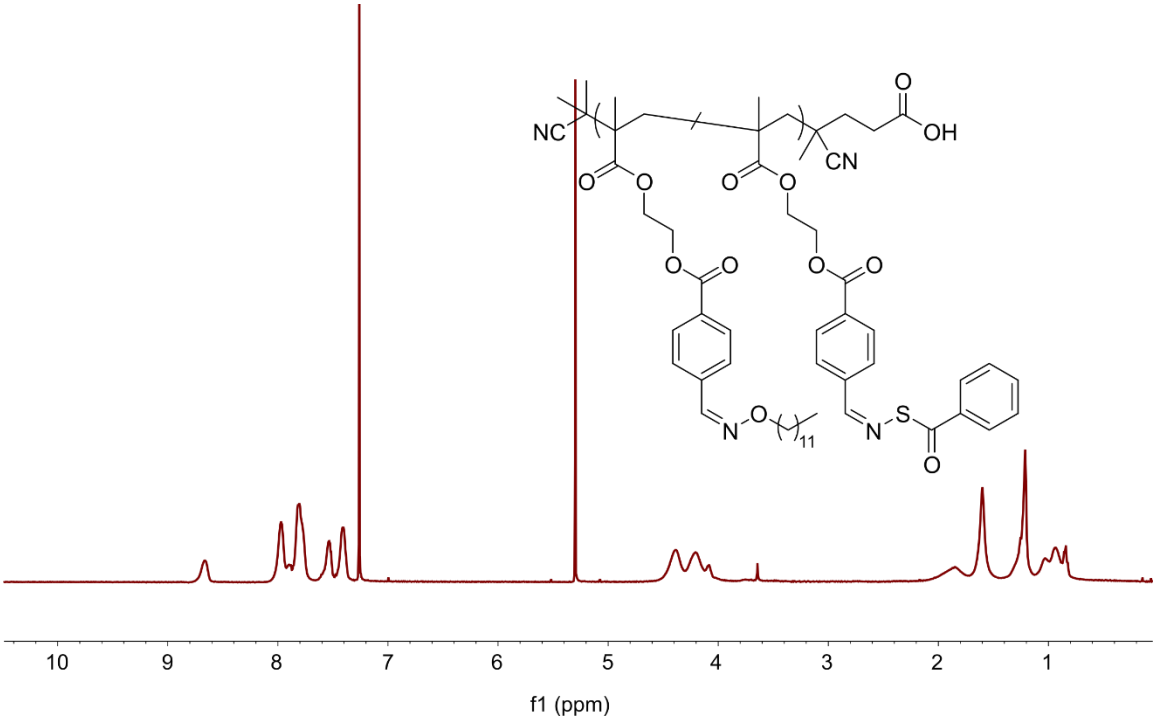

Figure S10. ^{1}H NMR spectrum of **polymer 4b** (poly(SATO-*co*-alkyl)).

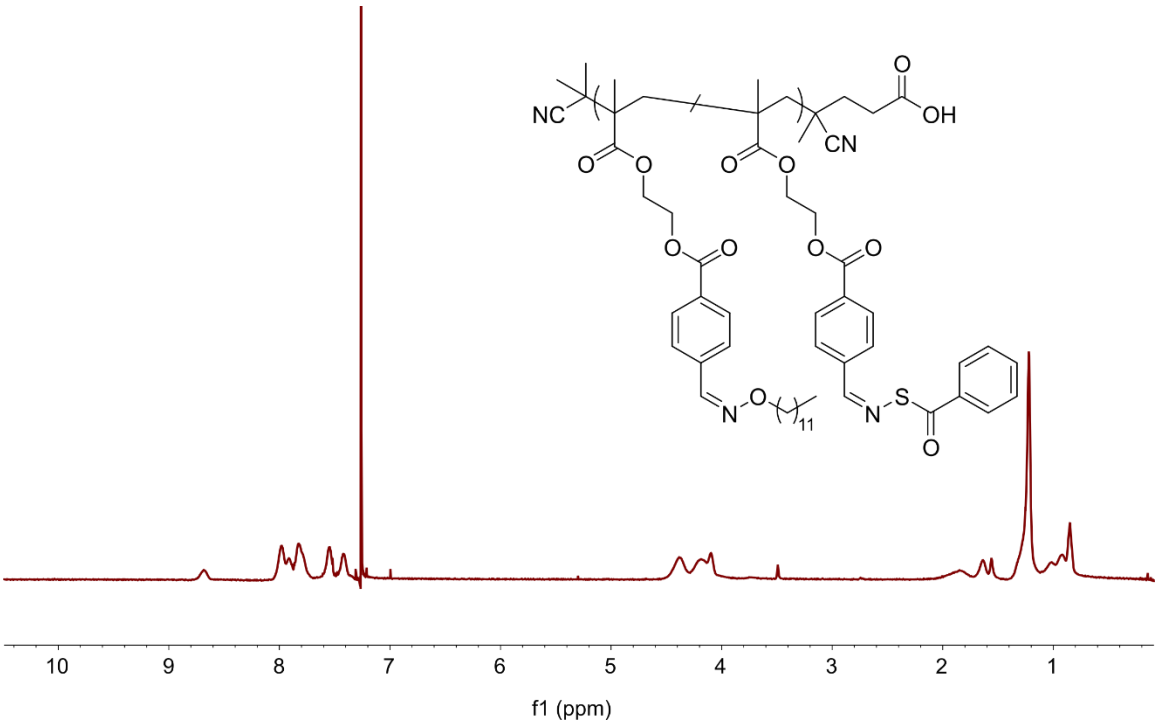

Figure S11. ^{1}H NMR spectrum of **polymer 4c** (poly(SATO-*co*-alkyl)).

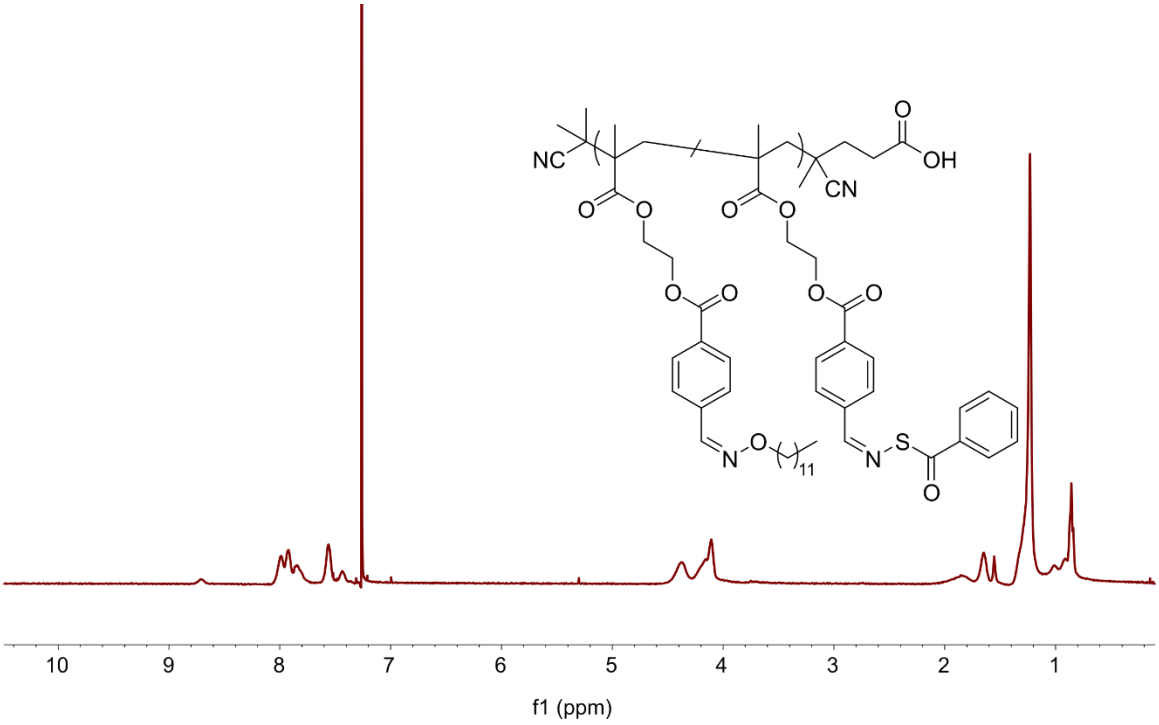

Figure S12. ^{1}H NMR spectrum of **Polymer 4d** (poly(SATO-*co*-alkyl)).

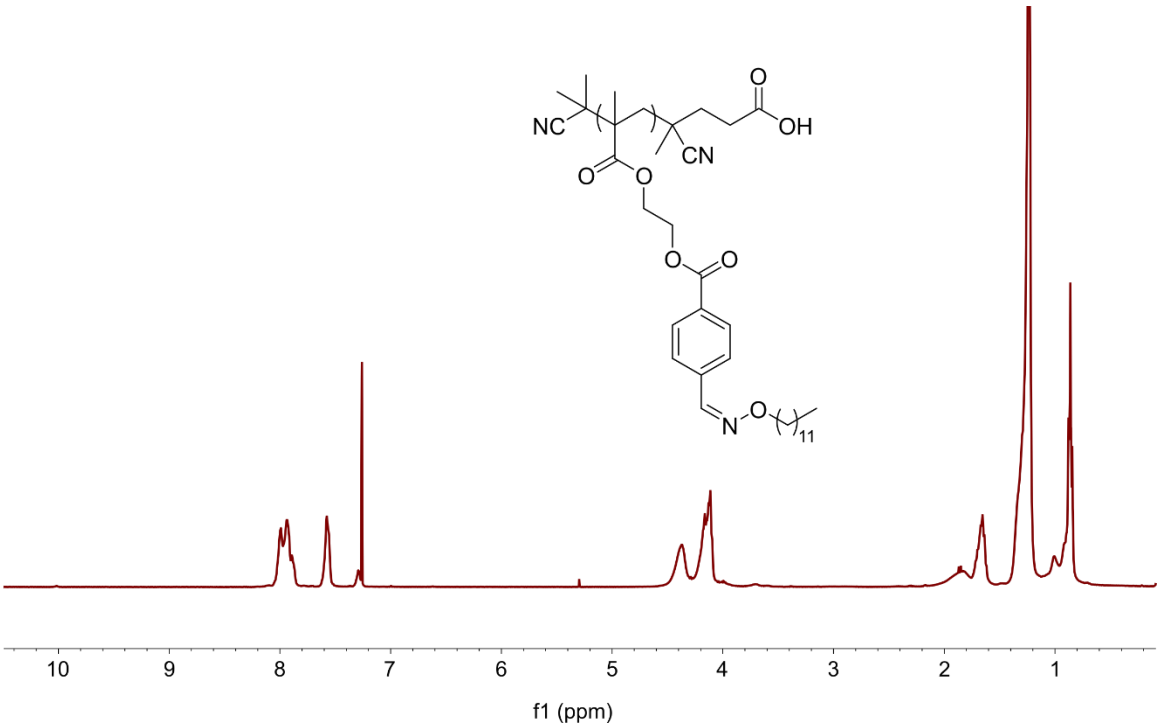

Figure S13. ^{1}H NMR spectrum of **polymer 4e** (poly(alkyl)).

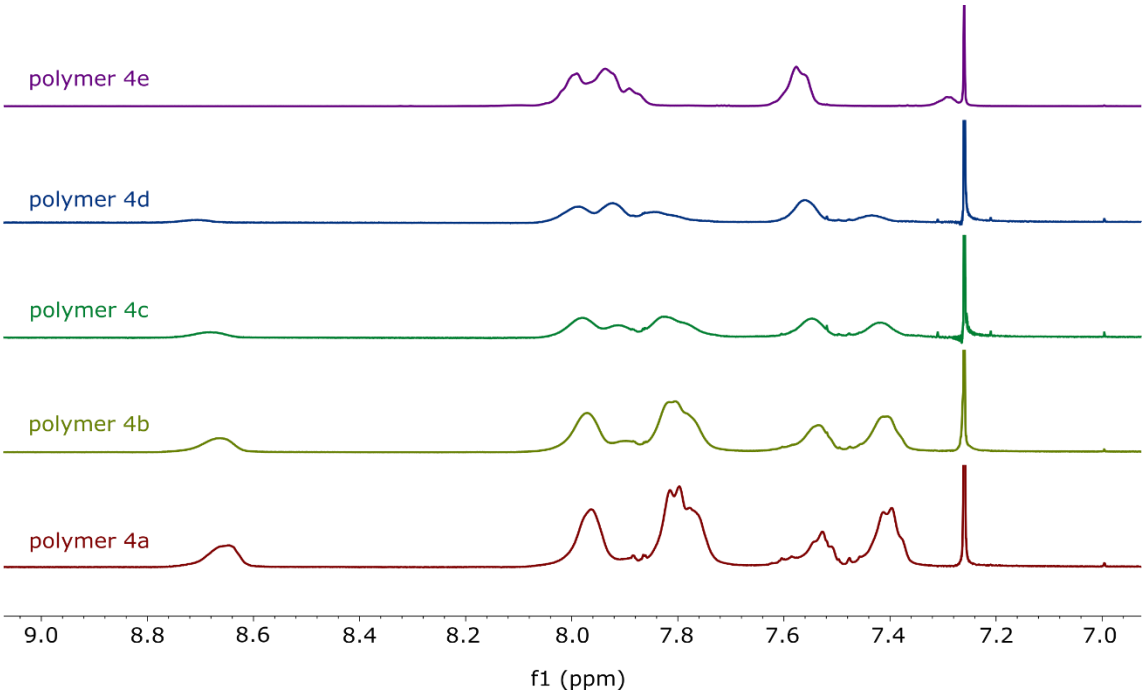

Figure S14. Stacked ^{1}H NMR spectra of polymers **4a-e** highlighting differences in monomer loading.

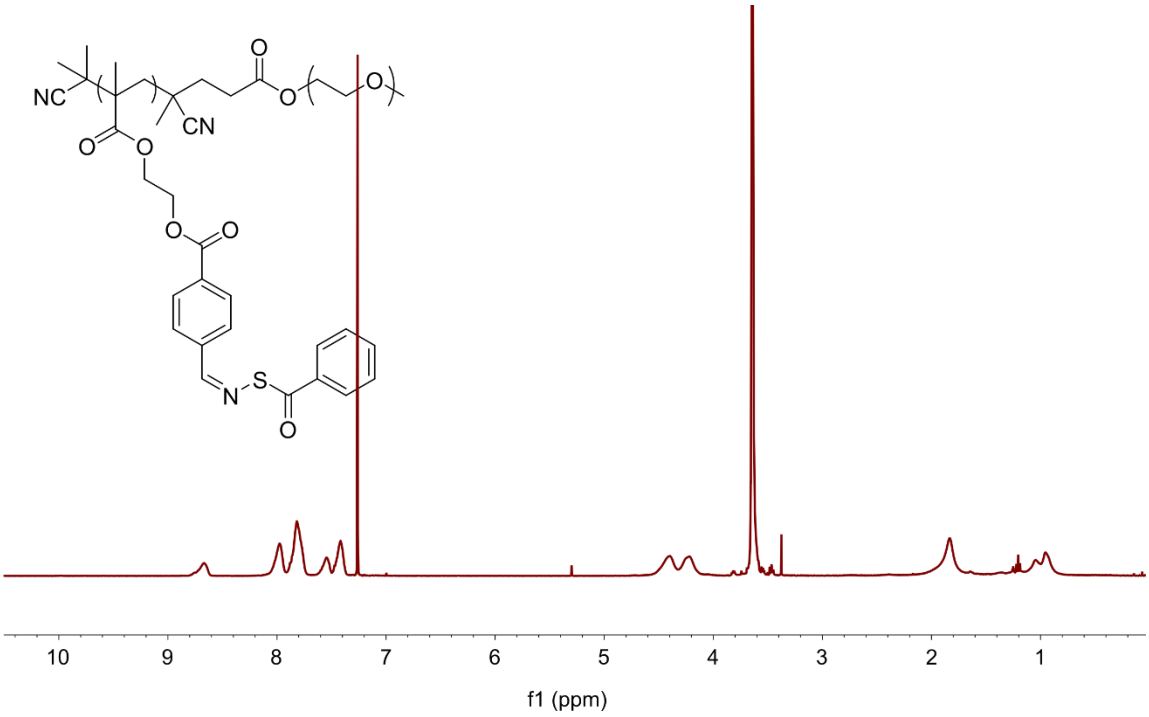

Figure S15. ^{1}H NMR spectrum of **polymer 5a** (PEG-*b*-(SATO)).

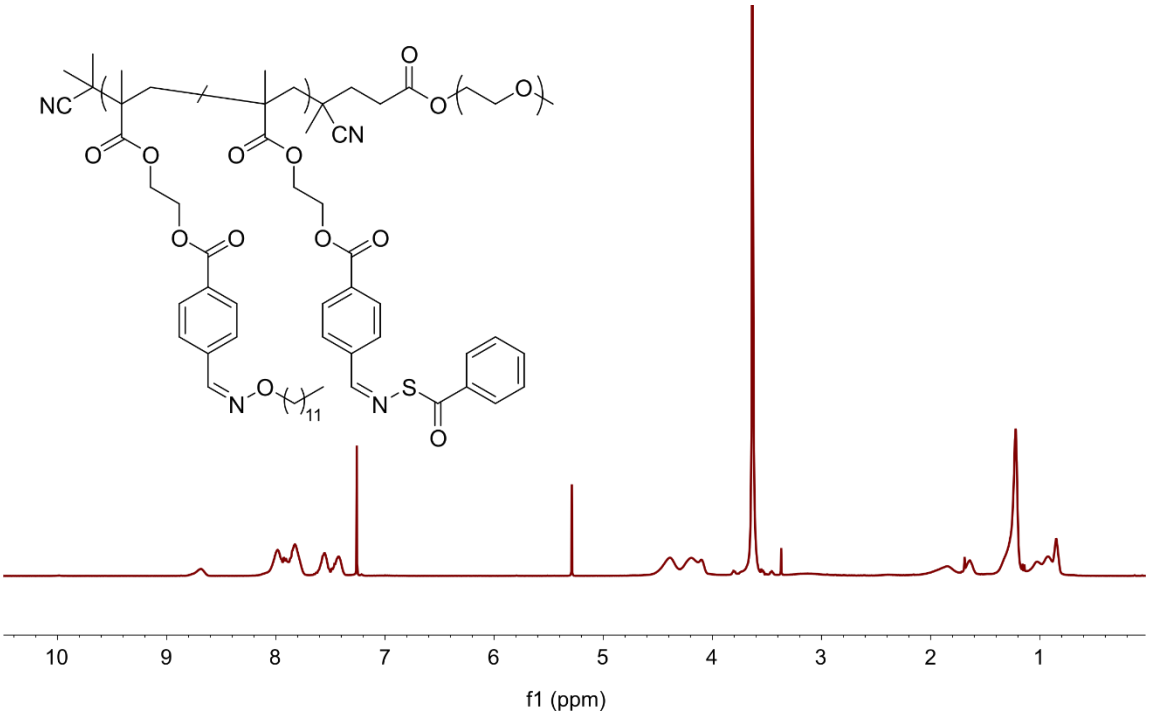

Figure S16. ^{1}H NMR spectrum of **polymer 5b** (PEG-*b*-(SATO-*co*-alkyl)).

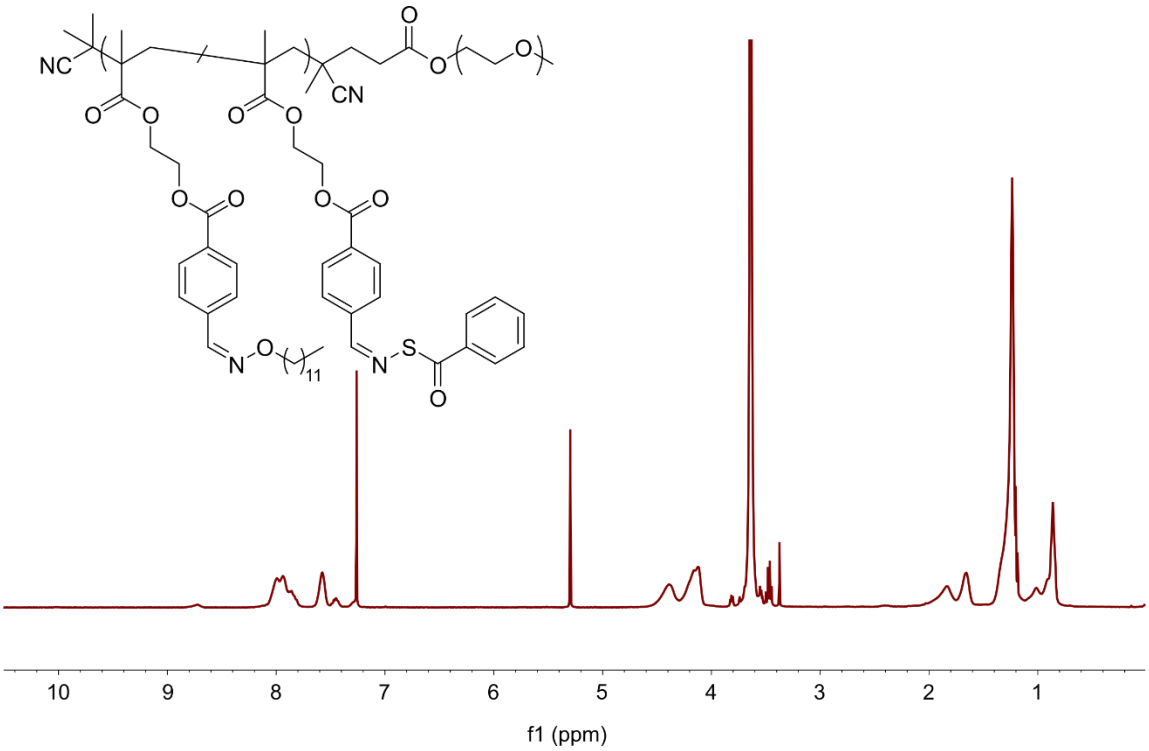

Figure S17. ^{1}H NMR spectrum of **polymer 5c** (PEG-*b*-(SATO-*co*-alkyl)).

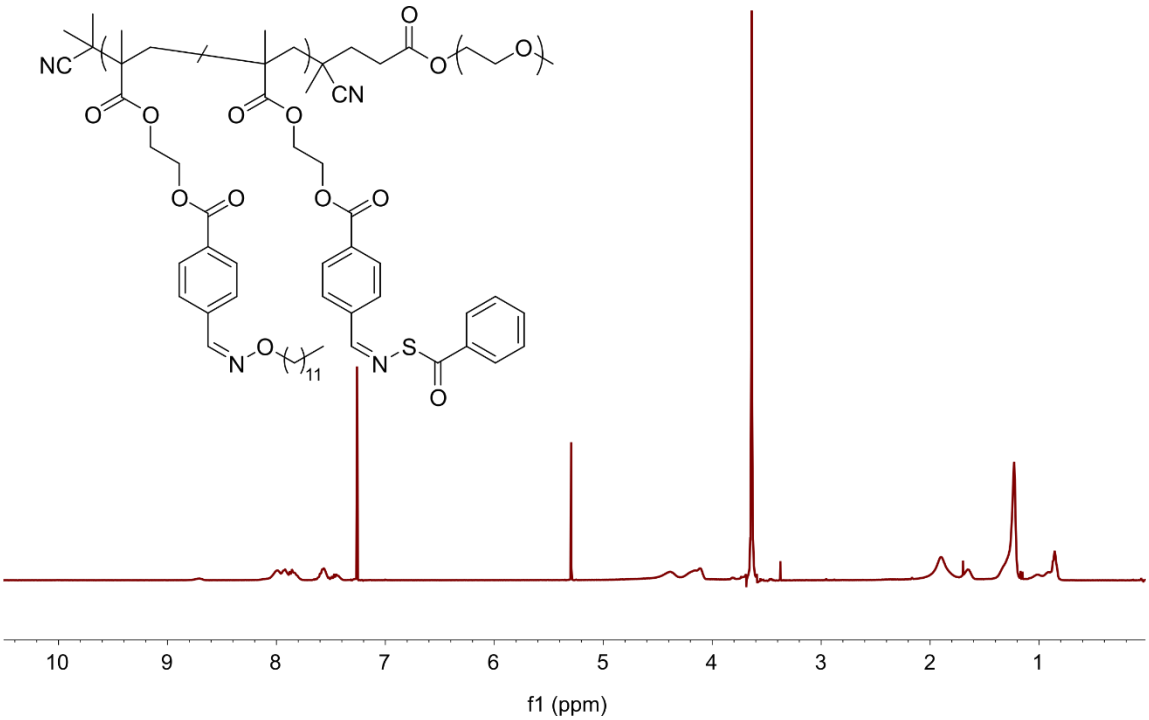

Figure S18. ^{1}H NMR spectrum of **polymer 5d** (PEG-*b*-(SATO-*co*-alkyl)).

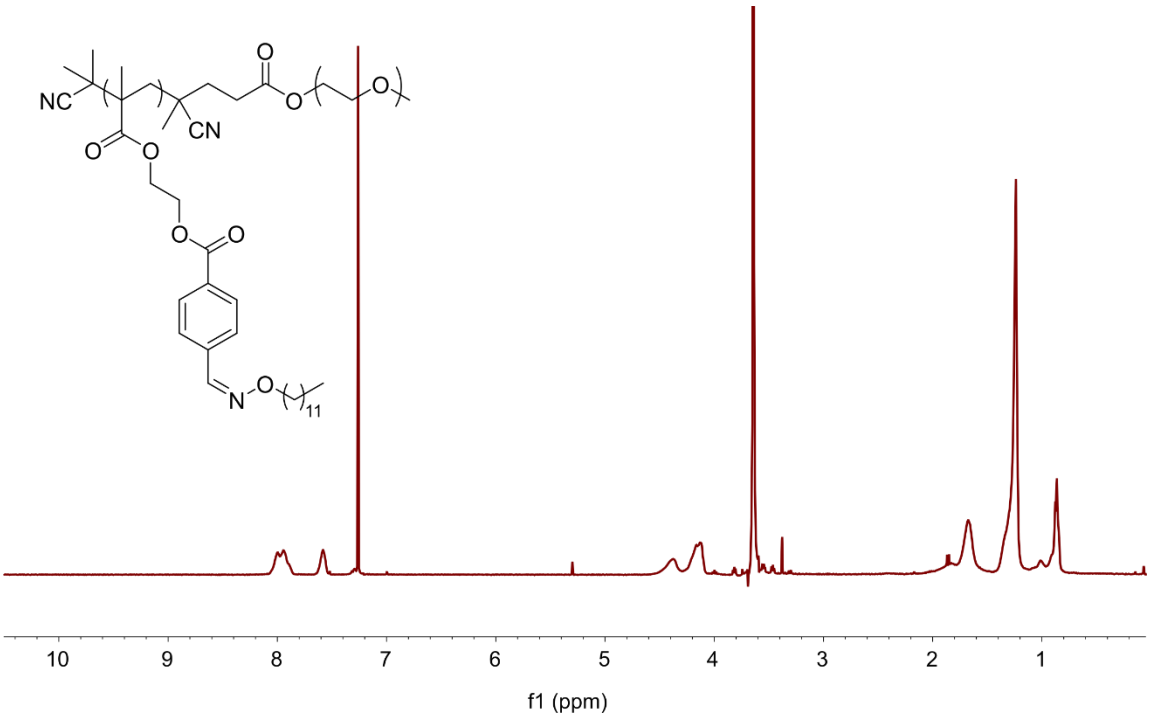

Figure S19. ^{1}H NMR spectrum of **polymer 5e** (PEG-*b*-(alkyl)).

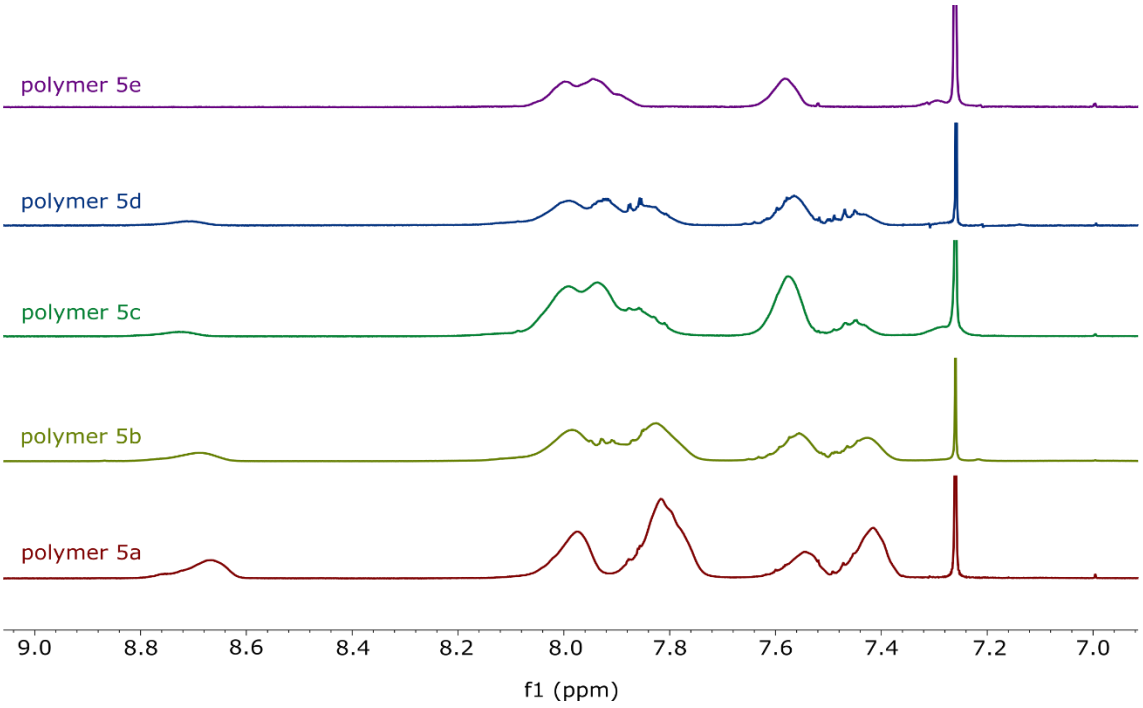

Figure S20. Stacked ^{1}H NMR spectra of polymers **5a-e** highlighting differences in monomer loading.

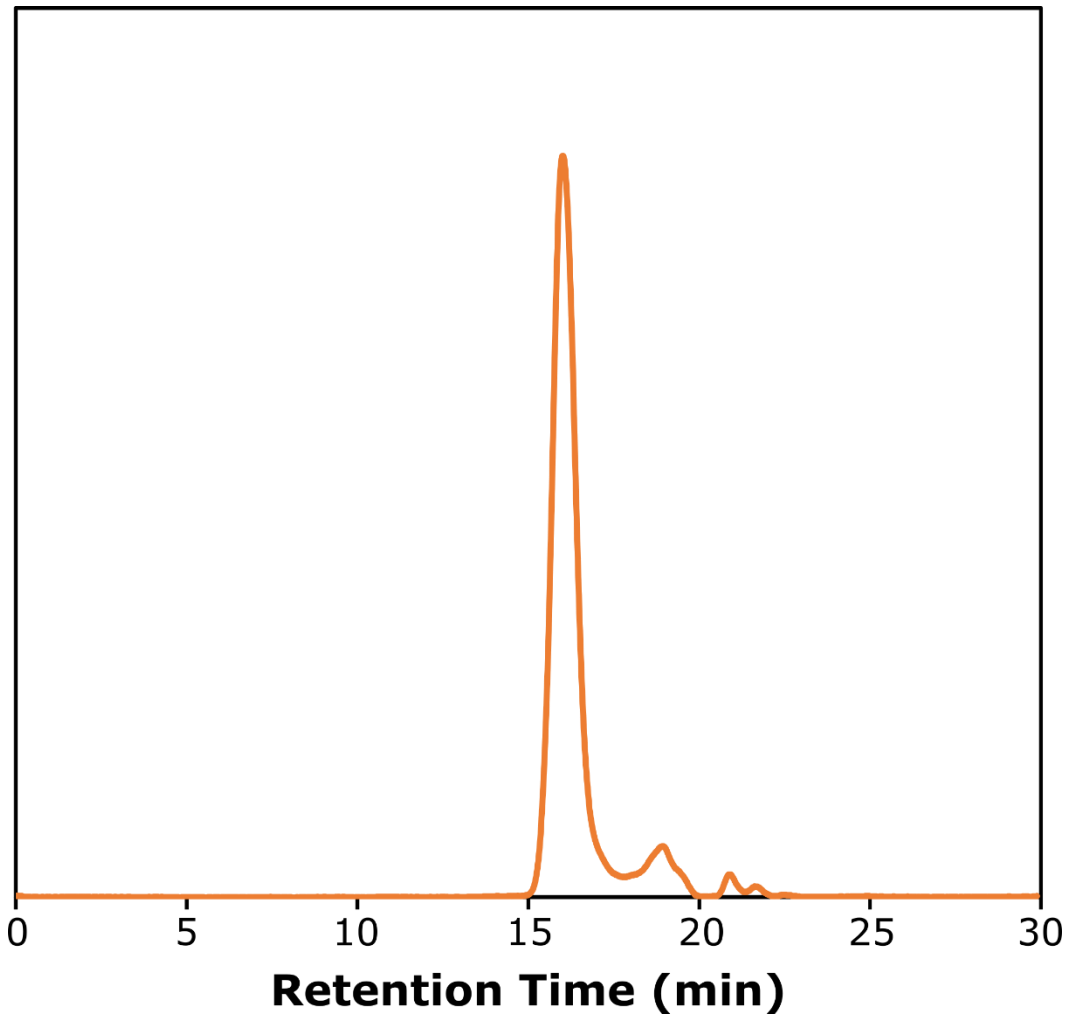

Figure S21. SEC trace of polymer **1** (PEG-*b*-poly(FBEMA)).

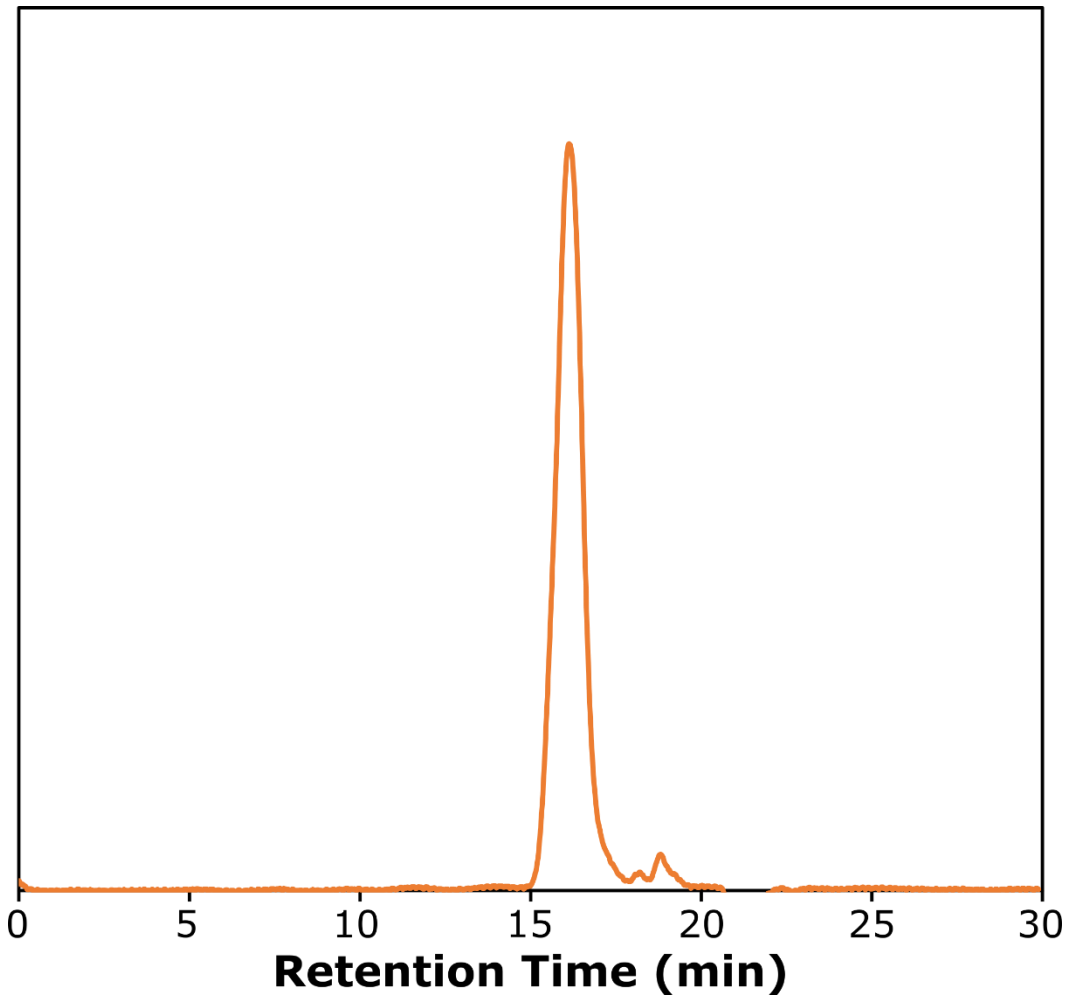

Figure S22. SEC trace of polymer **2** (PEG-*b*-poly(FBEMA) after end-group removal).

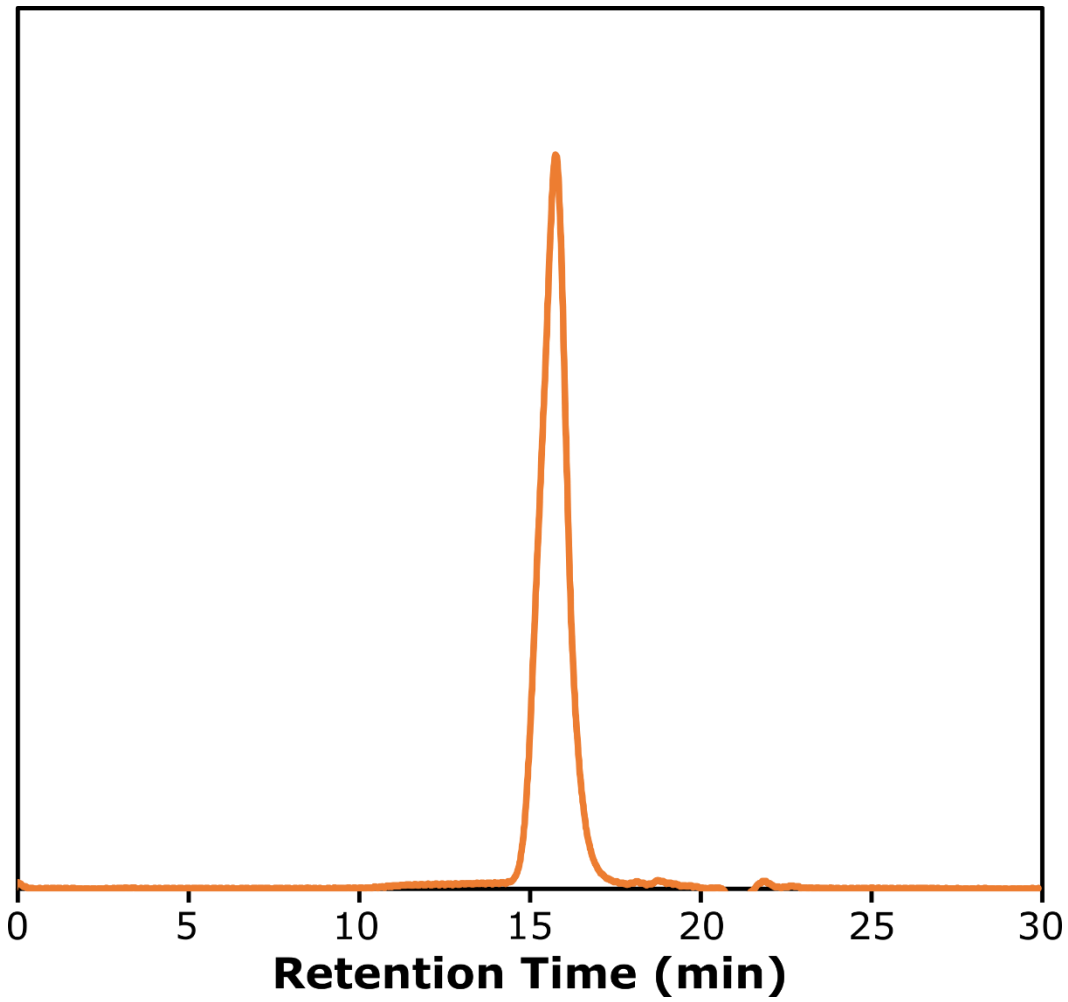

Figure S23. SEC trace of polymer **3a** (PEG-*b*-(SATO-F)).

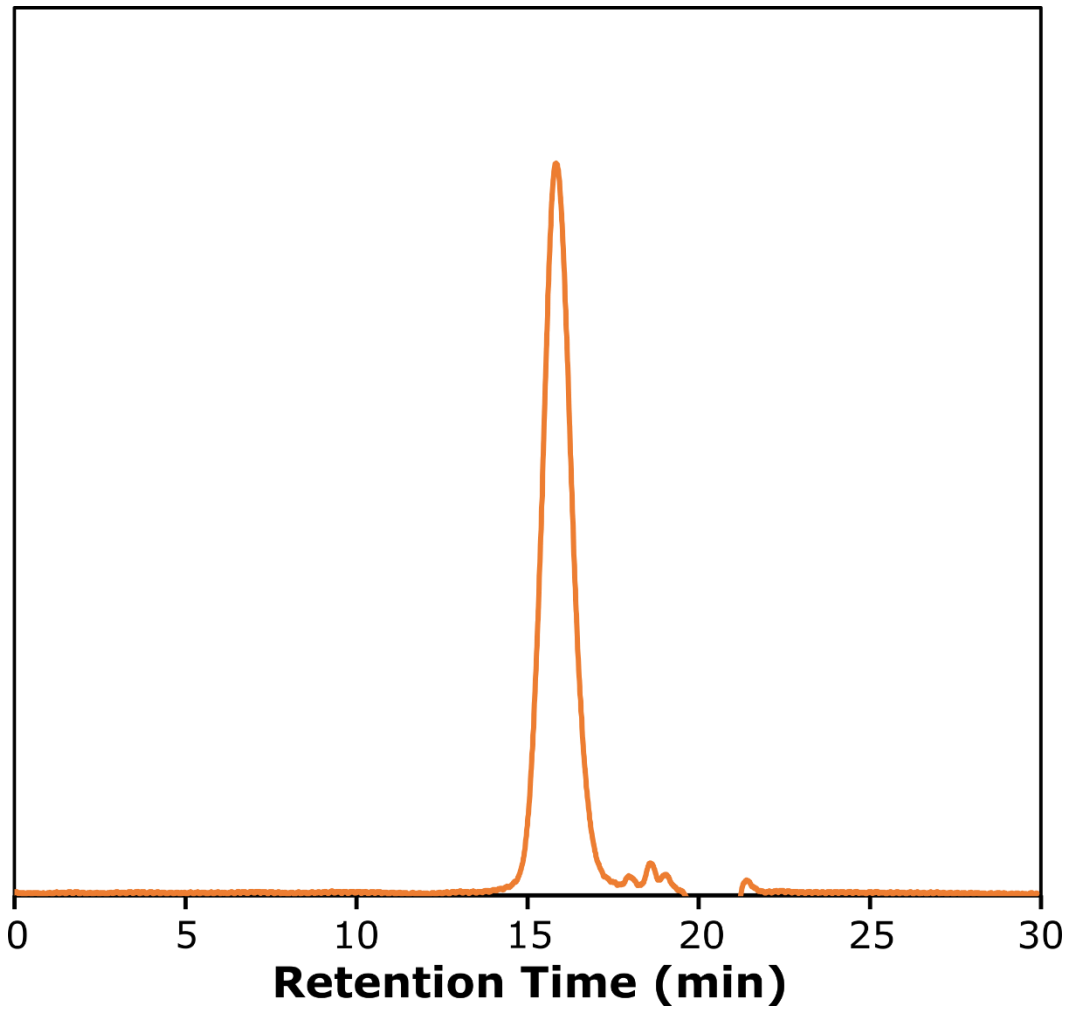

Figure S24. SEC trace of polymer **3b** (PEG-*b*-(SATO)).

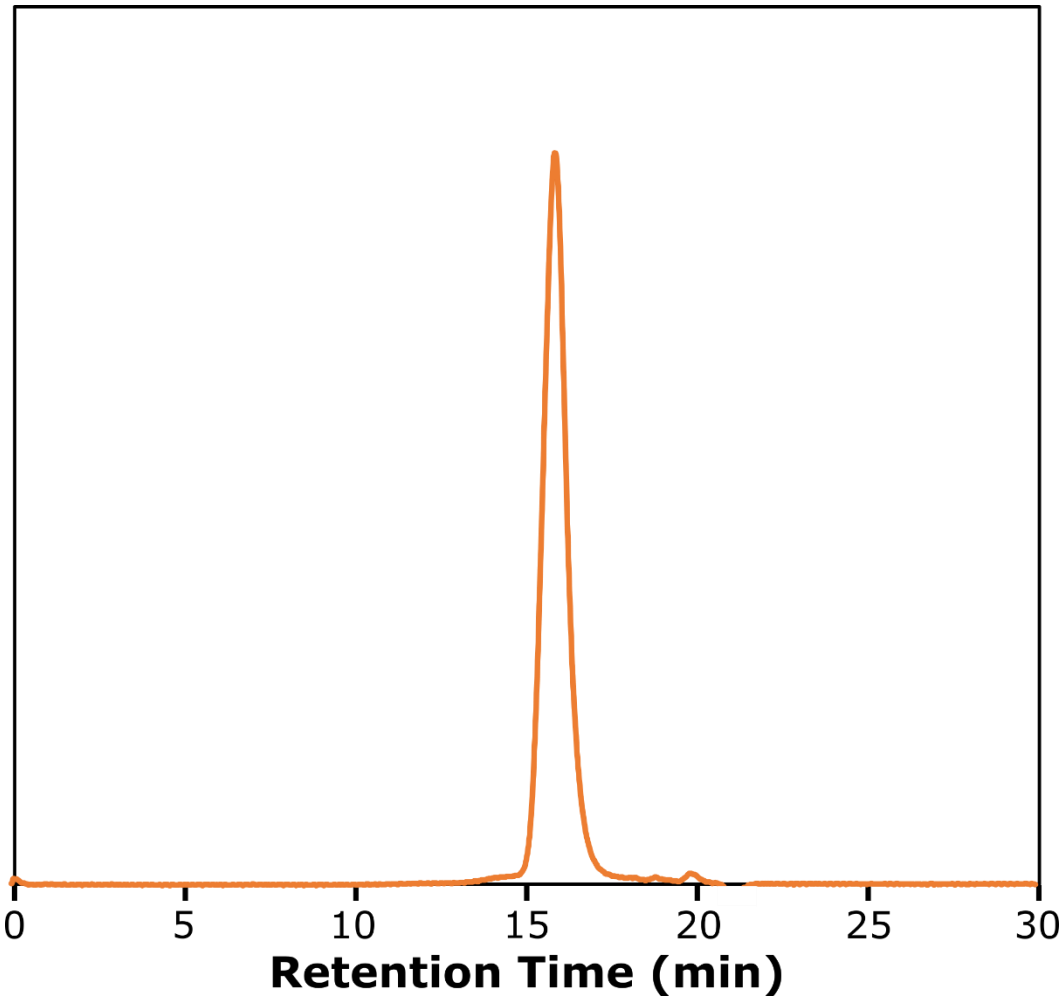

Figure S25. SEC trace of polymer **3c** (PEG-*b*-(SATO-OMe)).

Table S1. H_2S Release from SATO-functionalized small molecules and copolymers

Architecture	**$t_{1/2}$ H_2S Release (min)[a]**
Small molecule (**SATO1**, $C_6H_5COSN{=}CHC_6H_5$-COOH)	19 ± 1
Poly(FBEMA-SATO-*co*-OEGMA)	52 ± 1
Block copolymer (micelles)	206 ± 6

[a]H_2S half-lives measured using the methylene blue assay.

Table S2. Characterization of polymers **3a-c**.

Polymer	**para-Substituent**	$M_{n,\,SEC}$ **(kg mol^{-1})**[a]	$M_{n,theo}$ **(kg mol^{-1})**[b]	***Đ***[a]
3a	F	16	15.7	1.29
3b	H	16	15.3	1.21
3c	OMe	18	16.1	1.13

[a]Absolute molar mass measured by light scattering. [b]Calculated from conversions determined via ^{1}H NMR spectroscopy.

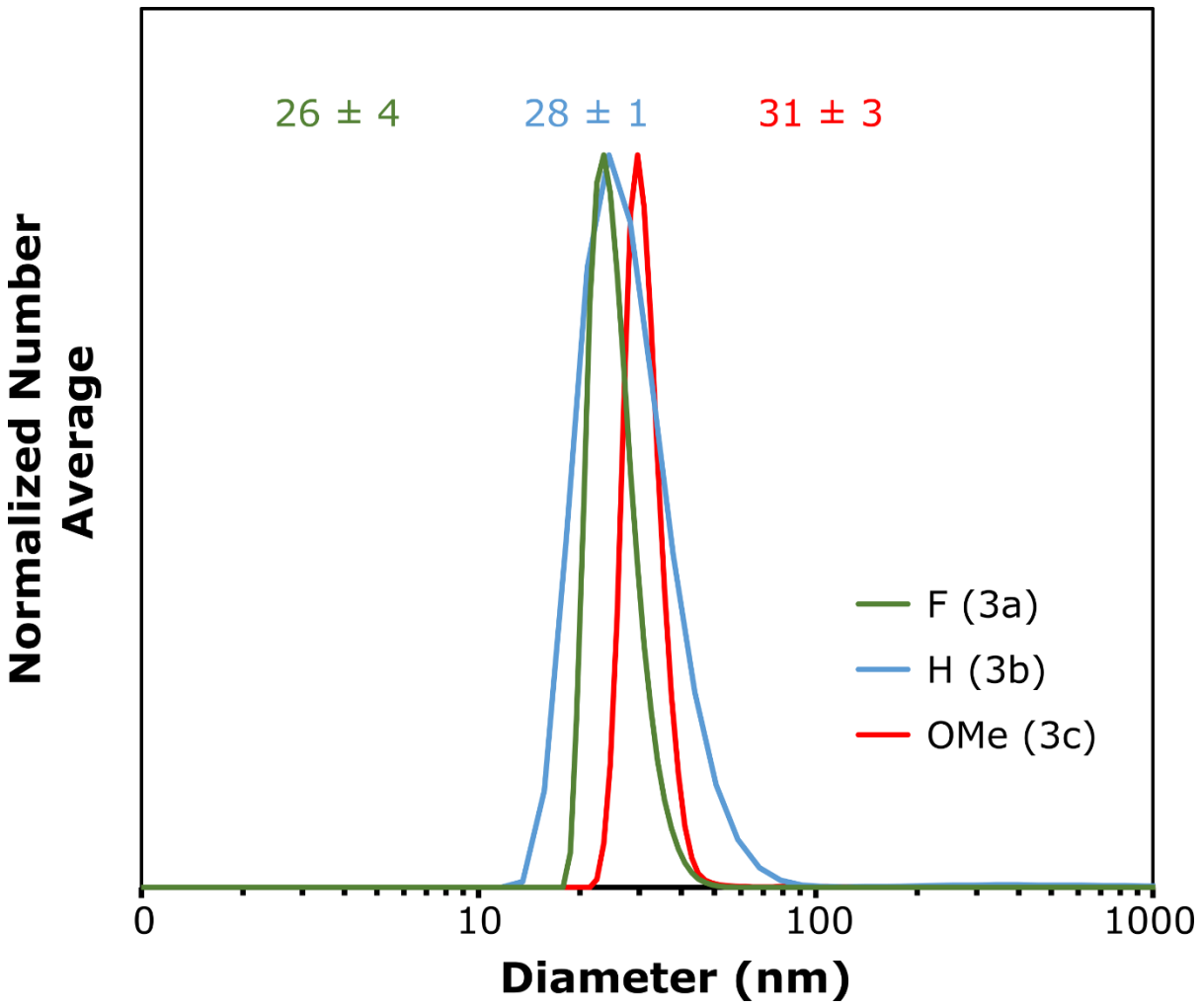

Figure S25. Effect of *p*-substituent on number average micelle size prepared from polymers **3a-c**.

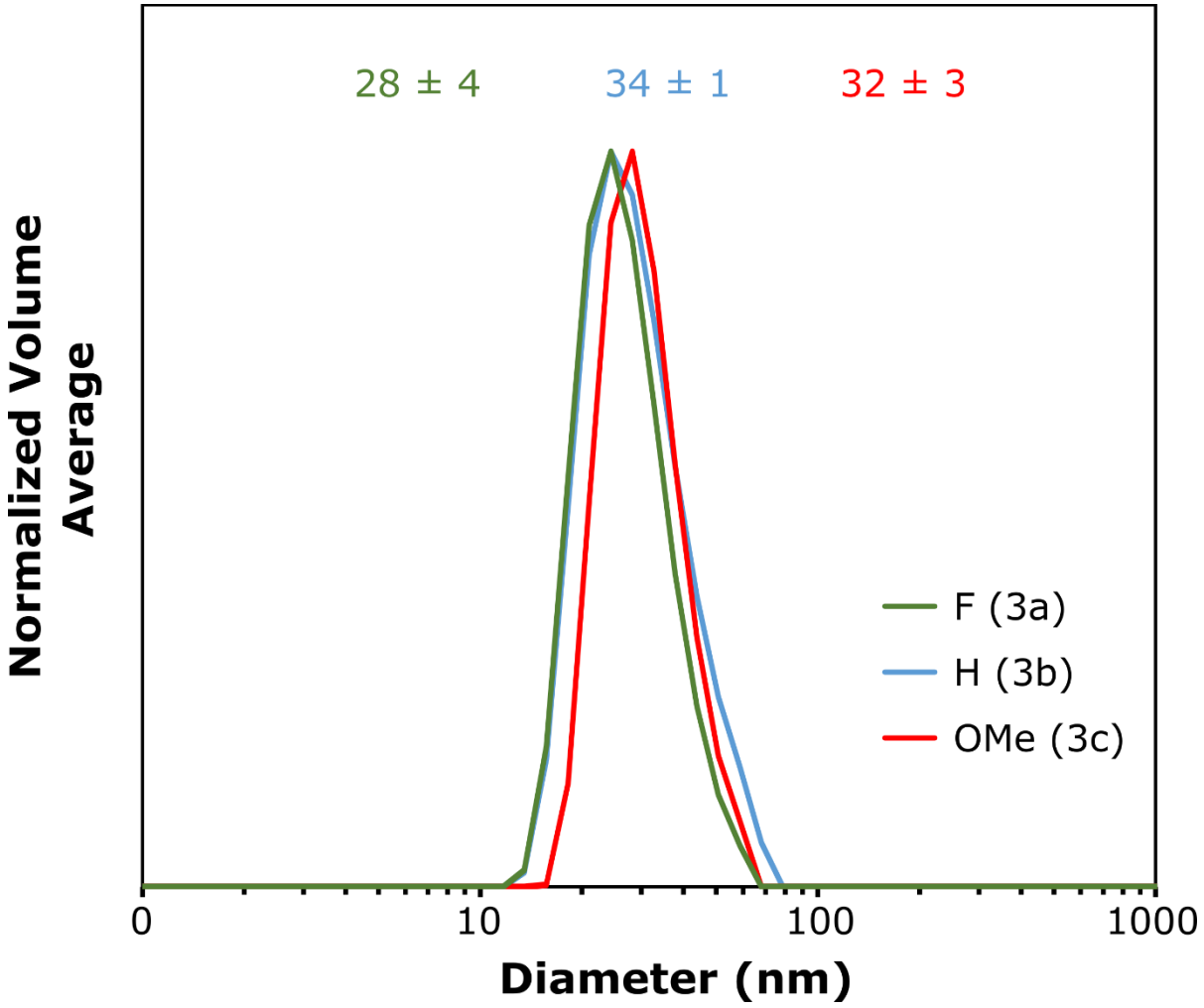

Figure S26. Effect of *p*-substituent on volume average micelle size prepared from polymers **3a-c**.

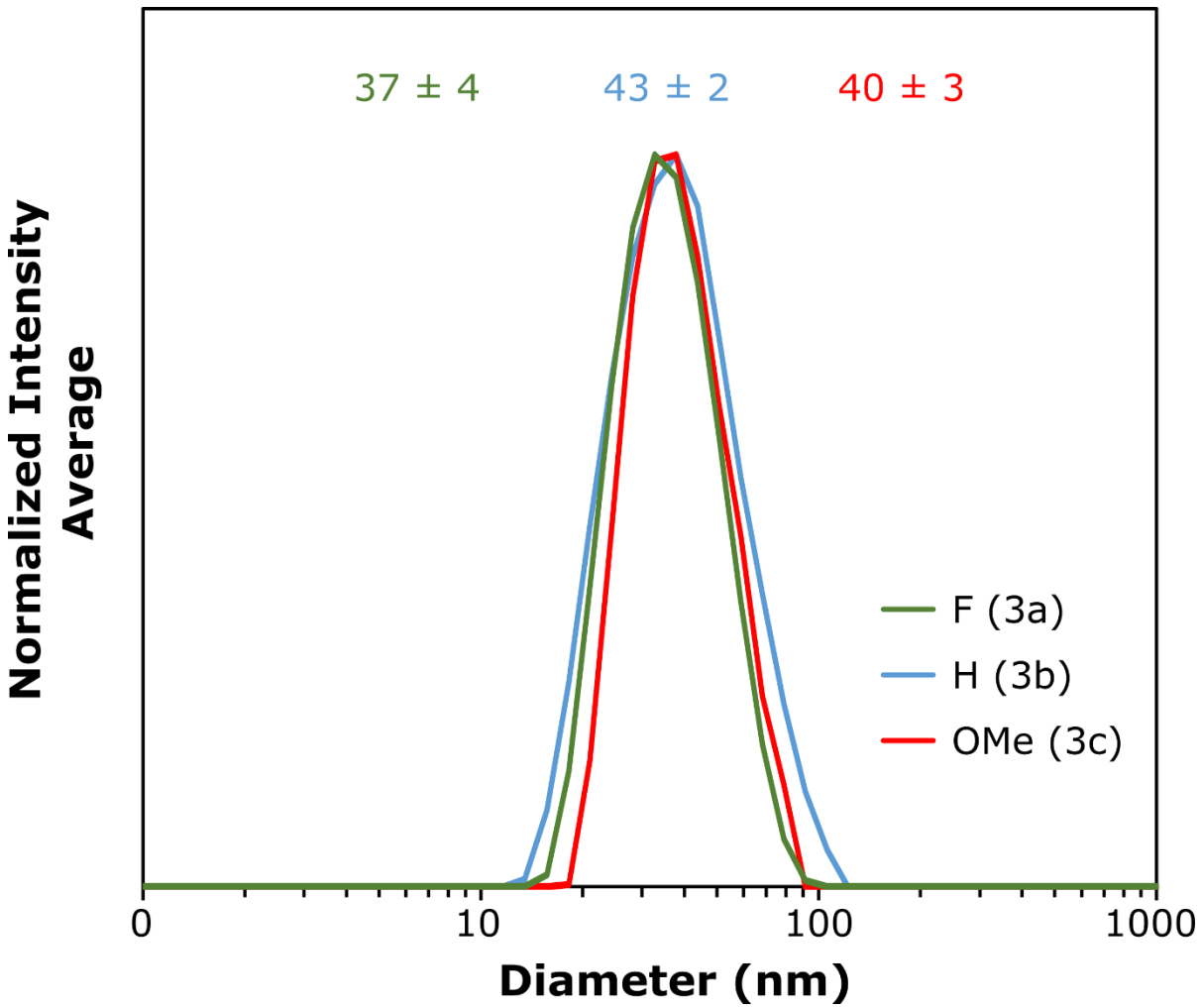

Figure S27. Effect of *p*-substituent on intensity average micelle size prepared from polymers **3a-c**.

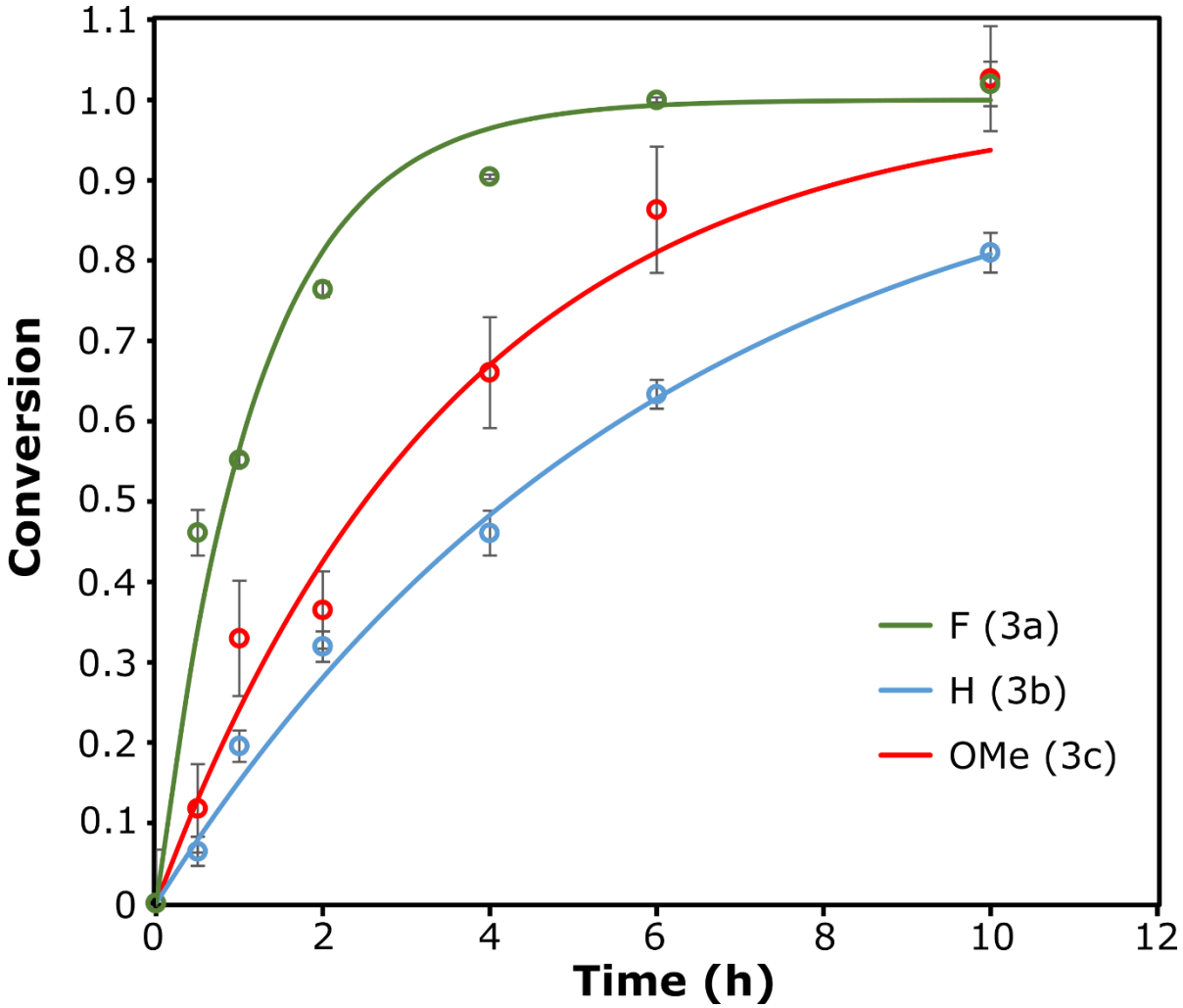

Figure S28. Effect of *p*-substituent on the rate of H_2S release from polymers **3a-c**. Rates were determined using the methylene blue assay. A SATO concentration of 250 μM was utilized for each experiment, and 1 mM Cys was applied to trigger H_2S release. Release reactions were conducted in phosphate buffer (pH = 7.0) at room temperature. The error bars represent the standard deviation in conversion of n=3 replicates.

Table S3. Effect of *p*-substituent on the rate of H_2S release.

Polymer	para-Substituent	$t_{1/2}$ H_2S release (h)[a]

3a	F	0.83 ± 0.2
3b	H	4.2 ± 0.3
3c	OMe	2.5 ± 0.5

[a]H_2S half-lives measured using the methylene blue assay.

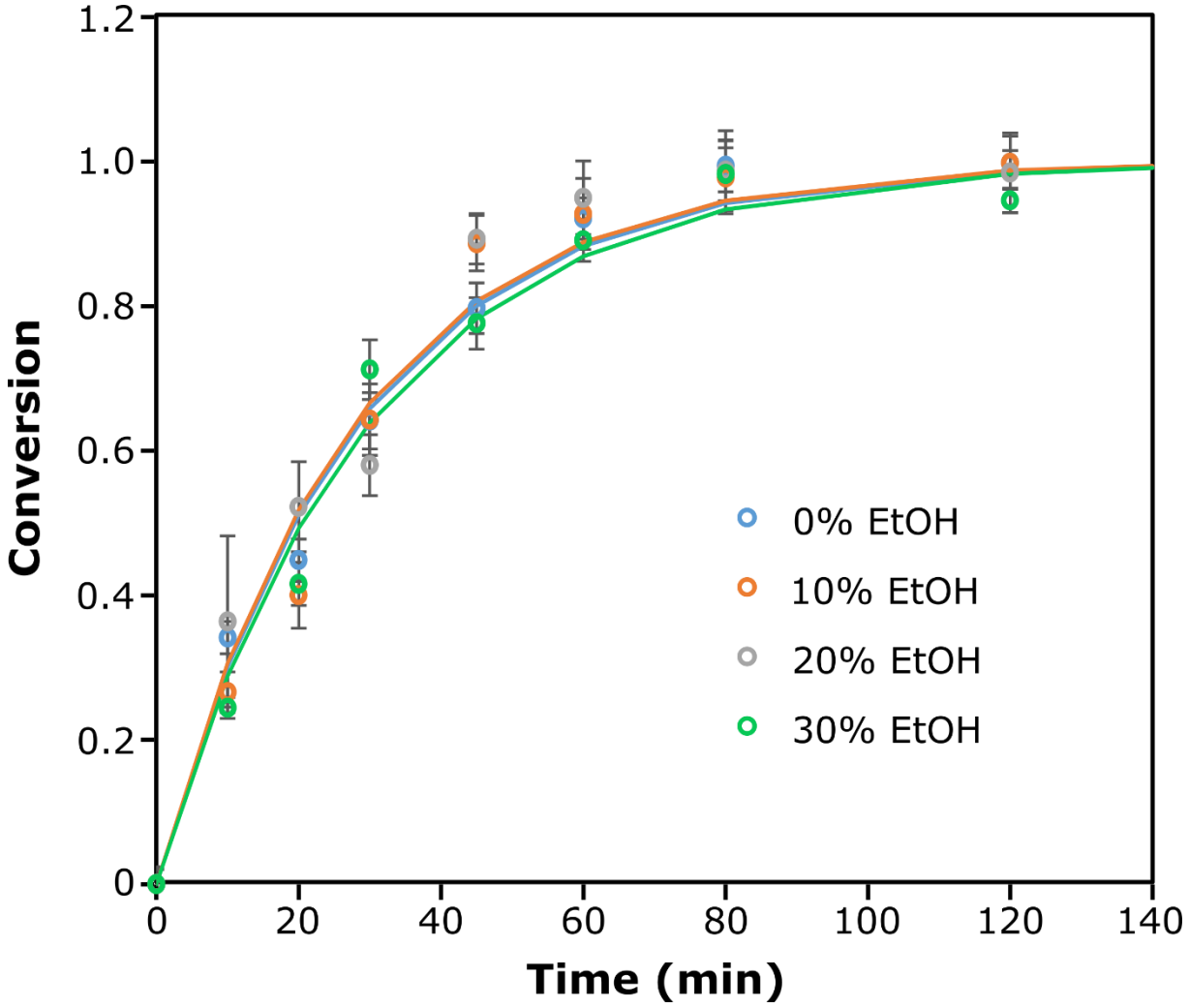

Figure S29. Effect of EtOH concentration on the rate of H_2S release from a small molecule **SATO1** ($C_6H_5COSN{=}CHC_6H_5$-COOH). Rates were measured using the methylene blue assay. A **SATO1** concentration of 250 μM was utilized for each experiment, and 1 mM Cys was applied to trigger H_2S release. Release reactions were conducted in 30% THF in phosphate buffer (pH = 7.0)

at room temperature. The error bars represent the standard deviation in conversion of n=4 replicates.

Table S4. Summary of H_2S release half-lives from small molecules SATOs based on EtOH concentration. Release half-lives were determined based on pseudo-first-order kinetics fits to the data in Figure S29.

Concentration	**$t_{1/2}$ (min)[a]**
0% EtOH	19 ± 1
10% EtOH	19 ± 1
20% EtOH	17 ± 2
30% EtOH	20 ± 1

[a]H_2S half-lives measured using the methylene blue assay.

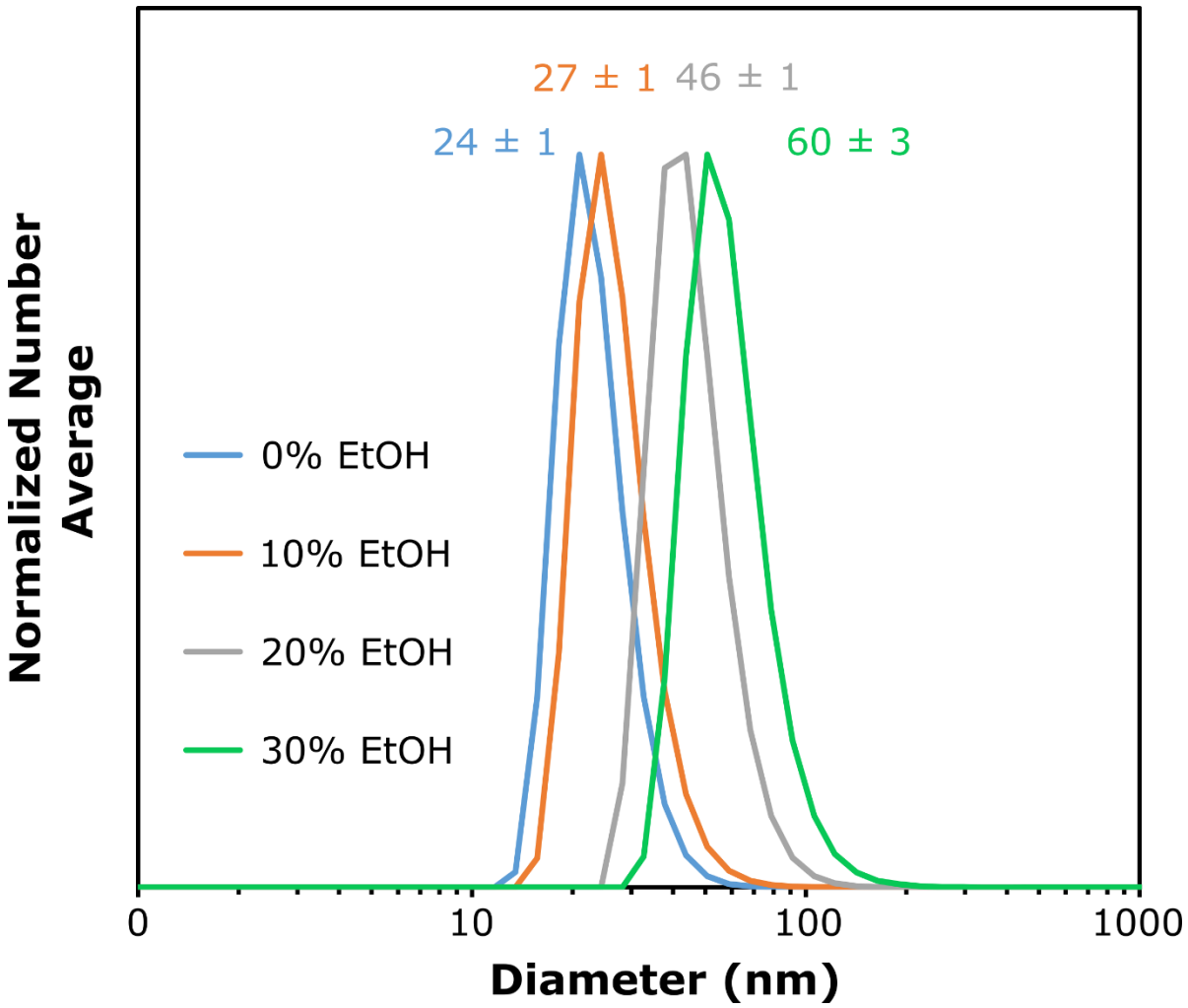

Figure S30. Effect of EtOH concentration on number average micelle size prepared using polymer **3b** (PEG-*b*-(SATO)).

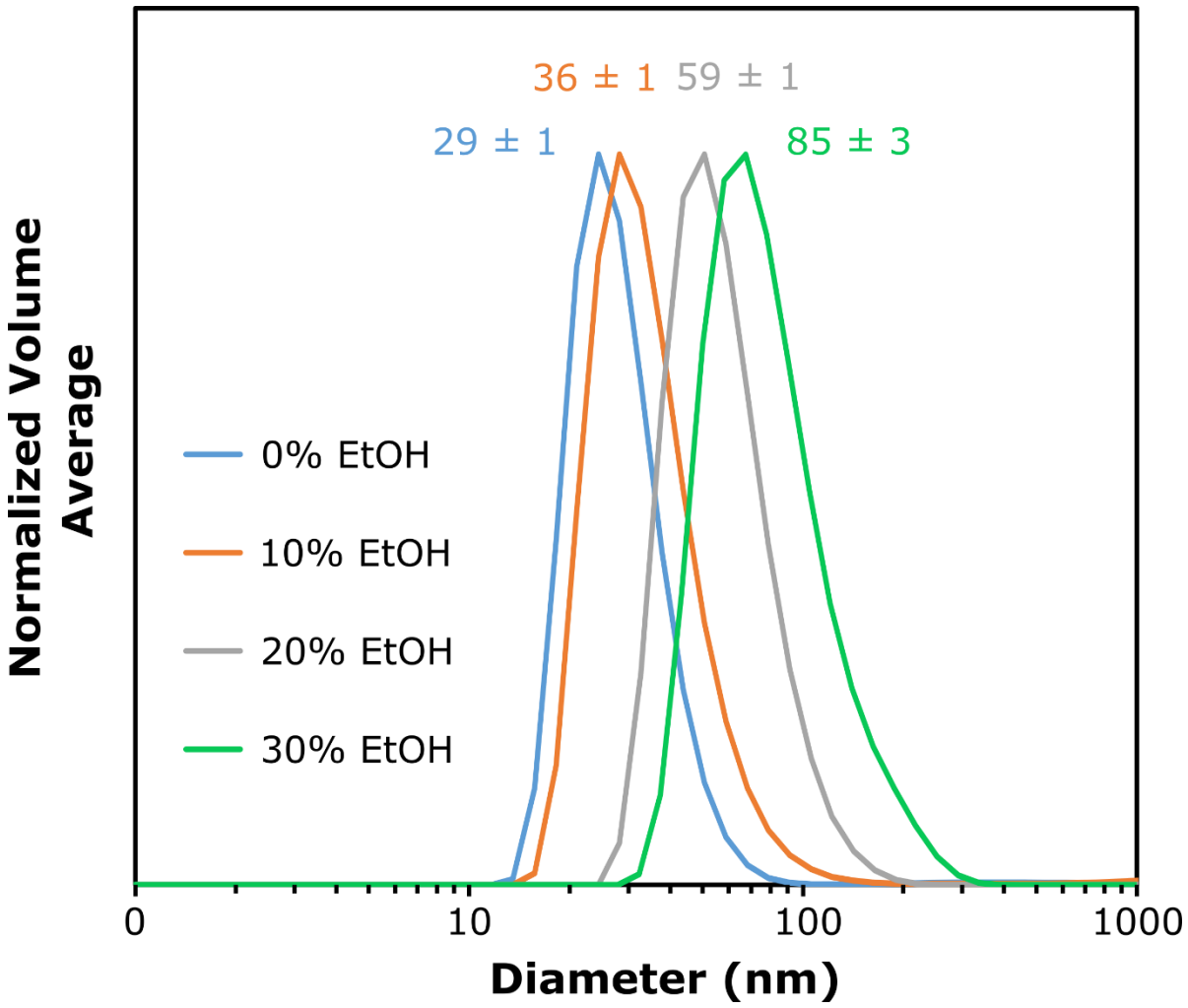

Figure S31. Effect of EtOH concentration on volume average micelle size prepared using polymer **3b** (PEG-*b*-(SATO)).

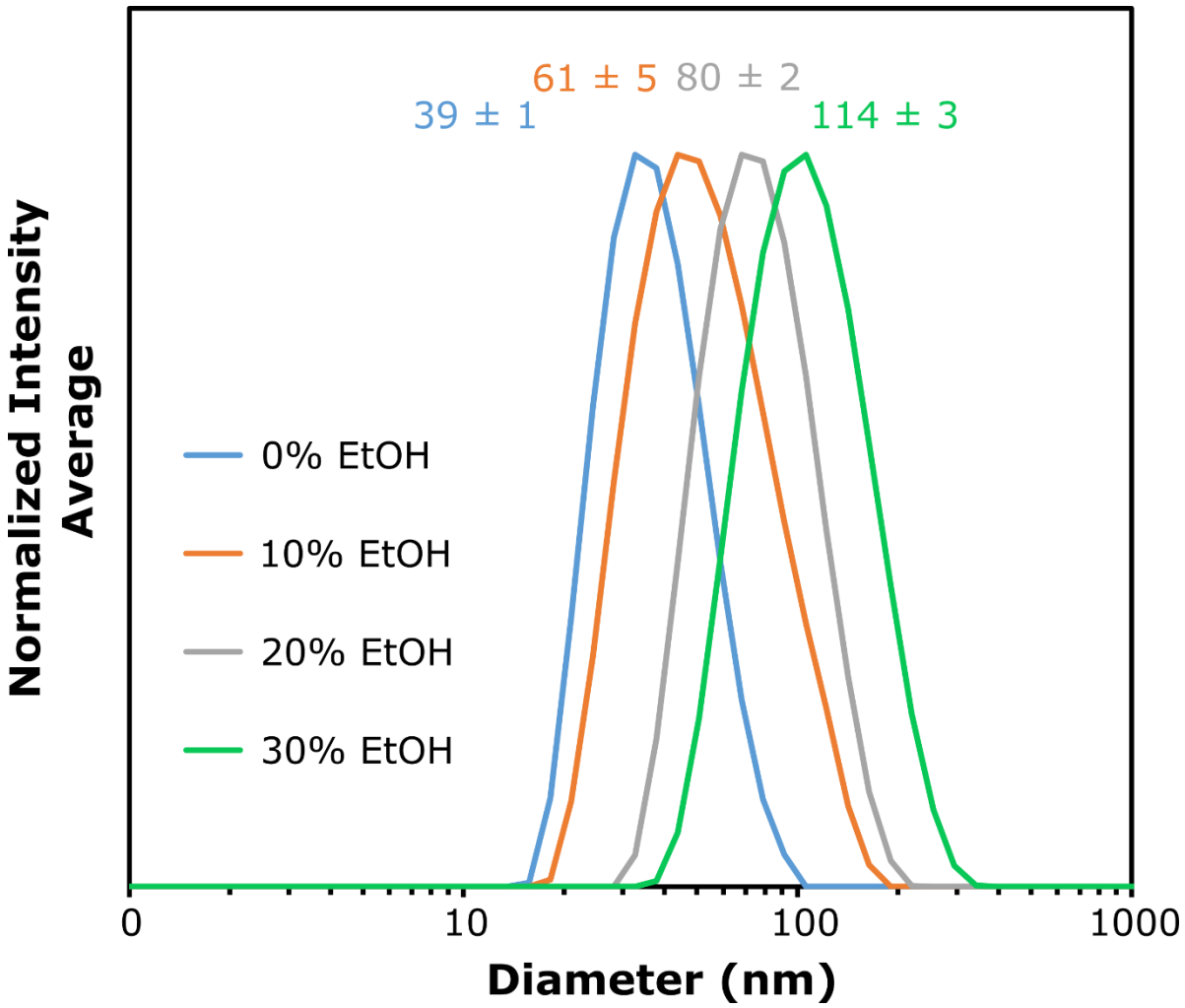

Figure S32. Effect of EtOH concentration on intensity average micelle size prepared using polymer **3b** (PEG-*b*-(SATO)).

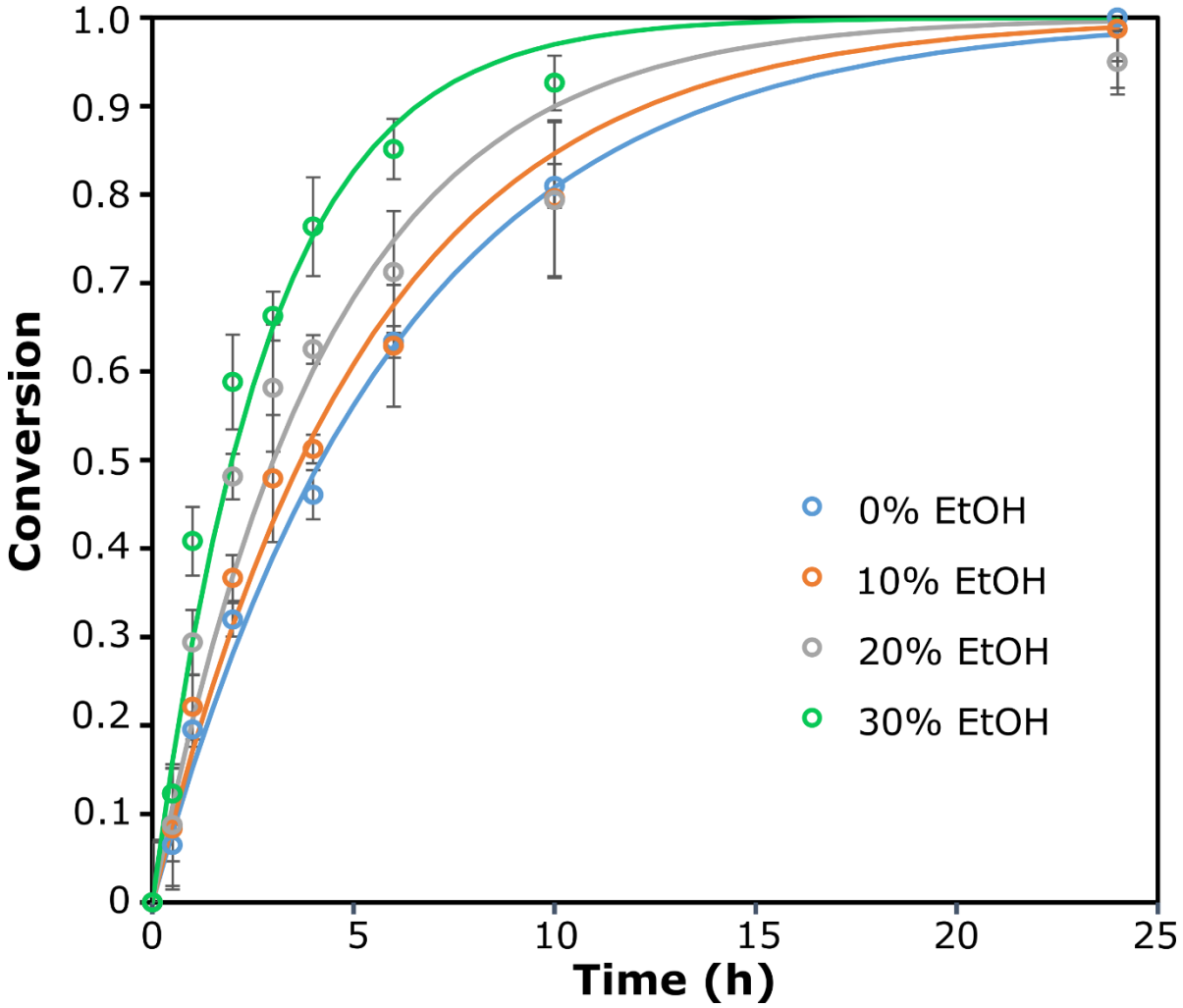

Figure S33. Effect of EtOH concentration on H_2S release from SATO micelles prepared using polymer **3b**. Rates were determined using the methylene blue assay. A SATO concentration of 250 μM was utilized for each experiment, and 1 mM Cys was applied to trigger H_2S release. Release reactions were conducted in EtOH/phosphate buffer (pH = 7.0) mixtures at room temperature. The error bars represent the standard deviation in conversion of n=3 replicates.

Table S5. Summary of H_2S release half-lives from SATO micelles based on EtOH concentration.

Concentration	**$t_{1/2}$ H_2S Release (h)[a]**

0% EtOH	4.2 ± 0.3
10% EtOH	3.7 ± 0.5
20% EtOH	2.0 ± 0.9
30% EtOH	1.8 ± 0.5

[a]H_2S half-lives measured using the methylene blue assay.

Table S6. Evaluation of post-polymerization modification of poly(FBEMA) homopolymers using oxime and SATHA nucleophiles.

Eq Oxime[a]	Eq SATHA[a]	Mol% Oxime[b]	Mol% SATO[b]	Mol% Aldehyde[b]
5	0	100	0	0
0	5	0	100	0
2.5	2.5	13	61	26

[a]Equivalents of nucleophile relative to the concentration of pendant aldehydes of poly(FBEMA). [b]Determined via relative integration of peaks corresponding to oxime, SATO, and aldehyde protons.

Equation S1.

$$Wt.\%\ SATO = \frac{(thiooxime\ peak\ area)(397.45\ g/mol)}{[(thiooxime\ peak\ area)(397.45 g/mol)] + [(oxime\ peak\ area)(445.60 g/mol\ )]}$$

Table S7. Summary of critical micelle concentrations for polymers **5a-e**.

Sample	**CMC (μg/mL)[a]**
5a	51 ± 4
5b	59 ± 2
5c	51 ± 6
5d	87 ± 3
5e	120 ± 2

[a]Critical micelle concentrations determined using the Nile red assay.

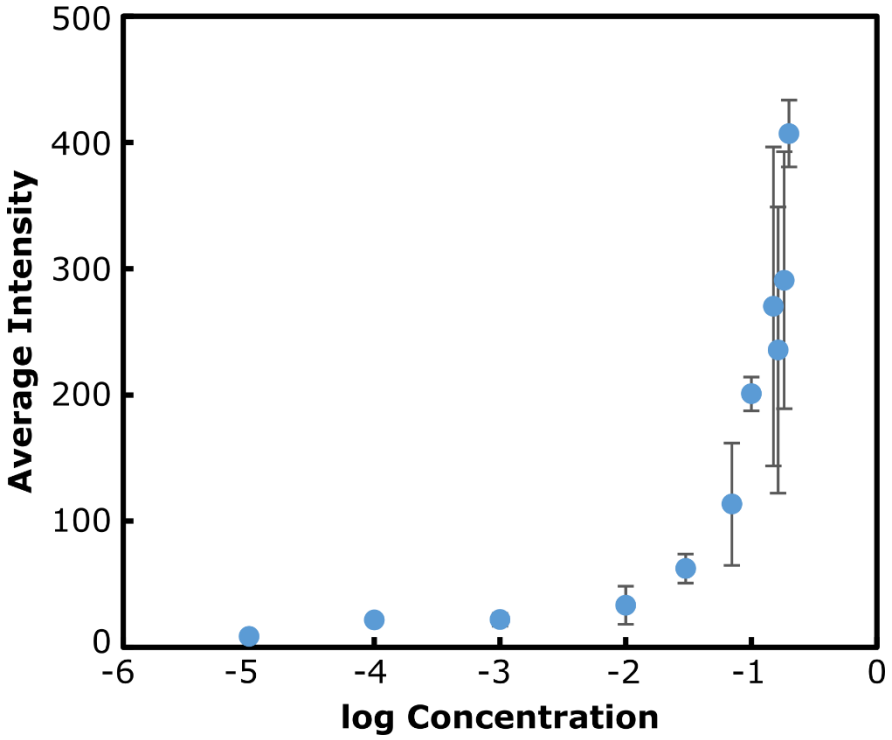

Fig S34. Critical micelle concentration plot for polymer **5a** (PEG-*b*-(SATO)) determined using the Nile Red assay.

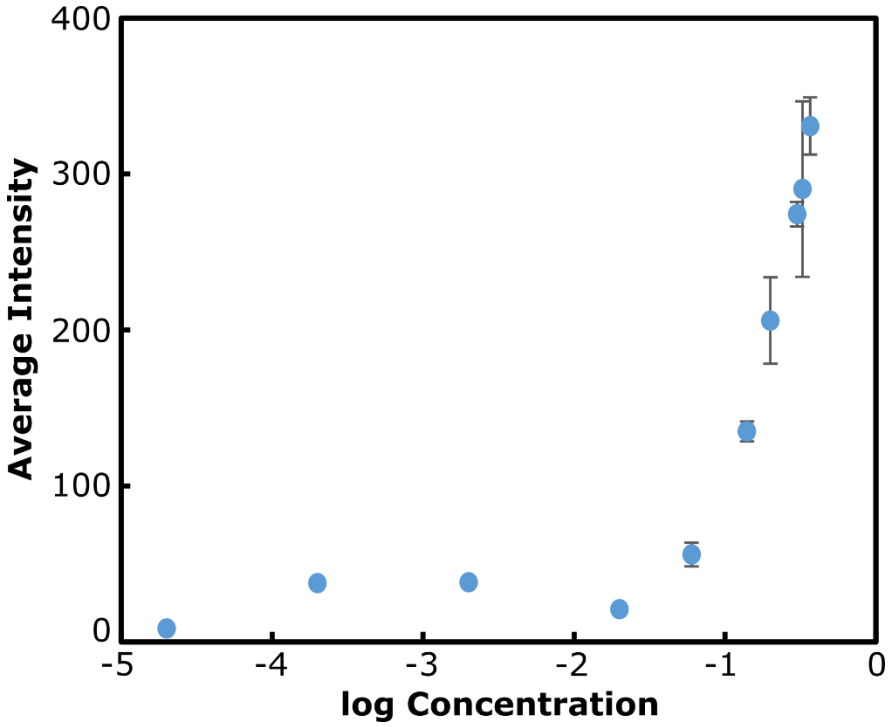

Fig S35. Critical micelle concentration plot for polymer **5b** (PEG-*b*-(SATO-*co*-alkyl)) determined using the Nile Red assay.

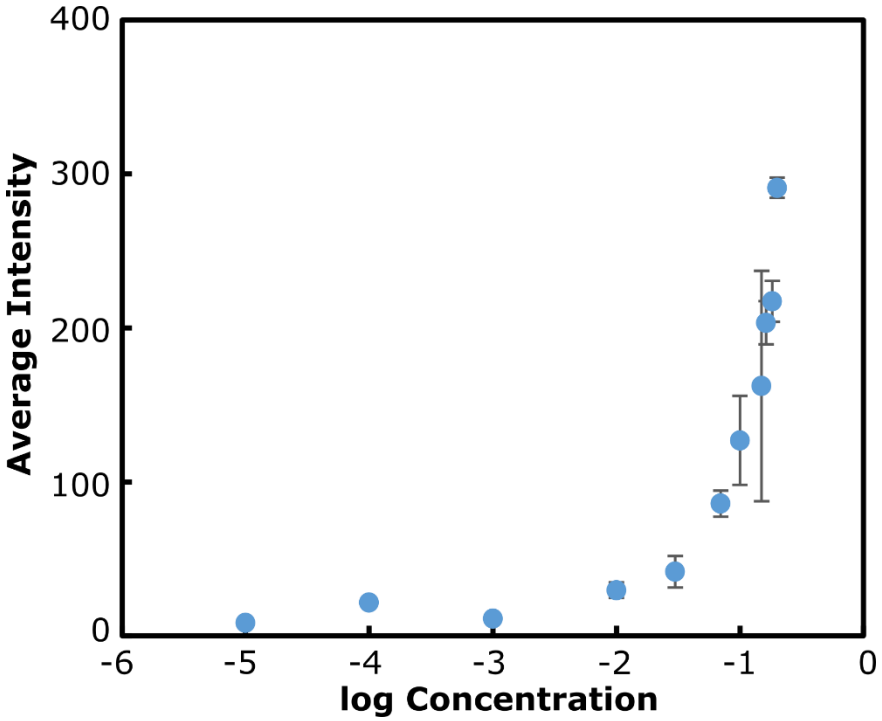

Fig S36. Critical micelle concentration plot for polymer **5c** (PEG-*b*-(SATO-*co*-alkyl)) determined using the Nile Red assay.

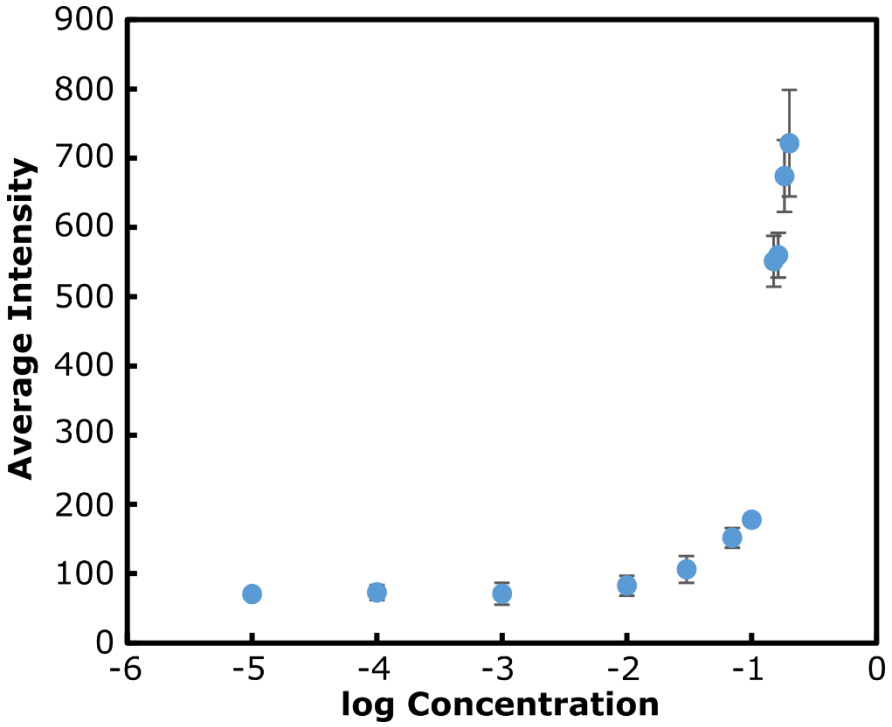

Fig S37. Critical micelle concentration plot for polymer **5d** (PEG-*b*-(SATO-*co*-alkyl)) determined using the Nile Red assay.

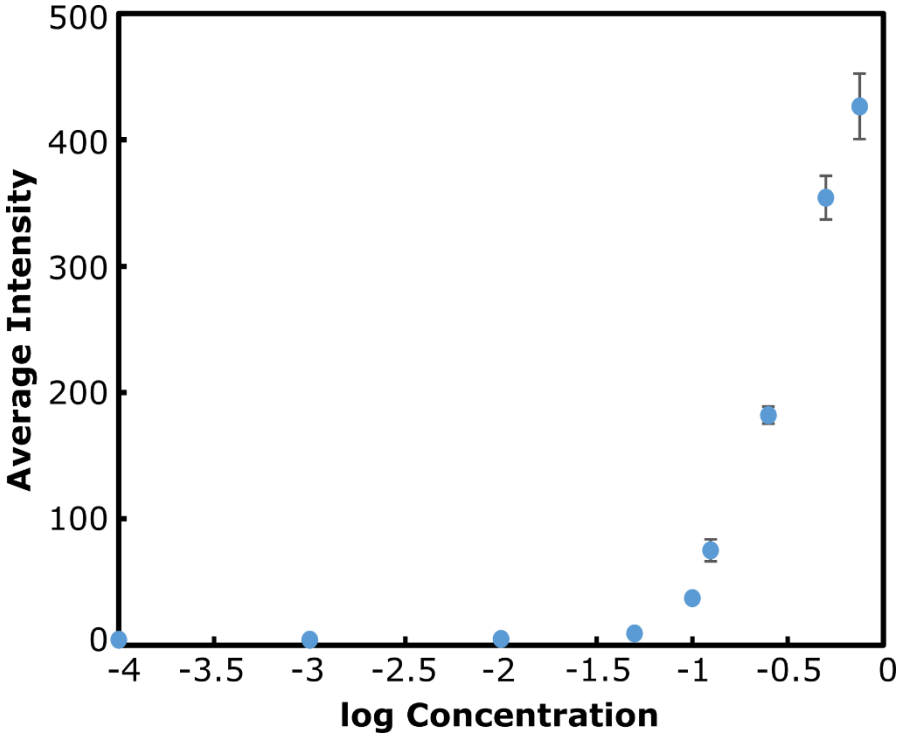

Fig S38. Critical micelle concentration plot for polymer **5e** (PEG-*b*-(alkyl)) determined using the Nile Red assay.

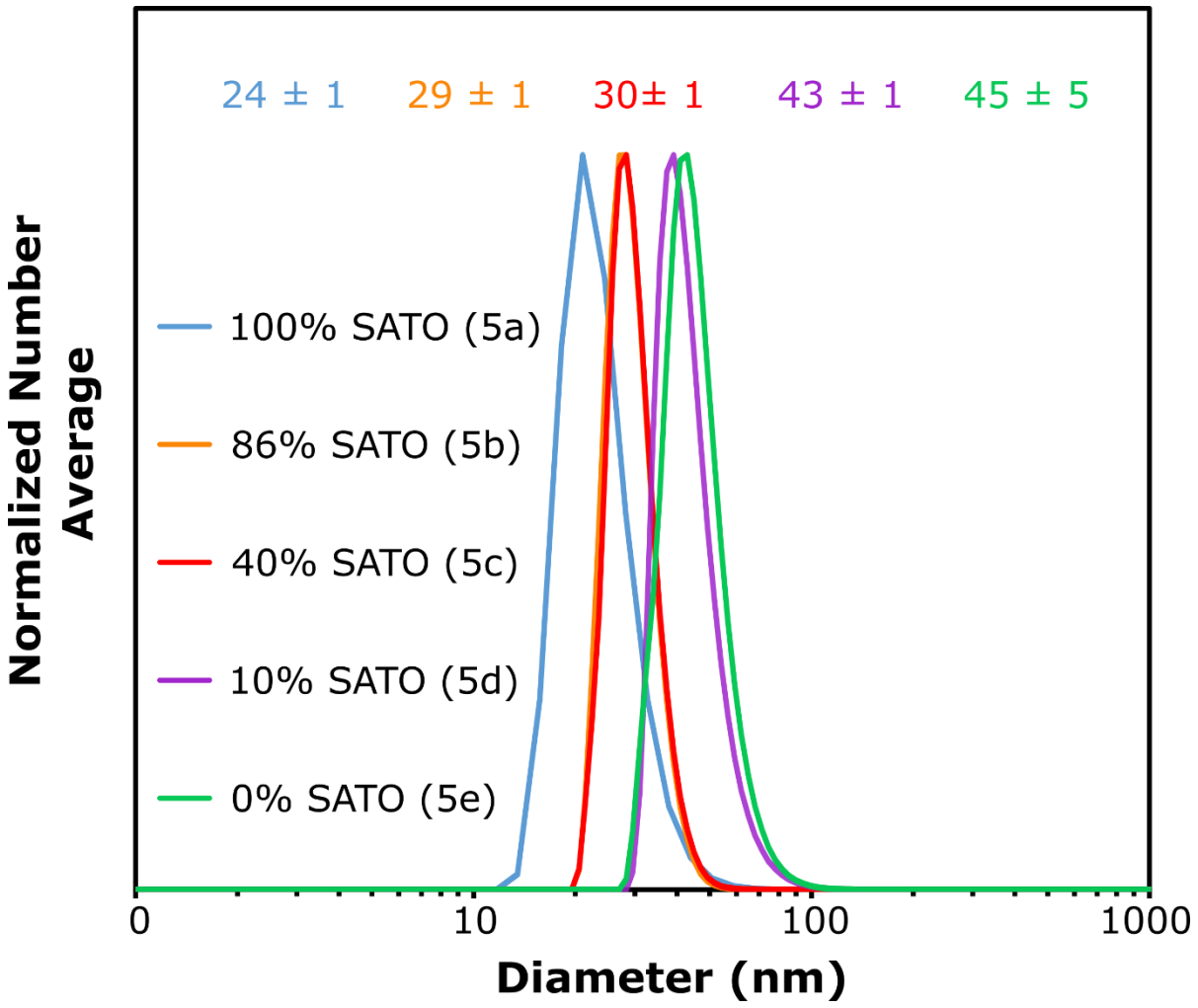

Figure S39. Effect of alkyl content on number average micelle size using polymers **5a-e**.

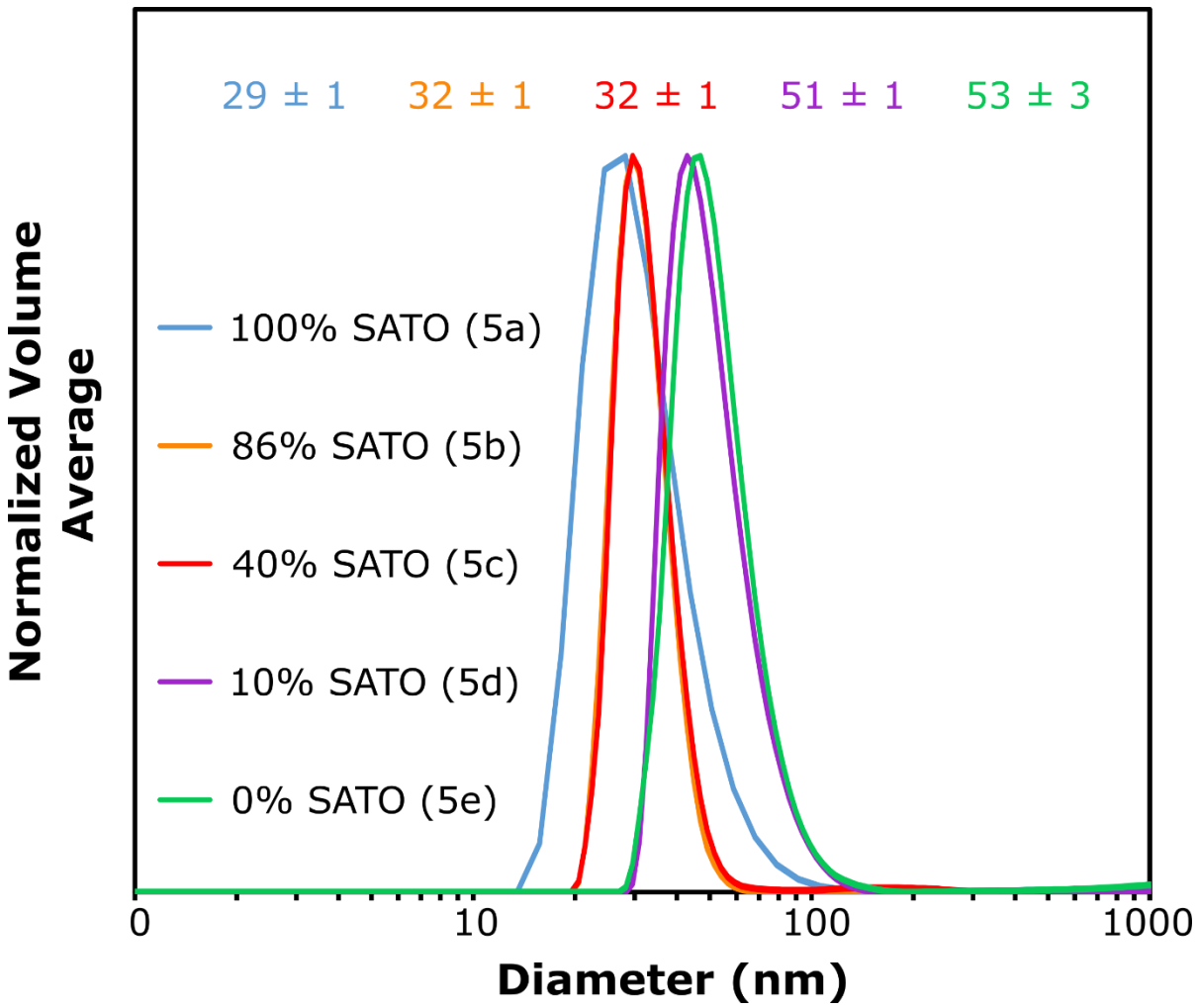

Figure S40. Effect of alkyl content on volume average micelle size using polymers **5a-e**.

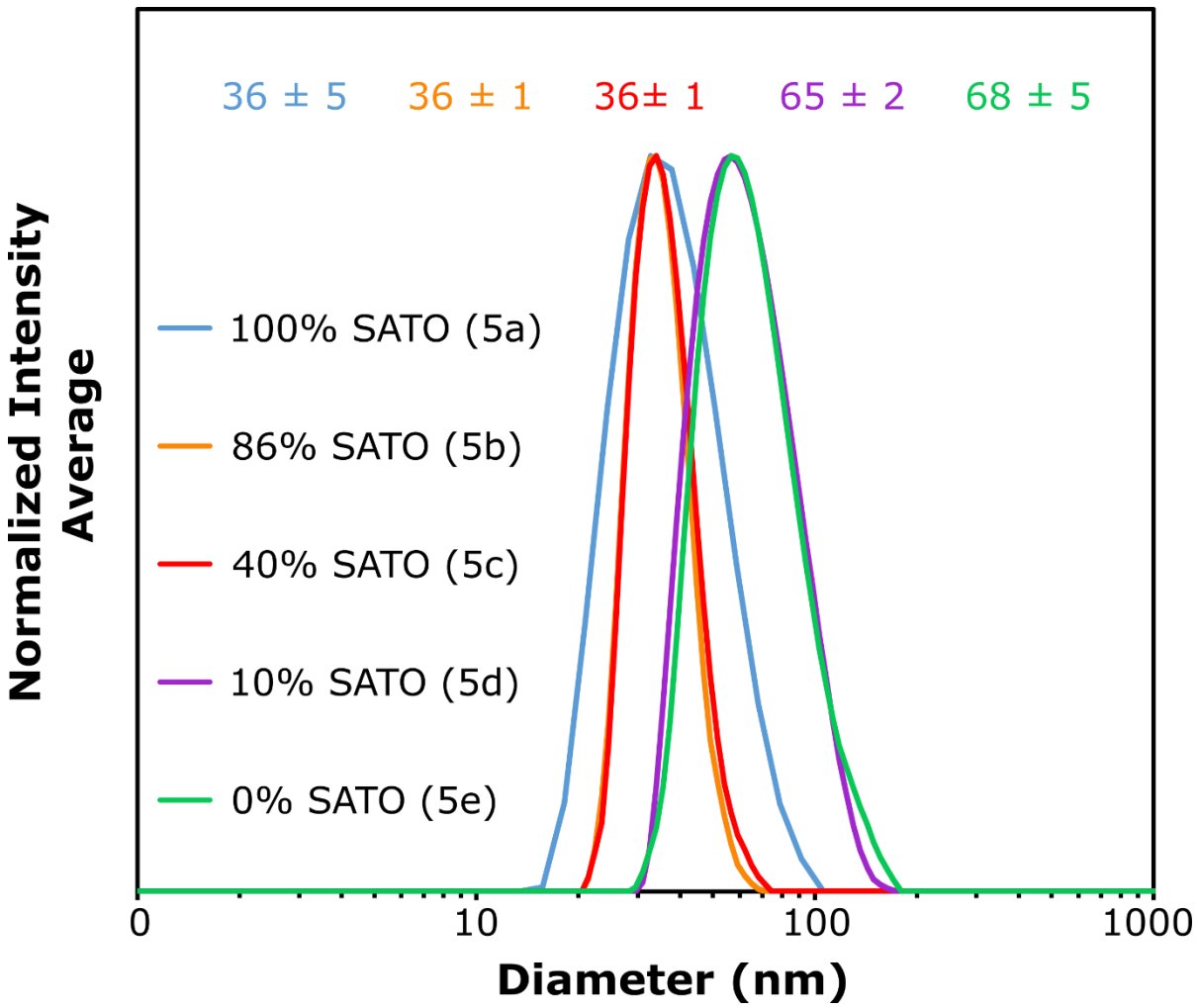

Figure S41. Effect of alkyl content on intensity average micelle size using polymers **5a-e**.

Scheme S1. H_2S release from SATOs.[a]

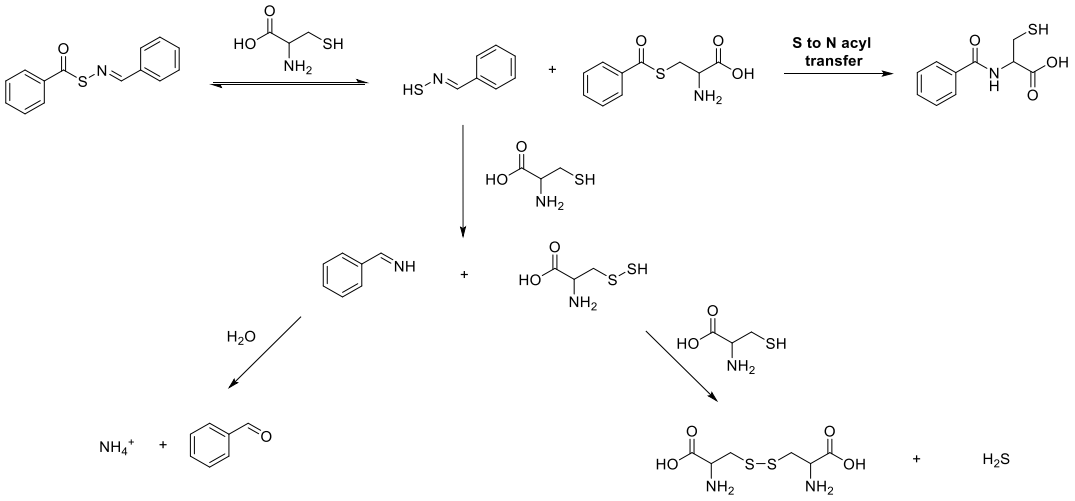

[a]Proposed mechanism of H_2S release from SATOs determined via product analysis.[1]

Experimental

References:

1. Foster, J. C.; Powell, C. R.; Radzinski, S. C.; Matson, J. B., *Org. Lett.* **2014**, *16* (6), 1558-1561.

2. Foster, J. C.; Matson, J. B., *Macromolecules* **2014**, *47* (15), 5089-5095.

3. Scott, T. A., *The Journal of Physical Chemistry* **1946**, *50* (5), 406-412.

4. Tanaka, Y.; Yamamoto, T.; Satomi, Y.; Kubota, H.; Makita, T., **1977**.

5. Dutta, D.; Pulsipher, A.; Luo, W.; Yousaf, M. N., *J. Am. Chem. Soc.* **2011**, *133* (22), 8704-8713.

6. Foster, J. C.; Radzinski, S. C.; Zou, X.; Finkielstein, C. V.; Matson, J. B., *Mol. Pharm.* **2017**, *14* (4), 1300-1306.

Chapter 3: Tuning Small Molecule Release from Polymer Micelles: The Effect of Crosslinking in the Hydrophobic Block

Reprinted (adapated) with permission from: Carrazzone, R. J. et al. *Eur. Polym. J.* **2020**, *141*, 110077. Copyright 2020 Elsevier Ltd. https://doi.org/10.1016/j.eurpolymj.2020.110077

3.1. Authors:

Ryan J. Carrazzone, [§,†,‡] Jeffrey C. Foster, [§,‡] Zhao Li, [§,‡] John B. Matson*[§,‡]

[§]Department of Chemistry, Virginia Tech, Blacksburg, Virginia 24060, United States

[†]Macromolecules Innovation Institute, Virginia Tech, Blacksburg, Virginia 24060, United States

[‡]Virginia Tech Center for Drug Discovery, Virginia Tech, Blacksburg, Virginia 24060, United States

3.2 Abstract:

Polymer micelles, used extensively as vehicles in the delivery of active pharmaceutical ingredients, represent a versatile polymer architecture in drug delivery systems. We hypothesized that degree of crosslinking in the hydrophobic core of amphiphilic block copolymer micelles could be used to tune the rate of release of the biological signaling gas (gasotransmitter) hydrogen sulfide (H_2S), a potential therapeutic. To test this hypothesis, we first synthesized amphiphilic block copolymers of the structure PEG-*b*-P(FBEA) (PEG = poly(ethylene glycol), FBEA = 2-(4-formylbenzoyloxy)ethyl acrylate). Using a modified arm-first approach, we then varied the crosslinking percentage in the core-forming block *via* addition of a *'O,O'*-alkanediyl bis(hydroxylamine) crosslinking agent. We followed incorporation of the crosslinker by ^{1}H NMR

spectroscopy, monitoring the appearance of the oxime signal resulting from reaction of pendant aryl aldehydes on the block copolymer with hydroxylamines on the crosslinker, which revealed crosslinking percentages of 5, 10, and 15%. We then installed H_2S-releasing *S*-aroylthiooxime (SATO) groups on the crosslinked polymers, yielding micelles with SATO units in their hydrophobic cores after self-assembly in water. H_2S release studies in water, using cysteine (Cys) as a trigger to induce H_2S release from the SATO groups in the micelle core, revealed increasing half-lives of H_2S release, from 117 ± 6 min to 210 ± 30 min, with increasing crosslinking density in the micelle core. This result was consistent with our hypothesis, and we speculate that core crosslinking limits the rate of Cys diffusion into the micelle core, decreasing the release rate. This method for tuning the release of covalently linked small molecules through modulation of micelle core crosslinking density may extend beyond H_2S to other drug delivery systems where precise control of release rate is needed.

3.3 Introduction:

Macromolecular and supramolecular delivery vehicles represent a wide class of drug delivery systems with potential for controlled release rates.[1-4] Delivery vehicles that assemble into higher-order structures in solution enable modulation of physical and pharmacokinetic properties of active pharmaceutical ingredients (APIs) without drastic changes in their chemical structure, leading to effects such as tunable release rates, extended circulation times, and targeted release.[5-7] Among these classes of delivery vehicles, polymer micelles provide a particularly versatile architecture with many tunable features, such as core and corona size, the number and nature of functional groups in the core or corona, and variable core chain mobility, all of which influence donor release kinetics.[8-10] The hydrophobic nature of many APIs promotes their encapsulation or

sequestration into hydrophobic micelle cores, which represents an effective strategy to overcome their low solubility in aqueous environments. As such, precise control over the diffusion of molecules into and out of micelles presents an appealing method for tuning donor release kinetics in micellar drug delivery systems.

Of particular interest to our group is delivery of endogenous biological signaling gases, known as gasotransmitters, which have recently emerged as powerful and widespread signaling molecules with vast therapeutic potential.[11,12] Gasotransmitters have short in vivo half-lives and are toxic at high concentrations, so sustained and controlled delivery is vital. Currently recognized gasotransmitters include nitric oxide (NO), carbon monoxide (CO), and hydrogen sulfide (H_2S), and all are produced and regulated endogenously in mammals, are membrane permeable, and interact with each other in a medley of cellular signaling processes.[13] By exploiting these endogenous pathways, gasotransmitters may exhibit unique therapeutic advantages over conventional small molecule APIs.

H_2S is the most recently recognized gasotransmitter and participates in an array of biological processes including cardioprotection,[14,15] vasodilation,[16-18] angiogenesis,[19-21] and others.[22-24] Mammals produce H_2S endogenously and systemically, with physical concentrations tightly regulated by various biosynthetic mechanisms. The presence of H_2S in many biological signaling pathways has prompted researchers to develop strategies for its exogenous delivery; a plethora of small molecules and polymers designed to release H_2S in response to a stimulus (termed H_2S donors) have been synthesized to help evaluate its role in signaling biology and exploit its therapeutic potential.[25-34] Emerging evidence indicates that controlled delivery in a sustained manner, mimicking the body's natural production of H_2S, is critical to its success as a therapeutic.[35] As such, recent interest has focused on developing drug delivery systems with

precise control over H_2S release rates.[36-42] Among these systems, polymer micelles have garnered much attention recently for their versatility.[34,43-46]

We envisioned that the wide range of structural tunability of polymer micelles would provide multiple mechanisms through which to control delivery of H_2S from H_2S donors tethered to the micelle core-forming block. Indeed, the idea of controlling diffusion into and out of the micelle core has been used previously to tune drug release rates.[10,46,47] For example, our group recently synthesized a series of H_2S-releasing polymer micelles with tunable release kinetics through control over polymer chain mobility in the micelle core.[46] We incorporated a plasticizing comonomer into the core-forming block of an amphiphilic block copolymer with *S*-aroylthiooxime (SATO) H_2S donors attached to the hydrophobic block to alter its glass transition temperature (T_g), with low T_g core-forming blocks resulting in highly mobile micelle cores. H_2S release required diffusion of a triggering molecule (cysteine, Cys) into the micelle core (see Scheme S1 for mechanism of Cys-triggered H_2S release from SATOs), so more mobile micelle cores exhibited faster Cys diffusion and consequently faster H_2S release rates. While we achieved a wide range of H_2S release kinetics with this method, incorporation of high levels of the plasticizing comonomer heavily diluted H_2S donor concentration. To address this problem, we considered core crosslinking, which can significantly influence chain mobility in a micelle core.[48-51] Specifically, we hypothesized that small amounts of crosslinking would reduce micelle core mobility, slowing diffusion of triggering Cys molecules into the core and reducing H_2S release rates (Figure 3-1). Thus, in this work, we aimed to utilize crosslinking in the micelle core to tune core mobility, and in turn, H_2S release kinetics, without drastically lowering the H_2S donor concentration.

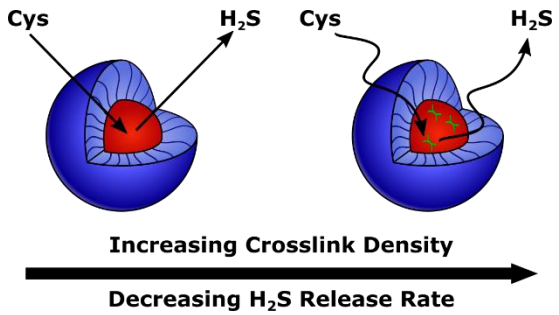

Figure 3-1. Schematic illustration showing the influence of hydrophobic block crosslinking density on H_2S release rate. Higher crosslinking density results in less mobile micelle cores, slowing diffusion of triggering Cys molecules into the core and decreasing the rate of H_2S release.

3.4 Results and Discussion:

3.4.1 Synthesis of Micelles with Crosslinks in the Hydrophobic Core

Because our previous work revealed that micelle cores with low T_g core-forming blocks released H_2S faster than those with more rigid, higher T_g core-forming blocks,[46] we expected core crosslinking to limit chain mobility, thus slowing H_2S release. Therefore, in order to achieve a range of H_2S release rates, we aimed to create H_2S releasing micelles with low T_g core-forming blocks, which would exhibit fast release profiles, and incorporate varying degrees of core crosslinking to reduce the release rate. To accomplish this goal, we first required a monomer capable of yielding low T_g polymers that could subsequently be functionalized with H_2S donors. Knowing that we could easily convert pendant aryl aldehydes into H_2S-releasing SATO groups,[56,57] and that polyacrylates exhibit lower T_g's than their polymethacrylate counterparts,[58] we selected the aryl aldehyde-functionalized acrylate 2-(4-formylbenzoyloxy)ethyl acrylate (FBEA) as the monomer for the hydrophobic, core-forming block of the polymer micelles. Based

on conditions described in a previous synthesis of the methacrylate derivative of this monomer,[54] we prepared FBEA by coupling 2-hydroxyethyl acrylate with 4-formylbenzoic acid using 1-ethyl-3-(3-dimethylaminopropyl)carbodiimide (EDC) as the coupling agent (Scheme 1A). Compared to the methacrylate monomer we had used in previous work, we expected the more flexible polyacrylate backbone of poly(FBEA) to afford greater chain mobility and result in micelles with faster H_2S release rates.

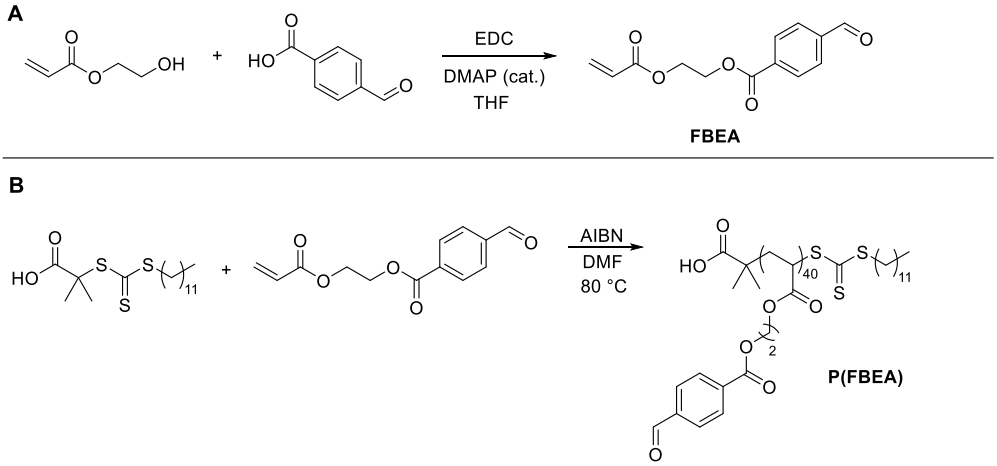

Scheme 3-1. Monomer and poly(FBEA) synthesis. (A) Synthesis of FBEA monomer and (B) homopolymerization of FBEA using RAFT. Polymerization conditions: [FBEA]/[CTA]/[AIBN] = 50:1:0.1, 33% w/v FBEA in DMF, 80 °C.

Polymerization of FBEA was carried out using reversible addition-fragmentation chain-transfer (RAFT) polymerization (Scheme 1B). To our knowledge, there are no reports of a reversible-deactivation radical polymerization of FBEA. As such, we performed kinetic analysis to assess the "livingness" of its polymerization. We utilized 2-(dodecylthiocarbonothioylthio)-2-methylpropionic acid (DMPA) as the chain transfer agent (CTA) because it is well suited for

polymerization of acrylate monomers *via* RAFT. Monomer conversion, determined by ^{1}H NMR spectroscopy, progressed linearly with time, which is indicative of a polymerization with good molecular weight control (Figure 3-2A). We observed a short induction time of around 10 min, consistent with reports on polymerization of acrylates with this CTA.[59] A plot of polymer M_n, as measured by SEC, versus % monomer conversion, showed linear evolution of molecular weight over time and low dispersity ($Đ$) throughout the polymerization, both of which also indicate good molecular weight control. Furthermore, polymer M_n values agreed well with expected molecular weights based on monomer conversion. Differential scanning calorimetry (DSC) showed that the polymer had a T_g of –55 °C (Figure S10), which we expected would afford micelles with highly mobile, rubbery cores.

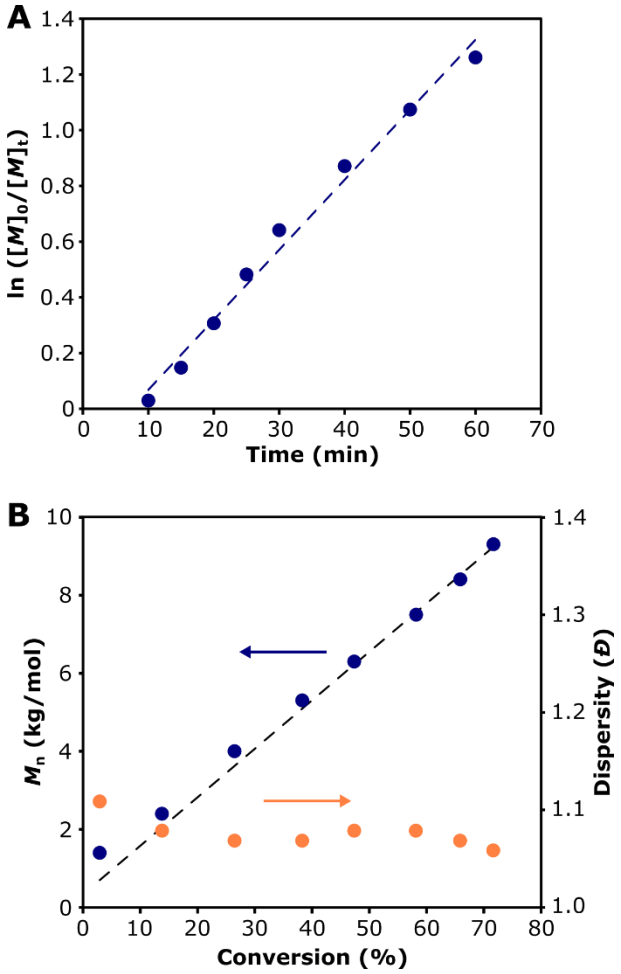

Figure 3-2. Kinetics of RAFT polymerization of FBEA: (A) Pseudo-first-order kinetics plot of the polymerization showing monomer conversion over time; the dashed blue line shows a linear fit to the data. (B) M_n (blue circles) and dispersity (orange circles), as determined by SEC with light scattering, versus monomer conversion, as determined by ^{1}H NMR spectroscopy; dashed line shows expected M_n based on monomer conversion. Linear evolution of molecular weight over time and good agreement between theoretical and measured molecular weight indicate a polymerization with a high degree of molecular weight control.

Next, we set out to prepare micelles with poly(FBEA) cores. We first synthesized trithiocarbonate-terminated poly(ethylene glycol) (PEG), termed **MacroCTA** here (Scheme 3-2A), according to a previously reported procedure.[53] We then utilized RAFT polymerization to grow hydrophobic poly(FBEA) from **MacroCTA**, resulting in an amphiphilic PEG-*b*-P(FBEA) block copolymer (Scheme 3-2B). We characterized this polymer by SEC, observing an M_n of 14 kg/mol with a dispersity of 1.13 (Figure S11). We expected the low dispersity to result in uniform micelle size distributions. Therefore, we used this batch of block copolymer for preparation of all micelles in order to have uniform micelle composition with crosslinking percentage in the hydrophobic block as the only variable.

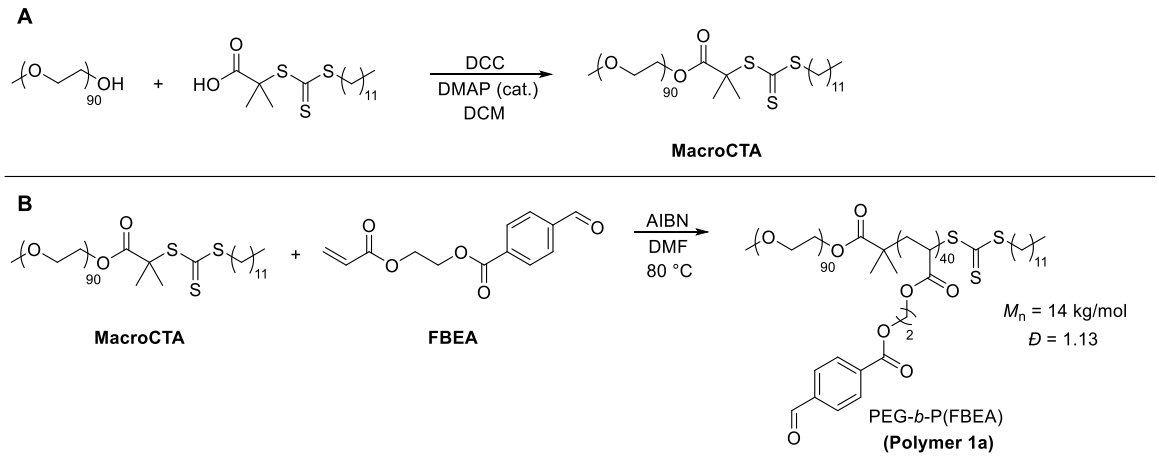

Scheme 3-2. MacroCTA and block copolymer synthesis. (A) Synthesis of **Macro-CTA**. (B) Preparation of PEG-*b*-P(FBEA) amphiphilic block copolymer. Polymerization conditions: [FBEA]/[MacroCTA]/[AIBN] = 50:1:0.1, 50% w/v FBEA in DMF, 80 °C).

Many methods for preparing crosslinked micelles have been reported.[60-63] Among these methods there are two prevalent strategies: crosslinking of pre-formed polymer assemblies, and crosslinking of unassembled polymer chains to induce formation of a polymer assembly (the arm-first approach). SATOs are reactive functional groups, so we planned to install them after crosslinking to avoid potential side reactions. Additionally, we expected that installation of SATOs into a micelle core could be hindered by the formation of crosslinks, so we avoided crosslinking pre-formed polymer assemblies. Instead, we utilized a modified version of the arm-first approach, with the goal of preparing lightly crosslinked polymer clusters, which could serve as precursor amphiphiles to H_2S-releasing micelles with crosslinks in the hydrophobic core. By taking this approach we allowed for facile installation of H_2S donors after the crosslinking reaction.

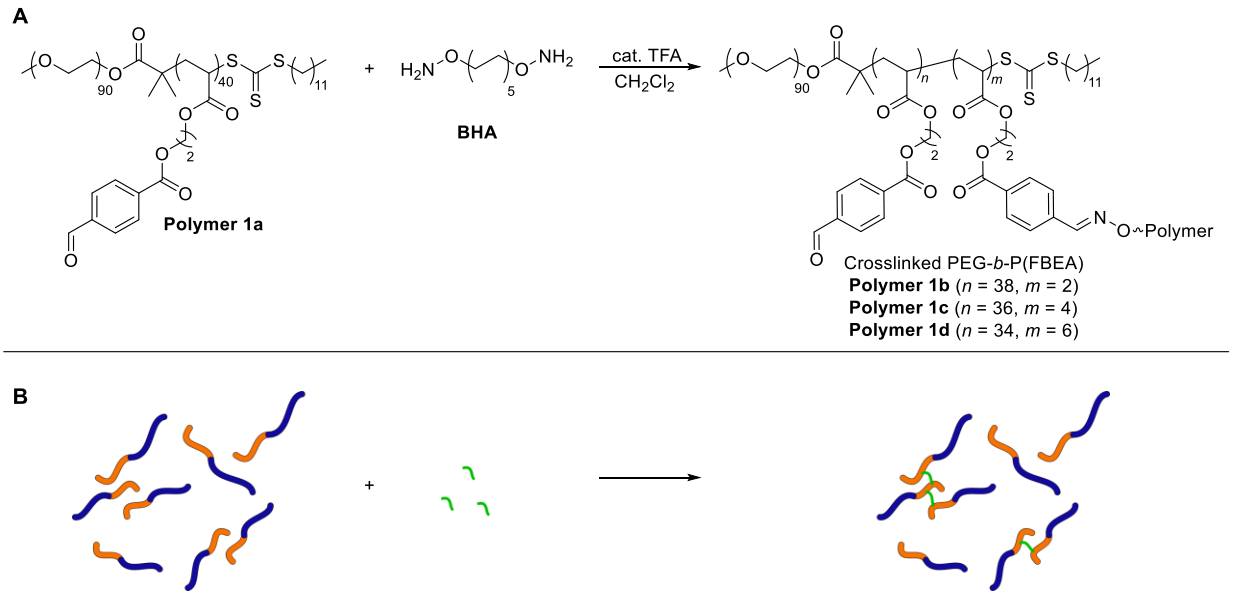

Scheme 3-3. (A) Chemical structures showing the preparation of crosslinked PEG-*b*-P(FBEA) polymer clusters. (B) Schematic illustration of this process; blue represents the hydrophilic PEG block, orange represents the hydrophobic P(FBEA) block, and green represents the BHA crosslinker.

To achieve our goal of preparing micelles with crosslinks in the hydrophobic core, we first synthesized a difunctional crosslinker with hydroxylamine functional groups, *O,O'*-(1,10-decanediyl) bis(hydroxylamine) or **BHA** for short, according to a previously reported procedure.[55] Reaction of an aldehyde with a hydroxylamine produces an oxime linkage, which we expected to be stable throughout the functionalization of remaining unreacted aldehydes based on our previous work.[46] In this method, PEG-*b*-P(FBEA) was dissolved in a good solvent for both blocks (CH_2Cl_2), then **BHA** was added in different amounts (5, 10, and 15 mol% hydroxylamines with respect to aldehyde groups) to create oxime linkages between the core-forming blocks (Scheme 3-3). After recovering the resulting polymer clusters (**Polymers 1b-d**), we measured the incorporation of

crosslinker by ^{1}H NMR spectroscopy (Figure 3-3). By comparing the integration of the aldehyde proton signal to that of the newly formed oxime proton signal, we determined crosslinking percentages of 5, 10, and 15 mol % for **Polymers 1b-d**. Although reaction of **BHA** with the trithiocarbonate group could be possible, the integrations of the oxime signal were consistent with our reaction stoichiometry suggesting that reaction of **BHA** with an aldehyde group is preferential. Analysis of the polymer clusters by SEC showed increasing molar mass and dispersity with increasing crosslinking percentage (from M_n = 49.9 kg/mol and $Đ$ = 1.43 to M_n = 61.3 kg/mol and $Đ$ = 1.63, Figures S13-15), signifying the formation of larger polymer clusters with more incorporation of **BHA** crosslinker (see SI for discussion). These results demonstrated that we could tune crosslinking percentage in the core-forming block by modifying the ratio of the **BHA** crosslinker to pendant aryl aldehyde groups on the block copolymer backbone.

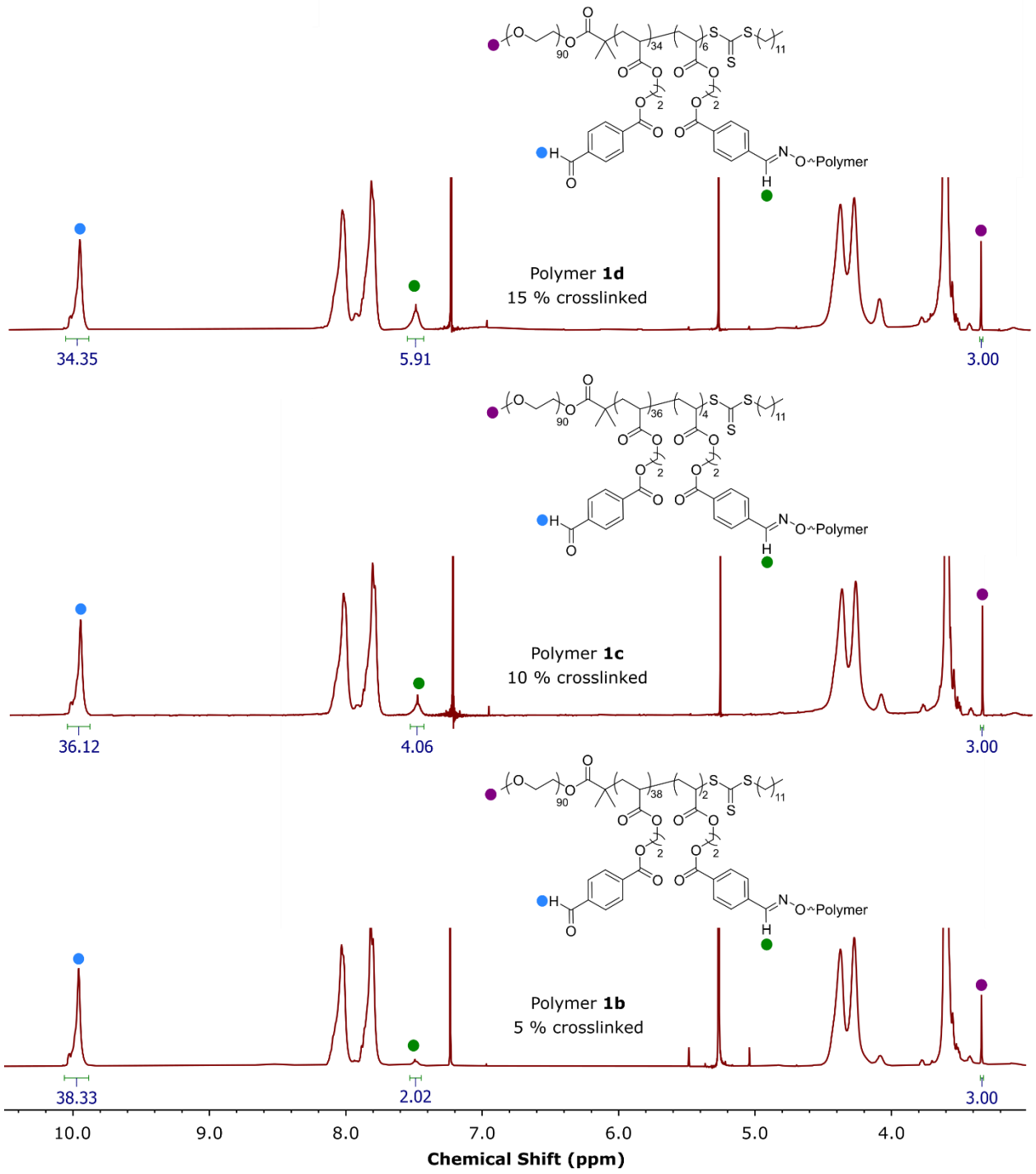

Figure 3-3. 1D ^{1}H NMR spectra of crosslinked polymer clusters of PEG-*b*-P(FBEA) (**Polymers 1b-d**) in $CDCl_3$, highlighting the ratio of aldehyde proton signal to oxime proton signal.

3.4.2 Installation of SATO H_2S Donors into the Micelle Cores:

After synthesizing polymer clusters with varying degrees of crosslinking in the P(FBEA) block, we sought to analyze how restricted chain mobility would impact H_2S release rates after installation of H_2S-releasing SATO groups and micelle formation. First, we reacted the remaining aldehydes on **Polymers 1a-d** with *S*-benzoylthiohydroxylamine (SBTHA) to produce **Polymers 2a-d**, which contained H_2S-releasing SATO groups (Scheme 3-4). We monitored conversion of aldehyde to SATO by ^{1}H NMR spectroscopy, following the disappearance of the aldehyde proton signal at 10.1 ppm and the emergence of the SATO proton signal at 8.6 ppm (Figure S12).

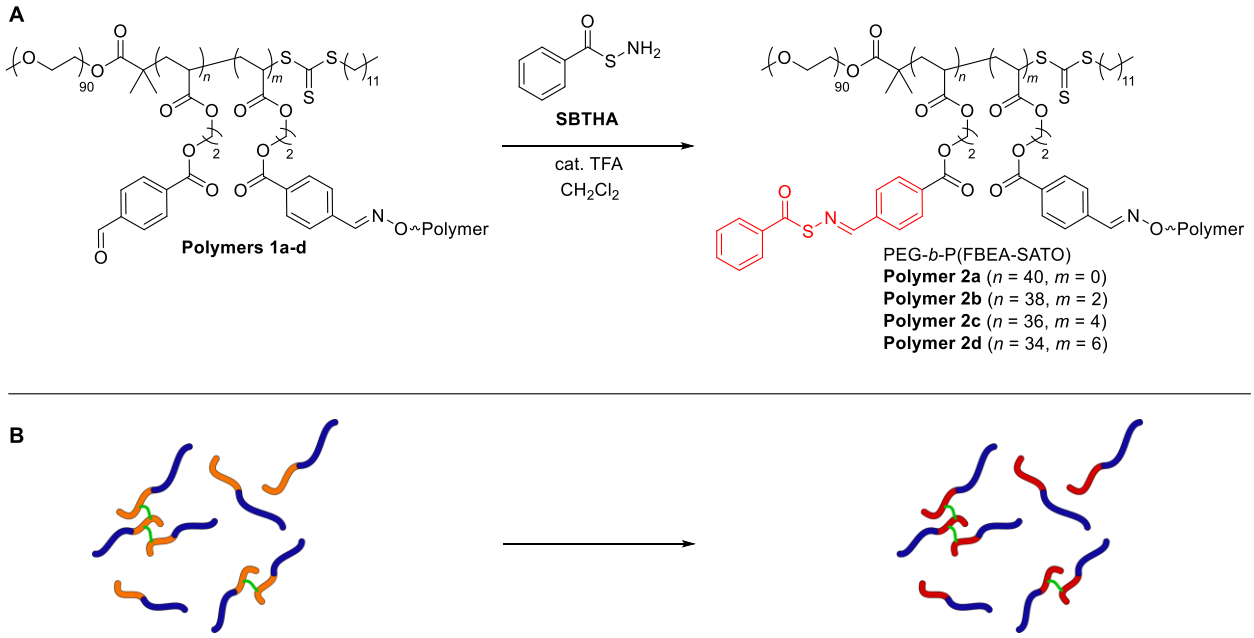

Scheme 3-4. (A) Chemical structures showing the preparation of crosslinked, H_2S-releasing amphiphilic block copolymers. H_2S-releasing SATO groups are colored in red. (B) Schematic illustration of this process; blue represents the hydrophilic PEG block, orange represents the hydrophobic P(FBEA) block, red represents the hydrophobic P(FBEA-SATO) block, and green represents the BHA crosslinker.

We then prepared micelles from **Polymers 2a-d** *via* the solvent switch method (Scheme 3-5). Briefly, we dissolved **Polymers 2a-d** in a good solvent for both blocks (THF) at a concentration of 3 mg/mL. Rapid addition of water while stirring to produce a 50% THF by volume solution then induced self-assembly into micelles. Dialysis against water removed the THF, resulting in micelle solutions in water with polymer concentrations near 1.5 mg/mL. Dilution of these solutions with water to a final concentration of 1 mg/mL afforded micelle solutions of **Polymers 2a-d** with SATO concentrations ranging from 1.7–2.0 mM.

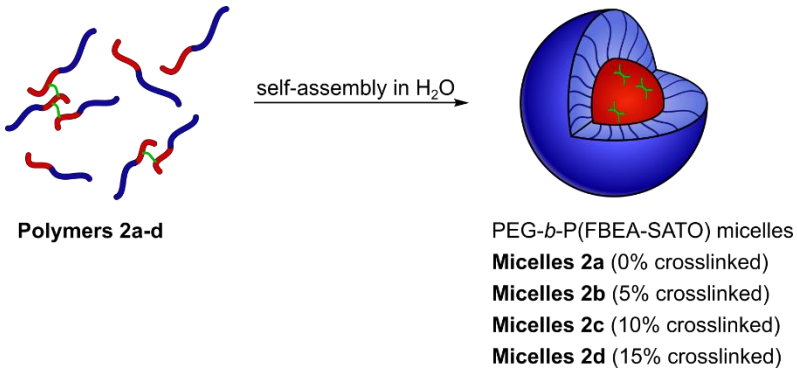

Scheme 3-5. Preparation of H_2S-releasing micelles with crosslinks in the hydrophobic core. Blue represents the hydrophilic PEG block, red represents the hydrophobic P(FBEA-SATO) block, and green represents the BHA crosslinker.

We employed dynamic light scattering (DLS) to analyze the size distributions for micelle solutions made from **Polymers 2a-d** (Table 1, Figures S16-18). We observed intensity-average hydrodynamic diameters (D_h) ranging from 28.0 ± 0.4 nm to 59 ± 1 nm, with micelle size increasing with increasing crosslinking percentage. We also observed an increase in micelle polydispersity index (PDI) upon crosslinking, from values near 0.03 for uncrosslinked micelles to

values near 0.2 for crosslinked micelles. We attribute these results to the modified version of the arm-first crosslinking approach, in which the crosslinking step creates clusters of polymer chains that later associate with other clusters or free polymer chains to form micelles. Polymer clusters are likely more uniform in size at a lower crosslinking percentage, leading to tighter packing and overall smaller micelles. Additionally, the assembly of polymer clusters of various sizes likely leads to an increase in the range of micelle sizes. TEM images of micelles prepared from **Polymers 2a-d** revealed a higher frequency of larger aggregates with increasing crosslinking percentage, further supporting this idea (Figures S19-22).

Table 3-1. Characterization of polymer assemblies.

Polymer	Crosslinking Percent[a]	Intensity-Average D_h (nm)[b]	Volume-Average D_h (nm)[b]	Number-Average D_h (nm)[b]	Micelle PDI[b]
2a	0	28.0 ± 0.4	24.0 ± 0.3	21.1 ± 0.2	0.037
2b	5	41 ± 2	32.5 ± 0.8	25.0 ± 0.7	0.212
2c	10	56 ± 2	54 ± 4	29 ± 1	0.213
2d	15	59 ± 1	56 ± 5	32 ± 1	0.199

[a]Measured by ratio of oxime and aldehyde proton signals *via* ^{1}H NMR spectroscopy (Figure 3-3).

[b]Measured by dynamic light scattering (DLS) at 1 mg/mL in DI water. Each measurement was conducted in triplicate (n = 3), and error bars reflect standard deviations.

3.4.3 Impact of Crosslinking Percentage of the Hydrophobic Block on H_2S Release Rate:

To observe the effect of core crosslinking on H_2S release rate, we conducted methylene blue assays on micelle samples prepared from **Polymers 2a-d**. The methylene blue assay is a common method for determining H_2S concentrations in solution that was standardized by Siegel

in 1965,[64] but dates back to Fischer's work in the late 1800s.[65] Briefly, released H_2S is scavenged by $Zn(OAc)_2$, forming ZnS salt in the reaction vial. Aliquots are withdrawn from the reaction vial at given timepoints and diluted with $FeCl_3$ and *p*-phenylene diamine, where captured sulfide reacts to form methylene blue dye. Because formation of methylene blue requires captured sulfide, the amount of H_2S released at each timepoint can be determined by measuring the absorbance at 750 nm, a characteristic wavelength of absorbance for methylene blue.

In these H_2S release studies, we maintained a concentration of 250 μM SATO functional groups and 1 mM cysteine across all experiments. By monitoring the production of methylene blue at varying timepoints, we evaluated H_2S release kinetics for the micelles at different crosslinking percentages. As shown in Figure 3-4 and Figures S23-S26, the most rapid H_2S release occurred from uncrosslinked micelles (**Polymer 2a**). In support of our hypothesis, we observed a decrease in the rate of H_2S release with increasing amounts of crosslinking in the micelle core, from a half-life of 117 ± 6 min for uncrosslinked micelles to a half-life of 210 ± 30 min for 15% crosslinked micelles. These results show that crosslinking of the core-forming block decreases the rate of H_2S release, which is consistent with our hypothesis. We speculate that the decreasing release rate arises from reduced core chain mobility that limits diffusion of triggering cysteine molecules into the micelle core. Alternatively, the varying release rates could result from differences in unimer percentages and/or unimer exchange rates arising from the differential molecular weights and solubilities of the polymer clusters. This is a topic that we are currently studying in depth with model systems.

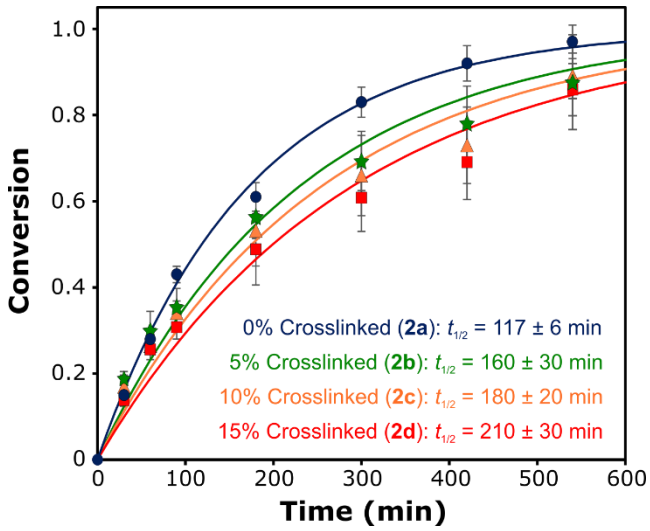

Figure 3-4. H_2S release kinetics from micelle solutions (0.125 – 0.144 mg/mL polymer concentrations) prepared from **Polymers 2a** (0% crosslinked, blue circles), **2b** (5% crosslinked, green stars), **2c** (10% crosslinked, orange triangles), and **2d** (15% crosslinked, red squares). The lines correspond to pseudo-first-order kinetics fits, from which half-life values ($t_{1/2}$) were calculated. H_2S release rates show a marked decrease with increasing crosslinking percentage.

We expect that the 2-fold change in release rate could be increased using different strategies. For example, a larger range of release rates might be observed when starting with a core-forming block with an even lower T_g. Additionally, a crosslinker with functionality >2 might have a more profound impact on Cys diffusion by further decreasing core mobility. As such, we are currently investigating methods to achieve H_2S-releasing micelles with a more expansive range of release rates through these and other core-crosslinking approaches.

3.5 Conclusions:

We have explored the influence of crosslinking in the micelle core on small molecule release rates by synthesizing and analyzing H_2S-releasing micelles with varying amounts of crosslinking in the hydrophobic block. Using a modified arm-first approach, we followed the reaction of aryl aldehyde groups using a *'O,O'*-alkanediyl bis(hydroxylamine) crosslinker by ^1H NMR spectroscopy. After micelle formation from crosslinked polymer clusters and installation of H_2S-releasing SATO groups onto the remaining aryl aldehydes, we observed increasing micelle size with increasing crosslinking percentage, likely due to the assembly of larger clusters at higher amounts of crosslinking. We observed a trend of decreasing H_2S release rate with increasing crosslinking percentage of the core-forming block, consistent with our hypothesis that crosslinking would lead to reduced micelle core mobility and therefore hindered diffusion of the Cys trigger necessary for H_2S release. We expect that further modifications to the core-forming block or crosslinker could result in an even greater impact on the rate of H_2S release. Ultimately, these findings will inform future designs for polymer micelle drug delivery systems where precise control over donor release profiles is needed.

3.6 Acknowledgements:

This work was supported by the US National Science Foundation (DMR-1454754), the US National Institutes of Health (R01GM123508), and the Dreyfus Foundation. We thank Prof. Richey Davis for use of the DLS instrument, Prof. Tim Long for use of the DSC instrument, Prof. Abby Whittington for use of the plate reader, and Kearsley Dillon, Sarah Swilley, and Yumeng (Jackie) Zhu for critical readings of the manuscript. The authors also thank Dr. Mehdi Ashraf-Khorassani for help with HRMS and confirmation of molecular structure. Any opinions, findings,

and conclusions or recommendations expressed in this material are those of the authors and do not necessarily reflect the views of the funding agencies.

3.7 References:

1. Cho, K.; Wang, X.; Nie, S.; Chen, Z.; Shin, D. M., *Clin. Cancer Res.* **2008**, *14* (5), 1310.

2. Kataoka, K.; Harada, A.; Nagasaki, Y., *Adv. Drug Del. Rev.* **2012**, *64*, 37-48.

3. Petros, R. A.; DeSimone, J. M., *Nat. Rev. Drug Discov.* **2010**, *9* (8), 615-627.

4. Wang, Y.; Cheetham, A. G.; Angacian, G.; Su, H.; Xie, L.; Cui, H., *Adv. Drug Del. Rev.* **2017**, *110-111*, 112-126.

5. Ulbrich, K.; Hola, K.; Subr, V.; Bakandritsos, A.; Tucek, J.; Zboril, R., *Chem. Rev.* **2016**, *116* (9), 5338-5431.

6. Tyler, B.; Gullotti, D.; Mangraviti, A.; Utsuki, T.; Brem, H., *Adv. Drug Del. Rev.* **2016**, *107*, 163-175.

7. Li, Z. B.; Ye, E. Y.; David; Lakshminarayanan, R.; Loh, X. J., *Small* **2016**, *12* (35), 4782-4806.

8. Biswas, S.; Kumari, P.; Lakhani, P. M.; Ghosh, B., *Eur. J. Pharm. Sci.* **2016**, *83* (Supplement C), 184-202.

9. Cabral, H.; Miyata, K.; Osada, K.; Kataoka, K., *Chem. Rev.* **2018**, *118* (14), 6844-6892.

10. Chan, D.; Yu, A. C.; Appel, E. A., *Biomacromolecules* **2017**, *18* (4), 1434-1439.

11. Wang, R., *Trends Biochem. Sci.* **2014**, *39* (5), 227-232.

12. Mustafa, A. K.; Gadalla, M. M.; Snyder, S. H., *Sci. Signal* **2009**, *2* (68), re2-re2.

13. Wang, R., *Proc. Natl. Acad. Sci.* **2012**, *109* (23), 8801.

14. Barr, L. A.; Calvert, J. W., *Circulation* **2014**, *78* (9), 2111-2118.

15. Calvert John, W.; Jha, S.; Gundewar, S.; Elrod John, W.; Ramachandran, A.; Pattillo Christopher, B.; Kevil Christopher, G.; Lefer David, J., *Circ. Res.* **2009**, *105* (4), 365-374.

16. Mustafa Asif, K.; Sikka, G.; Gazi Sadia, K.; Steppan, J.; Jung Sung, M.; Bhunia Anil, K.; Barodka Viachaslau, M.; Gazi Farah, K.; Barrow Roxanne, K.; Wang, R.; Amzel, L. M.; Berkowitz Dan, E.; Snyder Solomon, H., *Circ. Res.* **2011**, *109* (11), 1259-1268.

17. Tang, G.; Wu, L.; Liang, W.; Wang, R., *Mol. Pharmacol.* **2005**, *68* (6), 1757.

18. Zhao, W.; Zhang, J.; Lu, Y.; Wang, R., *EMBO J.* **2001**, *20* (21), 6008-6016.

19. Szabo, C., *Am. J. Physiol., Cell Physiol.* **2016**, *312* (1), C3-C15.

20. Szabo, C.; Papapetropoulos, A., *Br J Pharmacol* **2011**, *164* (3), 853-65.

21. Cai, W. J.; Wang, M. J.; Moore, P. K.; Jin, H. M.; Yao, T.; Zhu, Y. C., *Cardiovasc Res* **2007**, *76* (1), 29-40.

22. Bhatia, M.; Sidhapuriwala, J. N.; Wei Ng, S.; Tamizhselvi, R.; Moochhala, S. M., *J. Cell. Mol. Med.* **2008**, *12* (2), 580-590.

23. Campolo, M.; Esposito, E.; Ahmad, A.; Di Paola, R.; Wallace, J. L.; Cuzzocrea, S., *FASEB J.* **2013**, *27* (11), 4489-4499.

24. Giuliani, D.; Ottani, A.; Zaffe, D.; Galantucci, M.; Strinati, F.; Lodi, R.; Guarini, S., *Neurobiol Learn Mem* **2013**, *104*, 82-91.

25. Zhao, Y.; Pluth, M. D., *Angew. Chem. Int. Ed.* **2016**, *55* (47), 14638-14642.

26. Powell, C. R.; Dillon, K. M.; Matson, J. B., *Biochem. Pharmacol.* **2018**, *149*, 110-123.

27. Kaur, K.; Carrazzone, R. J.; Matson, J. B., *Antioxid. Redox. Sign.* **2019**, *32* (2), 79-95.

28. Li, Z.; Polhemus David, J.; Lefer David, J., *Circ. Res.* **2018**, *123* (5), 590-600.

29. Wallace, J. L.; Vaughan, D.; Dicay, M.; MacNaughton, W. K.; de Nucci, G., *Antioxid. Redox Signal.* **2017**, *28* (16), 1533-1540.

30. Wallace, J.; Buret, A.; Nagy, P.; Muscara, M.; Nucci, G. d., *Ann. Rheum. Dis.* **2019**, *78* (Suppl 2), 522-522.

31. Kodela, R.; Chattopadhyay, M.; Kashfi, K., *ACS Med. Chem. Lett.* **2012**, *3* (3), 257-262.

32. Xiao, Z.; Bonnard, T.; Shakouri-Motlagh, A.; Wylie, R. A. L.; Collins, J.; White, J.; Heath, D. E.; Hagemeyer, C. E.; Connal, L. A., *Chem. Eur. J.* **2017**, *23* (47), 11294-11300.

33. Hasegawa, U.; van der Vlies, A. J., *MedChemComm* **2015**, *6* (2), 273-276.

34. Foster, J. C.; Radzinski, S. C.; Zou, X.; Finkielstein, C. V.; Matson, J. B., *Mol. Pharm.* **2017**, *14* (4), 1300-1306.

35. Szabó, C., *Nat. Rev. Drug Discov.* **2007**, *6*, 917.

36. Ercole, F.; Mansfeld, F. M.; Kavallaris, M.; Whittaker, M. R.; Quinn, J. F.; Halls, M. L.; Davis, T. P., *Biomacromolecules* **2016**, *17* (1), 371-383.

37. Dillon, K. M.; Carrazzone, R. J.; Matson, J. B.; Kashfi, K., *Biochem. Pharmacol.* **2020**, 113931.

38. Wallace, J. L.; Wang, R., *Nat. Rev. Drug Discov.* **2015**, *14*, 329.

39. Urquhart, M. C.; Ercole, F.; Whittaker, M. R.; Boyd, B. J.; Davis, T. P.; Quinn, J. F., *Polym. Chem.* **2018**, *9* (35), 4431-4439.

40. Connal, L. A., *J. Mater. Chem. B* **2018**, *6* (44), 7122-7128.

41. Ercole, F.; Li, Y.; Whittaker, M. R.; Davis, T. P.; Quinn, J. F., *J. Mater. Chem. B* **2020**, *8* (17), 3896-3907.

42. Yu, S. H.; Esser, L.; Khor, S. Y.; Senyschyn, D.; Veldhuis, N. A.; Whittaker, M. R.; Ercole, F.; Davis, T. P.; Quinn, J. F., *J. Polym. Sci. A* **2019**, *57* (18), 1982-1993.

43. Ercole, F.; Whittaker, M. R.; Halls, M. L.; Boyd, B. J.; Davis, T. P.; Quinn, J. F., *Chem. Comm.* **2017**, *53* (57), 8030-8033.

44. Takatani-Nakase, T.; Katayama, M.; Matsui, C.; Hanaoka, K.; van der Vlies, A. J.; Takahashi, K.; Nakase, I.; Hasegawa, U., *Mol. BioSyst.* **2017**, *13* (9), 1705-1708.

45. Chen, J. J. Y.; van der Vlies, A. J.; Hasegawa, U., *Polym. Chem.* **2020**, *11* (27), 4454-4463.

46. Foster, J. C.; Carrazzone, R. J.; Spear, N. J.; Radzinski, S. C.; Arrington, K. J.; Matson, J. B., *Macromolecules* **2019**, *52* (3), 1104-1111.

47. Molla, M. R.; Rangadurai, P.; Antony, L.; Swaminathan, S.; de Pablo, J. J.; Thayumanavan, S., *Nat. Chem.* **2018**, *10* (6), 659-666.

48. Zheng, H.; Yin, L. Q.; Zhang, X. Q.; Zhang, H.; Hu, R.; Yin, Y. H.; Qiu, T.; Xiong, X.; Wang, Q., *J. Biomed. Nanotechnol.* **2016**, *12* (8), 1641-1653.

49. Wang, T. R.; Ma, X. Y.; Lei, Y.; Luo, Y. C., *Colloid Surf. B-Biointerfaces* **2016**, *148*, 1-11.

50. Modarresi-Saryazdi, S. M.; Haddadi-Asl, V.; Salami-Kalajahi, M., *J. Biomed. Mater. Res. A* **2018**, *106* (2), 342-348.

51. Talelli, M.; Barz, M.; Rijcken, C. J. F.; Kiessling, F.; Hennink, W. E.; Lammers, T., *Nano Today* **2015**, *10* (1), 93-117.

52. Skey, J.; O'Reilly, R. K., *Chem. Commun.* **2008**, (35), 4183-4185.

53. Chong, D.; Tan, J.; Zhang, J.; Zhou, Y.; Wan, X.; Zhang, J., *Chem. Commun.* **2018**, *54* (56), 7838-7841.

54. Foster, J. C.; Matson, J. B., *Macromolecules* **2014**, *47* (15), 5089-5095.

55. Li, R.-Y.; Jing, L.; Meng, J.-L.; Li, G., *Asian J. Chem.* **2014**, *26* (9), 2733-2735.

56. Foster, J. C.; Powell, C. R.; Radzinski, S. C.; Matson, J. B., *Org. Lett.* **2014**, *16* (6), 1558-1561.

57. Lin, L.; Qin, H.; Huang, J.; Liang, H.; Quan, D.; Lu, J., *Polym. Chem.* **2018**, *9* (21), 2942-2950.

58. Penzel, E.; Rieger, J.; Schneider, H. A., *Polymer* **1997**, *38* (2), 325-337.

59. Konkolewicz, D.; Hawkett, B. S.; Gray-Weale, A.; Perrier, S., **2009**, *47* (14), 3455-3466.

60. Joralemon, M. J.; O'Reilly, R. K.; Hawker, C. J.; Wooley, K. L., *J. Am. Chem. Soc.* **2005**, *127* (48), 16892-16899.

61. Dai, J.; Lin, S. D.; Cheng, D.; Zou, S. Y.; Shuai, X. T., *Angew. Chem.-Int. Edit.* **2011**, *50* (40), 9404-9408.

62. Wu, Z. M.; Liang, H.; Lu, J. A.; Deng, W. L., *J. Polym. Sci. Pol. Chem.* **2010**, *48* (15), 3323-3330.

63. Wang, K.; Peng, H.; Thurecht, K. J.; Puttick, S.; Whittaker, A. K., *Polym. Chem.* **2014**, *5* (5), 1760-1771.

64. Siegel, L. M., *Anal. Biochem.* **1965**, *11* (1), 126-132.

65. Fischer, E., *Ber. Dtsch, Chem. Ges.* **1883**, *16* (2), 2234-2236.

3.8 Experimental:

Materials

All reagents were obtained from commercial vendors and used as received unless otherwise stated. 2,2′-Azobis(2-methylpropionitrile) (AIBN) was recrystallized from methanol prior to use. Dry solvents were purified by passage through a solvent purification system (MBraun).

Instrumentation

NMR spectra were measured on an Agilent 400 MHz spectrometer. ^{1}H and ^{13}C NMR chemical shifts are reported in ppm relative to internal solvent resonances. Yields refer to chromatographically and spectroscopically pure compounds unless otherwise stated. Size exclusion chromatography (SEC) was carried out in THF at 1 mL/min at 30 °C on two Agilent PLgel 10 µm MIXED-B columns connected in series with a Wyatt Dawn Heleos 2 multi-angle light scattering detector and a Wyatt Optilab Rex refractive index detector. No calibration standards were used, and d*n*/d*c* values were obtained by assuming 100% mass recovery. Dynamic

light scattering (DLS) was conducted using a Malvern Zetasizer Nano operating at 25 °C. A solution of micelles was prepared at 1 mg/mL and filtered with a 0.2 μm filter prior to scanning. Calculations of the particle size distributions and distribution averages were conducted using CONTIN particle size distribution analysis routines with number, volume, and intensity averages. Measurements were made in triplicate and errors reflect standard deviations. Differential scanning calorimetry (DSC) studies were carried out on a Q-2000 DSC in aluminum pans operated with a dry nitrogen purge from -80 °C to 100 °C with a heating and cooling rate of 20 °C/min. Results are reported from the second heat cycle and figures are shown as exo down.High-resolution mass spectra were taken on an Agilent Technologies 6230 TOF LC/MS mass spectrometer.

Synthesis of 2-methyl-2-(dodecylsulfanylthiocarbonyl)sulfanyl propanoic acid (CTA)

Dodecanethiol (5.00 mL, 20.9 mmol) was dissolved in acetone (30 mL) in a round bottom flask. To the flask was added tribasic potassium phosphate (8.86 g, 41.7 mmol). The reaction mixture was stirred at rt for 10 min. CS_2 (3.78 mL, 62.6 mmol) was then added dropwise, and the reaction mixture was stirred for an additional 1 h. To the flask a solution of 2-bromo-2-methyl propanoic acid (3.91 g, 23.4 mmol) in 5 mL of acetone was added dropwise. The reaction mixture was stirred overnight at rt. Reaction conversion was monitored by TLC using CH_2Cl_2 as the eluent and visualized via a UV lamp. The reaction mixture was diluted with ~100 mL CH_2Cl_2, transferred to a separatory funnel, and washed consecutively with 1N HCl and brine. The organic layer was dried over Na_2SO_4 and concentrated via rotary evaporation. Silica gel was added to the concentrated solution before removing the rest of the solvent via rotary evaporation. The silica gel was dry-loaded onto a silica gel column, and the product was eluted with CH_2Cl_2. Product containing fractions, as determined by TLC (CH_2Cl_2 eluent and UV lamp visualization), were combined and concentrated via rotary evaporation to yield a yellow solid. The crude product was recrystallized

from hexanes to yield yellow crystals (4.88 g, 64% yield). ^{1}H NMR ($CDCl_3$) δ (ppm): 3.25 (2H, t, *J* = 7.4 Hz); 1.70 (6H, s); 1.64 (2H, m); 1.37 (2H, m); 1.25 (18H, m); 0.88 (3H, t, *J* = 6.9 Hz). ^{13}C NMR ($CDCl_3$) δ (ppm): 220.78, 178.84, 55.59, 37.12, 31.89-26.21, 23.69, 14.13. These spectra match those from published report.[1]

Synthesis of MacroCTA

A round bottom flask was charged with **CTA** (0.91 g, 2.50 mmol), polyethylene glycol monomethyl ether (M_n = 4,000 g/mol, 5.0 g, 1.25 mmol), 4-dimethylamino pyridine (0.15 g, 1.25 mmol), and anhydrous CH_2Cl_2 (5.0 mL). *N*,*N*'-Dicyclohexylcarbodiimide (DCC) (0.52 g, 2.50 mmol) was dissolved in 5.0 mL of anhydrous CH_2Cl_2 in a vial. The DCC solution was added dropwise to the flask containing the other reagents, and the reaction mixture was stirred at rt overnight. Reaction conversion was followed by TLC using CH_2Cl_2 as eluent and visualized via UV lamp. The precipitated solids were removed by filtration. The desired product was isolated via precipitation from diethyl ether and was purified by repeated precipitations (2-4) from CH_2Cl_2 into diethyl ether until complete removal of low molecular weight side products was confirmed by ^{1}H NMR spectroscopy to afford the product as a yellow solid (1.50 g, 69% yield). ^{1}H NMR ($CDCl_3$) δ (ppm): 4.24 (2H, t, *J* = 5.0 Hz); 3.81 (2H, t, *J* = 4.8 Hz); 3.63 (~360H, m); 1.37 (2H, m); 3.37 (3H, s); 3.25 (2H, t, *J* = 7.4 Hz); 1.69 (6H, s); 1.64 (2H, m); 1.25 (18H, m); 0.87 (3H, t, *J* = 6.6 Hz). ^{13}C NMR ($CDCl_3$) δ (ppm): 221.38, 172.81, 71.89, 70.52, 68.75, 65.01, 58.98, 55.89, 36.86, 31.85, 29.57, 29.49, 29.38, 29.27, 29.04, 28.88, 27.81, 25.29, 22.62, 14.07. These spectra match those from published reports.[2]

Synthesis of 2-(4-formylbenzoyloxy)ethyl acrylate (FBEA)

FBEA was prepared by modification of a literature procedure.[3] A round bottom flask was charged with 4-formylbenzoic acid (2.00 g, 13.3 mmol) and EDC (2.62 g, 16.0 mmol), and diluted with CH_2Cl_2 (20 mL). 2-Hydroxyethyl acrylate (1.61 mL, 14.0 mmol) was added in one portion, followed by 4-dimethylaminopyridine (16 mg, 0.13 mmol). Butylated hydroxytoluene (BHT) (30 mg, 0.13 mmol) was added to inhibit polymerization. The reaction mixture was stirred at rt until homogeneous (~24 h). The reaction mixture was then diluted with CH_2Cl_2 (30 mL) and washed with 1N HCl (3 x 30 mL). The organic layer was dried and concentrated onto silica gel. A silica column was dry-loaded with this material, and the crude reaction mixture was purified by column chromatography using 50% hexanes in CH_2Cl_2 as the eluent, affording the pure product after rotary evaporation of product-containing fractions, as observed by thin layer chromatography (TLC), as a clear oil (2.13 g, 64%). BHT (20 mg, 0.08 mmol) was added before storage at 0 °C. ^{1}H NMR ($CDCl_3$): δ 4.53 (m, 2H), 4.60 (m, 2H), 5.87 (dd, J = 1.4, 10.4 Hz, 1H), 6.15 (m, 1H), 6.45 (dd, J = 1.4, 17.3 Hz, 1H), 7.96 (d, J = 8.6 Hz, 2H), 8.20 (d, J = 8.4 Hz, 2H), 10.10 (s, 1H). ^{13}C NMR ($CDCl_3$): δ 191.70, 165.99, 165.42, 139.41, 134.82, 131.69, 130.42, 129.65, 128.01, 63.38, 62.16. HRMS (ESI-TOF) calcd. for $C_{26}H_{24}NaO_{10}$ $[2M+Na]^+$ 519.1267, found 519.1253.

Synthesis of O,O'-(decane-1,10-diyl)bis(hydroxylamine) (BHA) crosslinking agent

O,O'-(decane-1,10-diyl)bis(hydroxylamine) (**BHA**) was prepared using a modified literature procedure.[4] A round bottom flask was charged with *N*-hydroxyphthalimide (2.39 g, 14.7 mmol), triethylamine (NEt_3) (2.20 mL, 15.6 mmol), potassium iodide (3 mg, 0.018 mmol) and acetonitrile (15 mL). A solution of 1,10-dibromodecane (1.47 g, 4.9 mmol) in acetonitrile (5 mL) was added to the flask dropwise while stirring. Reaction conversion was monitored by TLC using 5% ethyl acetate in hexanes as eluent and visualized by iodine staining. The reaction mixture was stirred at room temperature until complete disappearance of 1,10-dibromodecane (~24 h). The reaction

mixture was diluted with CH_2Cl_2 (200 mL) and washed successively with alternating water and saturated sodium bicarbonate solutions until the aqueous layer was colorless. The organic layer was dried and concentrated by rotary evaporation to afford the crude 1,10-bis(*N*-phthalimidyloxy)decane product as a pale-yellow oil. This was used in the next step without further purification. 1,10-bis(*N*-phthalimidyloxy)decane (500 mg, 1.1 mmol) was dissolved in ethanol (2 mL) and distilled water (2 mL). Next, hydrazine (40% in H_2O) (390 µL, 6.5 mmol) was added in one portion. Reaction conversion was monitored by TLC using CH_2Cl_2 as eluent and visualized by iodine staining. The reaction mixture was stirred at room temperature until complete disappearance of 1,10-bis(*N*-phthalimidyloxy)decane (~3 h). The reaction mixture was concentrated to dryness and diluted with 1N NaOH (50 mL). The aqueous layer was extracted with ethyl acetate (3 x 25 mL). The organic layers were combined, dried, and loaded onto silica. A silica column was dry-loaded with this material, and the crude reaction mixture was purified by column chromatography using a gradient polarity eluent starting from CH_2Cl_2 and adding ethyl acetate up to 50%, affording the product after rotary evaporation of product-containing fractions, as determined by TLC, as a white solid (180 mg, 20%). ^{1}H NMR ($CDCl_3$): δ 3.65 (t, J = 7 Hz, 4H), 1.56 (m, 4H), 1.29 (m, 6H). ^{13}C NMR ($CDCl_3$): δ 76.22, 29.47, 29.46, 28.38, 25.99. These spectra are consistent with previous reports.[4]

Synthesis of P(FBEA)

Prior to use, FBEA monomer was passed through a plug of basic alumina to remove inhibitor (BHT). An oven-dried Schlenk tube was charged with FBEA (1.00 g, 4.0 mmol) and macroCTA (29 mg, 0.081 mmol), and diluted with DMF (2.0 mL). 100 µL of an AIBN solution (13 mg in 1.0 mL DMF) was added *via* syringe. The reaction mixture was deoxygenated by subjecting the contents to five freeze-pump-thaw cycles. The Schlenk tube was then backfilled with N_2 and

submerged in an oil bath maintained at 80 °C. Aliquots were removed periodically by N_2-purged syringe to monitor molar mass evolution by SEC and conversion by ^{1}H NMR spectroscopy. The polymerization was quenched by submerging the tube into liquid N_2 and exposing the reaction mixture to air. The resulting polymer was isolated *via* precipitation into diethyl ether.

Synthesis of PEG-b-P(FBEA)

Prior to use, FBEA monomer was passed through a plug of basic alumina to remove inhibitor (BHT). An oven-dried Schlenk tube was charged with FBEA (3.12 g, 12.6 mmol) and macroCTA (1.09 g, 0.25 μmol), and diluted with DMF (3.0 mL). 100 μL of an AIBN solution (20 mg in 1.0 mL DMF) was added *via* syringe. The reaction mixture was deoxygenated by subjecting the contents to five freeze-pump-thaw cycles. The Schlenk tube was then backfilled with N_2 and submerged in an oil bath maintained at 80 °C. Aliquots were removed periodically by N_2-purged syringe to monitor molar mass by SEC and conversion by ^{1}H NMR spectroscopy. The polymerization was quenched by submerging the tube into liquid N_2 and exposing the reaction mixture to air. The resulting polymer was isolated *via* precipitation into cold diethyl ether (3.33 g, 93%).

Representative procedure for crosslinking of the core-forming block

The procedure for preparation of **Polymer 1b** (5% crosslinked) is as follows: A scintillation vial was charged with PEG-*b*-P(FBEA) (100 mg, 6.9 μmol) and CH_2Cl_2 (1.9 mL). A solution of **BHA** crosslinker (28 mg, 140 μmol) in CH_2Cl_2 (2.0 mL) was prepared. 100 μL of this solution was added to the reaction mixture to achieve a total volume of 2 mL. A layer of molecular sieves and trifluoroacetic acid (10 μL, 130 μmol) were added to the reaction mixture. The reaction was

allowed to sit at rt overnight. The resulting crosslinked polymer was isolated *via* precipitation into cold diethyl ether. To prepare **Polymer 1c** (10% crosslinked) 200 μL of **BHA** solution was added to 1.8 mL CH_2Cl_2, and to prepare **Polymer 1d** (15% crosslinked) 300 μL of **BHA** solution was added to 1.7 mL CH_2Cl_2.

General procedure for preparation of H_2S releasing polymers

A scintillation vial was charged with PEG-*b*-P(FBEA) (100 mg, 6.9 umol) and *S*-benzoylthiohydroxylamine (160 mg, 1.1 mmol). The solids were dissolved in CH_2Cl_2 (2.0 mL). A layer of molecular sieves and trifluoroacetic acid (10 μL, 130 μmol) were added to the reaction mixture. The reaction was allowed to sit at rt overnight. The resulting *S*-aroylthiooxime functionalized polymer was isolated *via* precipitation into diethyl ether.

General procedure for preparation of micelles

A scintillation vial equipped with a stir bar was charged with polymer (10 mg) and THF (3 mL). Distilled water (3.0 mL) was added to the polymer solution in one portion, and the solution was allowed to stir for 15 min afterwards. The solution was transferred to dialysis tubing (6-8 kD MWCO) and dialyzed against distilled water (1 L) for 18 h, changing the water once after 2 h and again after 4 h. The resulting aqueous solution was removed from the dialysis tubing and diluted with distilled water to a final volume of 10.0 mL (1 mg/mL polymer concentration).

Measuring H_2S release kinetics by methylene blue

Reactions for kinetic studies were run in quadruplicate, with each reaction vial containing 20 μL of phosphate buffer (1 M in H_2O, pH = 7), 250-288 μL micelle solution (to reach 250 μM SATO

groups), 100 µL of $Zn(OAc)_2$ solution (40 mM in H_2O), 20 µL of cysteine solution (100 mM in H_2O), and DI H_2O to reach 2 mL total volume. Final concentrations were 250 µM SATO functional groups (0.125 – 0.144 mg/mL polymer concentrations), 2 mM $Zn(OAc)_2$, and 1 mM cysteine. A blank vial was run for each experiment containing DI H_2O instead of SATO solution. At predetermined timepoints, 100 µL aliquots were taken from each vial and diluted with 100 µL of $FeCl_3$ solution (30 mM in 1.2 M HCl) and 100 µL of *p*-phenylene diamine solution (20 mM in 7.2 M HCl). Each aliquot solution remained sealed in a microcentrifuge tube for a minimum of 24 h prior to addition of 250 µL to a 96-well plate. The absorbance for each aliquot was measured at 750 nm using a plate reader.

3.9 Supporting Information:

Synthesis of 2-methyl-2-(dodecylsulfanylthiocarbonyl)sulfanyl propanoic acid (CTA)

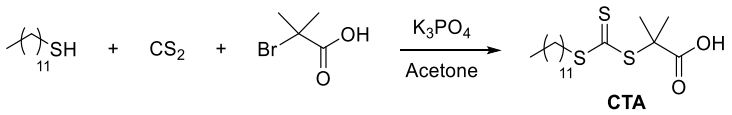

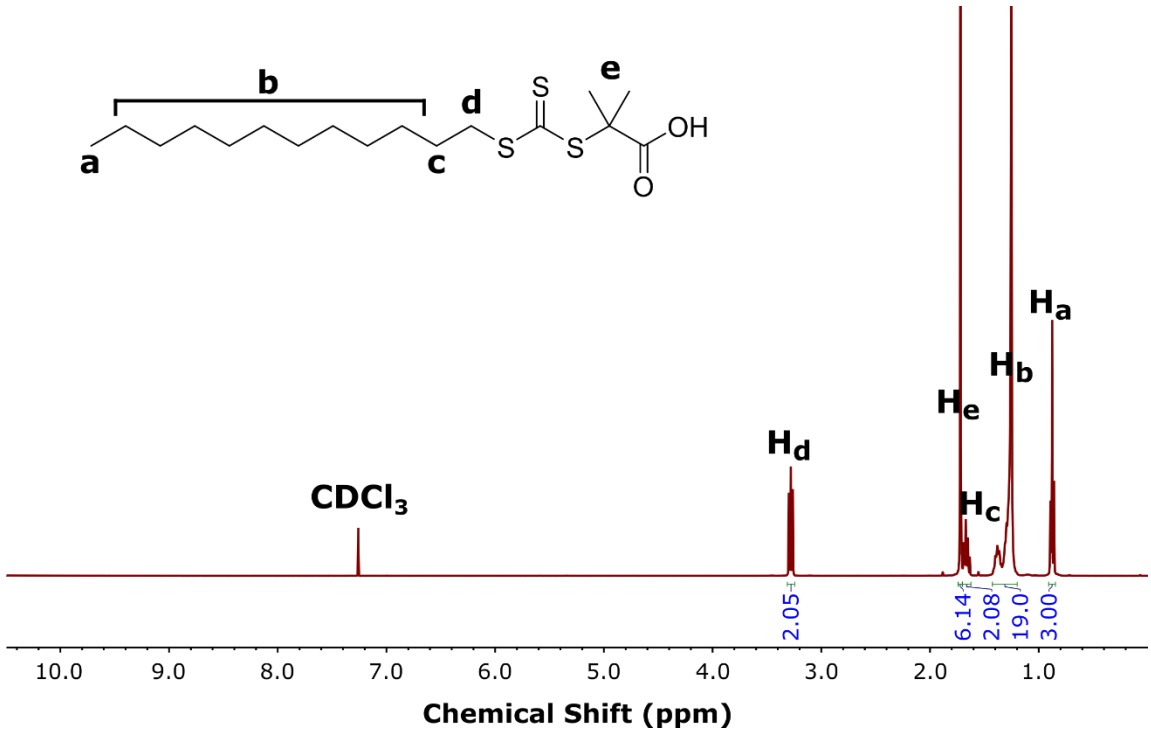

Figure S1. ^{1}H NMR spectrum of 2-methyl-2-(dodecylsulfanylthiocarbonyl)sulfanyl propanoic acid **(CTA)**.

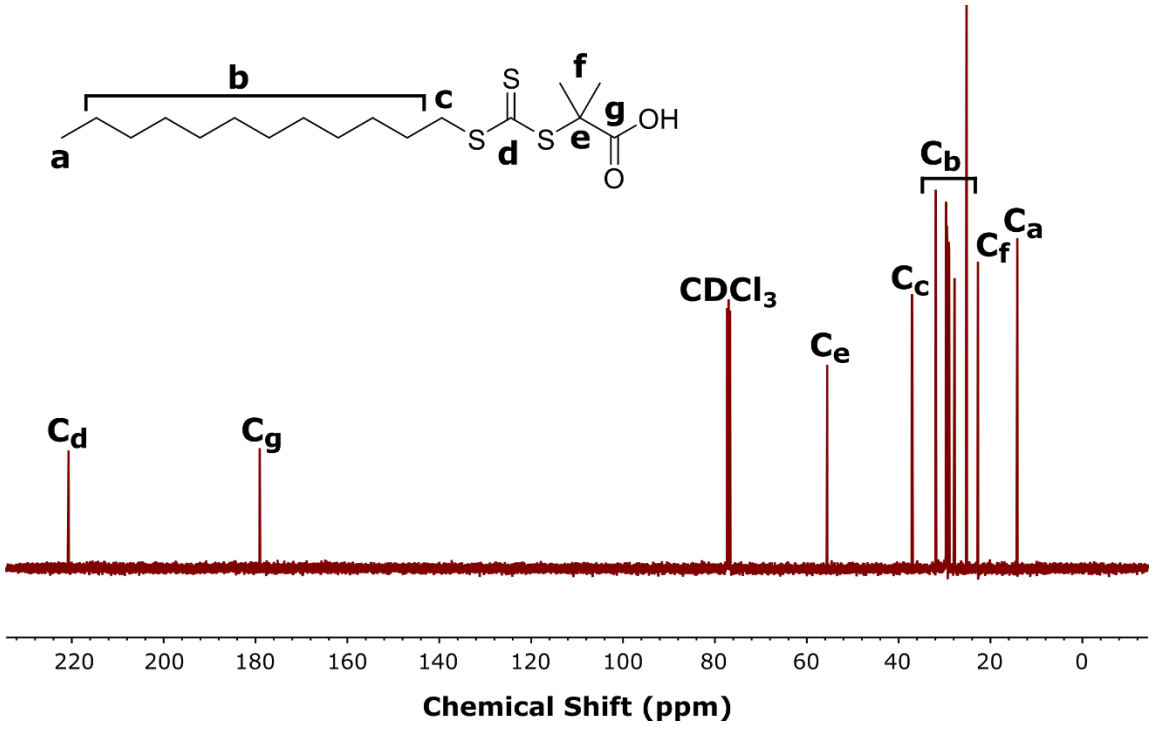

Figure S2. ^{13}C NMR spectrum of 2-methyl-2-(dodecylsulfanylthiocarbonyl)sulfanyl propanoic acid **(CTA)**.

Synthesis of MacroCTA

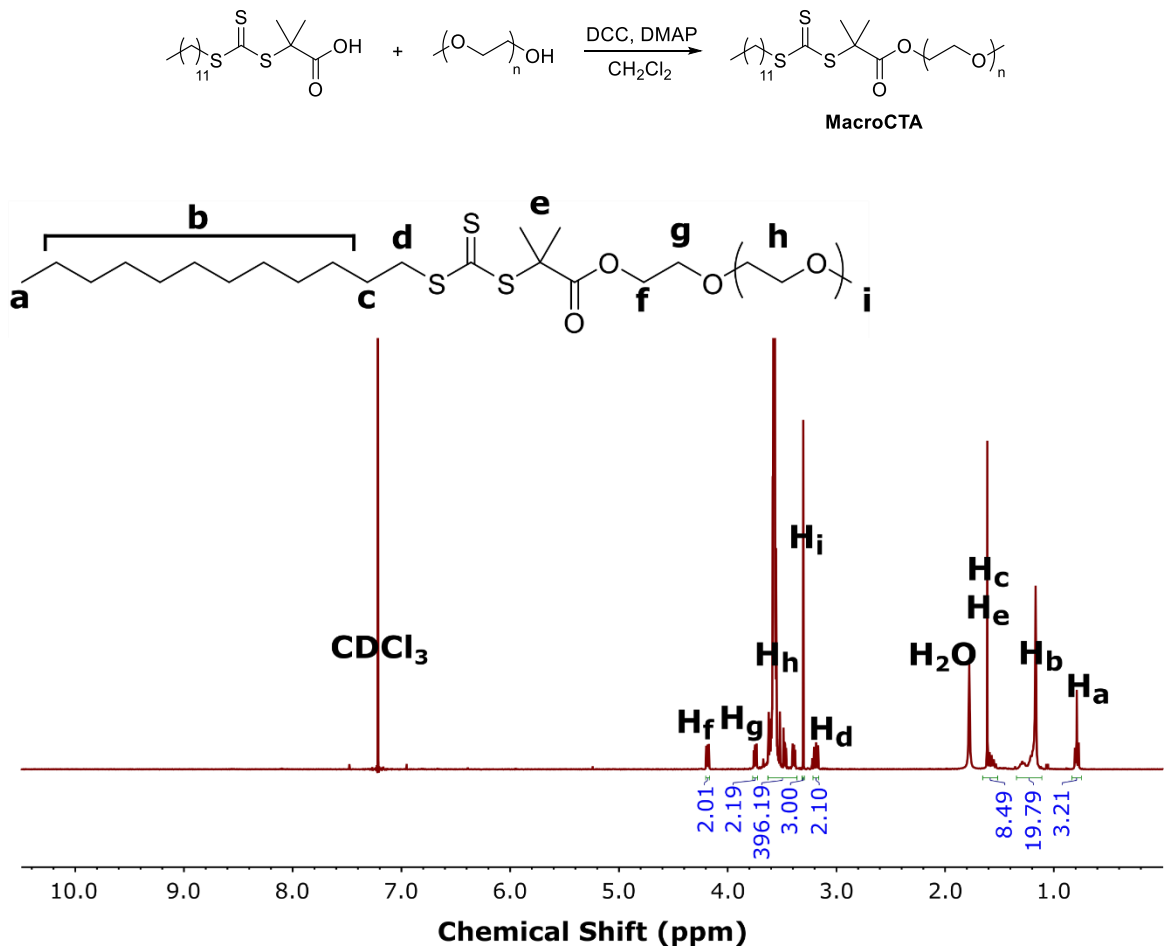

Figure S3. ^{1}H NMR spectrum of PEG-(2-methyl-2-(dodecylsulfanylthiocarbonyl)sulfanyl propanoic acid) **(MacroCTA)**.

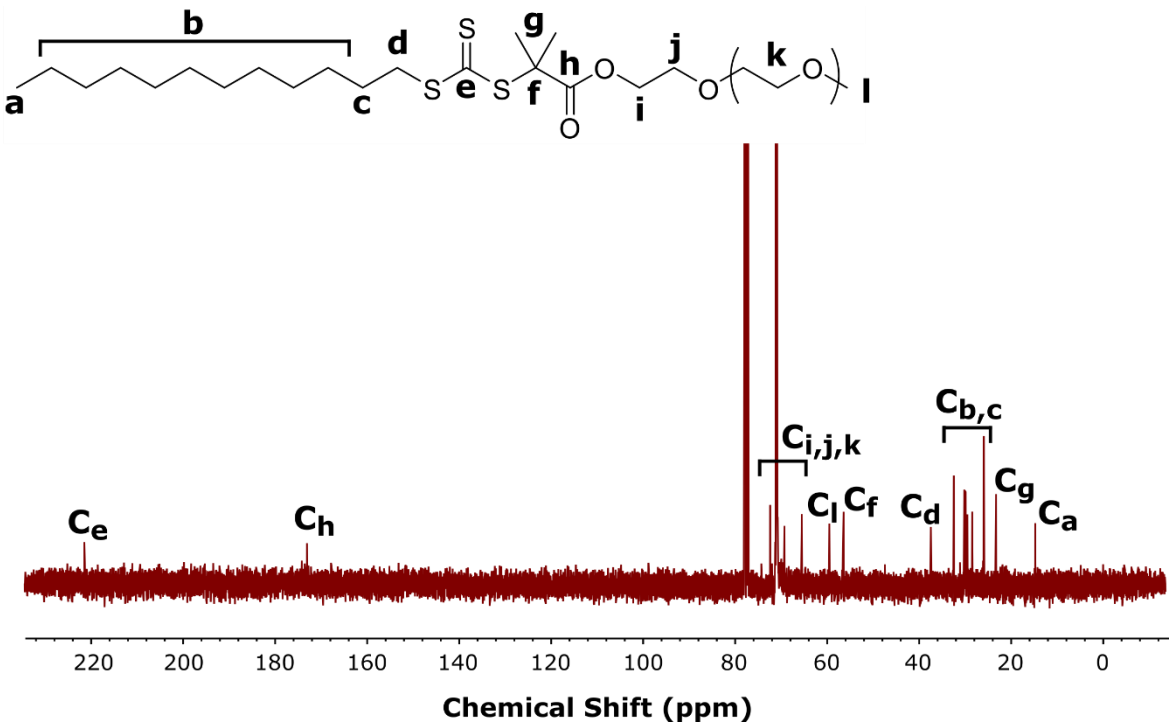

Figure S4. ^{13}C NMR spectrum of PEG-(2-methyl-2-(dodecylsulfanylthiocarbonyl)sulfanyl propanoic acid) **(MacroCTA)**.

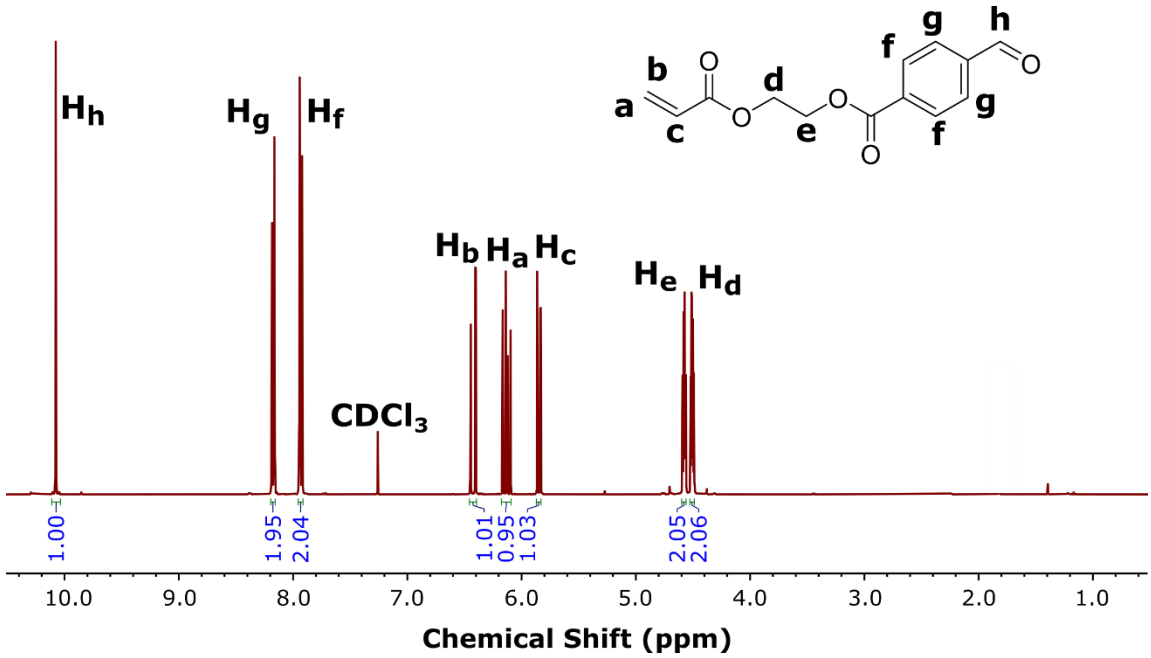

Figure S5. ^{1}H NMR spectrum of 2-(4-formylbenzoyloxy)ethyl acrylate (**FBEA**).

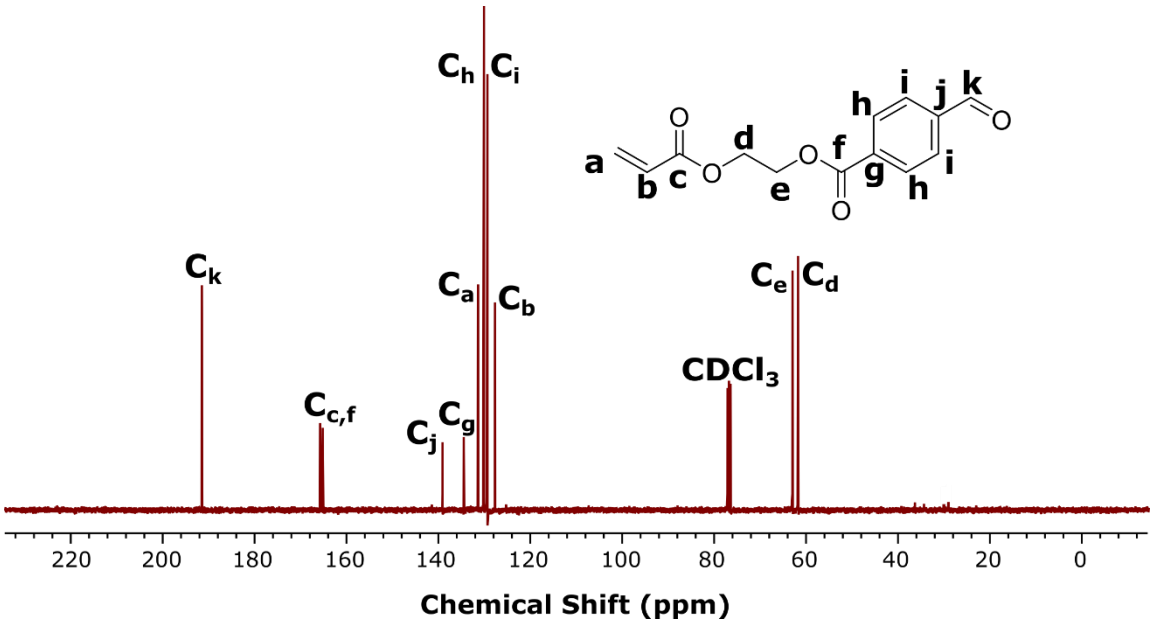

Figure S6. ^{13}C NMR spectrum of 2-(4-formylbenzoyloxy)ethyl acrylate (**FBEA**).

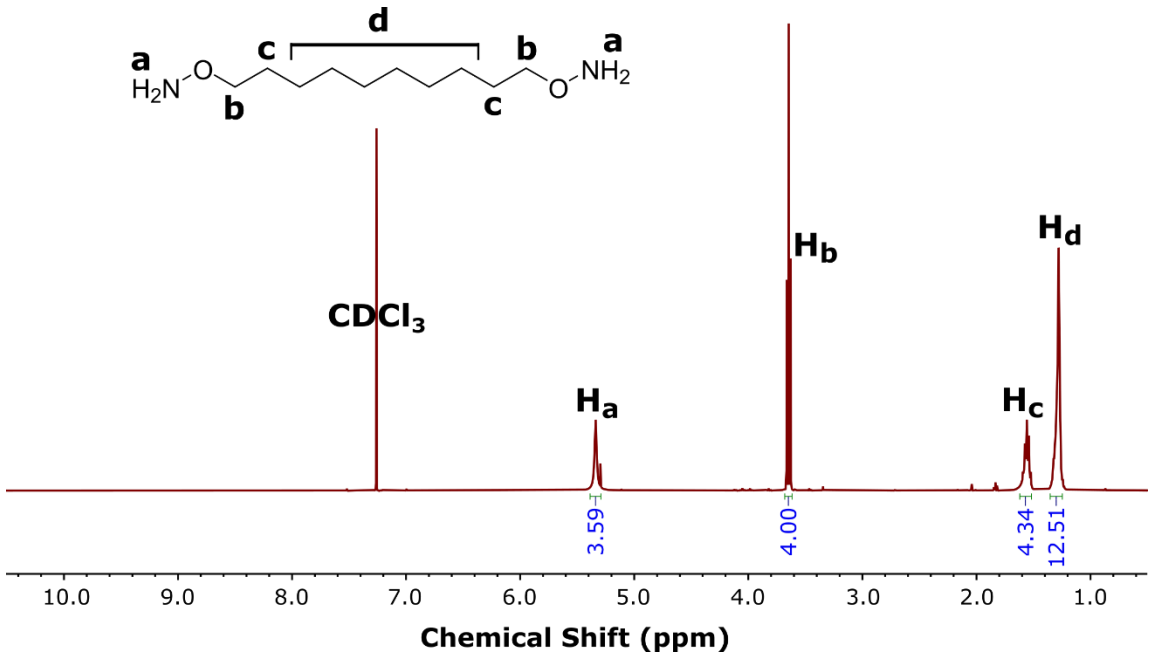

Figure S7. ^{1}H NMR spectrum of 1,10-bis(hydroxylamino)decane (**BHA**).

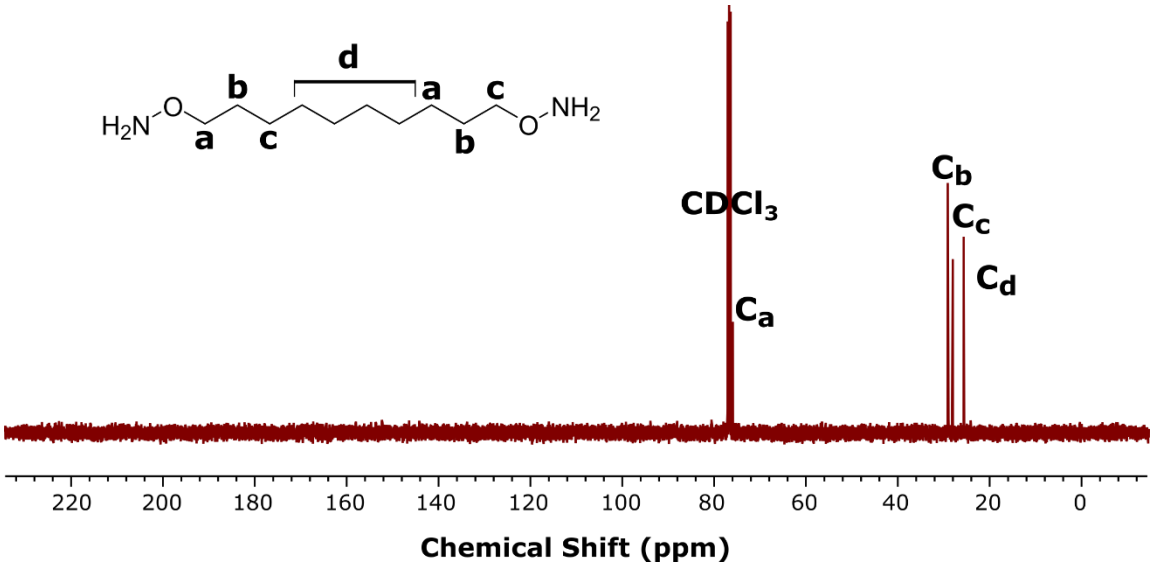

Figure S8. ^{13}C NMR spectrum of 1,10-bis(hydroxylamino)decane (**BHA**).

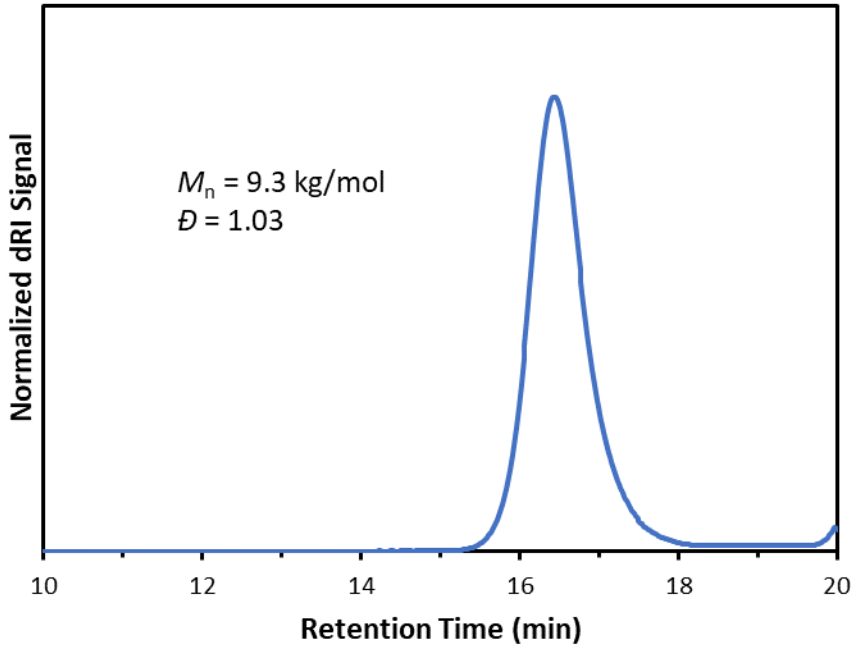

Figure S9. SEC trace of P(FBEA).

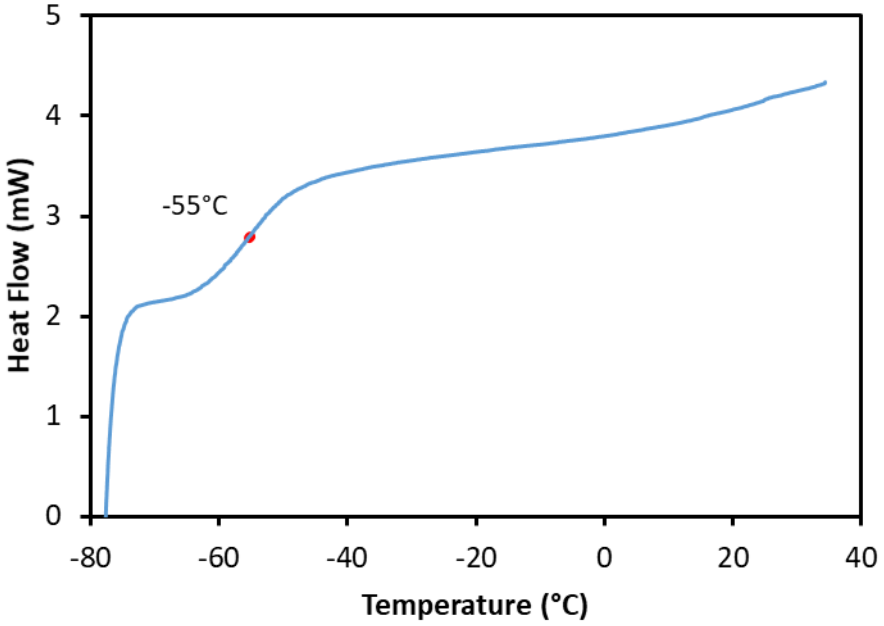

Figure S10. DSC trace of P(FBEA). Second heating cycle shown.

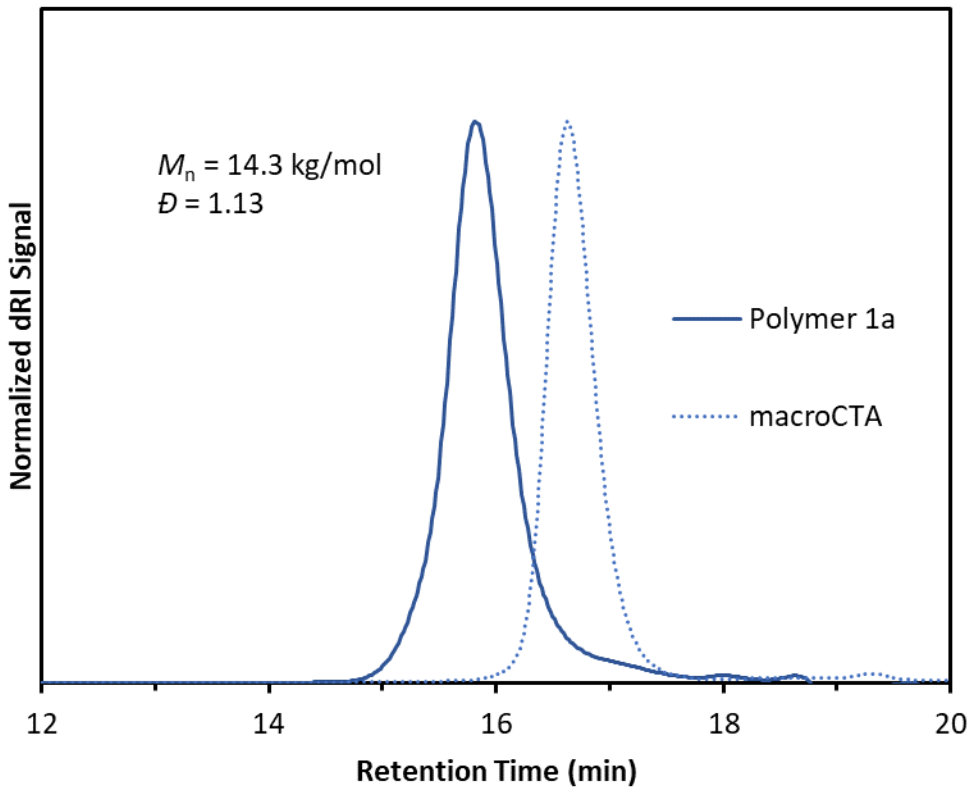

Figure S11. SEC trace of PEG-*b*-FBEA (**Polymer 1a**) and macroCTA.

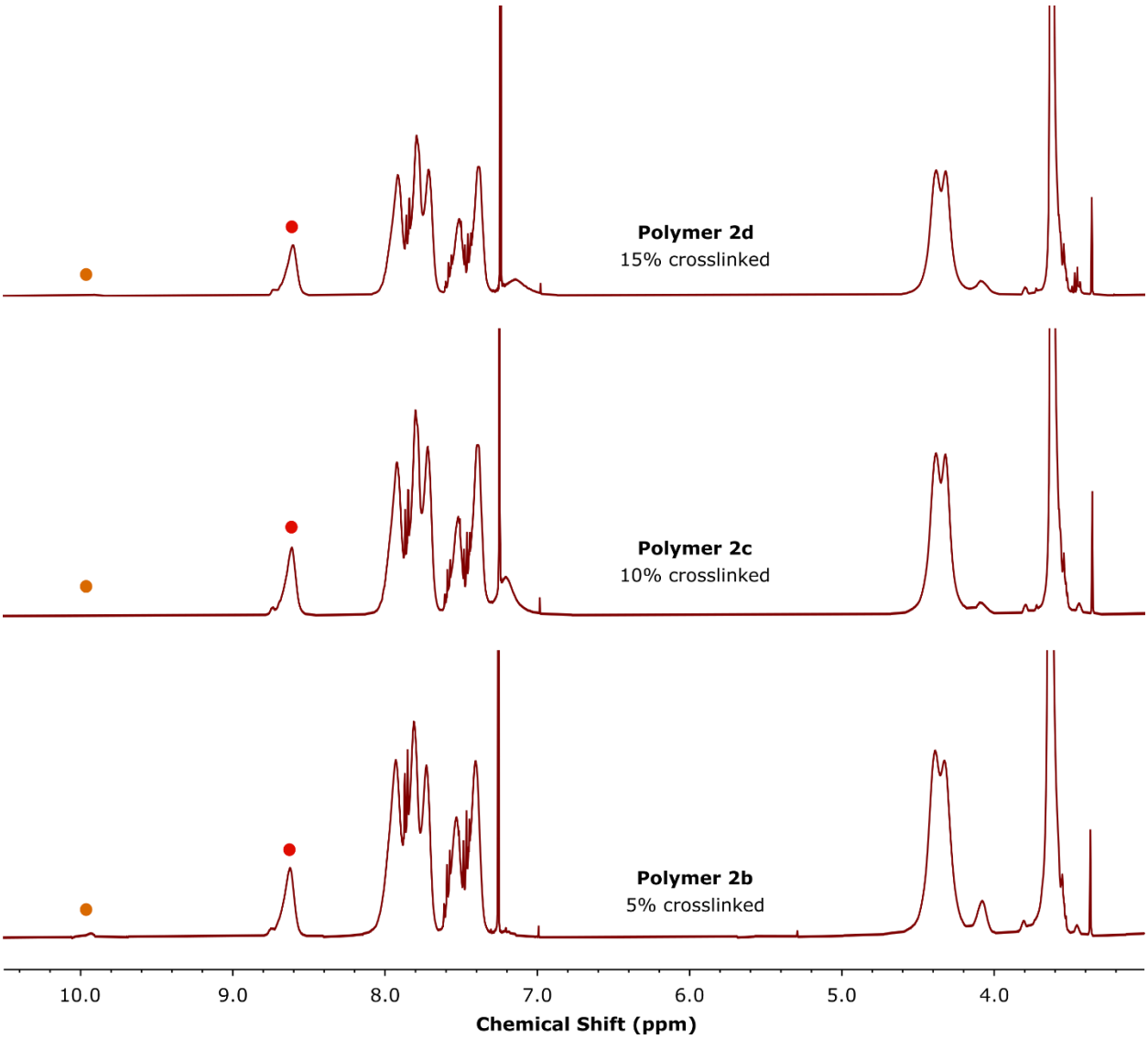

Figure S12. 1D ^{1}H NMR spectra of crosslinked polymer clusters of PEG-*b*-P(FBEA-SATO) (**Polymers 2b-d**), showing the disappearance of aldehyde proton signal (labeled with orange circle) and emergence of SATO proton signal (labeled with red circle).

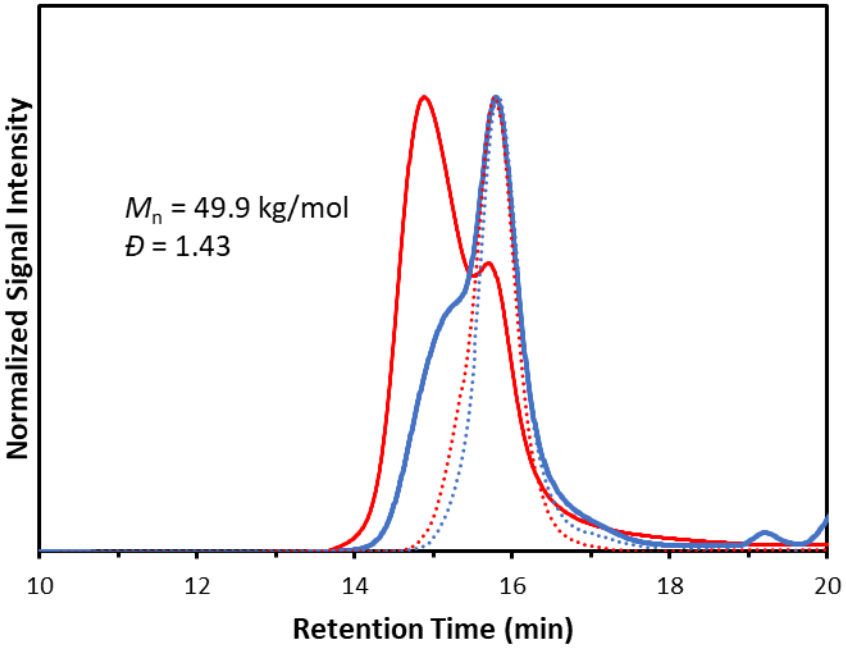

Figure S13. SEC traces of **Polymer 1a** (dotted lines) and **Polymer 1b** (solid lines) showing light scattering signal in red and differential refractive index signal in blue.

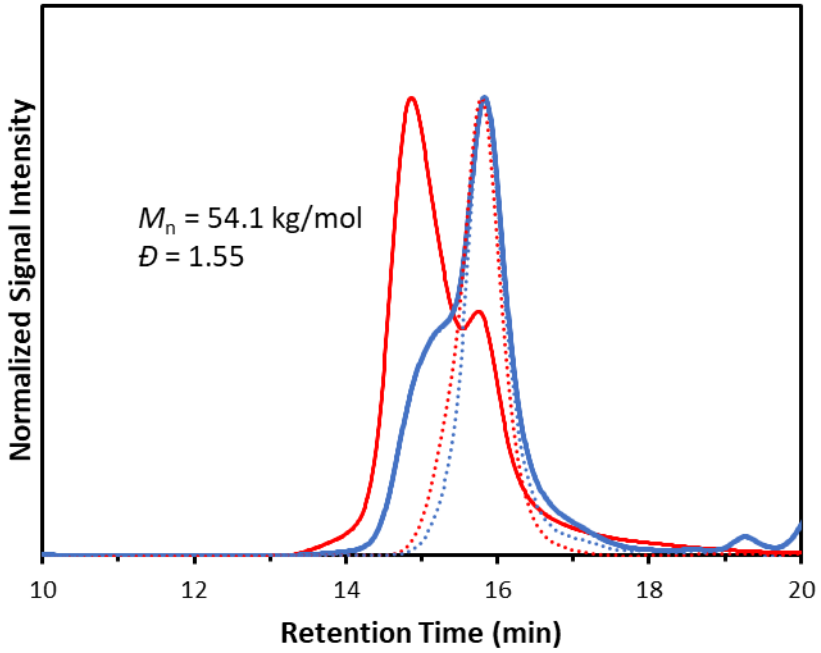

Figure S14. SEC traces of **Polymer 1a** (dotted lines) and **Polymer 1c** (solid lines) showing light scattering signal in red and differential refractive index signal in blue.

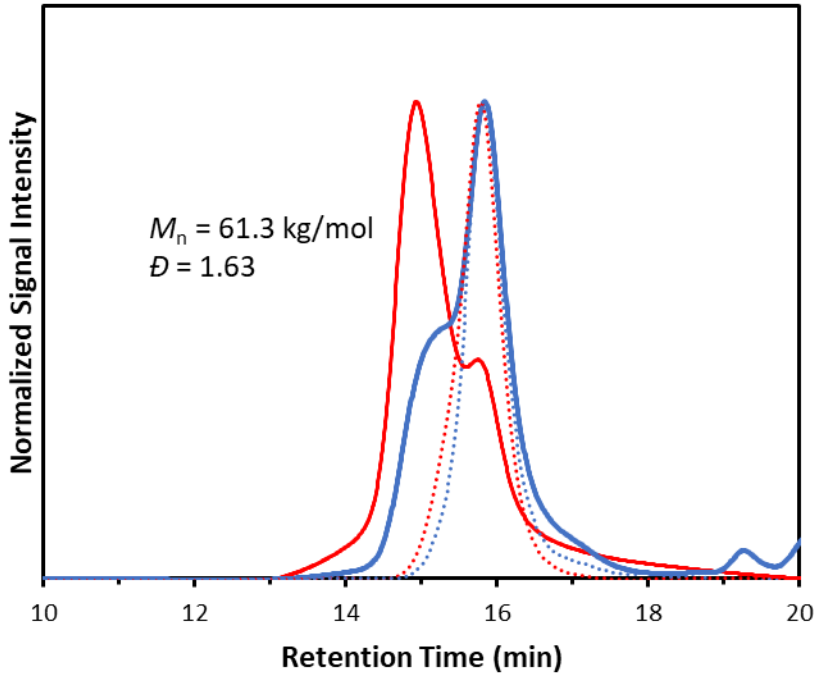

Figure S15. SEC traces of **Polymer 1a** (dotted lines) and **Polymer 1d** (solid lines) showing light scattering signal in red and differential refractive index signal in blue.

Discussion of SEC traces:

The SEC traces of **Polymers 1b-d** are bimodal, signifying the presence of uncrosslinked polymer chains in addition to crosslinked polymer clusters. The differential refractive index (dRI) traces show a large concentration of uncrosslinked polymer relative to crosslinked polymer clusters, which appear as a peak emerging off the leading edge of the native polymer peak. The dRI peak denoting polymer clusters grows with increasing crosslinking percentage, signifying the formation of more polymer clusters at higher crosslinking percentages. The polymer cluster peak also increases relative to the uncrosslinked polymer peak with increasing crosslinking percentage in the light scattering (LS) traces, reinforcing that there are more polymer clusters at higher crosslinking percentages. The signal from polymer clusters is more pronounced in the LS traces

versus the dRI traces as the LS signal is proportional to both mass and concentration while the dRI signal is not influenced by mass. The molecular weight for **Polymers 1b-d** increases from 49.9 kg/mol to 61.3 kg/mol with increasing crosslinking percentage. Importantly, all crosslinked polymers exhibit much larger molecular weights than the uncrosslinked polymer at 14.3 kg/mol, suggesting the clusters consist of multiple crosslinked polymer chains (i.e. dimers, trimers, and tetramers).

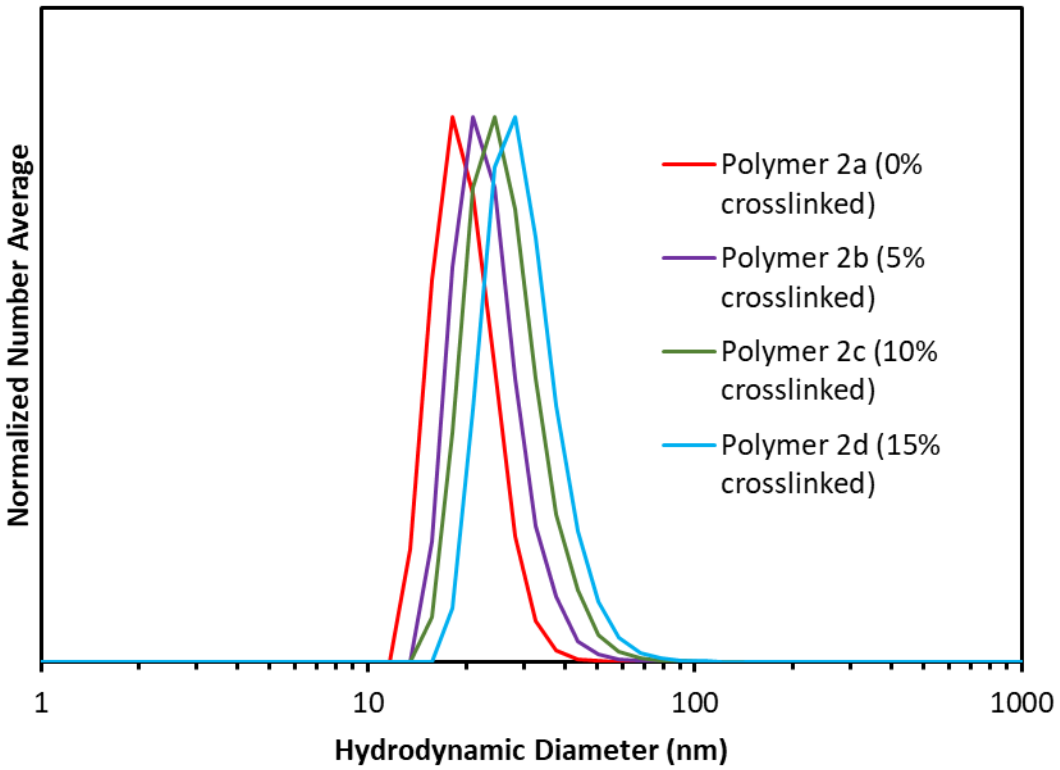

Figure S16. DLS traces showing number-average micelle sizes for micelle solutions at 0.1 mg/mL prepared from **Polymers 2a-d**.

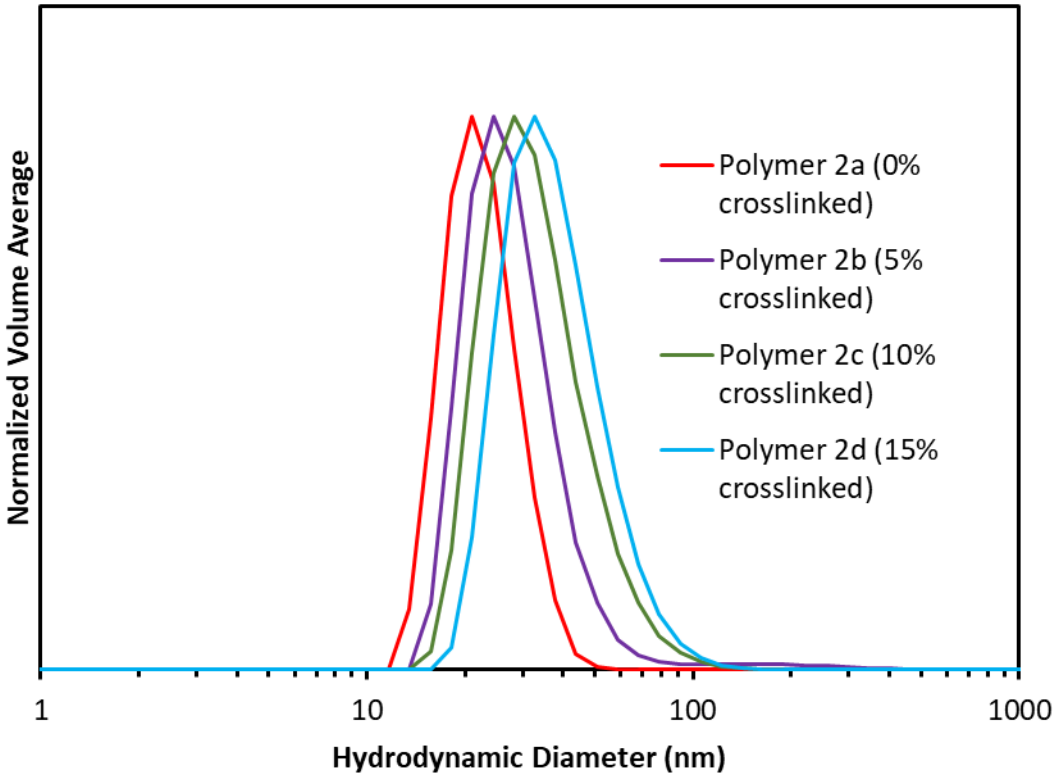

Figure S17. DLS traces showing volume-average micelle sizes for micelle solutions at 0.1 mg/mL prepared from **Polymers 2a-d**.

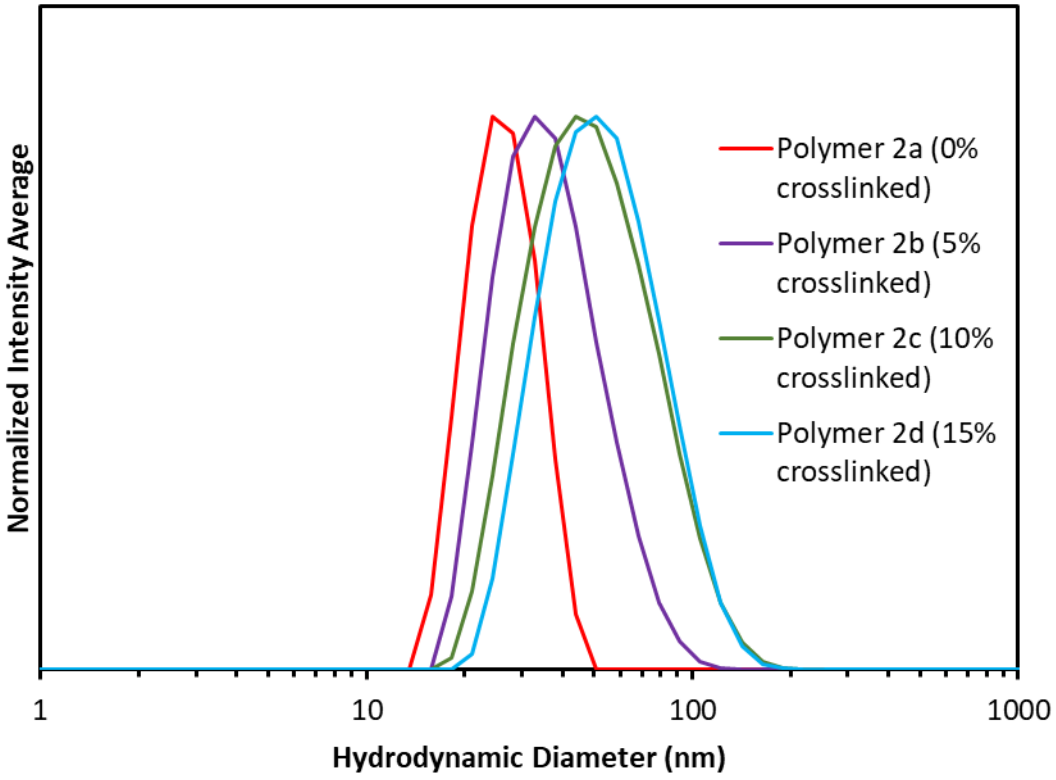

Figure S18. DLS traces showing intensity-average micelle sizes for micelle solutions at 0.1 mg/mL prepared from **Polymers 2a-d**.

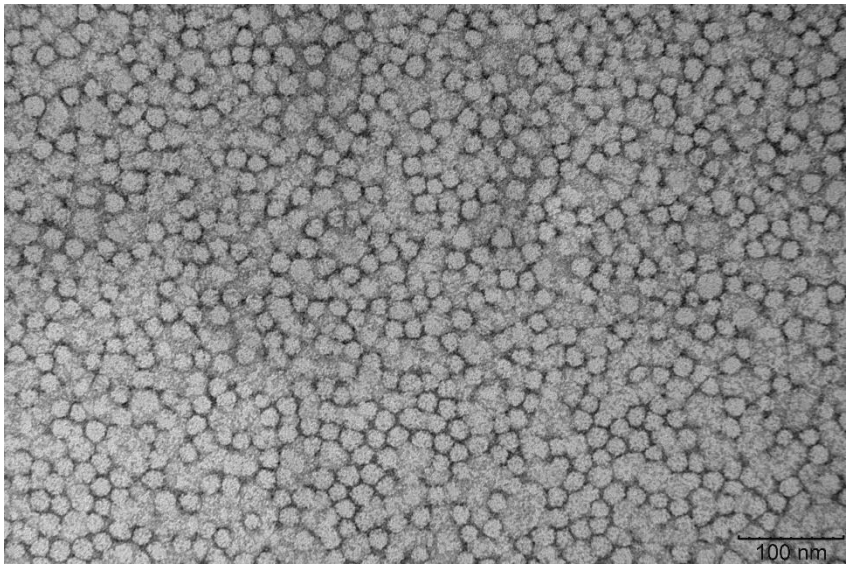

Figure S19. TEM image showing spherical micelles prepared from **Polymer 2a**.

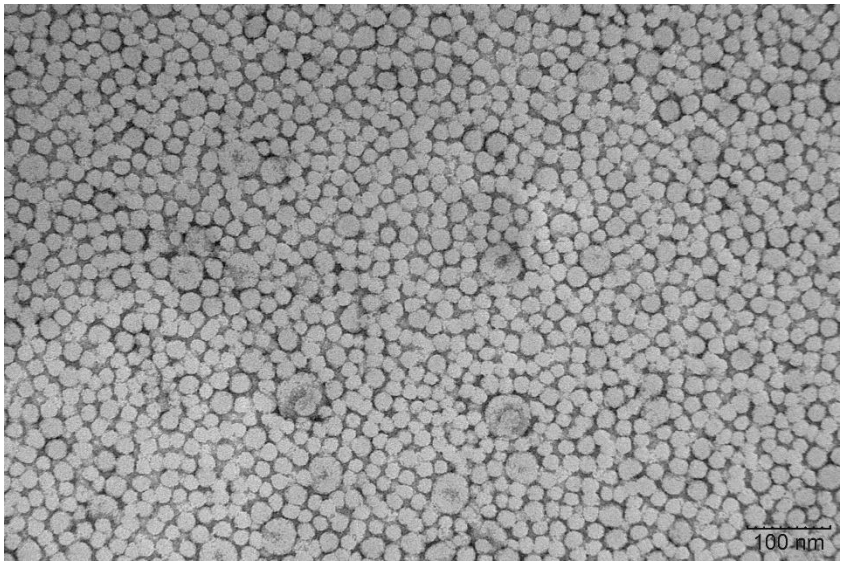

Figure S20. TEM image showing spherical micelles prepared from **Polymer 2b**.

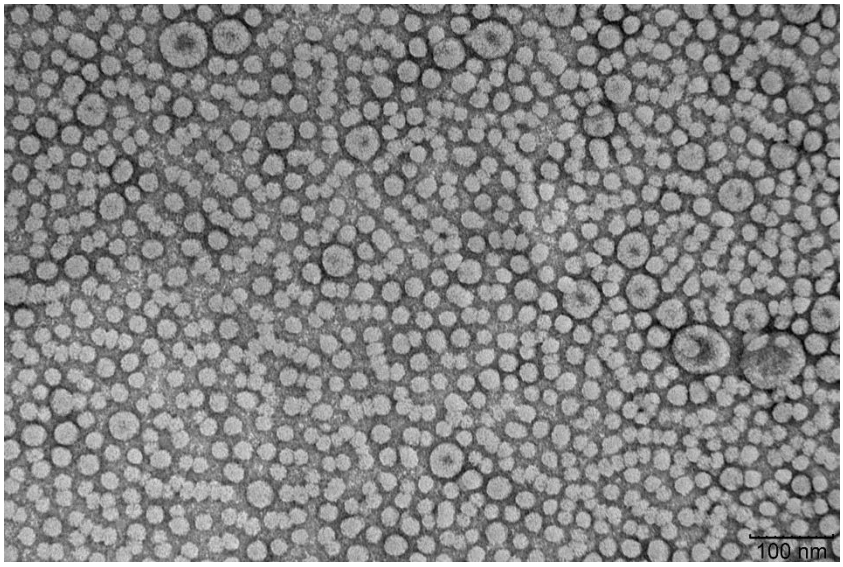

Figure S21. TEM image showing spherical micelles prepared from **Polymer 2c**.

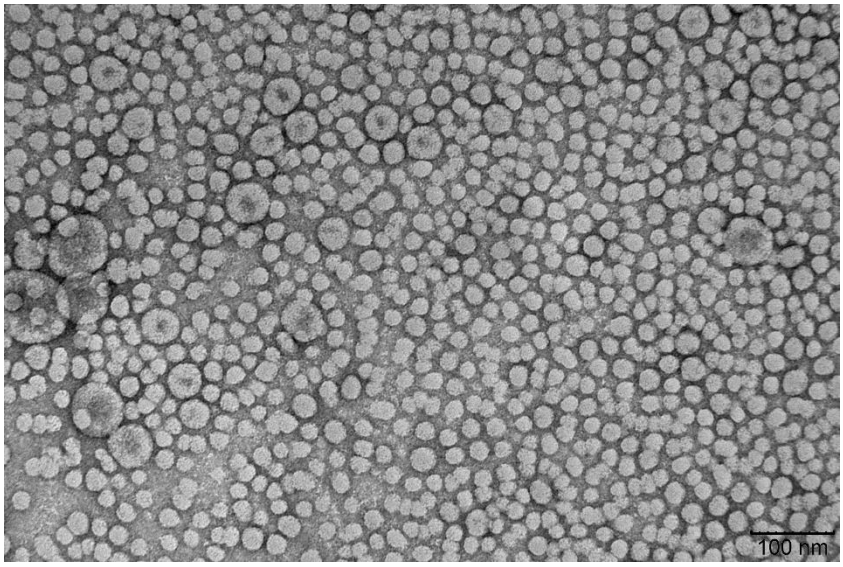

Figure S22. TEM image showing spherical micelles prepared from **Polymer 2d**.

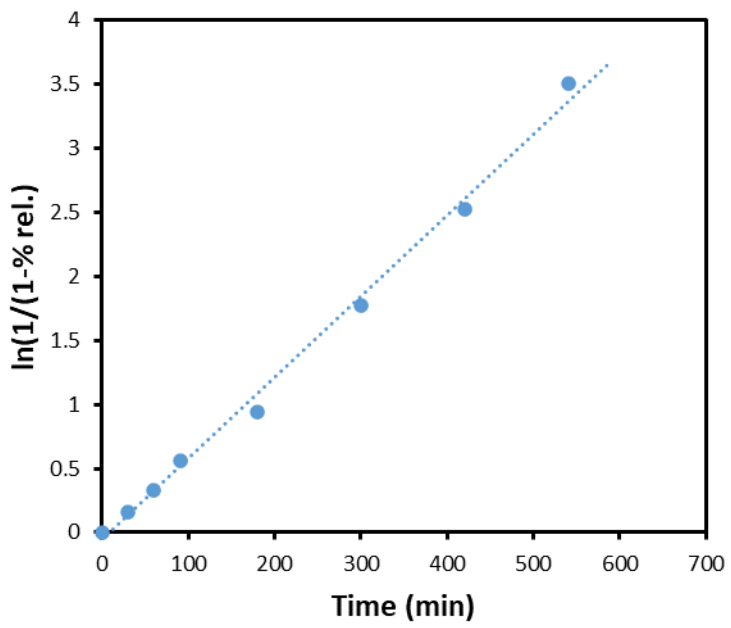

Figure S23. H_2S release from **Polymer 2a** as measured by methylene blue assay.

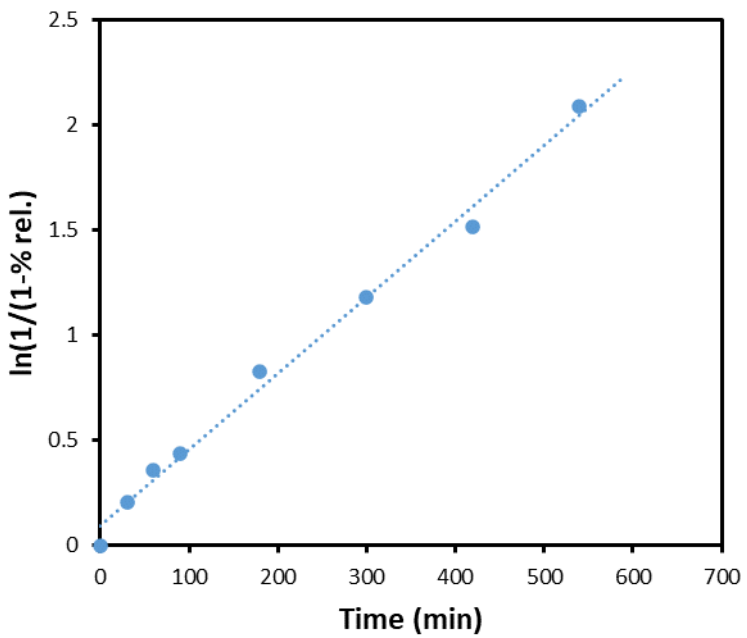

Figure S24. H_2S release from **Polymer 2b** as measured by methylene blue assay.

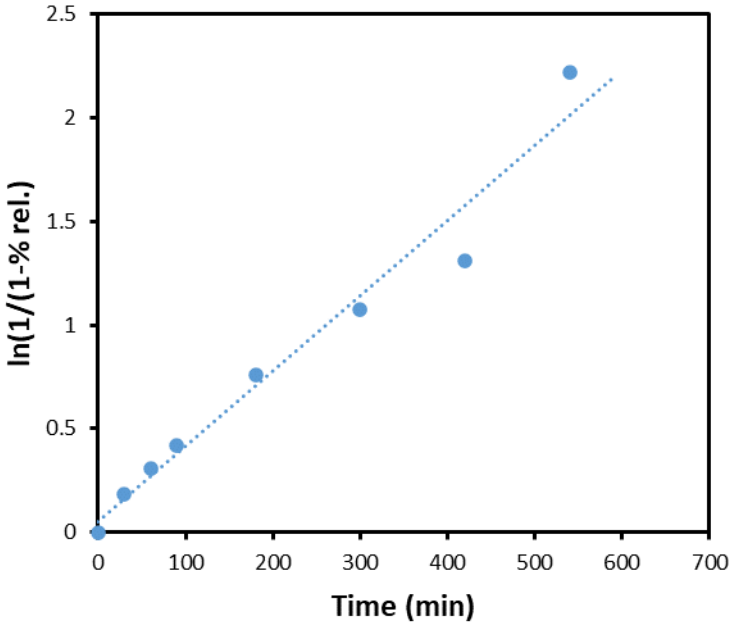

Figure S25. H_2S release from **Polymer 2c** as measured by methylene blue assay.

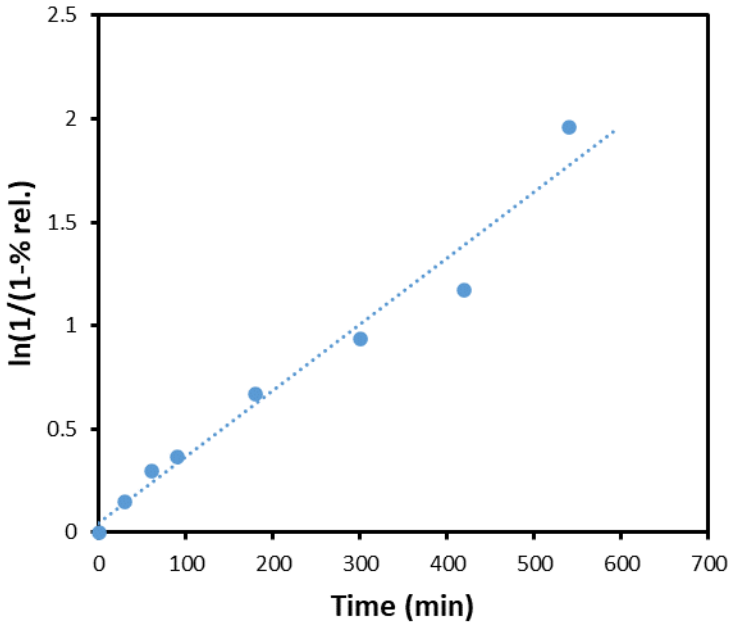

Figure S26. H_2S release from **Polymer 2d** as measured by methylene blue assay.

Scheme S1. H_2S release from SATOs.[a]

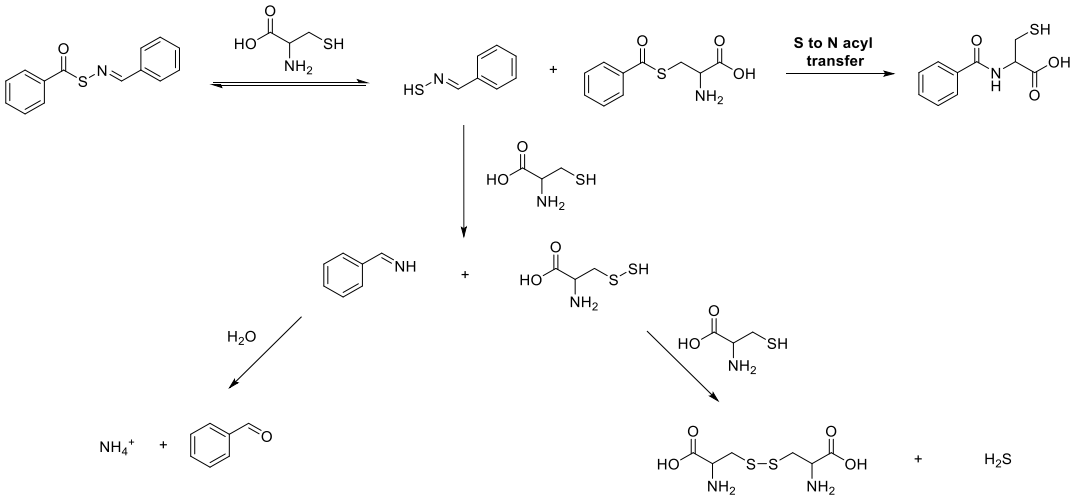

[a]Proposed mechanism of H_2S release from SATOs determined via product analysis.[5]

3.10 Supporting Information References:

1. Skey, J.; O'Reilly, R. K., *Chem. Comm.* **2008**, (35), 4183-4185.

2. Chong, D.; Tan, J.; Zhang, J.; Zhou, Y.; Wan, X.; Zhang, J., *Chem. Comm.* **2018**, *54* (56), 7838-7841.

3. Foster, J. C.; Matson, J. B., *Macromolecules* **2014**, *47* (15), 5089-5095.

4. Li, R.-Y.; Jing, L.; Meng, J.-L.; Li, G., *Asian J. Chem.* **2014**, *26* (9), 2733-2735.

5. Foster, J. C.; Powell, C. R.; Radzinski, S. C.; Matson, J. B., *Org. Lett.* **2014**, *16* (6), 1558-1561.

Chapter 4: Strong Variation of Micelle-Unimer Coexistence as a Function of Core Chain Mobility

This manuscript was submitted for publication in *Macromolecules*, and revisions are currently in progress.

4.1 Authors:

Ryan J. Carrazzone,[†,⊥] Xiuli Li,[†,⊥] Jeffrey C. Foster,[†,‡] Veera Venkata Shravan Uppala,[†] Candace E. Wall,[†] Alan R. Esker,[†] Louis A. Madsen,*[,†] and John B. Matson*[,†]

†*Department of Chemistry and Macromolecules Innovation Institute, Virginia Tech, Blacksburg, VA, 24061, United States*

‡ *Current address: Sandia National Lab, Albuquerque, NM, 87123*

⊥*These authors contributed equally to this work*

4.2 Abstract:

Polymeric micelles coexist in solution with unassembled chains (unimers). We have investigated the influence of glass transition temperature (T_g) (i.e., chain mobility) of the micelle core-forming blocks on micelle–unimer coexistence. We synthesized a series of seven PEG-*b*-P(*n*BA-*ran*-*t*BA) amphiphilic block copolymers (PEG = poly(ethylene glycol), *n*BA = *n*-butyl acrylate, *t*BA = *tert*-butyl acrylate) with similar molecular weights (12 kg/mol). Varying the *n*BA/*t*BA molar ratio enabled broad modulation of core block T_g with no significant change in core hydrophobicity or micelle size. NMR diffusometry revealed increasing unimer populations from

0% to 54% of total polymer concentration upon decreasing core block T_g from 25 to –46 °C. Additionally, unimer population at fixed polymer composition (and thus core T_g) increased with temperature. This study demonstrates the strong influence of core-forming block mobility on polymer self-assembly, providing information toward designing drug delivery systems and suggesting the need for new dynamical theory.

4.3 Introduction:

The spontaneous association of molecules by noncovalent interactions to form higher order structures, termed molecular self-assembly or simply self-assembly,[1] is pervasive throughout nature, often originating from regions of differing hydrophobicity among associating molecules. For example, key cellular components derive their structure and function largely from self-assembly, including cell membranes,[2] actin fibers,[3] and vesicles.[4] Synthetic materials, notably amphiphilic block copolymers (BCPs), also self-assemble to generate nanoscopic hydrophobic/hydrophilic domains that enable various applications ranging from delivery vehicles for hydrophobic drugs,[5-9] to scaffolds for the synthesis of unique polymer architectures,[10-12] to nanoscale compartments for catalysis.[13-14] As a result, a fundamental understanding of the parameters governing self-assembly of small molecules[15-17] and BCPs[18-19] has been established.

Amphiphilic BCPs exhibit various morphologies in bulk[20-21] and in solution,[22-23] and polymer characteristics (e.g., hydrophobicity of the core-forming block, ratio of hydrophilic to hydrophobic content, glass transition temperature (T_g) of the core-forming block) can greatly influence their self-assembly.[24-27] Beyond polymer characteristics, solution composition and preparation technique also can dramatically impact self-assembly.[19, 28-30] However, despite the vast

amount of research investigating the morphologies and self-assembly processes of amphiphilic BCPs, there is limited information on the equilibrium between nanostructures and free polymer chains in solution (unimers). This gap in the field is due in part to the typically low concentration of unimers relative to associated polymer chains in amphiphilic BCP systems; unimer concentration is usually assumed to be equal to the critical micelle concentration (CMC),[31] which is generally below the detection limits of common characterization techniques.[32-34] Furthermore, unimer populations can significantly impact the pharmacokinetics and biodistribution of amphiphilic BCPs.[35-37] As a result, there is growing interest in developing techniques to reliably quantify unimer populations.

One technique well suited for quantifying unimer populations in micelles is pulsed-field-gradient NMR diffusometry. This NMR technique is nondestructive and enables sensitive determination of diffusion coefficients for various mobile species in solution and in solid materials. Furthermore, NMR diffusometry can track species with molecular and elemental specificity and thus has been used to observe multiple diffusing species in a wide range of polymeric systems.[38-44] Relevant to this work, NMR diffusometry experiments can measure unimer and micelle populations for BCP systems.[33-34]

In this work, we aimed to investigate the influence of core block mobility (and thus T_g) on the micelle–unimer equilibrium by synthesizing a series of BCPs containing hydrophobic blocks of similar hydrophobicity but varying chain flexibility. This series of BCPs could then be analyzed by NMR diffusometry to observe the change in unimer populations as a function of two key thermodynamic variables—hydrophobic block composition and temperature. Ultimately, we envisioned that this systematic study of unimer–micelle coexistence would reveal how core block

mobility affects unimer populations, which could inform polymer micelle design for a variety of applications.

4.4 Results and Discussion:

Micelle core characteristics strongly impact the overall properties of a self-assembled structure, including effects such as influencing drug loading,[45] enabling fluorescent response,[46] and controlling release of active pharmaceutical ingredients.[47] Based on these findings, we hypothesized that a relationship between the T_g of the hydrophobic, core-forming block and micelle–unimer coexistence might exist. To test this hypothesis, we needed to prepare a series of BCPs with identical hydrophilic blocks but with hydrophobic blocks that had varying T_g's but were otherwise similar in terms of molecular weight and hydrophobicity. To achieve this goal, we turned to copolymerization, a technique that has long been recognized as an effective method for modifying the T_g of polymers.[48-49] We expected that copolymerizing two monomers with similar hydrophobicity but with greatly different polymer T_g's would allow for fine tuning of the core-forming block T_g. Two acrylate monomers, *n*-butyl acrylate (*n*BA) and *tert*-butyl acrylate (*t*BA), have similar partition coefficients (an indicator of hydrophobicity) but T_g's of –50 °C and 50 °C, respectively.[50-51] The isomeric *n*BA and *t*BA monomers also have reactivity ratios near 1.00 in radical copolymerization, enabling ideal random copolymerization behavior.[52] Therefore, we synthesized a series of BCPs containing poly(ethylene glycol) hydrophilic blocks and statistical copolymers of poly(*n*BA) and poly(*t*BA) as the hydrophobic blocks (Scheme 4-1).

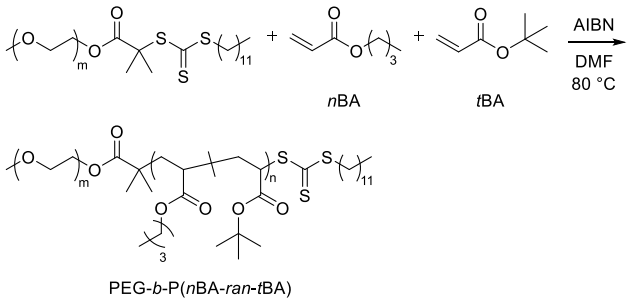

Scheme 4-1. Preparation of PEG-*b*-P(*n*BA-*ran*-*t*BA) BCPs.

We prepared this series of BCPs with varying core block composition in two steps. First, we synthesized a large batch of trithiocarbonate-terminated PEG to serve as the hydrophilic block in each of the BCPs (PEG M_n = 4 kg/mol). The trithiocarbonate unit served as a chain transfer agent (CTA) for reversible addition–fragmentation chain-transfer (RAFT) polymerization to control molecular weight. In the second step, we synthesized seven BCPs with varying *n*BA/*t*BA molar ratios by RAFT polymerization from the PEG CTA, yielding BCPs **1a–g**. By monitoring monomer disappearance over time, we found *n*BA and *t*BA were consumed at the same rate (Figure S25), confirming that the feed ratio and composition ratio were identical. We kept the hydrophilic/hydrophobic ratio constant while systematically changing the *n*BA/*t*BA molar ratio, resulting in a consistent BCP M_n near 12 kg/mol throughout the series (Table 4-1).

Table 4-1. Characterization of PEG-*b*-P(*n*BA-*ran*-*t*BA) block copolymers.

Polymer	Mol % *n*BA[a]	M_n (NMR) (kg/mol)[b]	M_n (GPC) (kg/mol)[c]	$Đ$[c]	T_g (°C)[d]	D_h (nm)[e]	N_{agg}[f]
Polymer						Micelle	
1a	100	12.0	12.2	1.07	-46	25.1 ± 0.1	83
1b	75	11.3	12.6	1.07	-35	28.9 ± 0.1	103
1c	60	11.9	11.9	1.12	-24	27.9 ± 0.1	101
1d	50	12.1	13.3	1.10	-20	26.2 ± 0.2	80
1e	40	11.6	11.7	1.11	-6	27.1 ± 0.6	77
1f	25	12.6	12.9	1.08	5	27.0 ± 0.2	87
1g	0	11.6	11.8	1.05	25	26.2 ± 0.5	72

[a]*n*BA/*t*BA molar ratio measured by ^{1}H NMR spectroscopy. [b]Measured by end-group analysis *via* ^{1}H NMR spectroscopy (Figures S14-20). [c]Measured by SEC in THF at 30 °C with multi-angle light scattering (Figures S4-10). [d]Of the hydrophobic block measured by DSC with a modulated heating rate (3 °C/min, ±2.5 °C, 60 s); data reported from second heat cycle (Figures S26-33). [e]Intensity average hydrodynamic diameter measured by dynamic light scattering (DLS) at 5 mg/mL in DI H_2O at rt (Figure S36). [f]Aggregation number derived by dividing M_w of micelle by M_w of BCP; M_w of micelles determined by SLS at 5 mg/mL in DI H_2O at rt (Figure S37, Equation S1).

We then evaluated each BCP by differential scanning calorimetry (DSC) to measure T_g's of the hydrophobic blocks (Figures S26-33). As shown in Table 4-1 and Figure 4-1, the T_g's for the hydrophobic blocks of polymers **1a** (100% *n*BA) and **1g** (100% *t*BA) were –46 °C and 25 °C, respectively. The 100% *t*BA BCP (polymer **1g**) showed a lower T_g than the reported value of 50 °C.[51] We attribute this discrepancy to the relatively low molecular weight of the *t*BA block and the PEG tethered to one chain end, both of which may reduce T_g. The T_g values of the hydrophobic block for BCPs **1b**–**1f** (25–75% *n*BA) closely fit approximations based on the Fox equation.[48]

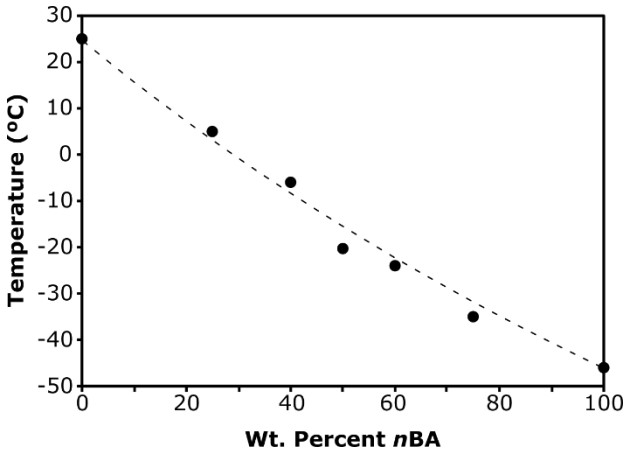

Figure 4-1. T_g for core-forming blocks of polymers **1a–g** (black circles) based on *n*BA/*t*BA molar ratio in the BCPs measured by DSC with a modulated heating rate (3 °C/min, ±2.5 °C, 60 s). The dotted black line represents a fit using the Fox equation (Equation S2) to the measured homopolymer T_g's. The core-forming block T_g varies predictably with polymer composition, providing access to a wide range of micelle core mobilities.

Having established that copolymerization of *n*BA and *t*BA could lead to polymers with predictable T_g values, we next aimed to confirm that copolymerization did not change the core-forming block hydrophobicity. We evaluated hydrophobicity through contact angle measurements of representative polymer films of poly(*n*BA-*ran*-*t*BA) random copolymers that lacked the hydrophilic PEG block.

First, we synthesized random copolymers of *n*BA and *t*BA using RAFT with a trithiocarbonate CTA (Figures S11-13). We chose *n*BA/*t*BA molar ratios of 1:0, 1:1, and 0:1 (polymers **2a**, **2b**, and **2c**, respectively) to span the entire series. We then prepared uniform films of polymers **2a**–**c** by spin coating from $CHCl_3$, followed by overnight drying to remove solvent. The initial contact angle of water changed from 95° for polymer **2a** (Figure 4-2A) to 100° for

polymer **2b** (Figure 4-2B) to 95° for polymer **2c** (Figure 4-2C). Given the typical error in contact angle measurements of a few degrees, we conclude that the hydrophobicity remains constant across the series with varying *n*BA/*t*BA molar ratios. Thus, we expect that hydrophobicity of the core-forming block for polymers **1a**–**g** also does not change across the series. We also evaluated the hydrophobicity of polymers **2a** and **2c** through NMR solubility experiments. We found that P*n*BA was more soluble than P*t*BA in D_2O by a factor of 2.5, but both polymers exhibited extremely hydrophobic character (Figures S34 and S35). The solubility of PEG in water at room temperature is around 60 wt%,[53] which is a factor of ~10^3 larger than the solubility of either acrylate polymer. As the solubility of the block copolymers in water will be governed primarily be the hydrophilic PEG block, we do not expect this small change in solubility to account for any differences in unimer percentages. Thus, we conclude that hydrophobicity of the core-forming block for polymers **1a**–**g** does not change across the series.

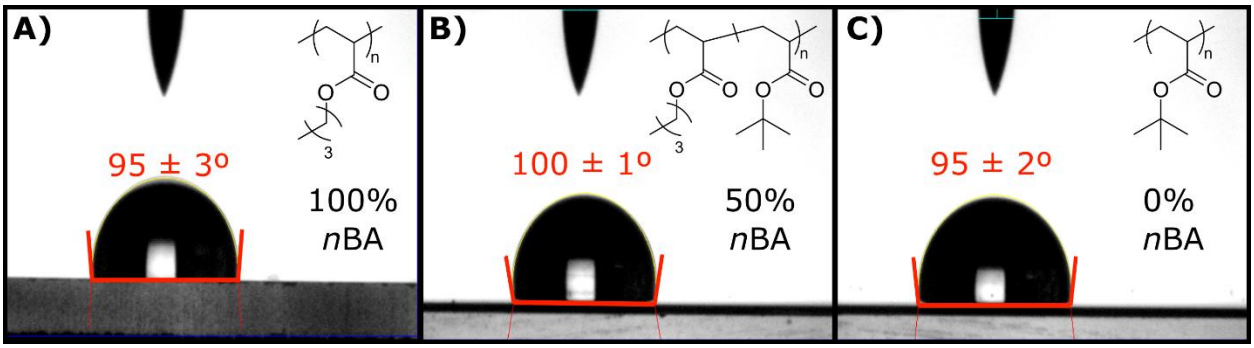

Figure 4-2. Initial contact angle measurements of water droplets on films of polymers **2a-c**. Polymer films were created by spin coating polymer solutions (5 wt% in $CHCl_3$) at 5000 rpm onto glass slides, followed by drying at 30 °C. Contact angle measurements were performed in triplicate with representative images and average results reported. The relatively consistent contact angle implies that the degree of hydrophobicity (intermolecular interactions) does not depend on *n*BA/*t*BA molar ratio.

After determining that T_g varies with the *n*BA/*t*BA molar ratio for polymers **1a**–**g**, and that the hydrophobicity of the core-forming block does not change significantly, we next sought to investigate the change in micelle–unimer coexistence across the series. To prepare micelles from each amphiphilic BCP, we used the solvent switch method. Briefly, we first dissolved each polymer in THF, a good solvent for both blocks. We then diluted these polymer solutions by dropwise addition of H_2O to generate a 12.5% THF in H_2O solution. We subsequently transferred the polymer solutions to dialysis tubing (MWCO 8 kDa) and dialyzed against H_2O.

We utilized dynamic light scattering (DLS) to analyze the micelle size distributions from each BCP formulation (Tables 4-1 and S1, Figure S36). We observed intensity-average hydrodynamic diameters ranging from 25.1 to 28.9 nm, with no apparent trend in micelle size relating to micelle core mobility. This narrow size range is expected due to the similar molecular weights and hydrophobic weight fractions of the BCPs. Additionally, we observed low micelle polydispersity indices for each sample, indicating samples were free of high molecular weight aggregates. We then employed static light scattering (SLS) to obtain the M_w of micelles in solution for each micelle sample (Figure S35). From the SLS data, we estimated the aggregation number (N_{agg}) of each sample by dividing micelle M_w by the M_w of each respective BCP (Table 4-1, Equation S1). We observed N_{agg} values ranging from 72 to 103, again with no apparent relation to micelle core mobility, reinforcing that the *n*BA/*t*BA molar ratio in the core-forming block did not influence polymer micelle size.

Despite similar micelle sizes, we expected the varying chain mobility of core-forming blocks throughout polymers **1a**–**g** to yield differences in micelle–unimer coexistence. We first investigated the mobility of the hydrophobic core blocks with 1-dimensional (1D) ^{1}H NMR

spectroscopy. In NMR spectra of polymer solutions with relatively slow chain dynamics (where spectrometer shims do not determine linewidth), the full width at half-maximum (FWHM) of peaks is inversely proportional to the spin-spin relaxation time (T_2) *via* the relation FWHM = $1/\pi T_2$. T_2 characterizes the dephasing of net magnetization in the transverse plane and provides information on molecular mobility.[33, 54] In other words, decreasing T_2 values result in broader signal linewidths, which indicate molecular environments with increasingly limited mobility. As shown in Figure 3A, *n*BA and *t*BA alkyl proton peaks appear in the range 0.5–2 ppm in spectra for BCPs **1a**, **1d**, and **1g**. For 100% *n*BA polymer micelles (polymer **1a**, shown in purple), the alkyl proton peak(s) FWHM is ≈40 Hz compared to ≈80 Hz for 50% *n*BA polymer micelles (polymer **1d**, shown in green) and ≈200 Hz for 0% *n*BA polymer micelles (polymer **1g**, shown in red). The broadening of alkyl region signals with increasing *t*BA content in the core block signifies reduced chain mobility in the micelle cores. This result agrees with the trend of increasing measured T_g for core blocks with increasing *t*BA content.

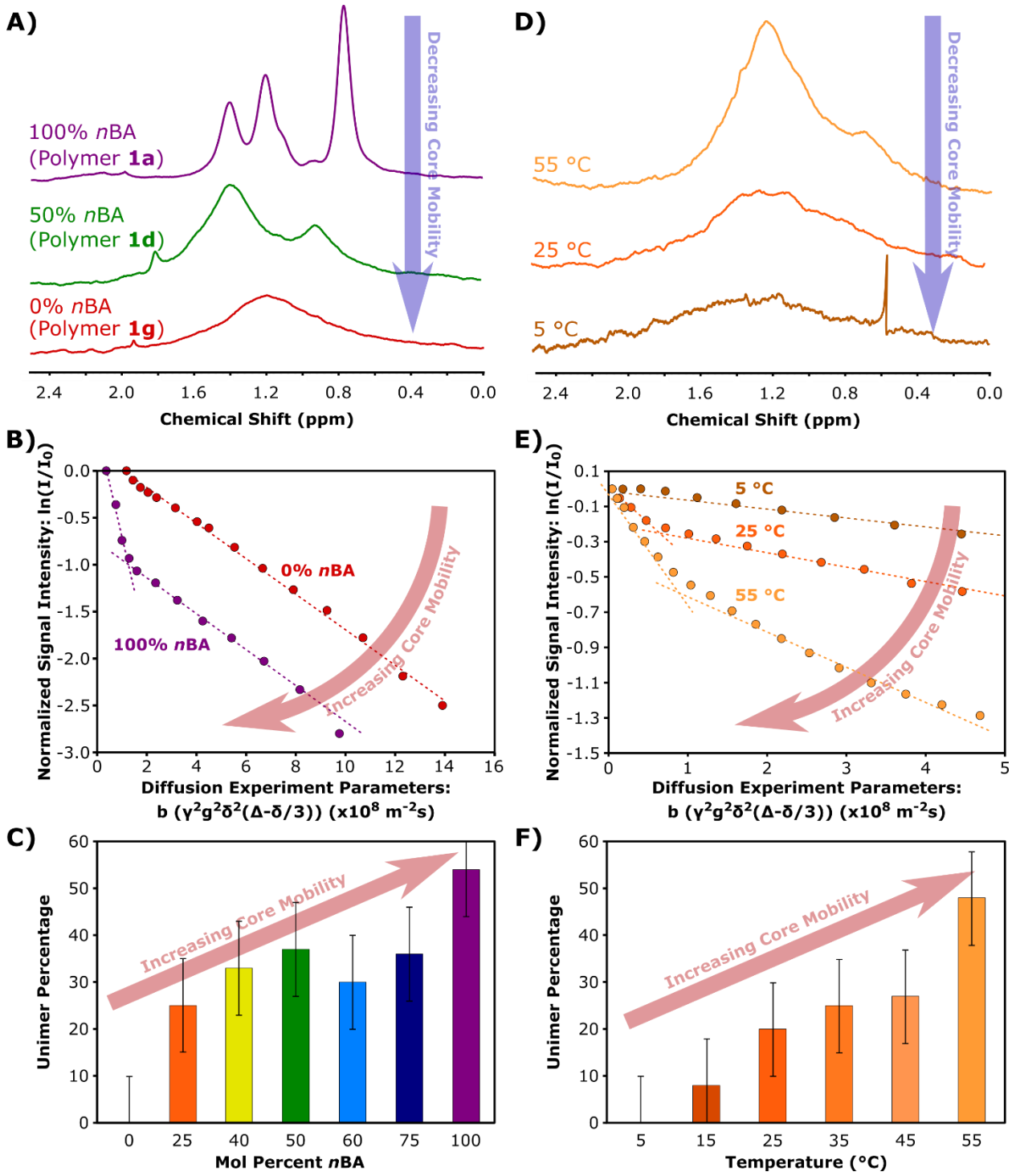

Figure 4-3. A) 1D ^{1}H NMR spectra overlay of micelle solutions made from 100, 50, and 0 mol% *n*BA BCPs (polymers **1a**, **1d**, and **1g**, respectively) at 5 mg/mL in H_2O solvent. B) Stejskal−Tanner plots of micelle solutions as a function of core-forming block composition at 25

°C (*b* is the Stejskal–Tanner factor, *g* is the magnetic gradient strength, γ is the gyromagnetic ratio of the nucleus probed, δ is the gradient pulse duration, and Δ is the gradient pulse spacing). Dashed lines are included as a guide to the eye and represent single- or two-component diffusion coefficients (they do not represent fit lines). C) Unimer percentages derived from signal decay curves for micelle solutions as a function of core-forming block composition. D) ^{1}H NMR spectra overlay of 25% *n*BA polymer micelle solutions (from polymer **1f**) at 5, 25, and 55 °C at 5 mg/mL (See also Figure S50 for similar plots for 0% and 50% *n*BA polymers). E) Stejskal−Tanner plots of polymer **1f** micelle solutions as a function of temperature with dashed lines as a guide to the eye for single- or two-component diffusion coefficients (they do not represent fit lines). F) Unimer percentages derived from signal decay curves for polymer **1f** micelle solutions as a function of temperature. Strikingly, core mobility strongly correlates with micelle–unimer coexistence. Error bars are ±10% for unimer percentages.

To further investigate the influence of core-forming block T_g on micelle dynamics and on populations of unimers and micelles in solution, we then employed NMR diffusometry to probe translational motion of the different mobile populations. In brief, NMR diffusometry involves the principle that if there are chemical species of differing mobility that do not exchange quickly relative to the time scale of diffusion (Δ = 25 ms in this study, see SI for details), we can extract distinct diffusion coefficients for each moving species. In amphiphilic BCP systems, diffusion rates of unassembled unimeric polymer chains versus assembled nanostructures (micelles) in solution are sufficiently different such that we can also extract the relative populations of each species.[33-34] We access the relative populations of unimers versus micelle assemblies through Stejskal−Tanner signal attenuation plots. By plotting the natural log of normalized NMR signal

intensity (I/I_0) versus the b factor that contains all known NMR experimental parameters ($\gamma^2\delta^2g^2(\Delta\text{-}\delta/3)$, see SI for details) in a signal attenuation curve, we extract diffusion coefficients D from linear regressions. A single linear fit indicates a single diffusing species in solution, while multi-component fitting implies multiple species diffusing at different rates. In a micellar system, fast diffusing unimers contribute to a rapid signal decay at lower magnetic gradient strength (g) while slower diffusing micelles contribute to a slow signal decay at higher gradient strength. As such, the signal decay curve of a sample containing both micelles and unimers shows rapid decay at low gradient strength, followed by more gradual decay at higher gradient strengths. The relative intensities (weighting) of these decay regimes can then yield the micelle and unimer populations in the sample.

Throughout this BCP series, we observed significant changes in the signal decay curves, demonstrating shifts in the micelle–unimer equilibrium. As shown in Figure 4-3B, 100% *n*BA polymer micelles (polymer **1a**, shown in purple) and 0% *n*BA polymer micelles (polymer **1g**, shown in red) displayed drastically different signal decay curves. The 0% *n*BA polymer micelles showed a relatively slow signal decay curve with a single component linear fit, which corresponds to a single diffusing species in solution (micelles). Conversely, the 100% *n*BA polymer micelles exhibited a signal decay curve with a two-component fit, indicating that there were two diffusing species in solution (slow-diffusing micelles and fast-diffusing unimers). As previously mentioned, the experimental timescale is much faster than unimer exchange, signifying these differences in micelle–unimer coexistence do not arise from differences in unimer exchange kinetics. We have measured free unimer content on heating and cooling on other block copolymer micelles and have so far obtained the same free vs. micelle-associated unimer fractions.[34]

To evaluate the influence of core block T_g on micelle–unimer coexistence, we extracted the micelle and unimer populations for solutions of polymers **1a**–**g** from fits to their signal decay curves, shown in Figure 4-3C (also Figures S38-42). The stark difference in unimer populations between the 100% and 0% *n*BA micelles suggests that the 0% *n*BA micelles exist in a 'frozen core' state at the temperature of the NMR experiment (25 °C).[55] Interestingly, NMR diffusometry experiments before and after thermal annealing of several samples revealed no changes in unimer percentage (Figures S43-45), indicating that these results are thermally robust and reversible, and are due to differences in chain mobility (or some system parameter closely correlated to mobility) and not due to kinetic trapping of micelle chains. Additionally, NMR diffusometry experiments on 25% *n*BA micelles (polymer **1f**) at concentrations ranging from 3–10 mg/mL revealed no changes in unimer percentages (Figure S46). Overall, we observed a general trend of increasing unimer population with decreasing core-forming block T_g throughout the series, with three notable regimes of unimer percentage (0–10, 20–30, and 40–50), indicating a relationship between core mobility and unimer population. In traditional theories of micellization,[15-16, 18-19] core molecular dynamics should not explicitly affect micelle–unimer equilibrium partitioning, but the present results suggest that new theory may be needed.

We also performed NMR diffusometry experiments on a 25% *n*BA micelle sample (polymer **1f**, T_g = 5 °C) as a function of temperature. As shown in Figure 4-3D, the micelle core exhibited higher mobility (narrower signal linewidths) at elevated temperature (55 °C) and showed the lowest mobility at $T = T_g$. NMR diffusometry signal-decay curves for 25% *n*BA micelles at different temperatures, shown in Figure 4-3E, showed significant increases in unimer population with increasing temperature, as expected based on results from the compositional experiments summarized in Figure 4-3C. Additionally, unimer populations derived from the signal decay

curves, shown in Figure 4-3F, (also Figures S47-49) increased monotonically with temperature and fell within the three regimes we had observed during the compositional experiments, reinforcing our hypothesis that micelle core mobility directly impacts micelle–unimer coexistence. Variable temperature NMR diffusometry experiments on two other polymer micelle compositions (polymers **1d** and **1g**, 50% and 0% nBA, respectively) revealed a consistent population of 40–50% unimers for high core mobility micelles (polymer **1d**) and a change from 0 to 25% unimers with increasing temperature past the T_g for low core mobility micelles (polymer **1g**) (Figure S50). However, we recognize that temperature affects other aspects of the system as well, including solvent quality and interfacial tension,[56] so although the correlation is strong between core mobility and free unimer percentage, these results may not be solely due to increasing core mobility with increasing temperature.

We also note that we explored the time required to reach quasi-equilibrium conditions for these micelles. For representative compositions and temperatures (Figures S43–S50), we measured diffusion immediately after making any temperature changes in quick (5-10 min) intervals and found that the measurements (diffusion coefficient values and free unimer fractions) reached plateau values after 30 min and did not further evolve for at least a month. This demonstrates that, once formulated, these micellar systems come to quasi-equilibrium rapidly and then are stable for periods longer than are relevant to drug delivery technologies.

The assembly of polymer amphiphiles into micelles is a thermodynamic process, driven by the increased entropy of water molecules excluded from the core and the increased hydrophobic interactions of the core-forming block.[18] Because mobility of the core-forming block should not theoretically impact micelle–unimer coexistence and would instead be more important for kinetic

processes (i.e., unimer exchange), we are working to further investigate how micelle core mobility impacts unimer populations.

4.5 Conclusions:

In summary, we have explored in detail the relationship between micelle core mobility and micelle–unimer coexistence. By synthesizing and characterizing a series of amphiphilic BCPs with varying *n*BA/*t*BA molar ratio in the hydrophobic blocks, we observed an overall trend of increasing unimer populations with decreasing T_g of the core-forming block. We verified the decoupling of effects of core chain mobility (varying T_g and experimental temperature) from changes in micelle core hydrophobicity *via* contact angle measurements of homopolymer films, which showed no significant difference in hydrophobicity relative to the *n*BA/*t*BA molar ratio. We investigated the relationship between core mobility and unimer population by variable temperature NMR spectroscopy and diffusometry experiments, which showed increasing unimer population and chain mobility with increasing temperature. Our results contradict the usual assumption from micellar theory that the chain mobility of the core should have no effect on polymer chain phase behavior (i.e., micelle–unimer coexistence), thus leading to potentially new directions in theoretical study. We expect these findings will inspire new insights into micellar behaviors and inform future designs for amphiphilic block copolymer systems, particularly in applications where large unimer concentrations may induce undesired (or desired) effects.

4.6 Acknowledgements:

This work was supported by the US National Science Foundation (CBET 1437767 and CHE 1904746) and the US National Institutes of Health (R01GM123508). We thank Prof. Richey Davis for helpful discussions and for use of the DLS instrument, Prof. Tim Long and Dr. Ryan Mondschein for DSC assistance, and Kearsley Dillon, Sarah Swilley-Sanchez, and Yumeng (Jackie) Zhu for critical readings of the manuscript. Any opinions, findings, and conclusions or recommendations expressed in this material are those of the authors and do not necessarily reflect the views of the funding agencies.

4.7 References:

1. Richard, G. J.; Christopher, K. O.; Philip, H.; Pavel, K.; Graeme, M.; Michel, V., *Pure Appl. Chem.* **2012**, *85* (2), 463-492.

2. Bangham, A. D., *Chem. Phys. Lipids* **1993**, *64* (1), 275-285.

3. Dobson, C. M., *Nature* **2003**, *426* (6968), 884-890.

4. Discher, D. E.; Eisenberg, A., *Science* **2002**, *297* (5583), 967.

5. Allen, T. M.; Cullis, P. R., *Adv Drug Deliv Rev* **2013**, *65* (1), 36-48.

6. Allen, T. M.; Cullis, P. R., *Science* **2004**, *303* (5665), 1818.

7. Adams, M. L.; Lavasanifar, A.; Kwon, G. S., *J. Pharm. Sci.* **2003**, *92* (7), 1343-1355.

8. Biswas, S.; Kumari, P.; Lakhani, P. M.; Ghosh, B., *Eur. J. Pharm. Sci.* **2016**, *83* (Supplement C), 184-202.

9. Kataoka, K.; Harada, A.; Nagasaki, Y., *Adv. Drug Deliv. Rev.* **2012**, *64*, 37-48.

10. Cheng, C.; Qi, K.; Khoshdel, E.; Wooley, K. L., *J. Am. Chem. Soc.* **2006**, *128* (21), 6808-6809.

11. Ievins, A. D.; Moughton, A. O.; O'Reilly, R. K., *Macromolecules* **2008**, *41* (10), 3571-3578.

12. Moughton, A. O.; O'Reilly, R. K., *J. Am. Chem. Soc.* **2008**, *130* (27), 8714-8725.

13. Gallou, F.; Isley, N. A.; Ganic, A.; Onken, U.; Parmentier, M., *Green Chem.* **2016**, *18* (1), 14-19.

14. Klingelhöfer, S.; Heitz, W.; Greiner, A.; Oestreich, S.; Förster, S.; Antonietti, M., *J. Am. Chem. Soc.* **1997**, *119* (42), 10116-10120.

15. Israelachvili, J. N.; Mitchell, D. J.; Ninham, B. W., *J. Chem. Soc., Faraday Trans.* **1976**, *72* (0), 1525-1568.

16. Israelachvili, J. N.; Marčelja, S.; Horn, R. G., *Q. Rev. Biophys.* **1980**, *13* (2), 121-200.

17. Fong, C.; Le, T.; Drummond, C. J., *Chem. Soc. Rev.* **2012**, *41* (3), 1297-1322.

18. Mai, Y.; Eisenberg, A., *Chem. Soc. Rev.* **2012**, *41* (18), 5969-5985.

19. Riess, G., *Prog. Polym. Sci.* **2003**, *28* (7), 1107-1170.

20. Darling, S. B., *Prog. Polym. Sci.* **2007**, *32* (10), 1152-1204.

21. Bates, F. S.; Fredrickson, G., *Physics today* **2000**, *52*.

22. Williams, R. J.; Pitto-barry, A.; Kirby, N.; Dove, A. P.; Reilly, R. K. O., *Macromolecules* **2016**.

23. Zhang, L.; Eisenberg, A., *J. Am. Chem. Soc.* **1996**, *118* (13), 3168-3181.

24. Shen, H.; Eisenberg, A., *Macromolecules* **2000**, *33* (7), 2561-2572.

25. Figg, C. A.; Carmean, R. N.; Bentz, K. C.; Mukherjee, S.; Savin, D. A.; Sumerlin, B. S., *Macromolecules* **2017**, *50* (3), 935-943.

26. Yamamoto, Y.; Yasugi, K.; Harada, A.; Nagasaki, Y.; Kataoka, K., *J Control Release* **2002**, *82* (2-3), 359-371.

27. Foster, J. C.; Varlas, S.; Couturaud, B.; Jones, J. R.; Keogh, R.; Mathers, R. T.; O'Reilly, R. K., *Angew. Chem. Int. Ed.* **2018**, *57* (48), 15733-15737.

28. Choucair, A.; Eisenberg, A., *Eur. Phys. J. E* **2003**, *10* (1), 37-44.

29. Zhang, L.; Eisenberg, A., *Macromolecules* **1999**, *32* (7), 2239-2249.

30. Cui, H.; Chen, Z.; Zhong, S.; Wooley, K. L.; Pochan, D. J., *Science* **2007**, *317* (5838), 647.

31. Oerlemans, C.; Bult, W.; Bos, M.; Storm, G.; Nijsen, J. F. W.; Hennink, W. E., *Pharm. Res.* **2010**, *27* (12), 2569-2589.

32. Nakamura, K.; Endo, R.; Takeda, M., *J. Polym. Sci., Polym. Phys. Ed.* **1976**, *14* (7), 1287-1295.

33. Kidd, B. E.; Li, X.; Piemonte, R. C.; Cooksey, T. J.; Singh, A.; Robertson, M. L.; Madsen, L. A., *Macromolecules* **2017**, *50* (11), 4335-4343.

34. Li, X.; Cooksey, T. J.; Kidd, B. E.; Robertson, M. L.; Madsen, L. A., *Macromolecules* **2018**, *51* (20), 8127-8135.

35. Batrakova, E.; Lee, S.; Li, S.; Venne, A.; Alakhov, V.; Kabanov, A., *Pharm. Res.* **1999**, *16* (9), 1373-1379.

36. Batrakova, E. V.; Li, S.; Li, Y.; Alakhov, V. Y.; Elmquist, W. F.; Kabanov, A. V., *J Control Release* **2004**, *100* (3), 389-397.

37. Panova, I. G.; Spiridonov, V. V.; Kaplan, I. B.; Trubinov, S. S.; Elizova, N. V.; Melnichenko, A. A.; Orekhov, A. N.; Yaroslavov, A. A., *Biochem.-Moscow* **2015**, *80* (8), 1057-1064.

38. Pettersson, E.; Topgaard, D.; Stilbs, P.; Söderman, O., *Langmuir* **2004**, *20* (4), 1138-1143.

39. Frise, A. E.; Pagès, G.; Shtein, M.; Pri Bar, I.; Regev, O.; Furó, I., *J. Phys. Chem. B* **2012**, *116* (9), 2635-2642.

40. Ulrich, K.; Galvosas, P.; Kärger, J.; Grinberg, F., *Phys. Rev. Lett.* **2009**, *102* (3), 037801.

41. Thieu, L. M.; Zhu, L.; Korovich, A. G.; Hickner, M. A.; Madsen, L. A., *Macromolecules* **2019**, *52* (1), 24-35.

42. Wilmsmeyer, K. G.; Li, X.; Madsen, L. A., *Liq. Cryst.* **2018**, *45* (6), 844-856.

43. Kidd, B. E.; Forbey, S. J.; Steuber, F. W.; Moore, R. B.; Madsen, L. A., *Macromolecules* **2015**, *48* (13), 4481-4490.

44. Bostwick, J. E.; Zanelotti, C. J.; Iacob, C.; Korovich, A. G.; Madsen, L. A.; Colby, R. H., *Macromolecules* **2020**, *53* (4), 1405-1414.

45. Yamamoto, T.; Yokoyama, M.; Opanasopit, P.; Hayama, A.; Kawano, K.; Maitani, Y., *J Control Release* **2007**, *123* (1), 11-18.

46. Yan, Q.; Yuan, J. Y.; Yuan, W. Z.; Zhou, M.; Yin, Y. W.; Pan, C. Y., *Chem. Comm.* **2008**, (46), 6188-6190.

47. Foster, J. C.; Carrazzone, R. J.; Spear, N. J.; Radzinski, S. C.; Arrington, K. J.; Matson, J. B., *Macromolecules* **2019**, *52* (3), 1104-1111.

48. FOX, T., *Bull. Am. Phys. Soc.* **1956**, *1*, 123.

49. Saby-Dubreuil, A. C.; Guerrier, B.; Allain, C.; Johannsmann, D., *Polymer* **2001**, *42* (4), 1383-1391.

50. Yamauchi, K.; Lizotte, J. R.; Long, T. E., *Macromolecules* **2003**, *36* (4), 1083-1088.

51. Tsui, O. K. C.; Wang, X. P.; Ho, J. Y. L.; Ng, T. K.; Xiao, X., *Macromolecules* **2000**, *33* (11), 4198-4204.

52. Min, K.; Kwon Oh, J.; Matyjaszewski, K., *J. Polym. Sci., Part A: Polym. Chem.* **2007**, *45* (8), 1413-1423.

53. Chen, J.; Spear, S. K.; Huddleston, J. G.; Rogers, R. D., *Green Chem.* **2005**, *7* (2), 64-82.

54. Levitt, M. H., *Spin Dynamics*. John Wiley and Sons Ltd.: England, 2008; Vol. 2.

55. Dai, J.; Alaei, Z.; Plazzotta, B.; Pedersen, J. S.; Furó, I., *J. Phys. Chem. B* **2017**, *121* (45), 10353-10363.

56. Doncom, K. E. B.; Pitto-Barry, A.; Willcock, H.; Lu, A.; McKenzie, B. E.; Kirby, N.; O'Reilly, R. K., *Soft Matter* **2015**, *11* (18), 3666-3676.

4.8 Experimental:

Materials

All reagents were obtained from commercial vendors and used as received unless otherwise stated. 2,2′-Azobis(2-methylpropionitrile) (AIBN) was recrystallized from methanol prior to use. Monomers *n*-butyl acrylate (*n*BA) and *tert*-butyl acrylate (*t*BA) were purchased from Alfa Aesar and passed through a plug of basic alumina prior to use. Dry solvents were purified by passage through a solvent purification system (MBraun).

Methods

NMR spectra for characterization of molecular structures were measured on an Agilent 400 MHz spectrometer. ^{1}H and ^{13}C NMR chemical shifts are reported in ppm relative to internal solvent resonances. Yields refer to chromatographically and spectroscopically pure compounds unless otherwise stated. Size exclusion chromatography (SEC) was carried out in THF at 1 mL/min at 30 °C on two Agilent PLgel 10 µm MIXED-B columns connected in series with a Wyatt Dawn Heleos 2 multi-angle light scattering detector and a Wyatt Optilab Rex refractive index detector. No calibration standards were used, and d*n*/d*c* values were obtained by offline differential refractive index measurements. Dynamic light scattering (DLS) was conducted using a Malvern Zetasizer Nano operating at 25 °C. A solution of micelles was prepared at 5 mg/mL and filtered with a 0.2 µm filter prior to scanning. Calculations of the particle size distributions and distribution averages were conducted using CONTIN particle size distribution analysis routines with number, volume, and intensity averages. Measurements were made in triplicate and errors reflect standard deviations. Static light scattering measurements were performed with a Wyatt Dawn Heleos 2 multi-angle light scattering detector operating in batch mode. Micelle solutions were prepared at

known concentrations and filtered with a 0.2 µm filter prior to scanning. Absolute weight-average molecular weights of aggregates were calculated using Wyatt ASTRA software. Differential scanning calorimetry (DSC) studies were carried out on a Q-2000 DSC in aluminum pans operated with a dry nitrogen purge from -10 °C to 100 °C with a heating and cooling rate of 5 °C/min modulated ±3 °C/min. Results are reported from the second heat cycle and figures are shown as exo down.

Synthesis of 2-methyl-2-(dodecylsulfanylthiocarbonyl)sulfanyl propanoic acid (CTA)

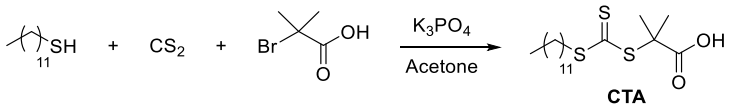

Dodecanethiol (5 mL, 20.9 mmol) was dissolved in acetone (30 mL) in a round bottom flask. To the flask was added tribasic potassium phosphate (8.86 g, 41.7 mmol). The reaction mixture was stirred at rt for 10 min. CS_2 (3.78 mL, 62.6 mmol) was added dropwise, and the reaction mixture was stirred for an additional 1 h. To the flask a solution of 2-bromo-2-methyl propanoic acid (3.91 g, 23.4 mmol) in 5 mL of acetone was added dropwise. The reaction mixture was stirred overnight at rt. Reaction conversion was monitored by TLC using CH_2Cl_2 as eluent and visualized via UV lamp. The reaction mixture was diluted with ~100 mL of CH_2Cl_2, transferred to a separatory funnel, and washed consecutively with 1N HCl and brine. The organic layer was dried over Na_2SO_4 and concentrated via rotary evaporation. Silica gel was added to the concentrated solution before removing the rest of the solvent via rotary evaporation. The silica was dry-loaded onto a silica gel column, and the product was eluted with CH_2Cl_2. The product containing fractions, as determined by TLC (CH_2Cl_2 eluent and UV lamp visualization), were combined and concentrated via rotary evaporation to yield a yellow solid. The crude product was recrystallized from hexanes

to yield yellow crystals (4.88 g, 64% yield).The ^{1}H and ^{13}C NMR spectra matched those from published reports.[1]

^{1}H NMR (400 MHz, $CDCl_3$) δ (ppm): 3.25 (2H, t, J = 7.4 Hz, H_d); 1.70 (6H, s, H_e); 1.64 (2H, m, H_c); 1.37 (2H, m, H_b); 1.25 (18H, m, H_b); 0.88 (3H, t, J = 6.9 Hz, H_a)

^{13}C NMR (400 MHz, $CDCl_3$) δ (ppm): 220.78 (C_d); 178.84 (C_g); 55.59 (C_e); 37.12 (C_c); 31.89-26.21 (C_b); 23.69 (C_f); 14.13 (C_a)

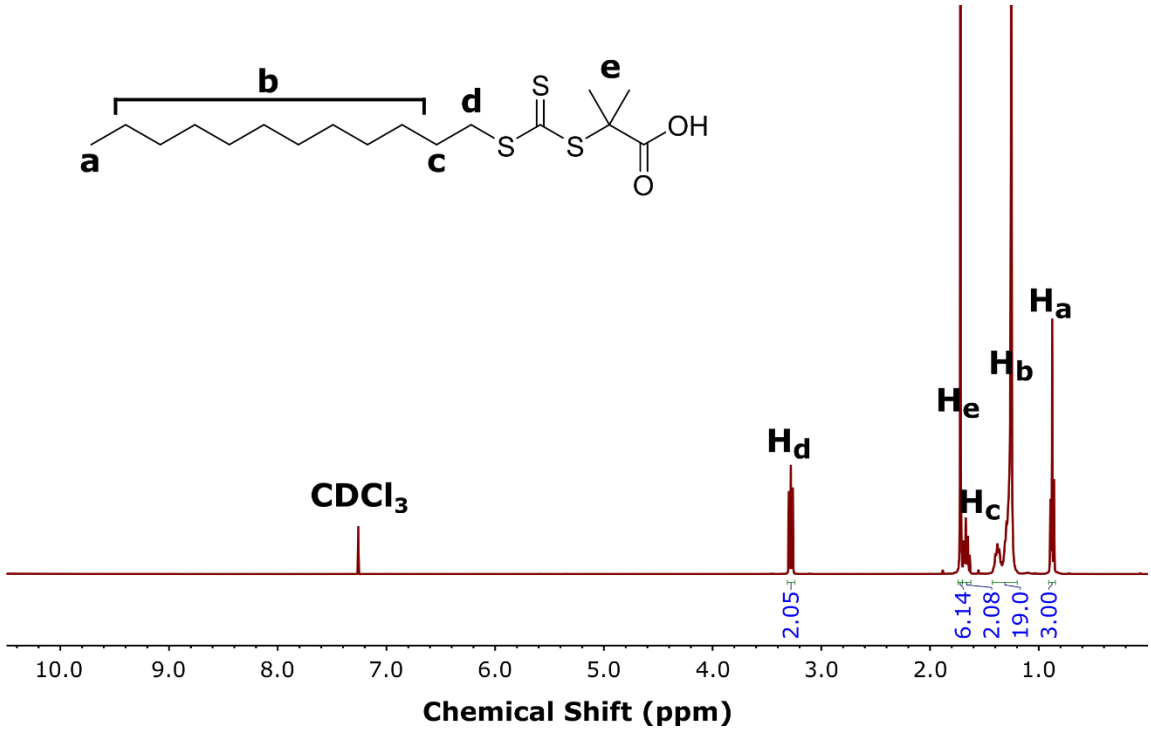

Figure S1. ^{1}H NMR spectrum of 2-methyl-2-(dodecylsulfanylthiocarbonyl)sulfanyl propanoic acid **(CTA)**.

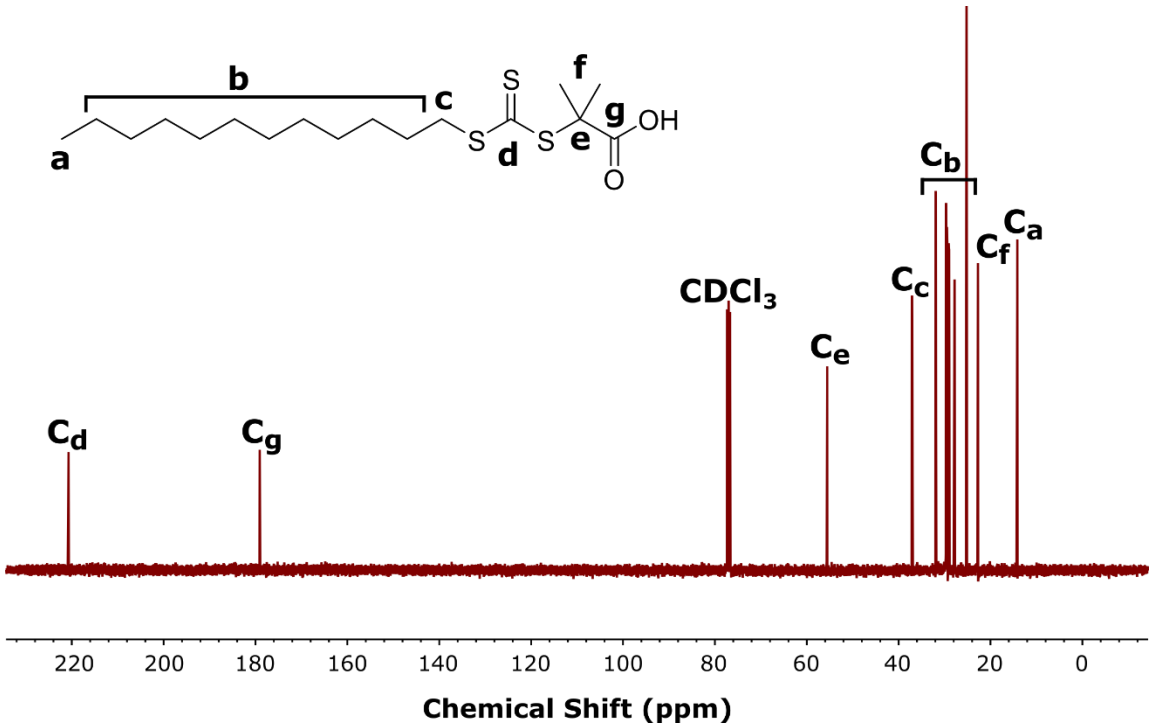

Figure S2. ^{13}C NMR spectrum of 2-methyl-2-(dodecylsulfanylthiocarbonyl)sulfanyl propanoic acid **(CTA)**.

Synthesis of macroCTA

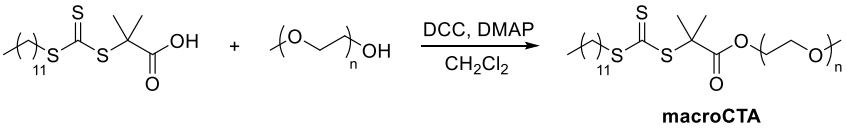

A round bottom flask was charged with **CTA** (0.91 g, 2.50 mmol), polyethylene glycol monomethyl ether (M_n = 4,000 g/mol, 5.0 g, 1.25 mmol), 4-dimethylamino pyridine (0.15 g, 1.25 mmol), and anhydrous CH_2Cl_2 (5.0 mL). *N*,*N*'-Dicyclohexylcarbodiimide (DCC) (0.52 g, 2.50 mmol) was dissolved in 5.0 mL of anhydrous CH_2Cl_2 in a vial. The DCC solution was added dropwise to the flask containing the other reagents, and the reaction mixture was stirred at rt overnight. Reaction conversion was followed by TLC using CH_2Cl_2 as eluent and visualized via UV lamp. The precipitated solids were removed by filtration. The desired product was isolated via

precipitation from diethyl ether and was purified by repeated precipitations (2-4) from CH_2Cl_2 into diethyl ether until complete removal low molecular weight side products was confirmed by ^{1}H NMR spectroscopy to afford the product as a yellow solid (1.50 g, 69% yield). The ^{1}H NMR spectrum matched those from published reports.[2]

^{1}H NMR (400 MHz, $CDCl_3$) δ (ppm): 4.24 (2H, t, *J* = 5.0 Hz, H_f); 3.81 (2H, t, *J* = 4.8 Hz, H_g); 3.63 (~360H, m, H_h); 1.37 (2H, m, H_b); 3.37 (3H, s, H_i); 3.25 (2H, t, *J* = 7.4 Hz, H_d); 1.69 (6H, s, H_e); 1.64 (2H, m, H_c); 1.25 (18H, m, H_b); 0.87 (3H, t, *J* = 6.6 Hz, H_a)

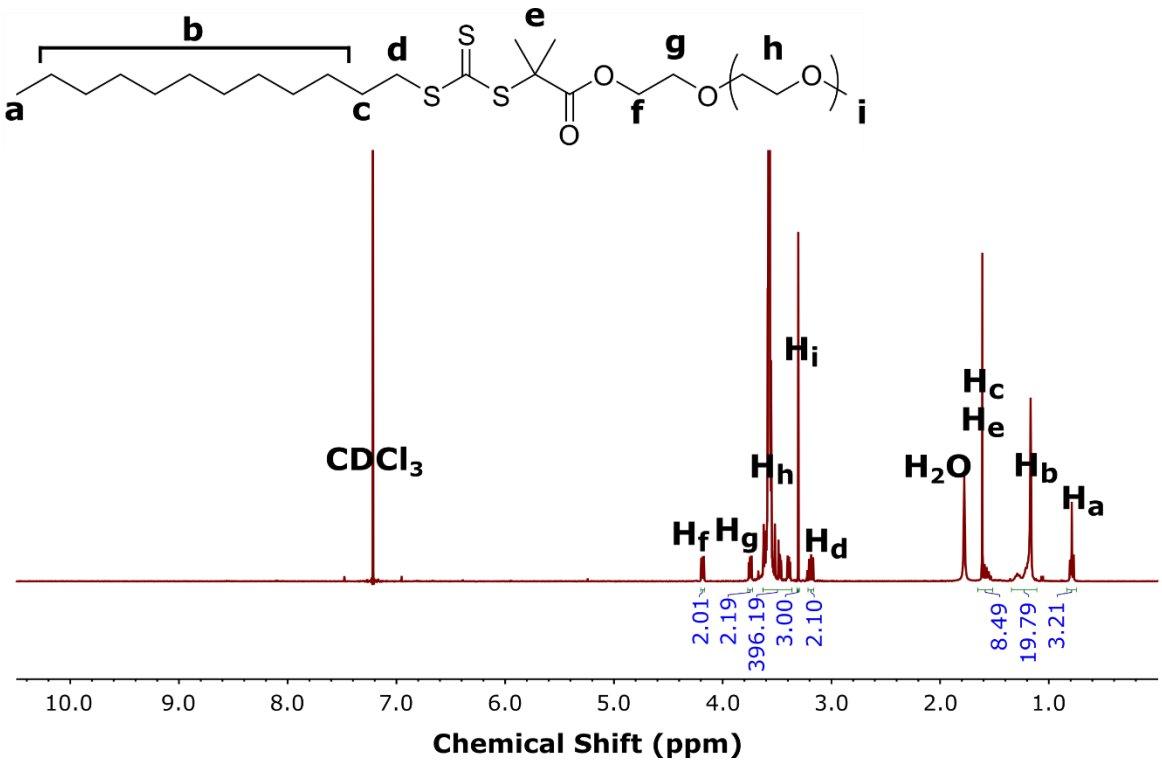

Figure S3. ^{1}H NMR spectrum of PEG-(2-methyl-2-(dodecylsulfanylthiocarbonyl)sulfanyl propanoic acid) **(macroCTA)**.

Synthesis of PEG-b-poly(nBA-ran-tBA) copolymers

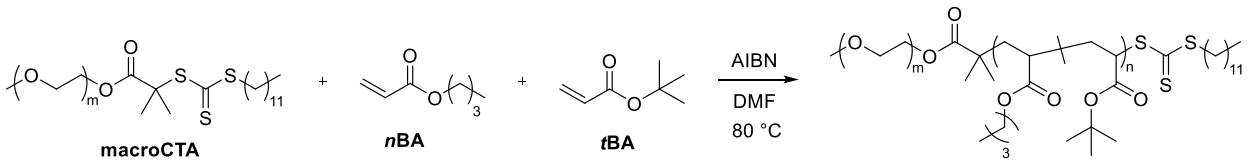

A typical polymerization procedure is as follows: An oven-dried Schlenk tube was equipped with a magnetic stir bar and was evacuated on a Schlenk line and refilled with N_2 gas. Next, **macroCTA** (200 mg, 0.046 mmol), ***n*BA** (0.185 mL, 1.29 mmol), ***t*BA** (0.187 mL, 1.29 mmol), and 1.5 mL of anhydrous DMF were added via gas-tight syringe through a septum under N_2 flow. A separate solution of AIBN was prepared by dissolving 3.8 mg (0.023 mmol) in 1 mL of anhydrous DMF in a vial. 100 μL of this solution was added to the Schlenk tube. The tube was then deoxygenated by subjecting the contents to three freeze−pump−thaw cycles. The Schlenk tube was then backfilled with N_2 and submerged in an oil bath maintained at 80 °C. Samples were removed periodically by N_2-purged syringe to monitor molar mass evolution by SEC and monomer conversion by ^{1}H NMR spectroscopy. The polymerization was quenched by submerging the tube into liquid N_2 and exposing the reaction mixture to air. The resulting PEG-*b*-poly(*n*BA-*ran*-*t*BA) was isolated via precipitation into a large excess of cold 1:1 hexanes:ether. If necessary, further precipitations from CH_2Cl_2 into cold 1:1 hexanes:ether were performed to remove residual monomer.

Synthesis of Poly(nBA-ran-tBA) copolymers

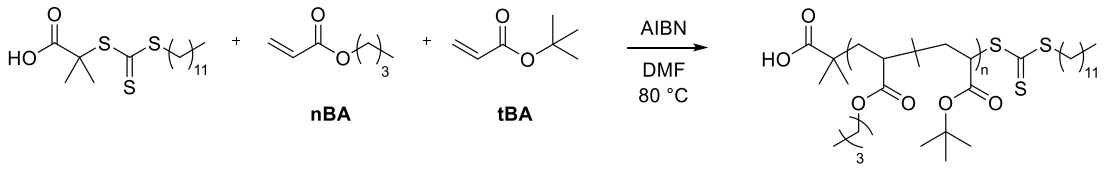

A typical polymerization procedure is as follows: An oven-dried Schlenk tube was equipped with a magnetic stir bar and was evacuated on a Schlenk line and refilled with N_2 gas. Next **CTA** (25 mg, 0.069 mmol), ***n*BA** (980 μL, 6.9 mmol), ***t*BA** (990 μL, 6.9 mmol), and 1.5 mL of anhydrous DMF were added via gas-tight syringe through a septum under N_2 flow. A separate solution of AIBN was prepared by dissolving 11 mg (0.069 mmol) in 1 mL of anhydrous DMF in a vial. 100 μL of this solution was added to the Schlenk tube. The tube was then deoxygenated by subjecting the contents to three freeze−pump−thaw cycles. The Schlenk tube was then backfilled with N_2 and submerged in an oil bath maintained at 80 °C. Samples were removed periodically by N_2-purged syringe to monitor molar mass evolution by SEC and monomer conversion by ^{1}H NMR spectroscopy. The polymerization was quenched by submerging the tube into liquid N_2 and exposing the reaction mixture to air. The resulting Poly(*n*BA-*ran*-*t*BA) was isolated via precipitation into a large excess of cold 3:1 hexanes:ether. If necessary, further precipitations from CH_2Cl_2 into cold 3:1 hexanes:ether were performed to remove residual monomer.

PEG-b-P(nBA-ran-tBA) micelle assembly

A typical micelle assembly procedure is as follows: A scintillation vial equipped with a stir bar was charged with polymer (50 mg) and THF (1 mL). Distilled H_2O (7 mL) was added dropwise to the vial via syringe pump over 70 minutes, and the solution was allowed to stir afterwards for 15 min. The solution was transferred to dialysis tubing (6-8 kD MWCO) and dialyzed against distilled water for 18 h, changing the water once after 2 h and again after 4 h. The resulting aqueous solution

was removed from the dialysis tubing and diluted with distilled water to a final volume of 10.0 mL (5 mg/mL polymer concentration).

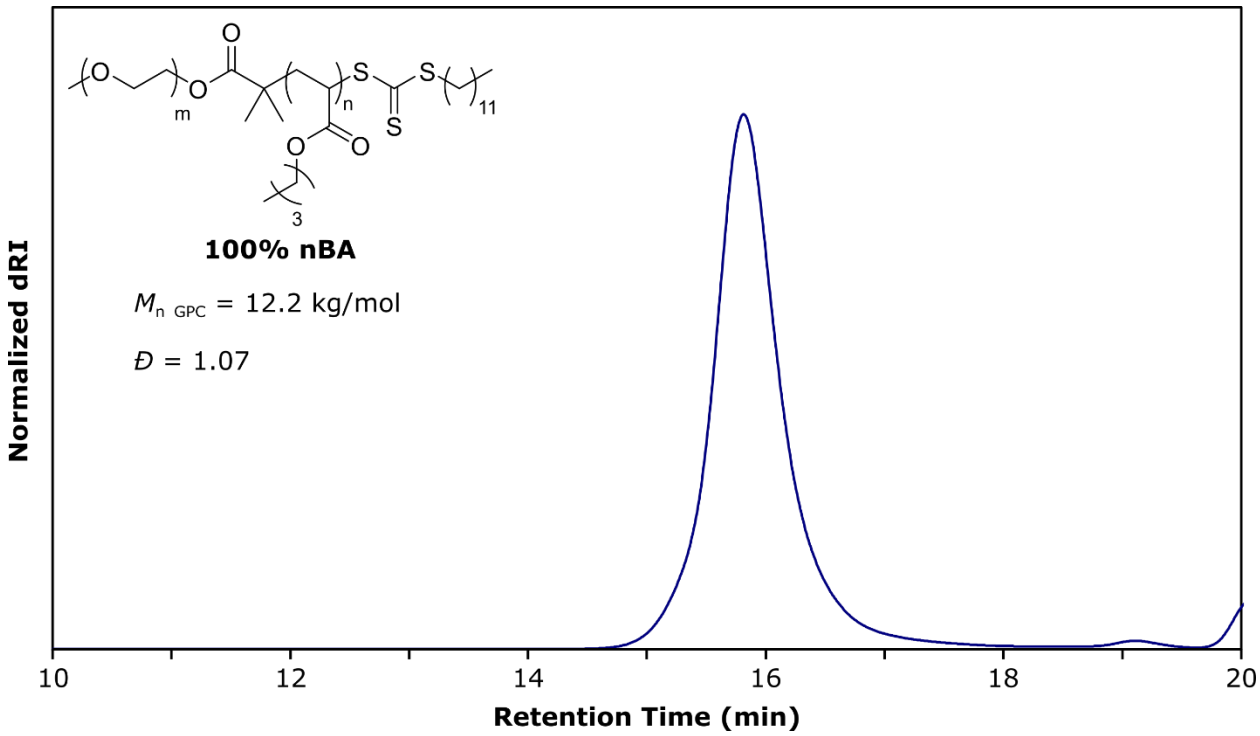

Figure S4. SEC trace of polymer **1a** (PEG-*b*-P(*n*BA)).

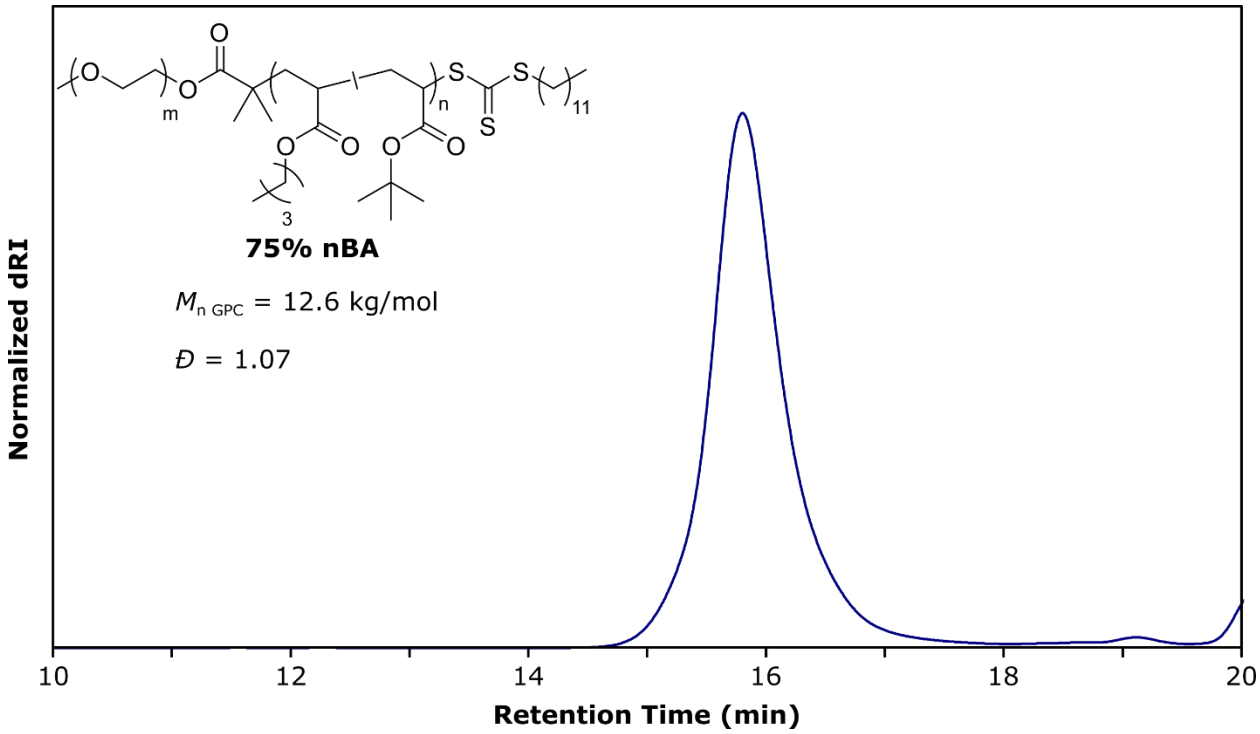

Figure S5. SEC trace of polymer **1b** (PEG-*b*-P(*n*BA-*ran*-*t*BA)).

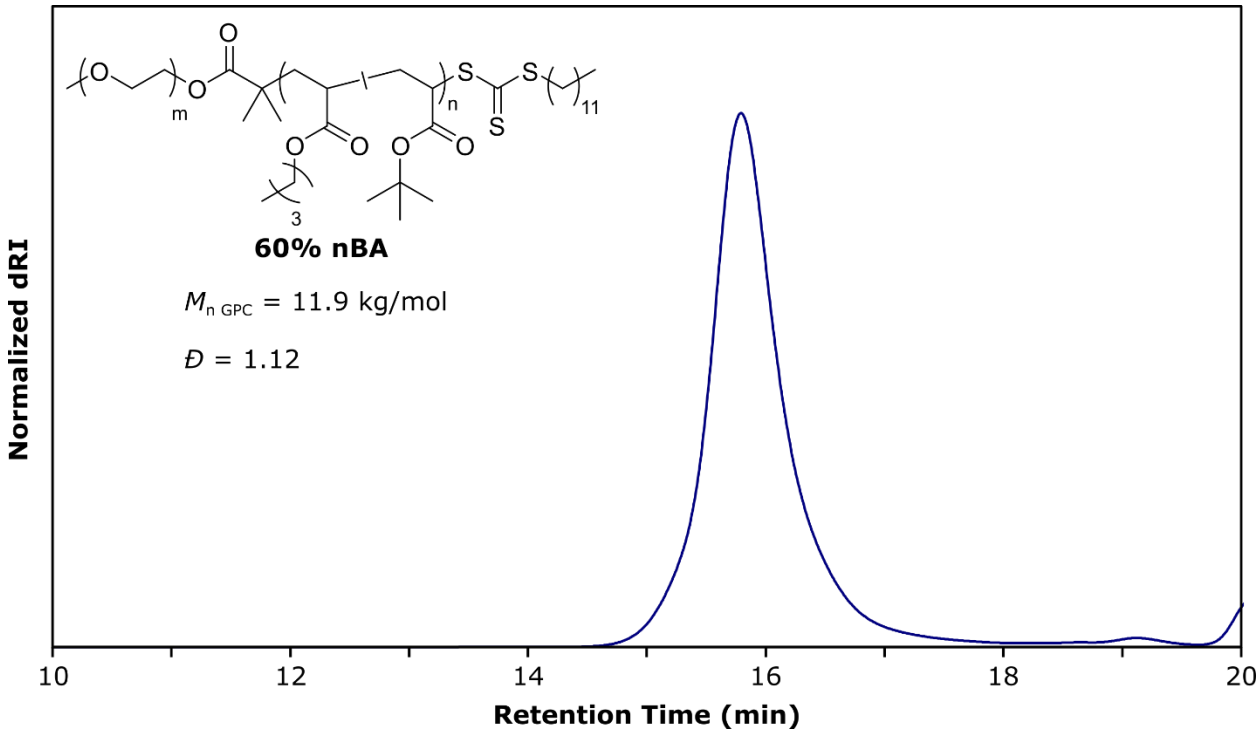

Figure S6. SEC trace of polymer **1c** (PEG-*b*-P(*n*BA-*ran*-*t*BA)).

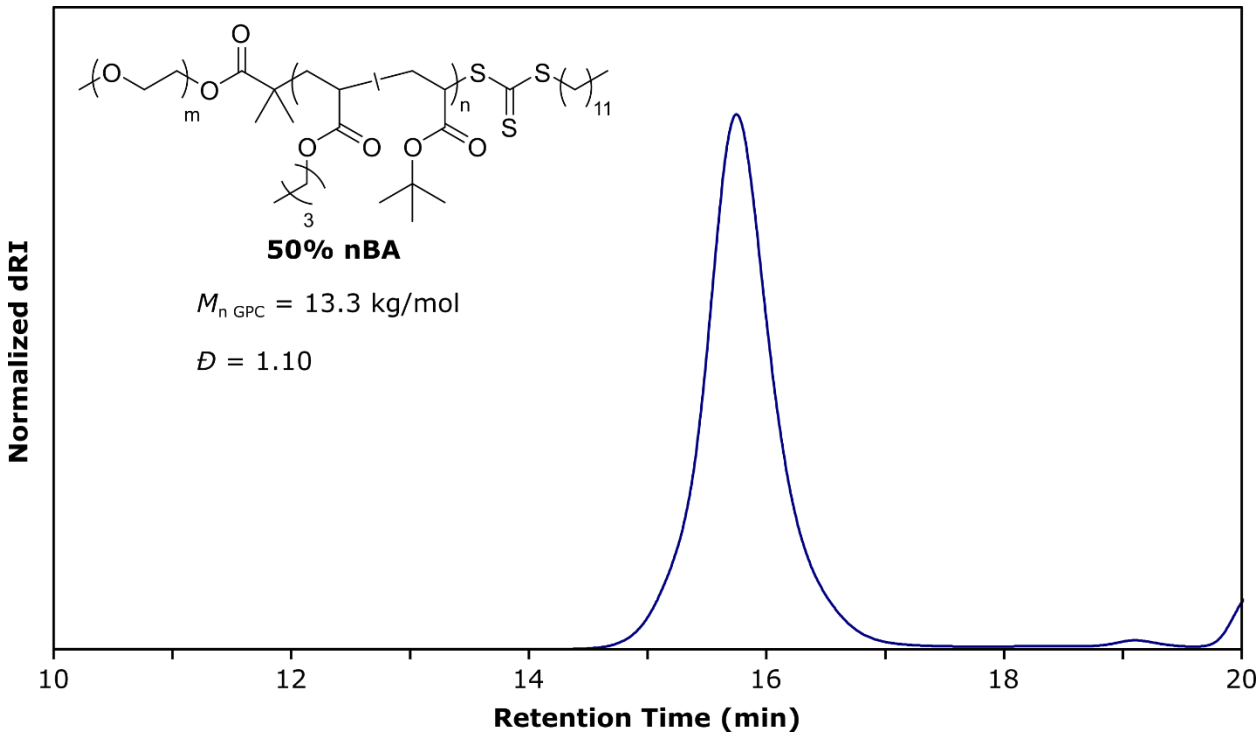

Figure S7. SEC trace of polymer **1d** (PEG-*b*-P(*n*BA-*ran*-*t*BA)).

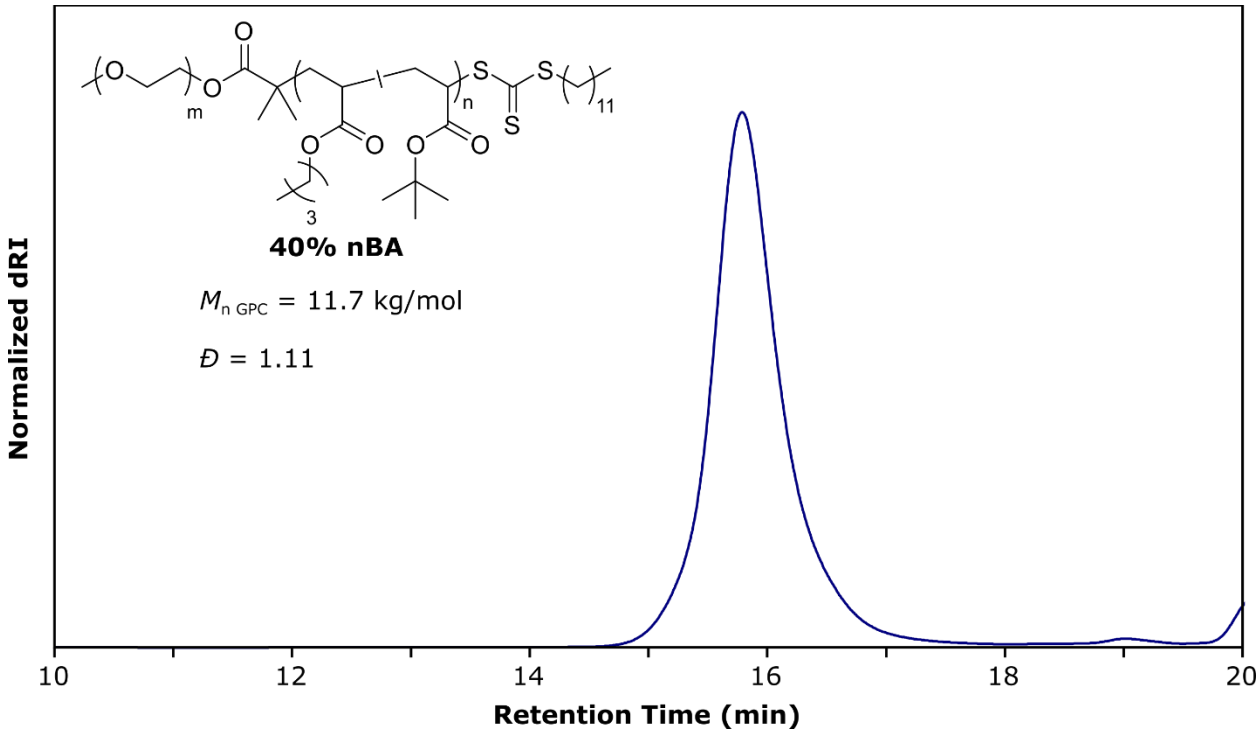

Figure S8. SEC trace of polymer **1e** (PEG-*b*-P(*n*BA-*ran*-*t*BA)).

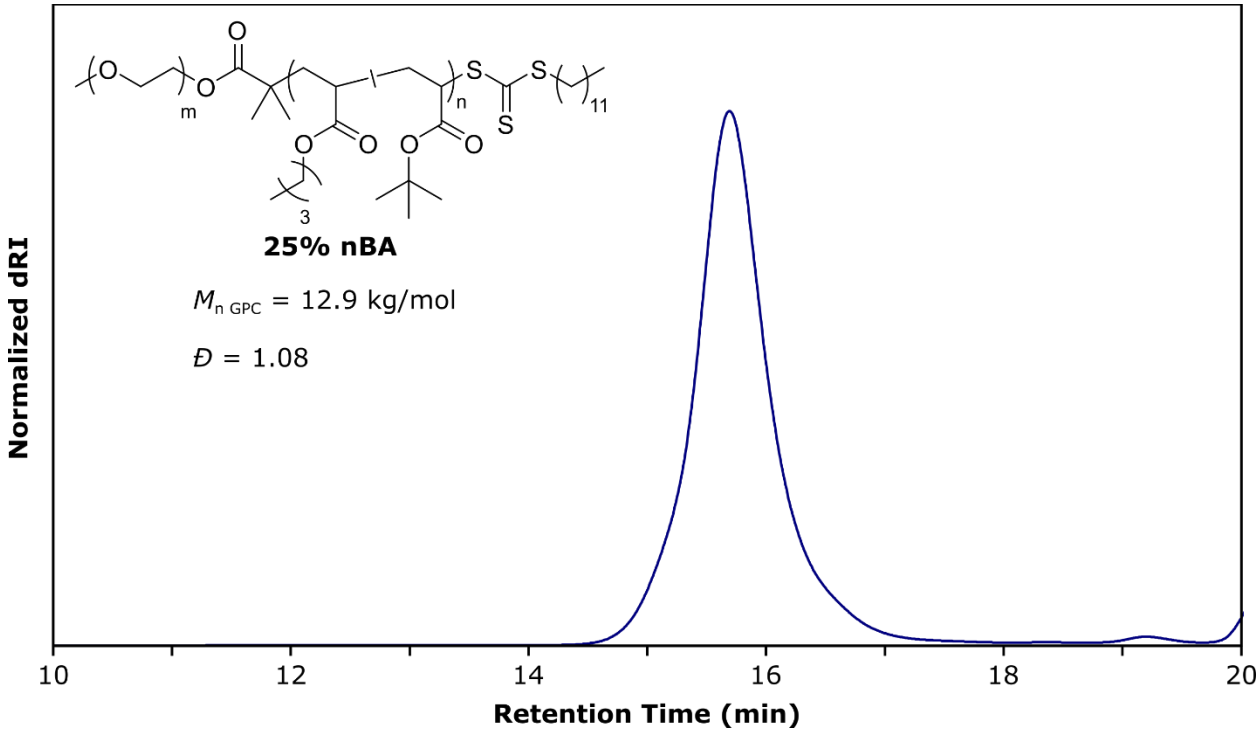

Figure S9. SEC trace of polymer **1f** (PEG-*b*-P(*n*BA-*ran*-*t*BA)).

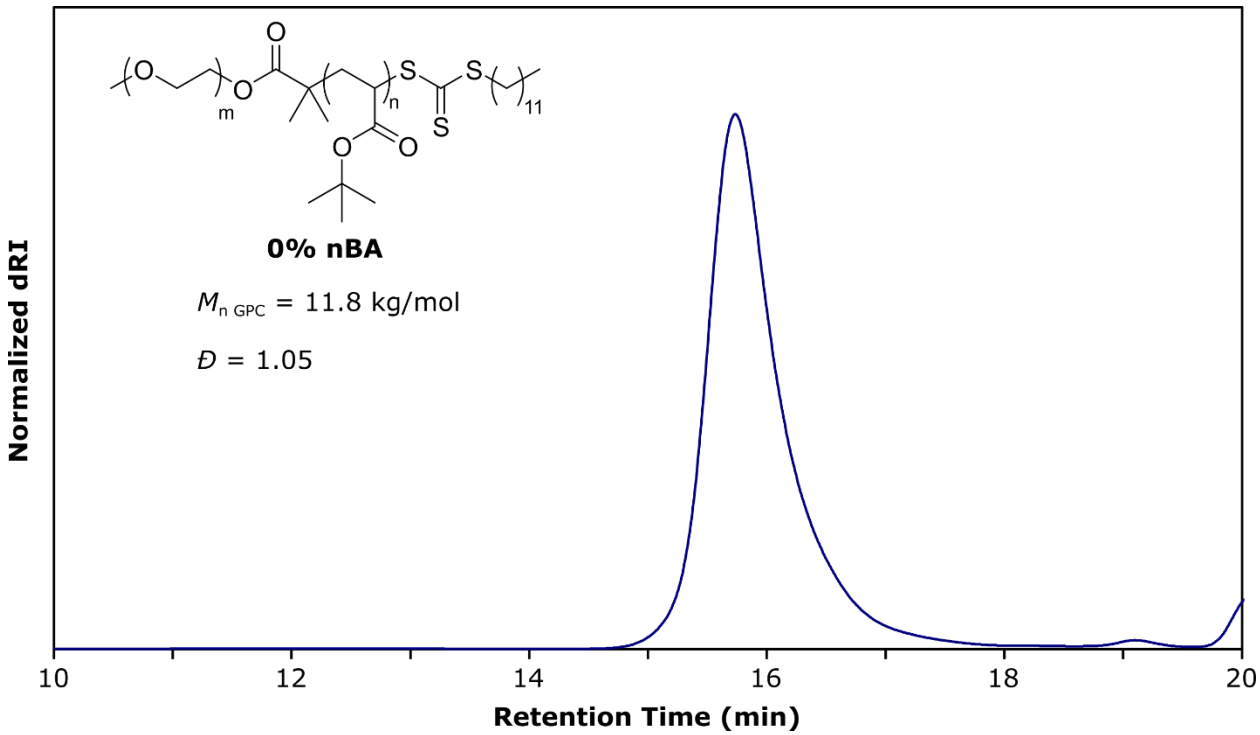

Figure S10. SEC trace of polymer **1g** (PEG-*b*-P(*t*BA)).

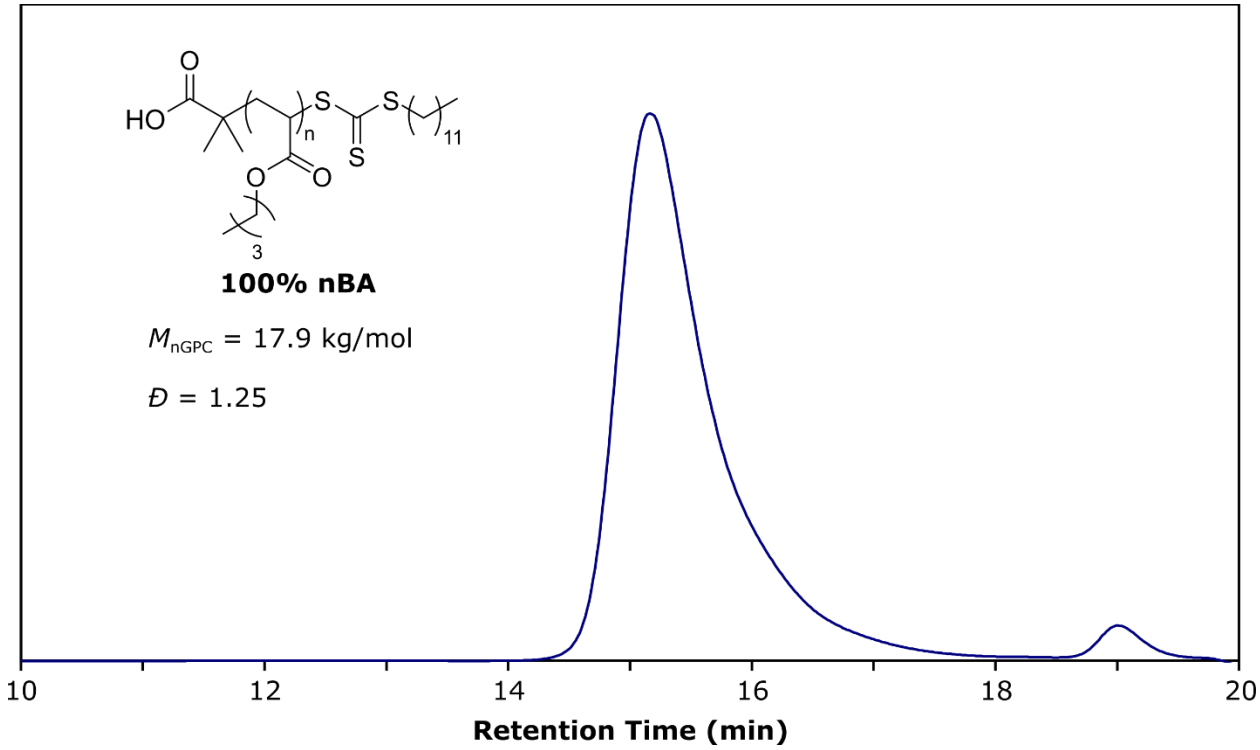

Figure S11. SEC trace of polymer **2a** (P(*n*BA)).

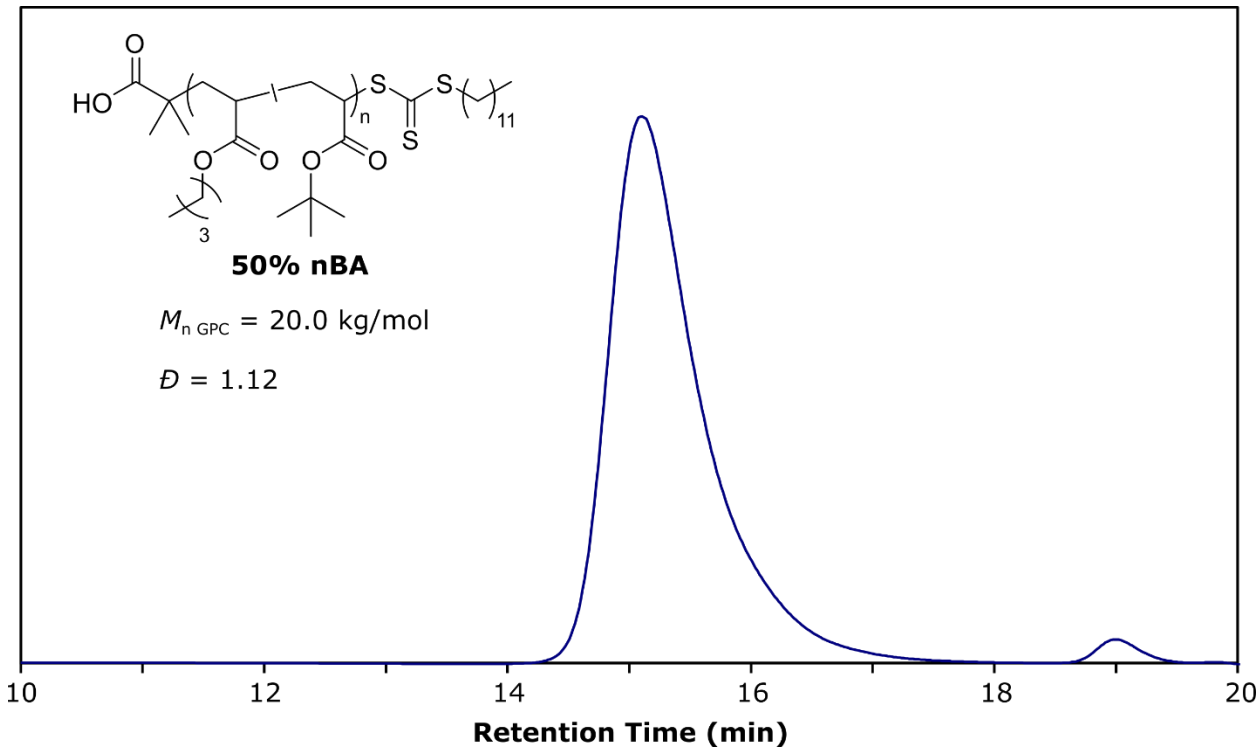

Figure S12. SEC trace of polymer **2b** (P(*n*BA-*ran*-*t*BA)).

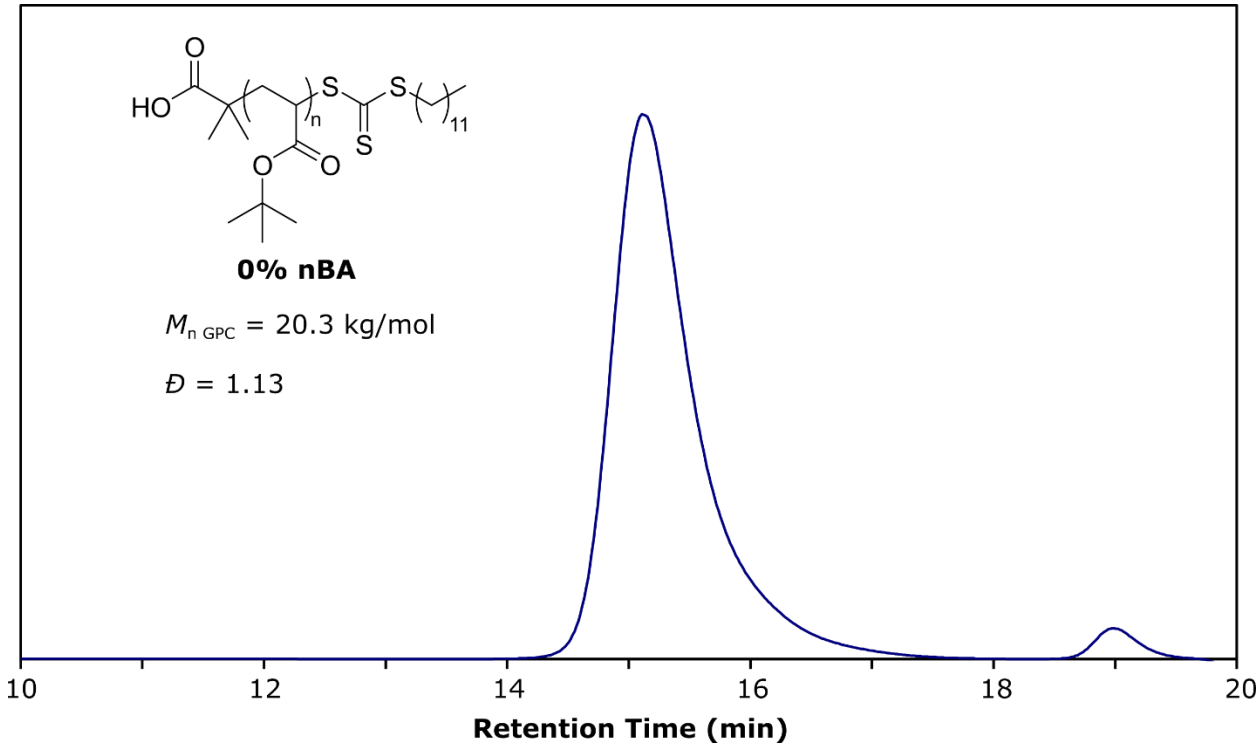

Figure S13. SEC trace of polymer **2c** (P(*t*BA)).

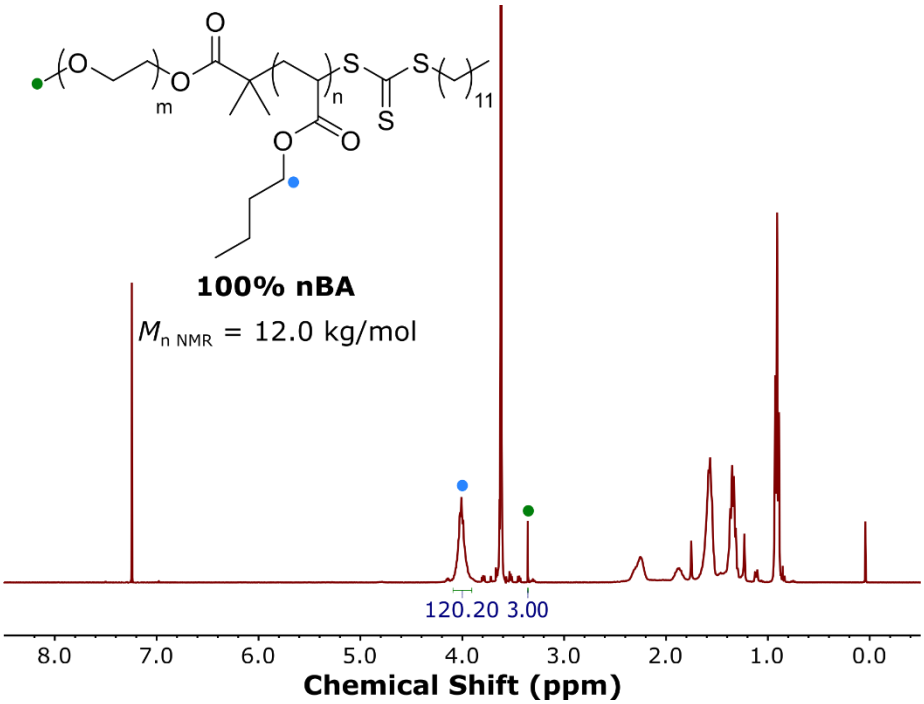

Figure S14. ^{1}H NMR spectrum of polymer **1a** (PEG-*b*-P(*n*BA)).

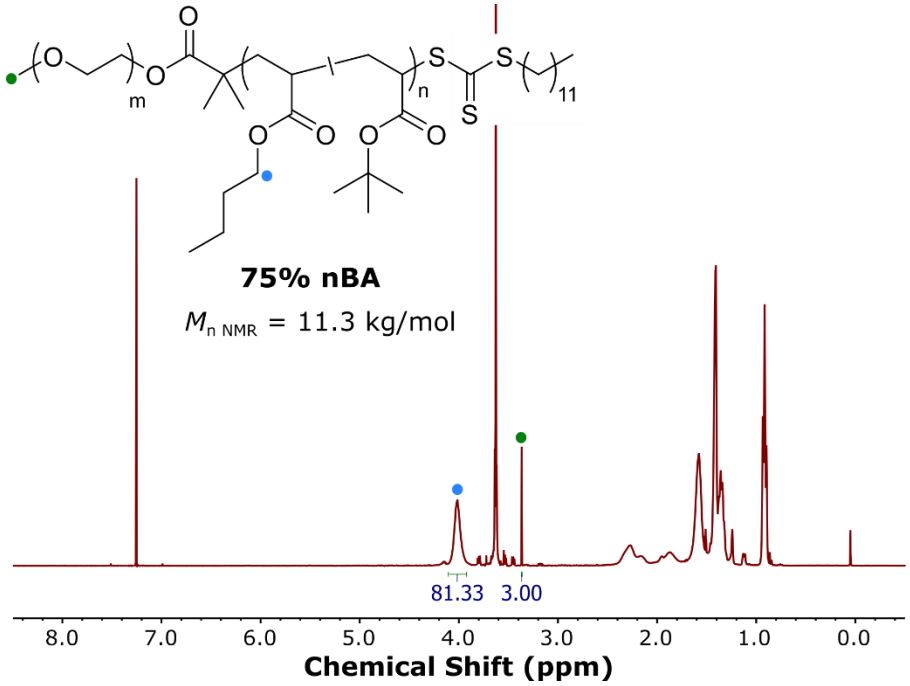

Figure S15. ^{1}H NMR spectrum of polymer **1b** (PEG-*b*-P(*n*BA-*ran*-*t*BA)).

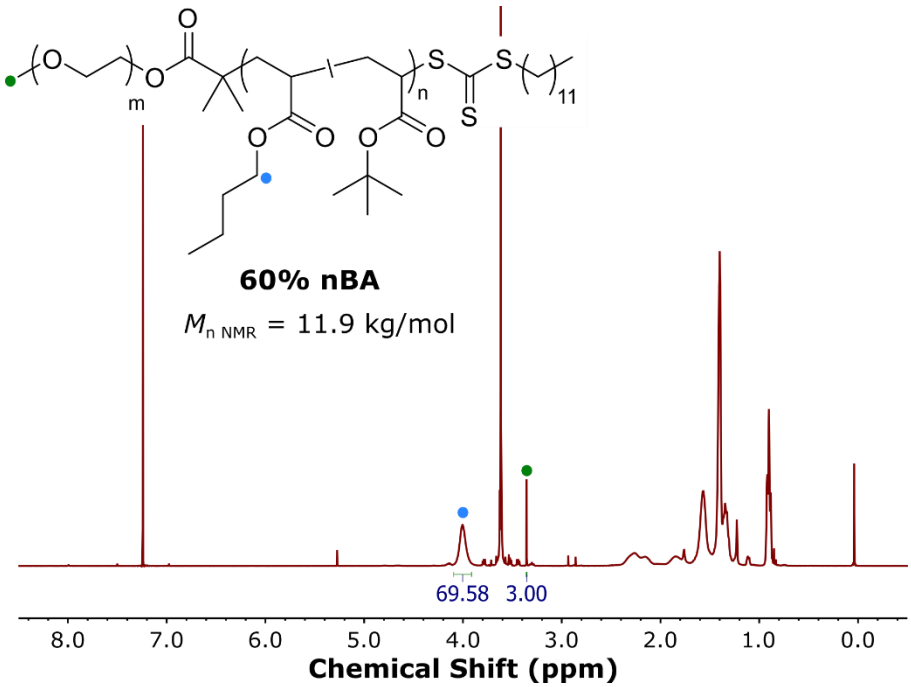

Figure S16. ^{1}H NMR spectrum of polymer **1c** (PEG-*b*-P(*n*BA-*ran*-*t*BA)).

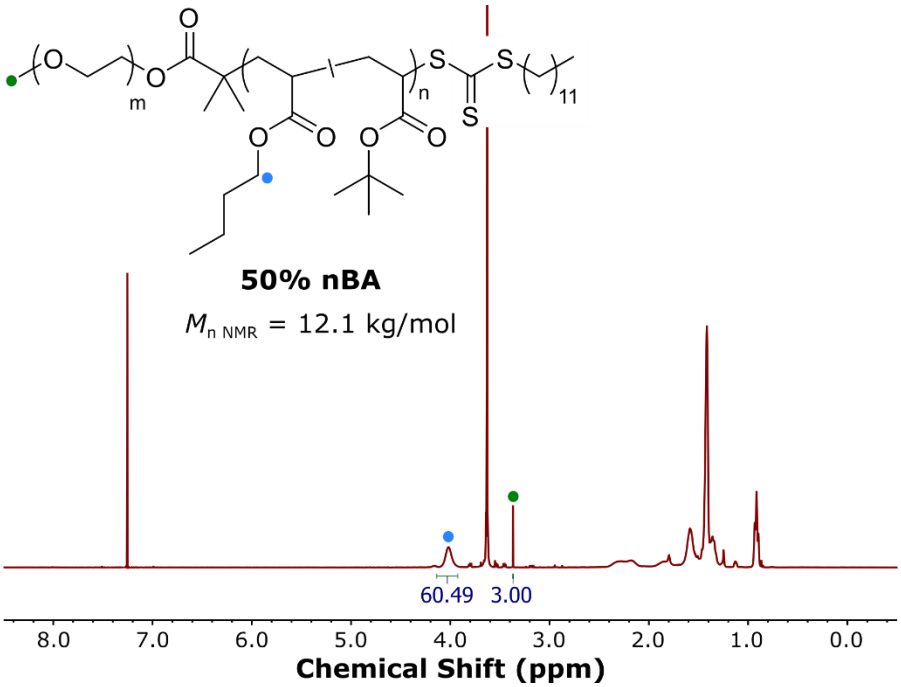

Figure S17. ^{1}H NMR spectrum of polymer **1d** (PEG-*b*-P(*n*BA-*ran*-*t*BA)).

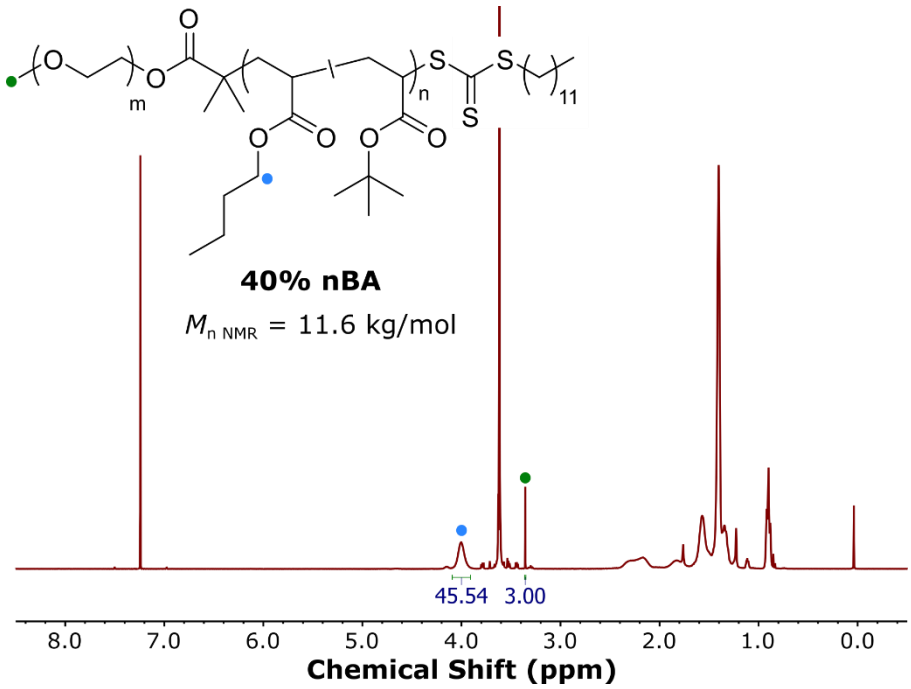

Figure S18. ^{1}H NMR spectrum of polymer **1e** (PEG-*b*-P(*n*BA-*ran*-*t*BA)).

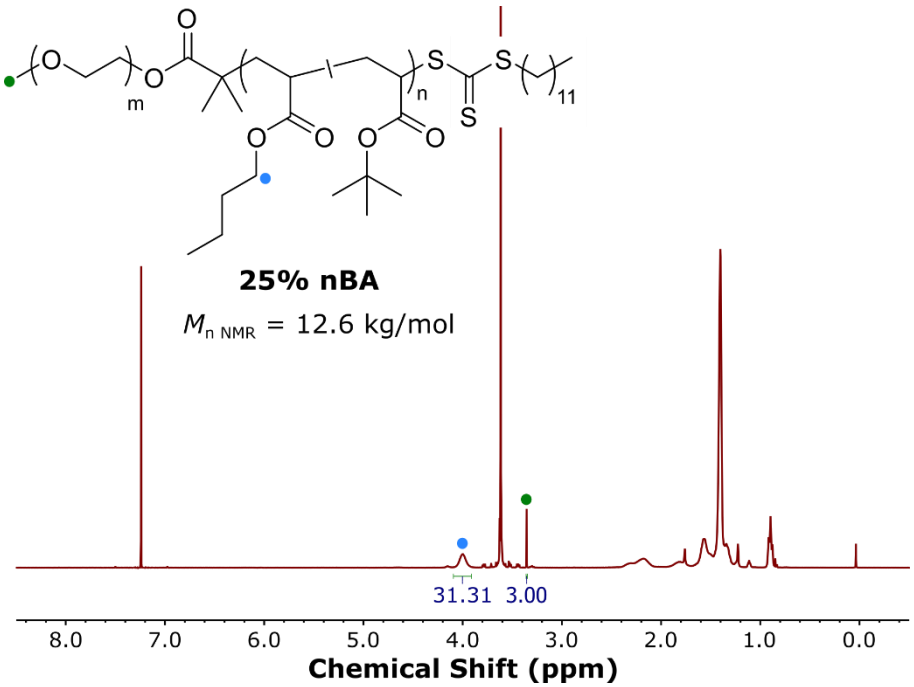

Figure S19. ^{1}H NMR spectrum of polymer **1f** (PEG-*b*-P(*n*BA-*ran*-*t*BA)).

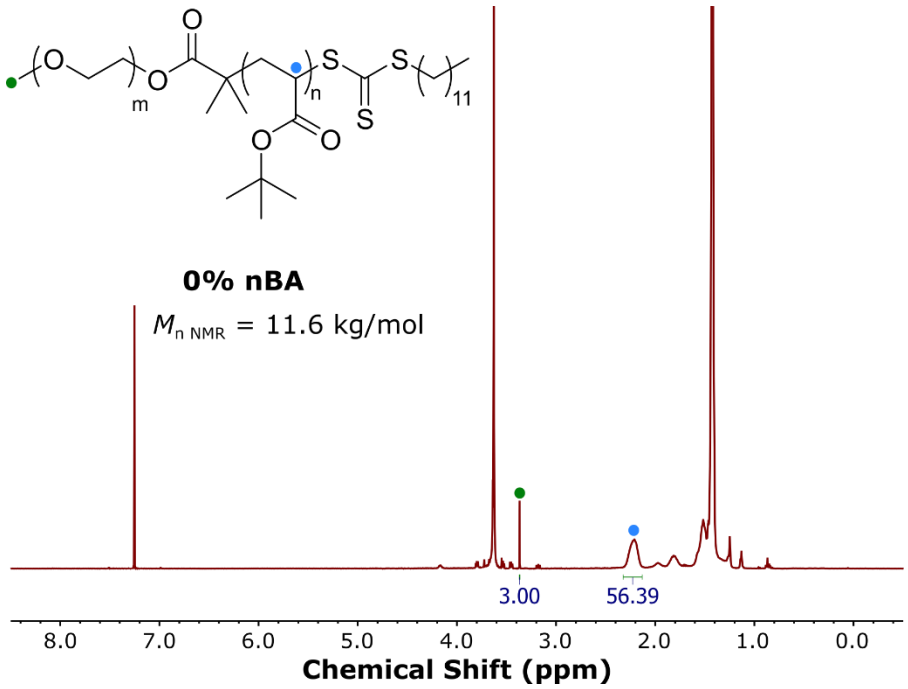

Figure S20. ^{1}H NMR spectrum of polymer **1g** (PEG-*b*-P(*t*BA)).

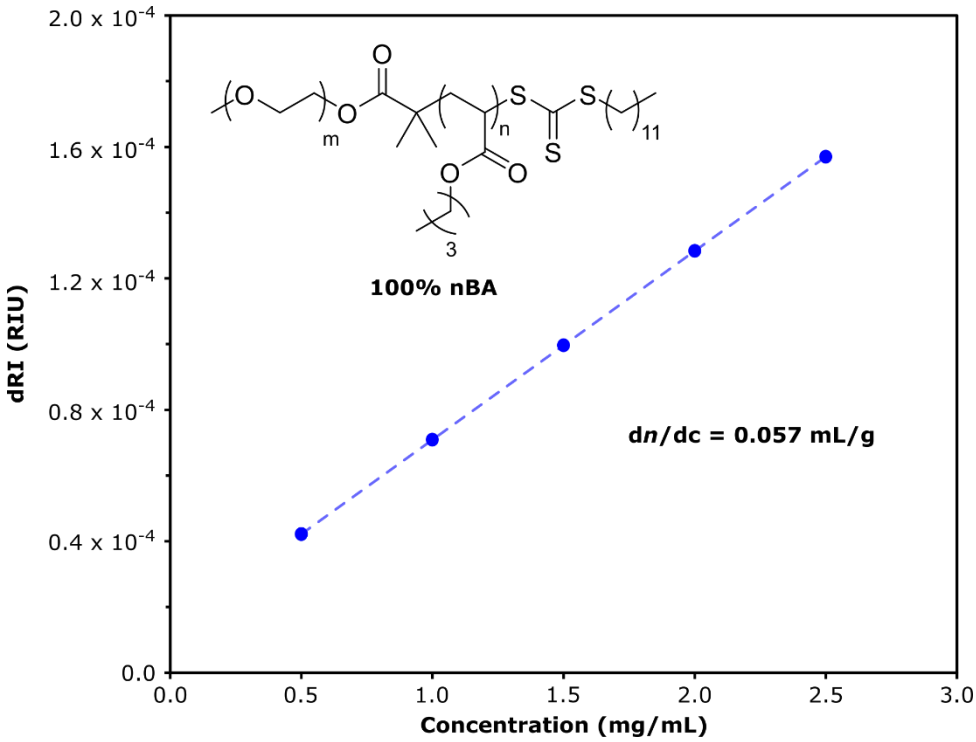

Figure S21. Concentration versus differential refractive index plot for polymer **1a** (PEG-*b*-P(*n*BA)). Measurements performed in THF at 25 °C.

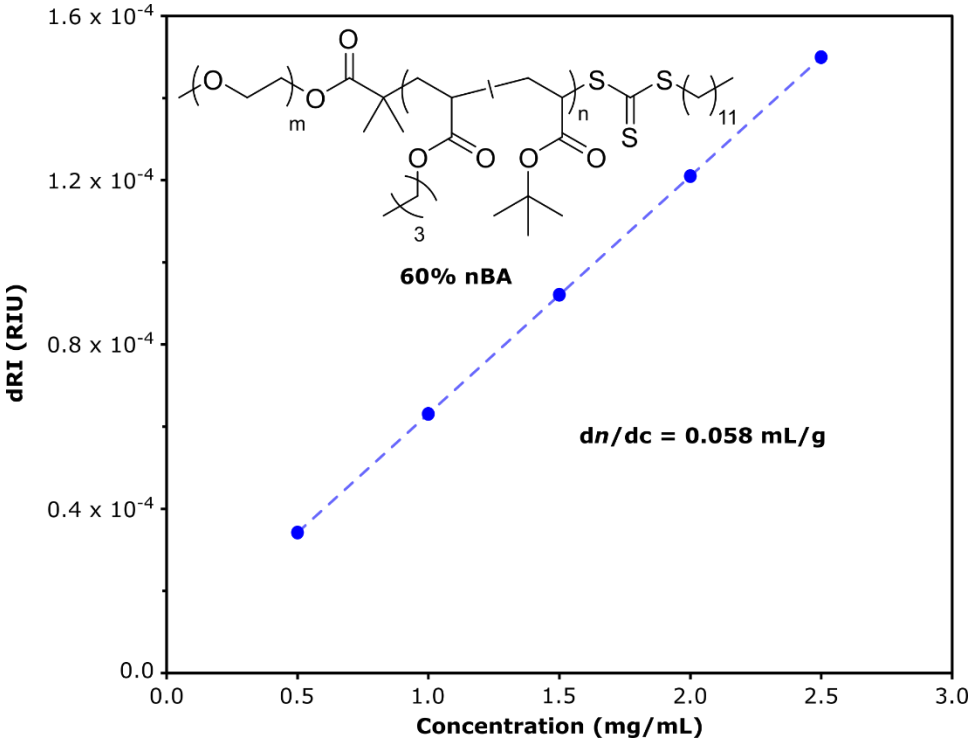

Figure S22. Concentration versus differential refractive index plot for polymer **1c** (PEG-*b*-P(*n*BA-*ran*-*t*BA)). Measurements performed in THF at 25 °C.

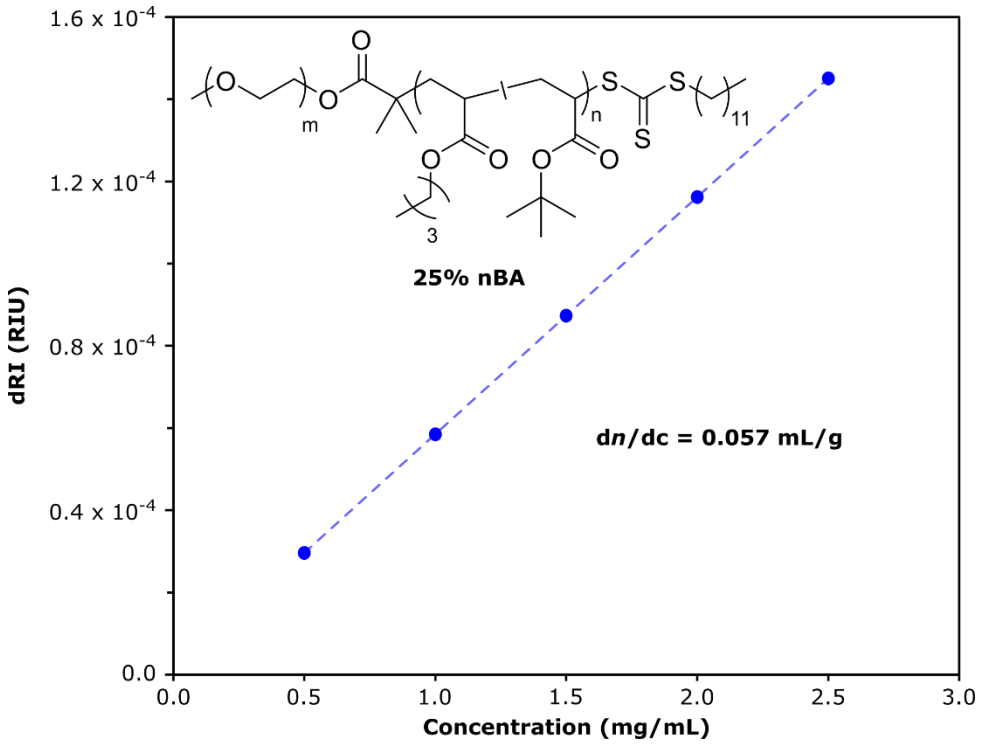

Figure S23. Concentration versus differential refractive index plot for polymer **1f** (PEG-*b*-P(*n*BA-*ran*-*t*BA)). Measurements performed in THF at 25 °C.

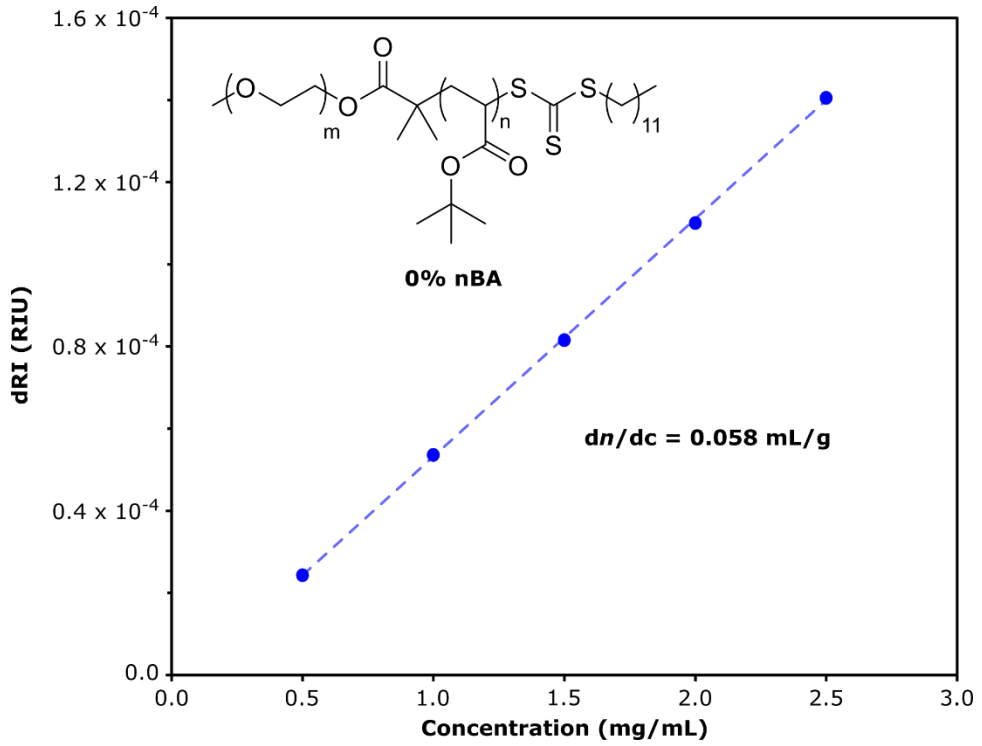

Figure S24. Concentration versus differential refractive index plot for polymer **1g** (PEG-*b*-P(*t*BA)). Measurements performed in THF at 25 °C.

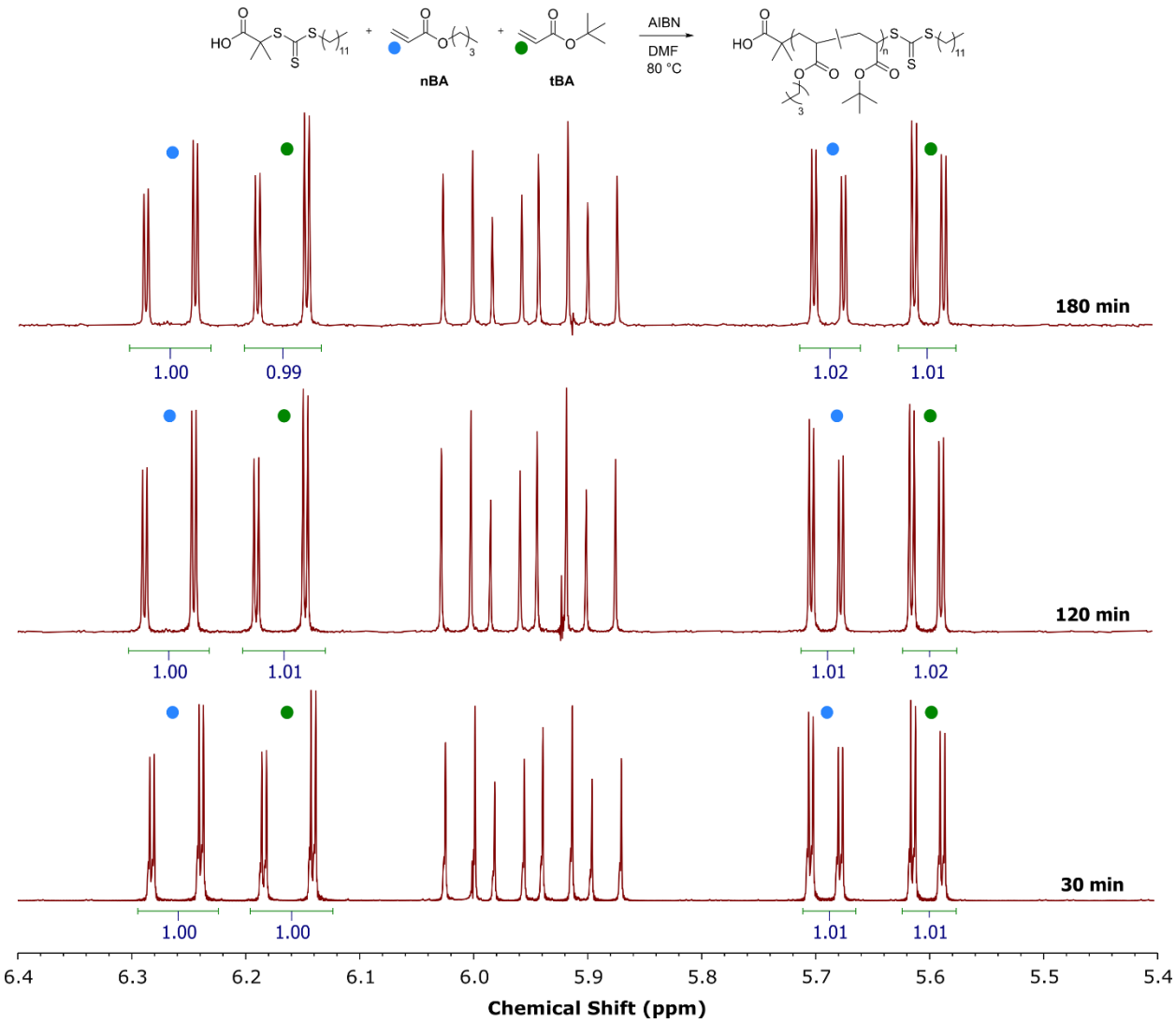

Figure S25. ^{1}H NMR spectra of aliquots of an *n*BA/*t*BA polymerization at several timepoints. The colored dots denote the vinyl proton signals of *n*BA or *t*BA monomer. The ratio of signals does not change over the course of the polymerization, signifying the monomers are incorporating into the polymer equally.

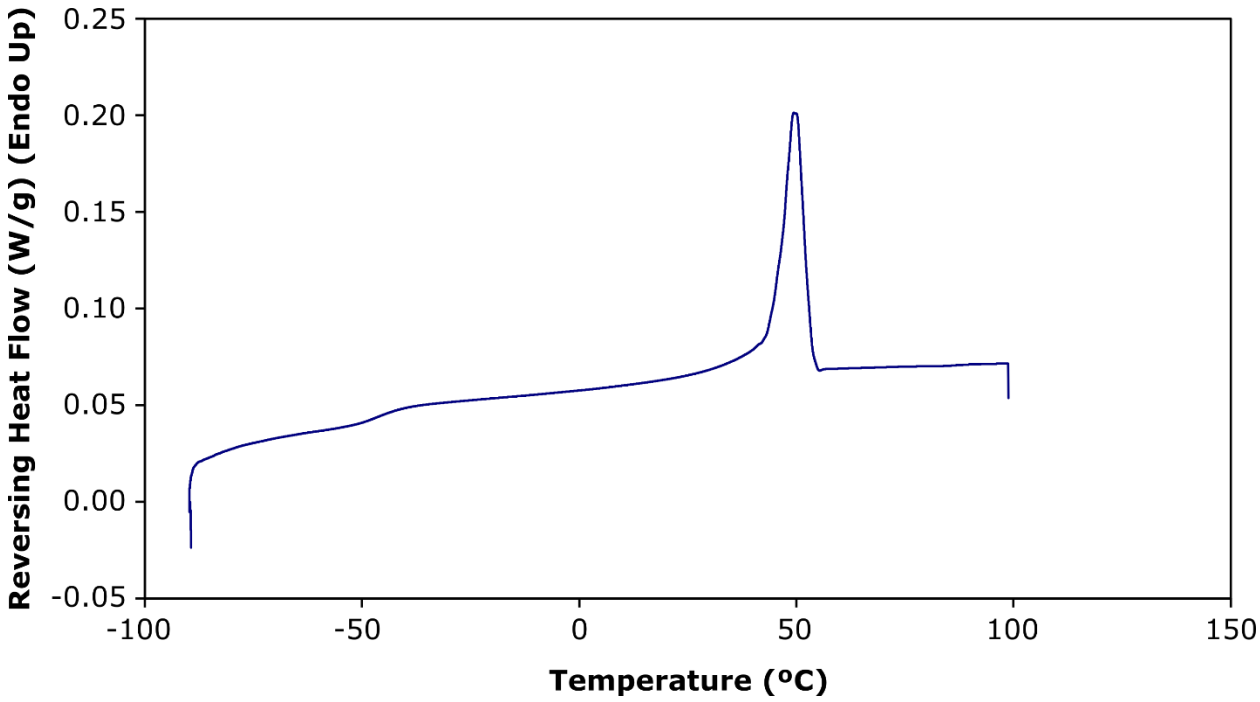

Figure S26. DSC trace of polymer **1a** (PEG-*b*-P(*n*BA)). Second heating cycle shown.

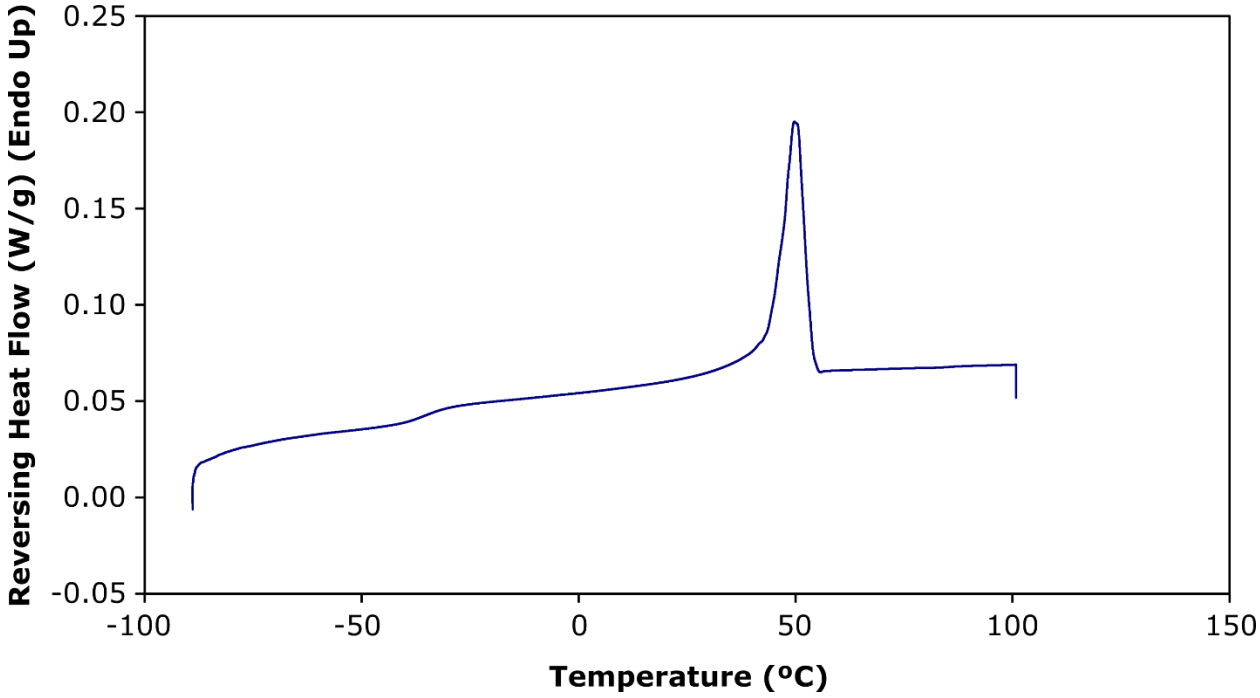

Figure S27. DSC trace of polymer **1b** (PEG-*b*-P(*n*BA-*ran*-*t*BA)). Second heating cycle shown.

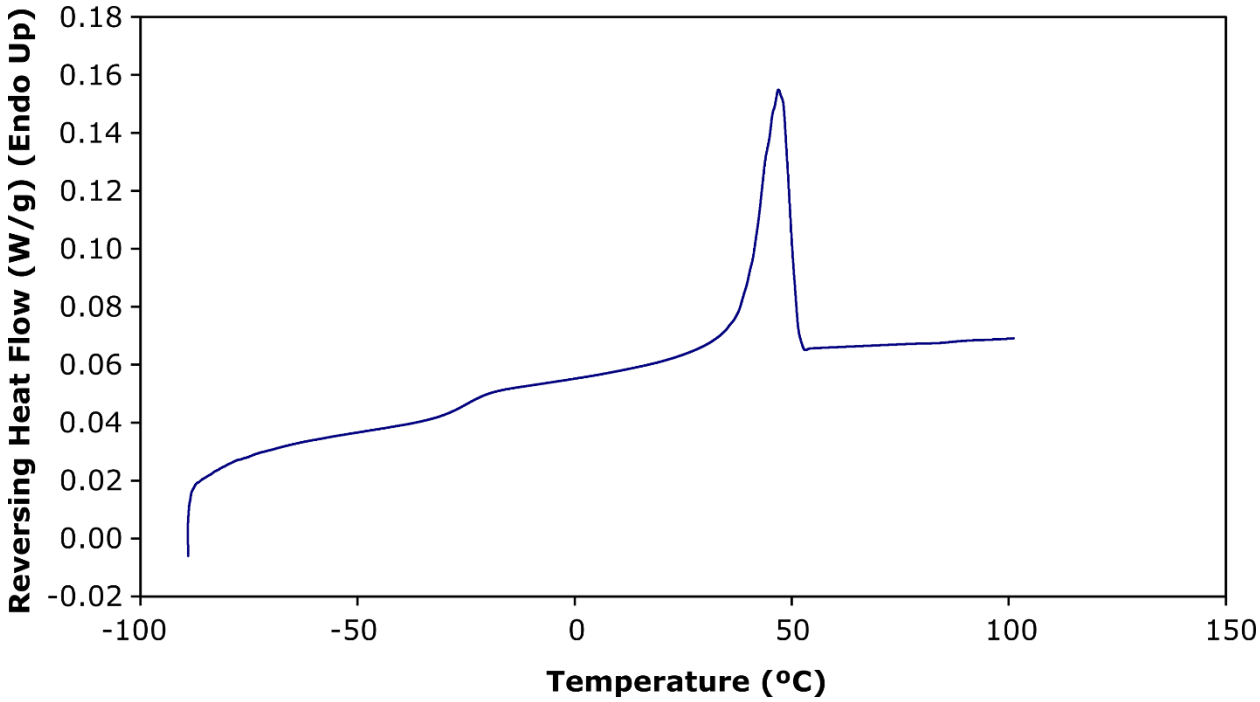

Figure S28. DSC trace of polymer **1c** (PEG-*b*-P(*n*BA-*ran*-*t*BA)). Second heating cycle shown.

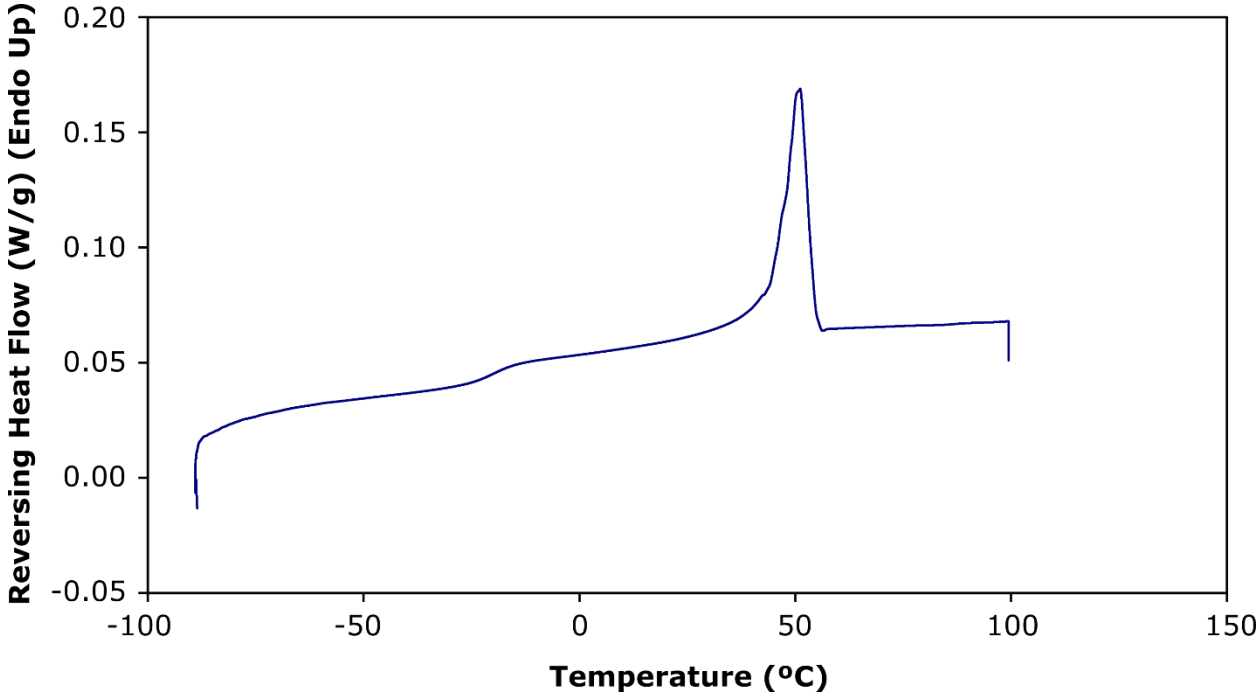

Figure S29. DSC trace of polymer **1d** (PEG-*b*-P(*n*BA-*ran*-*t*BA)). Second heating cycle shown.

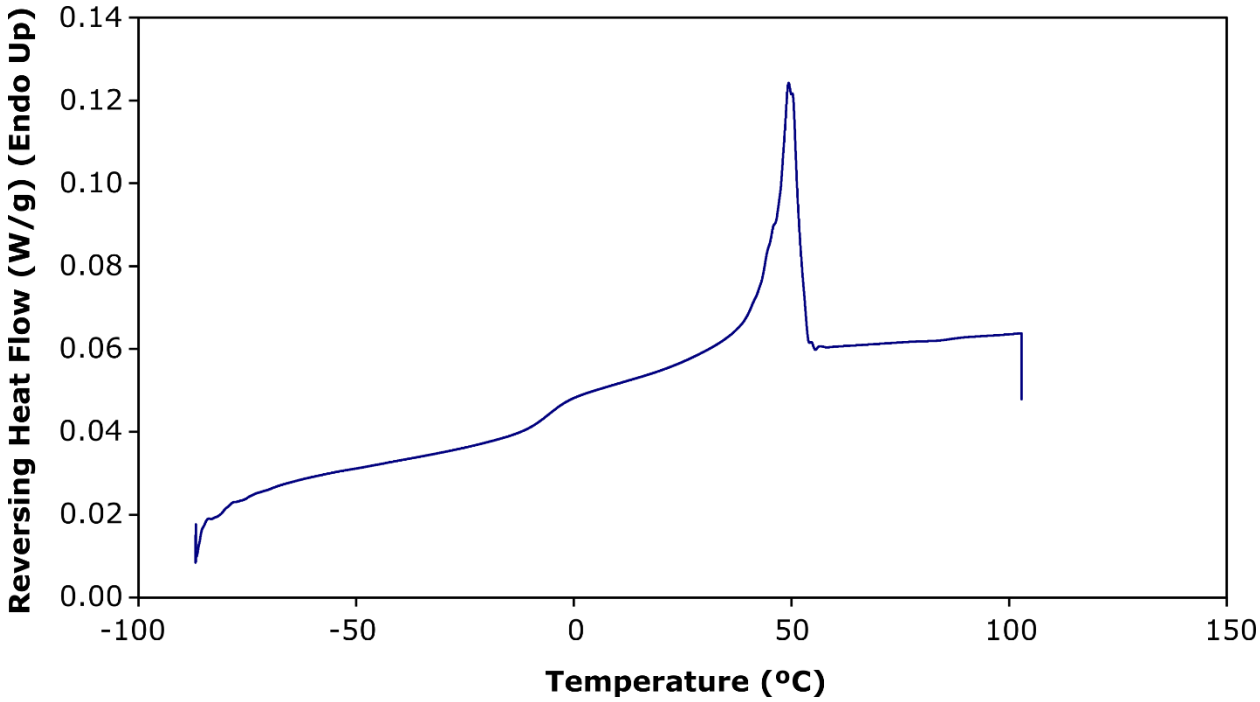

Figure S30. DSC trace of polymer **1e** (PEG-*b*-P(*n*BA-*ran*-*t*BA)). Second heating cycle shown.

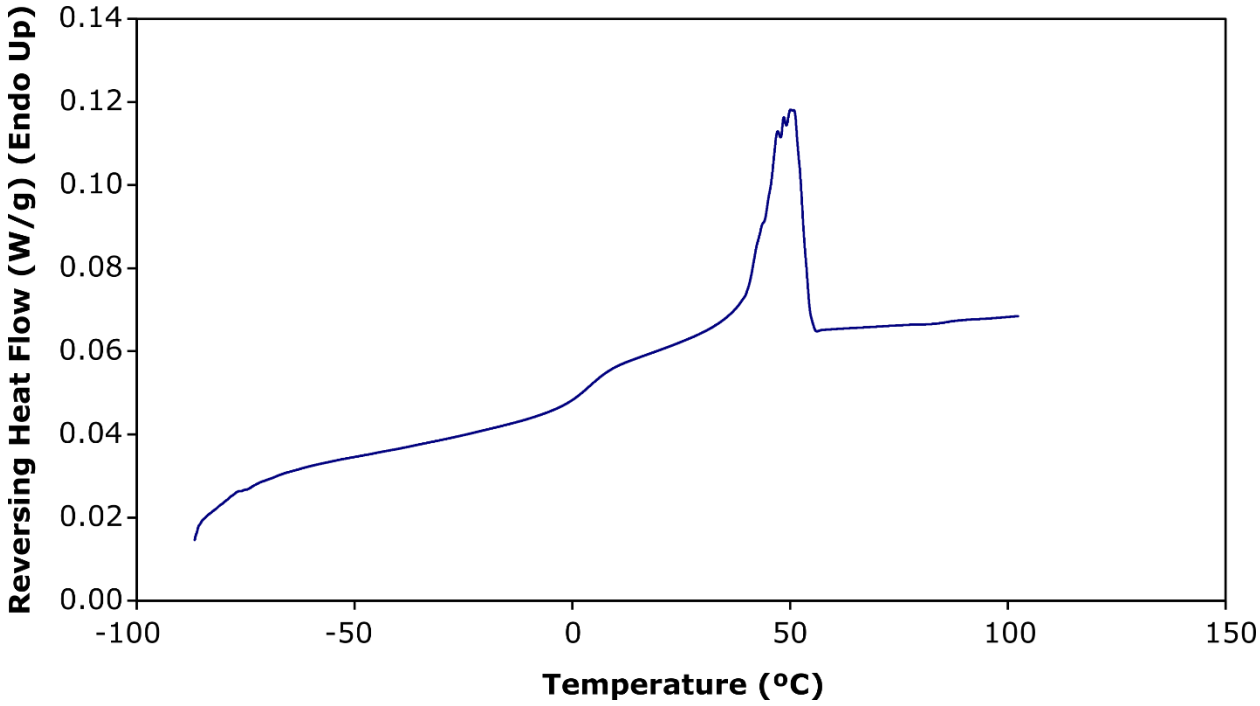

Figure S31. DSC trace of polymer **1e** (PEG-*b*-P(*n*BA-*ran*-*t*BA)). Second heating cycle shown.

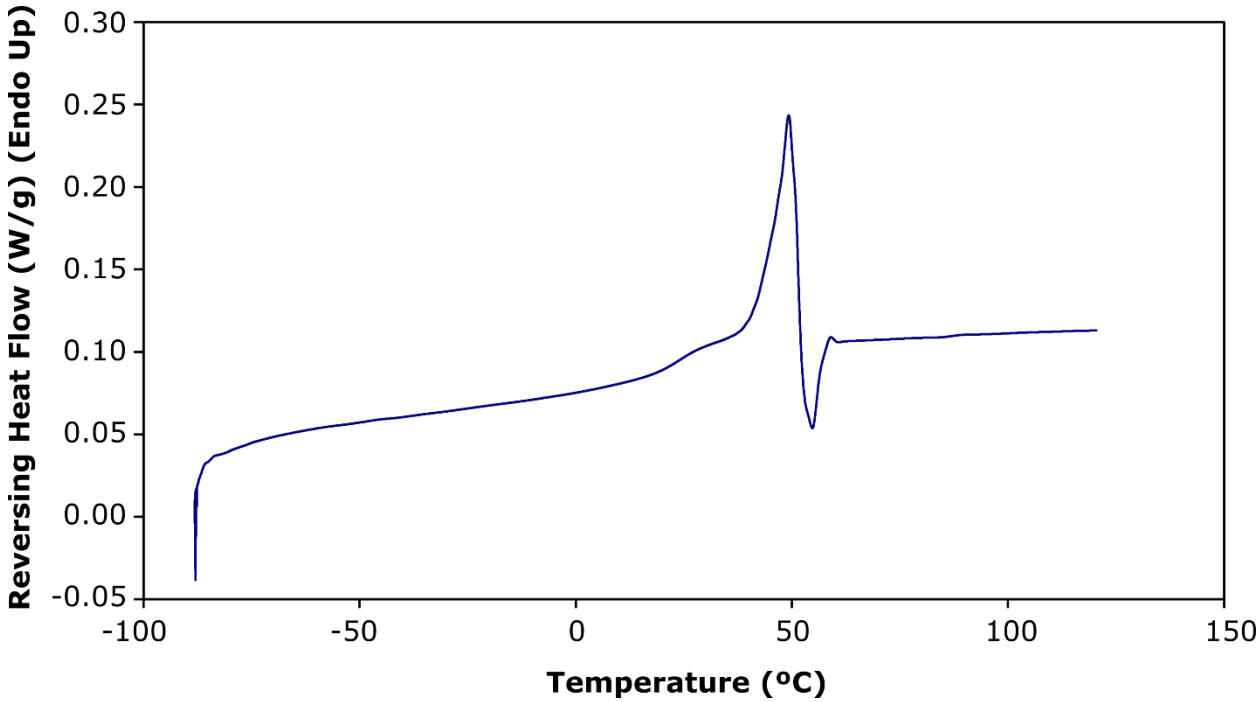

Figure S32. DSC trace of polymer **1g** (PEG-*b*-P(*t*BA)). Second heating cycle shown.

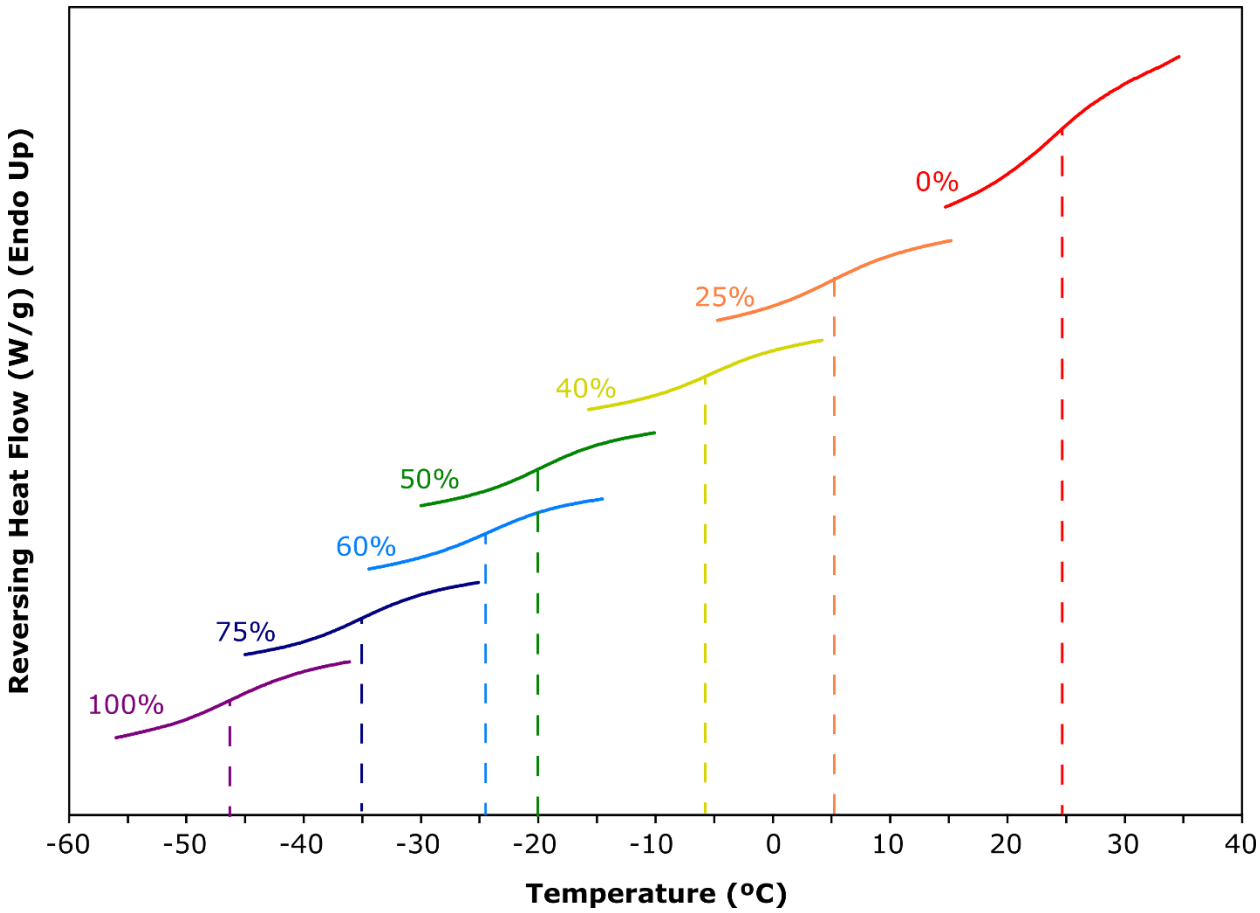

Figure S33. Excerpts from DSC traces of polymers **1a-g** highlighting glass transition temperatures for hydrophobic blocks. Second heating cycle shown.

NMR Solubility Experiments

A representative NMR solubility experiment is as follows: A one dram glass vial was charged with polymer **2a** (65 mg), fully protonated DMSO as an internal standard (19 mg), and D_2O (850 mg). The mixture was vortexed for 15 minutes and allowed to stand at room temperature overnight. The polymer did not fully dissolve and solid polymer settled to the bottom of the vial. The polymer-saturated D_2O solution was then transferred to an NMR tube, and a ^1H NMR spectrum was

obtained (256 scans, 5 s relaxation delay). Solubility was determined by comparing the proton signal from DMSO to the proton signal from the polymer (Figures S34 and S35).

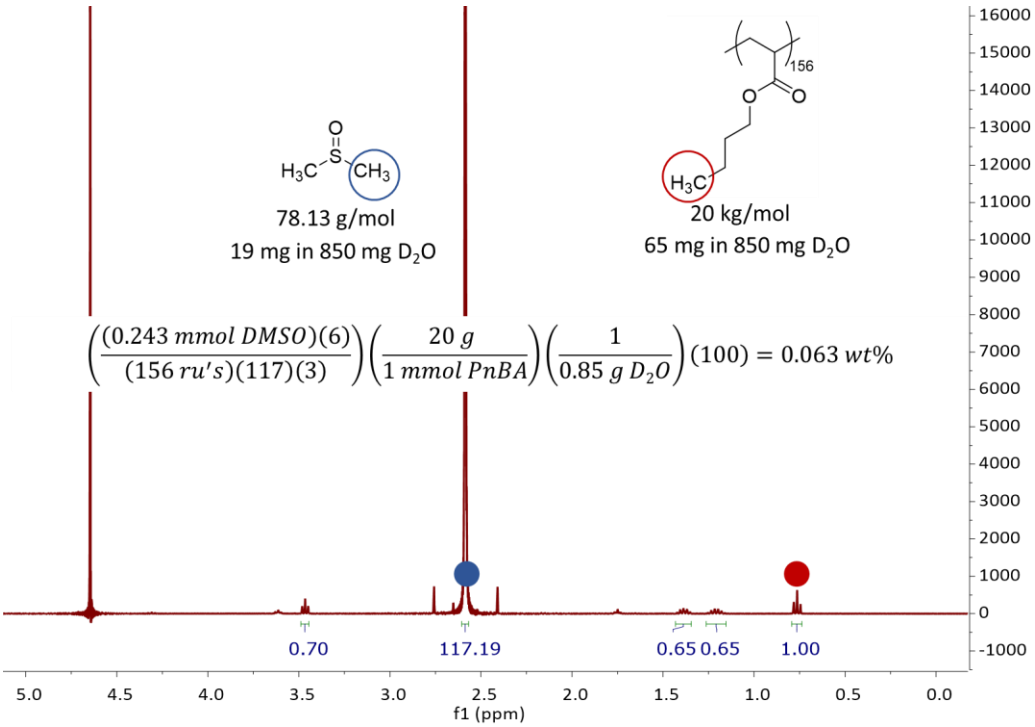

Figure S34. Solution ^{1}H NMR experiment showing the solubility of polymer **2a** in D_2O. Polymer was allowed to dissolve overnight prior to measurement.

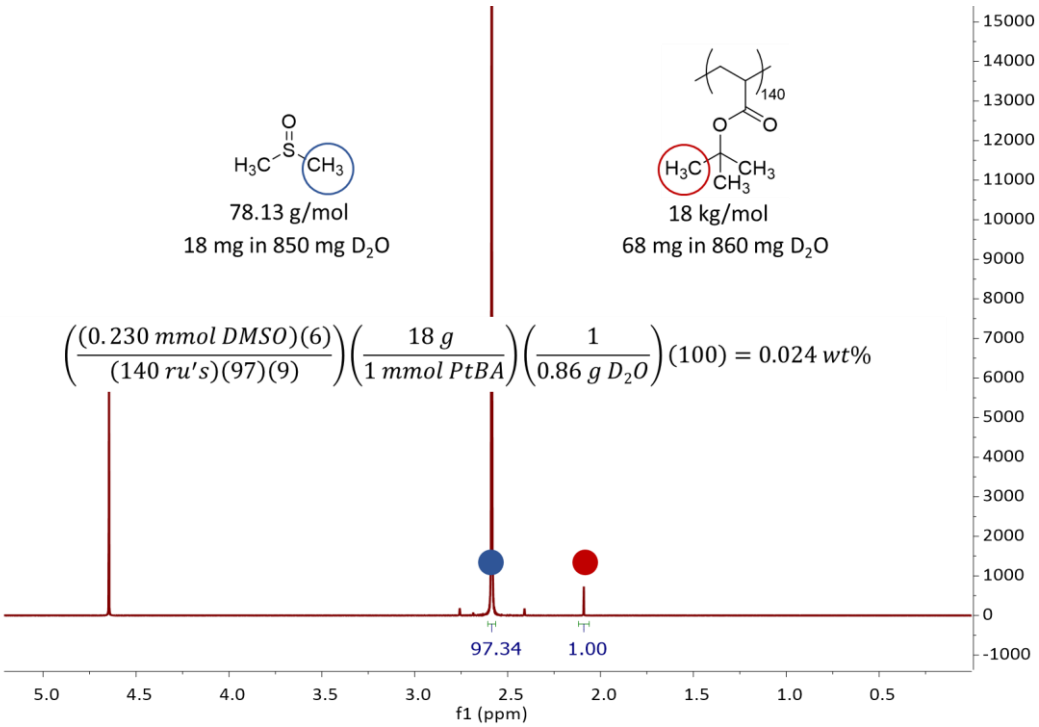

Figure S35. Solution ^{1}H NMR experiment showing the solubility of polymer **2c** in D_2O. Polymer was allowed to dissolve overnight prior to measurement.

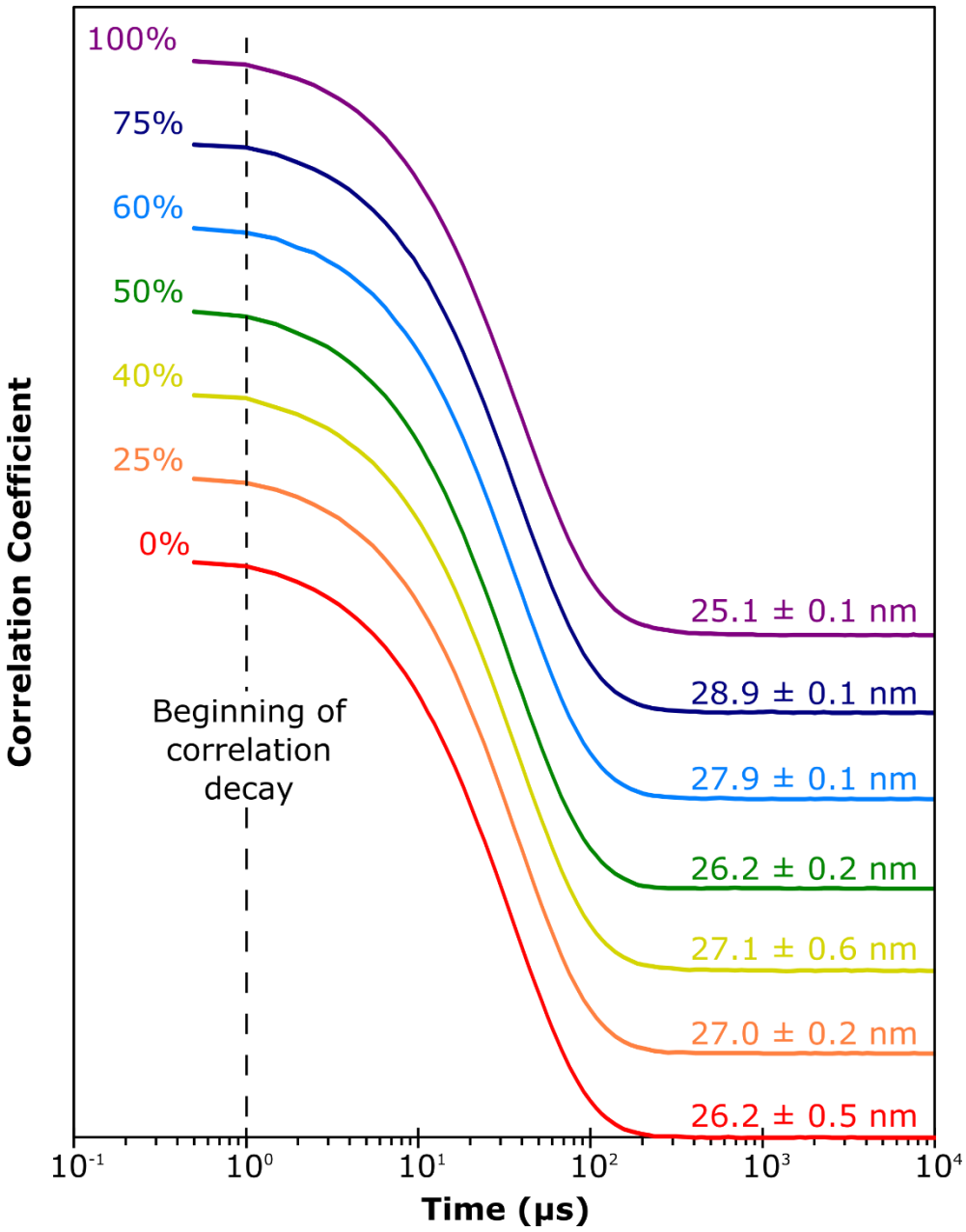

Figure S36. Correlation decay functions for micelle solutions (5 mg/mL in DI H_2O) of polymers **1a-g**. Intensity average hydrodynamic diameters calculated using CONTIN particle size distribution analysis.

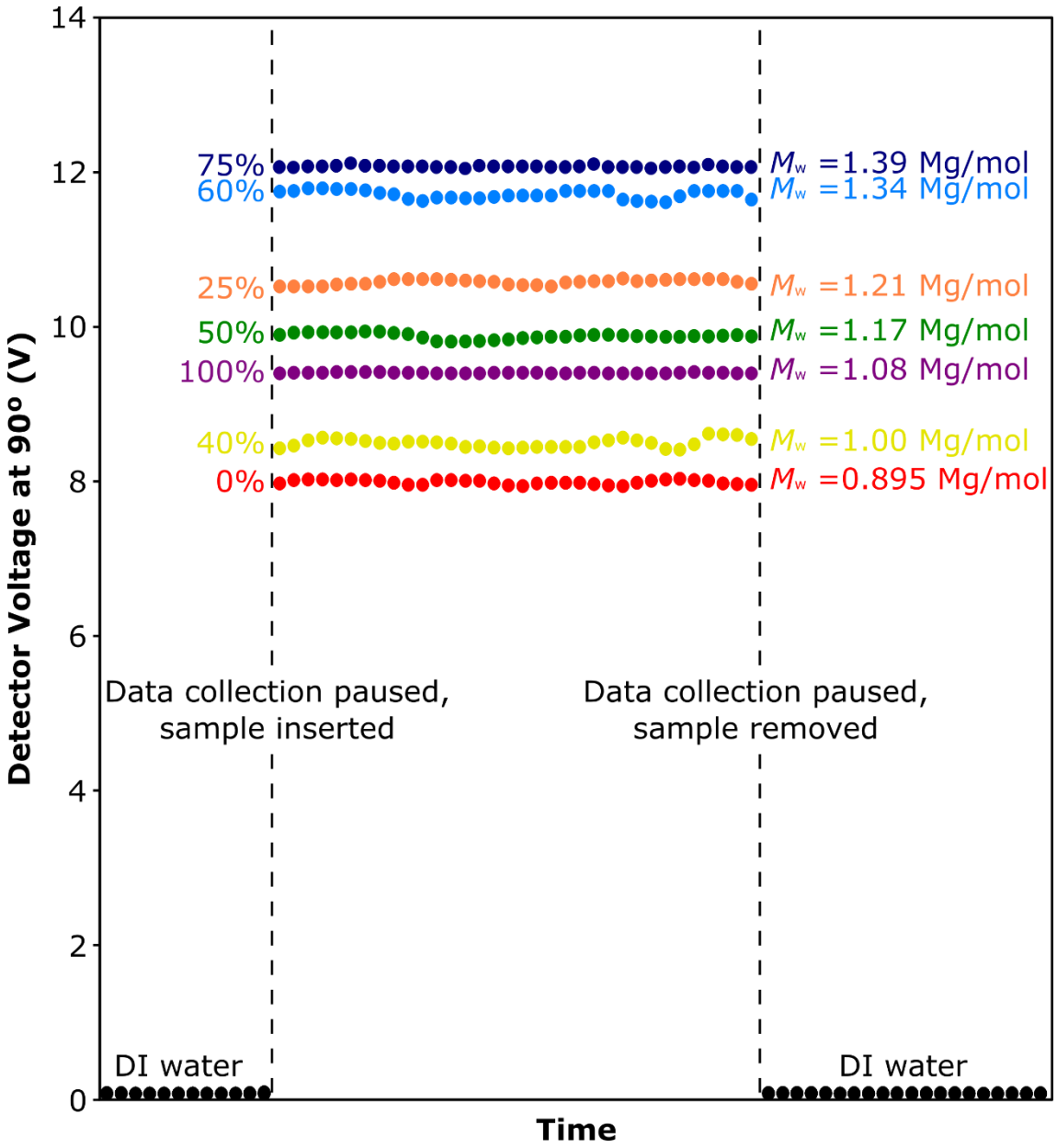

Figure S37. Static light scattering intensity at 90° for micelle solutions (5 mg/mL in DI H_2O) of polymers **1 a-g**. M_w calculated through multi-angle light scattering analysis using ASTRA VII software.

Equation S1.

$$N_{agg} = \frac{(M_w\ of\ polymer\ micelle)}{(M_w\ of\ block\ copolymer)}$$

Table S1. DLS Characterization of micelles from polymers **1a-g**.

Polymer	Mol% nBA[a]	Number average D_h (nm)[b]	Volume average D_h (nm)[b]	Intensity average D_h (nm)[b]	Micelle PDI[c]
1a	100	19.5 ± 0.1	21.9 ± 0.1	25.1 ± 0.1	0.014
1b	75	18.6 ± 0.1	19.5 ± 0.1	28.9 ± 0.1	0.110
1c	60	20.2 ± 0.1	23.4 ± 0.1	27.9 ± 0.1	0.060
1d	50	19.7 ± 0.2	22.3 ± 0.1	26.2 ± 0.2	0.046
1e	40	20.0 ± 0.1	22.9 ± 0.2	27.1 ± 0.6	0.051
1f	25	20.2 ± 0.2	23.1 ± 0.2	27.0 ± 0.2	0.043
1g	0	19.0 ± 0.2	21.9 ± 0.1	26.2 ± 0.5	0.059

[a] *n*BA/*t*BA molar ratio measured by ^{1}H NMR spectroscopy. [b] Hydrodynamic diameter measured by DLS at 5 mg/mL in DI H_2O. Result reported as average of 3 measurements with error reflecting standard deviation. [c] Micelle polydispersity index measured by DLS at 5 mg/mL in DI H_2O.

NMR diffusometry acquisition details and signal-decay plots

Self-diffusion coefficients of polymers in solution were determined using a 400 MHz (9.4 T) Bruker Avance III WB NMR spectrometer, equipped with a MIC probe coupled to a Diff60 single-axis (z) gradient. The pulsed-gradient stimulated echo (PGSTE) sequence[3] was used for ^{1}H diffusometry with a 90° RF pulse length of 4.5 μs, a half sinusoid gradient pulse length of δ = 3.14

ms (effective rectangular pulse length = 2 ms), diffusion time Δ = 25 ms, and post-gradient delay = 1 ms for all measurements. Maximum gradient strengths were adjusted in the range 200-500 $G \cdot cm^{-1}$ to achieve 80 – 99% signal attenuation in 32 steps. Sufficient signal-to-noise ratio (SNR) for each data point was achieved with 32 – 256 scans. Acquisition times and relaxation delay times were each 1 s, and 3 Hz line broadening was applied during data processing. Relaxation delay times of 1 s were used to allow complete relaxation for polymer signals. At elevated temperature, the sample was equilibrated for more than 10 min before running experiments at the set temperature to thermally equilibrate.

1D ^{1}H NMR spectra on micelle solutions were acquired with 32 scans, acquisition time of 1.5 s, relaxation delay time of 3 s, and processing with 3 Hz line broadening.

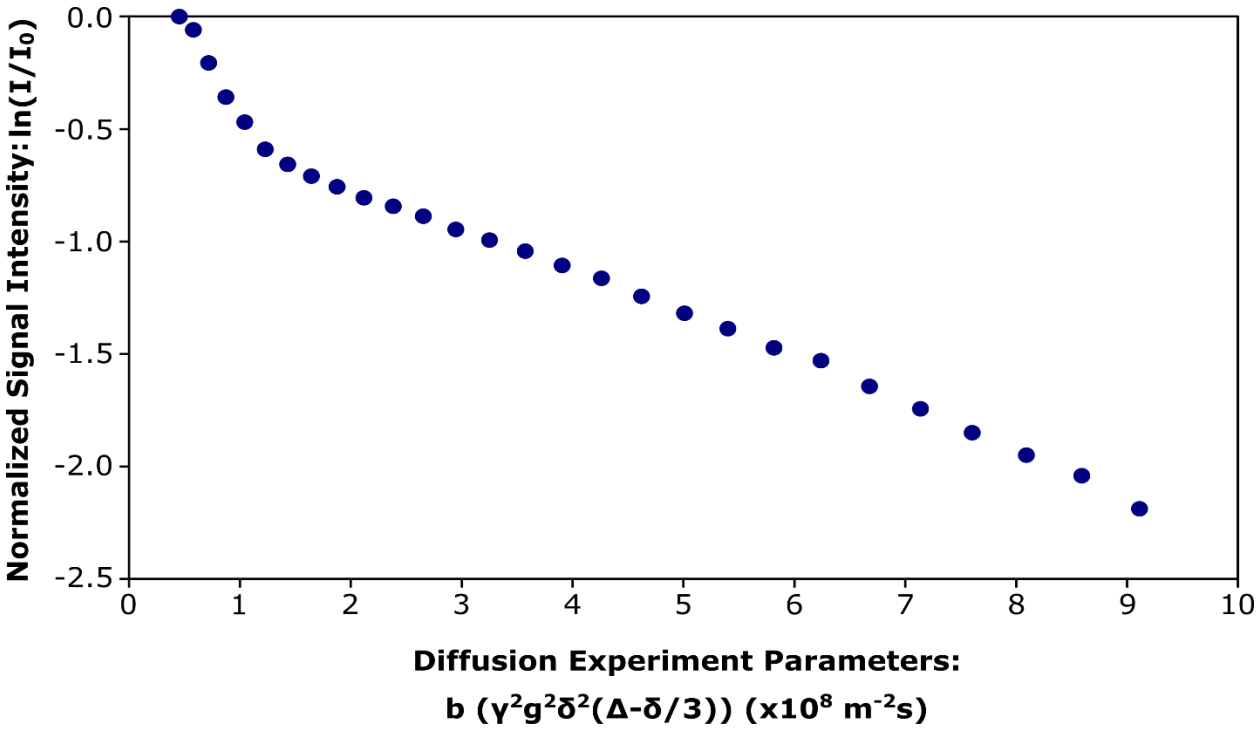

Figure S38. NMR diffusometry signal decay curve of micelle sample from polymer 1b (75% *n*BA) at 25 °C.

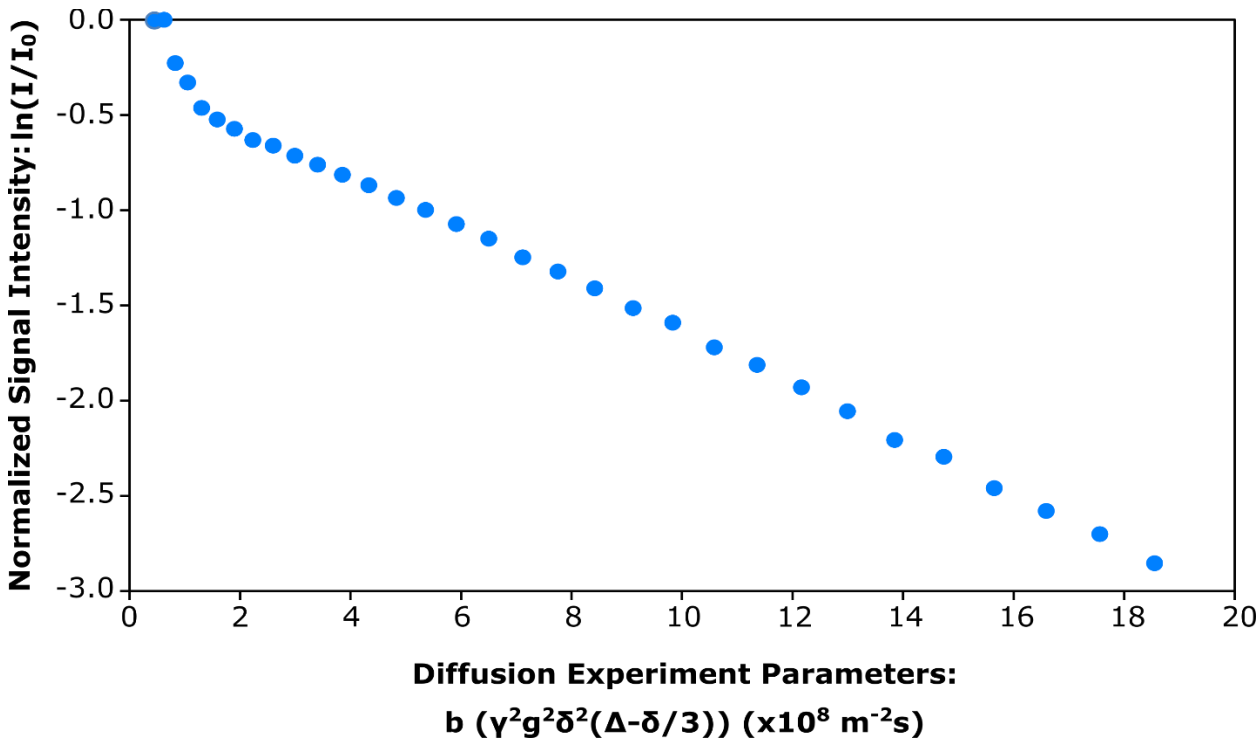

Figure S39. NMR diffusometry signal decay curve of micelle sample from polymer 1c (60% *n*BA) at 25 °C.

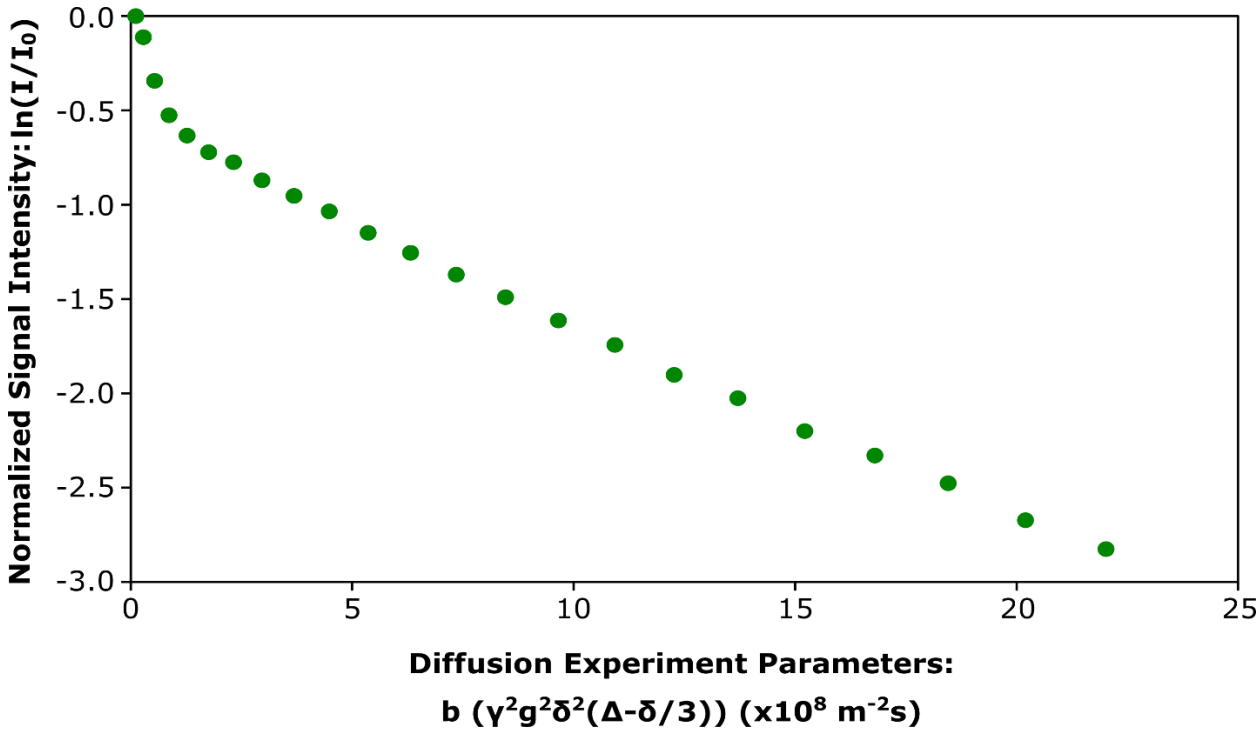

Figure S40. NMR diffusometry signal decay curve of micelle sample from polymer 1d (50% *n*BA) at 25 °C.

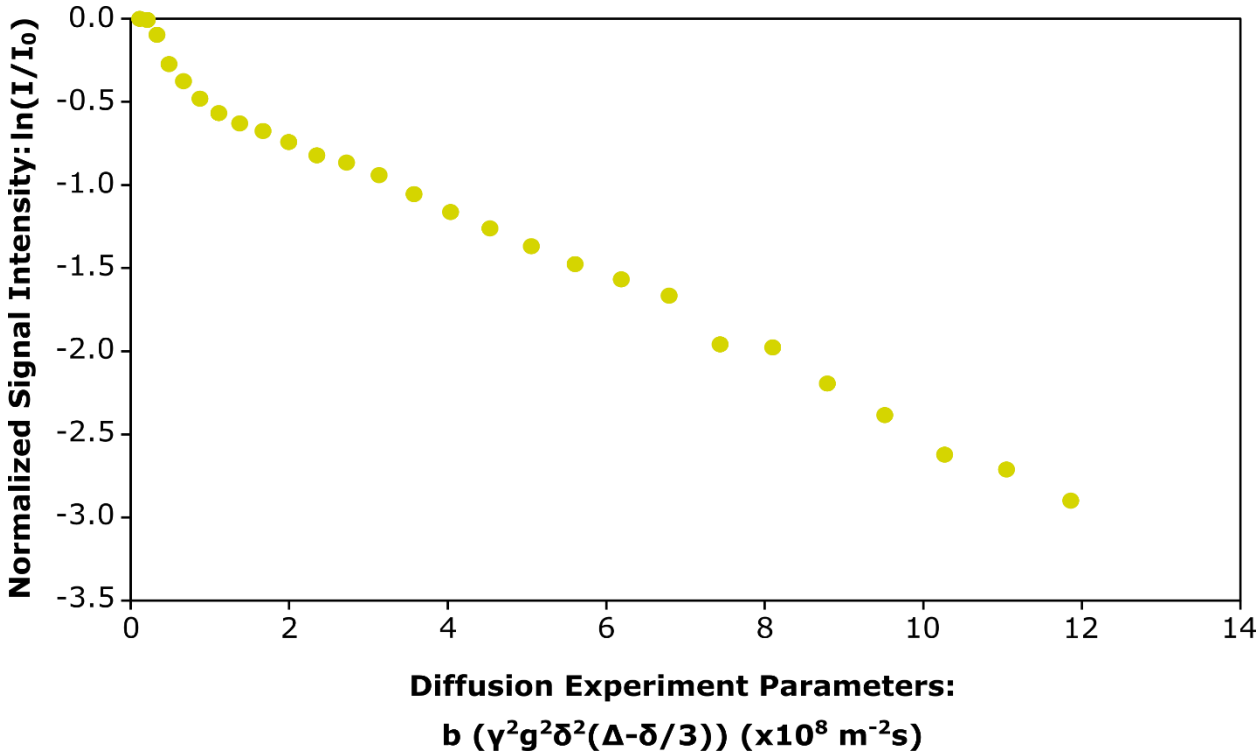

Figure S41. NMR diffusometry signal decay curve of micelle sample from polymer 1e (40% *n*BA) at 25 °C.

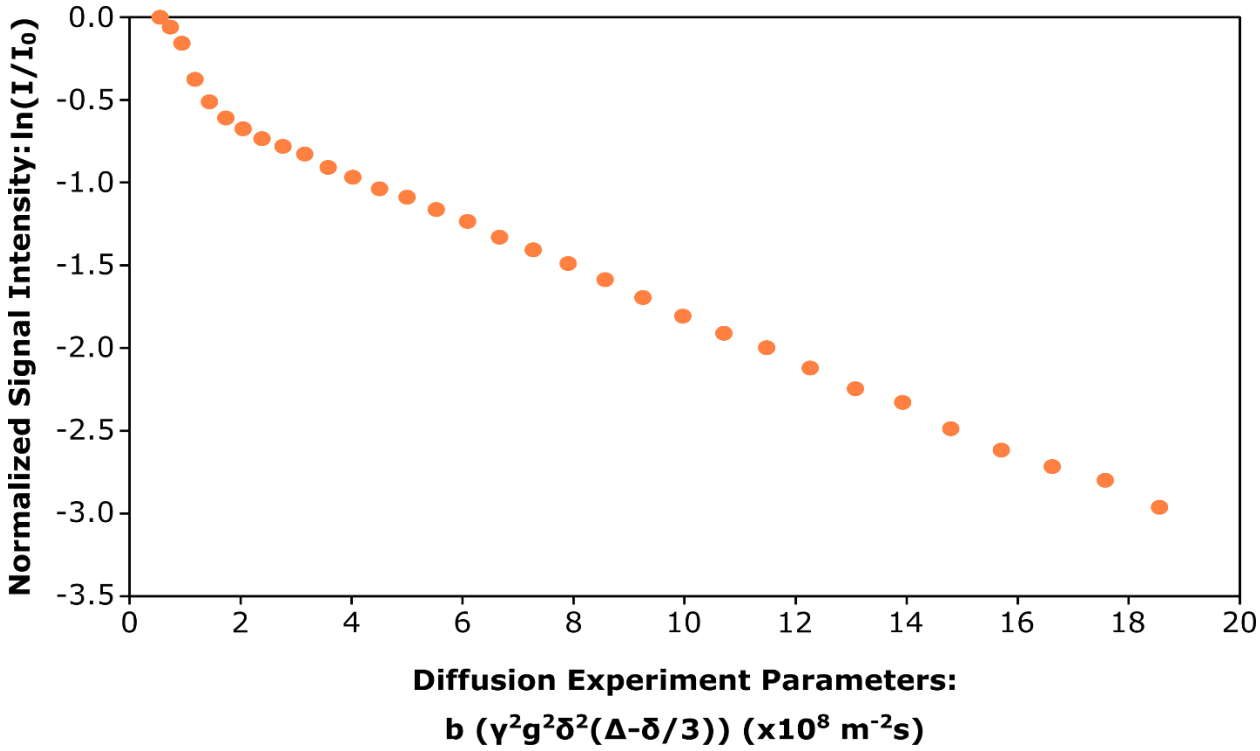

Figure S42. NMR diffusometry signal decay curve of micelle sample from polymer 1f (25% *n*BA) at 25 °C.

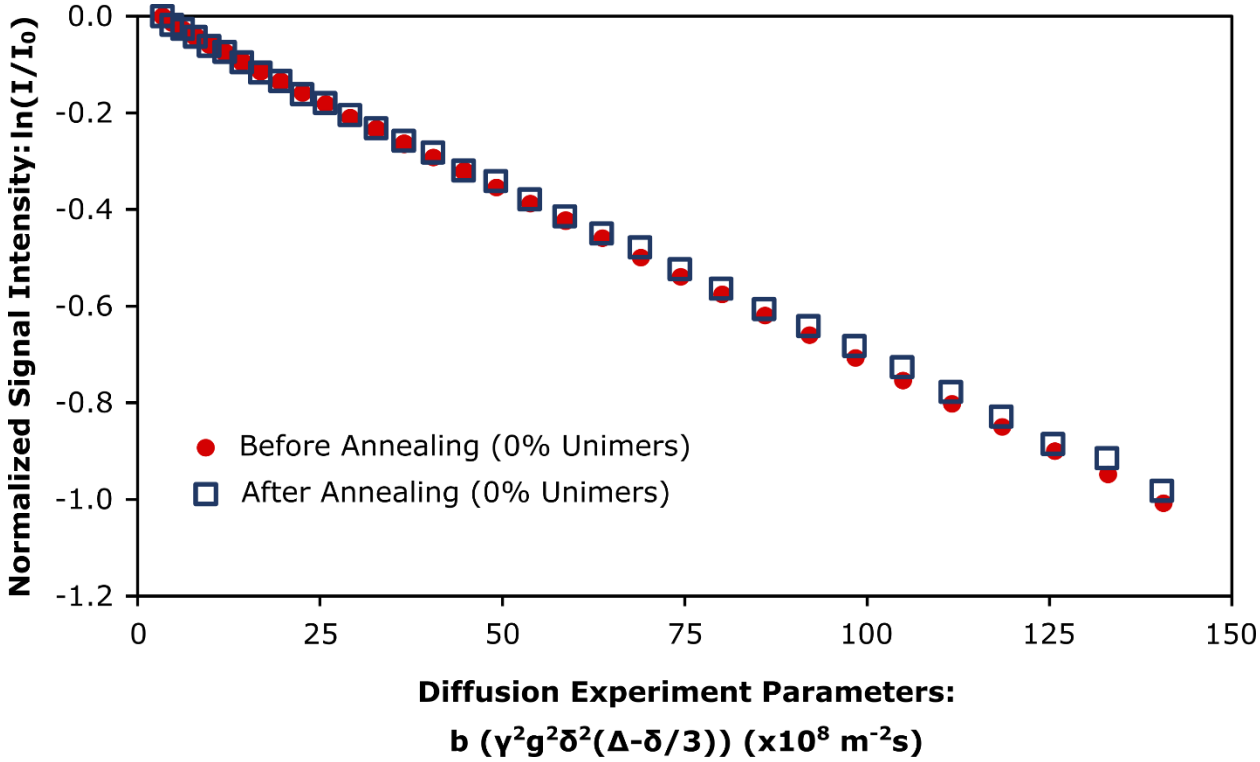

Figure S43. NMR diffusometry signal decay curve of micelle sample from polymer 1g (0% *n*BA) at 25 °C before and after thermal annealing. The temperature was held at 60 °C for one hour prior to second measurement. The sample, at each temperature, was equilibrated for at least 30 minutes before diffusion experiments were performed. Free unimer percentage did not depend on thermal history.

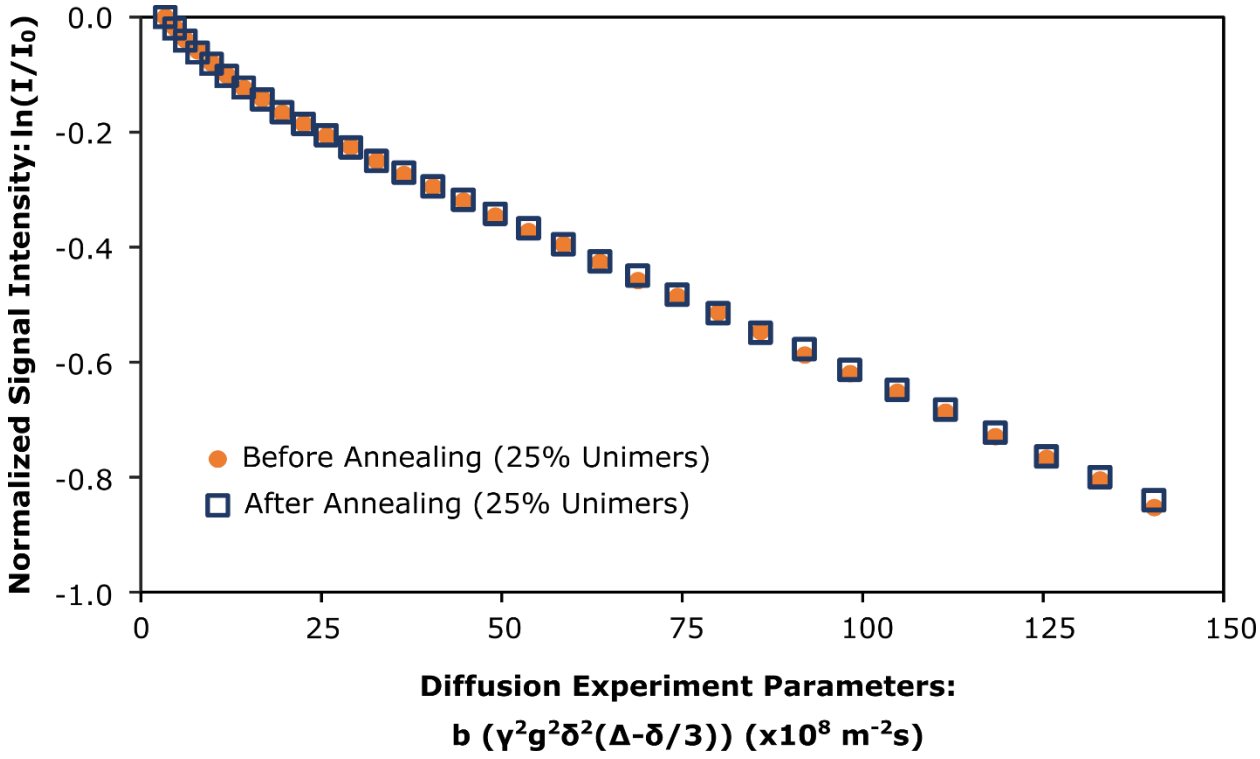

Figure S44. NMR diffusometry signal decay curve of micelle sample from polymer 1f (25% *n*BA) at 25 °C before and after thermal annealing. The temperature was held at 60 °C for one hour prior to second measurement. The sample, at each temperature, was equilibrated for at least 30 minutes before diffusion experiments were performed. Free unimer percentage did not depend on thermal history.

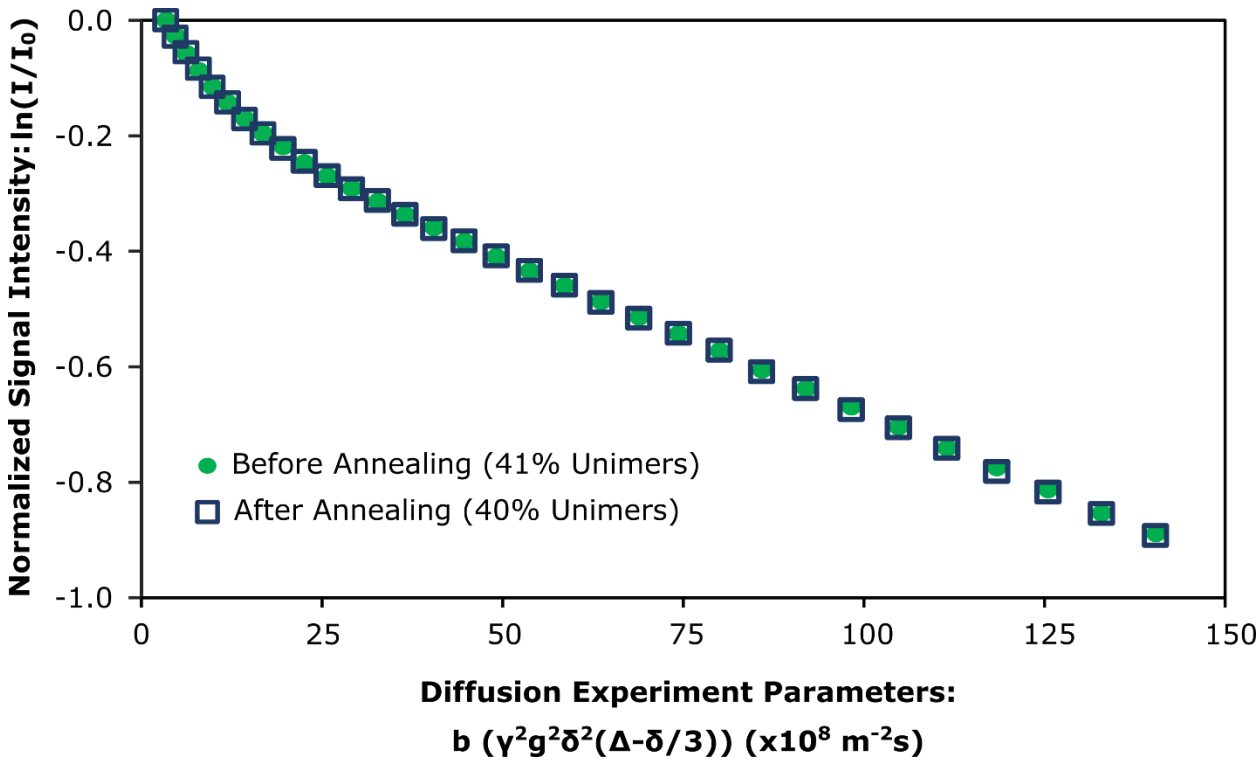

Figure S45. NMR diffusometry signal decay curve of micelle sample from polymer 1d (50% *n*BA) at 25 °C before and after thermal annealing. The temperature was held at 60 °C for one hour prior to second measurement. The sample, at each temperature, was equilibrated for at least 30 minutes before diffusion experiments were performed. Free unimer percentage did not depend on thermal history.

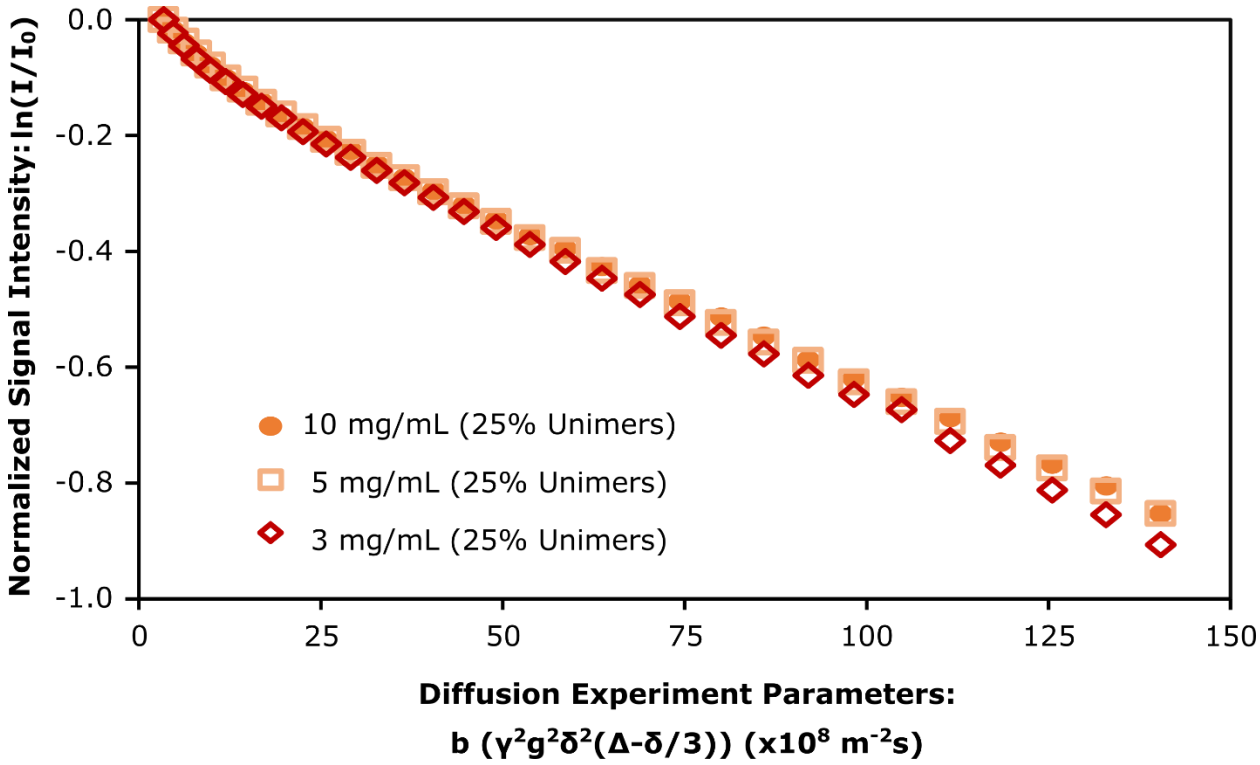

Figure S46. NMR diffusometry signal decay curve of micelle samples from polymer 1f (25% *n*BA) at 10, 5, and 3 mg/mL at 25 °C. The samples, at each concentration, were equilibrated for at least 30 minutes before diffusion experiments were performed. Free unimer percentage did not depend on total polymer concentration.

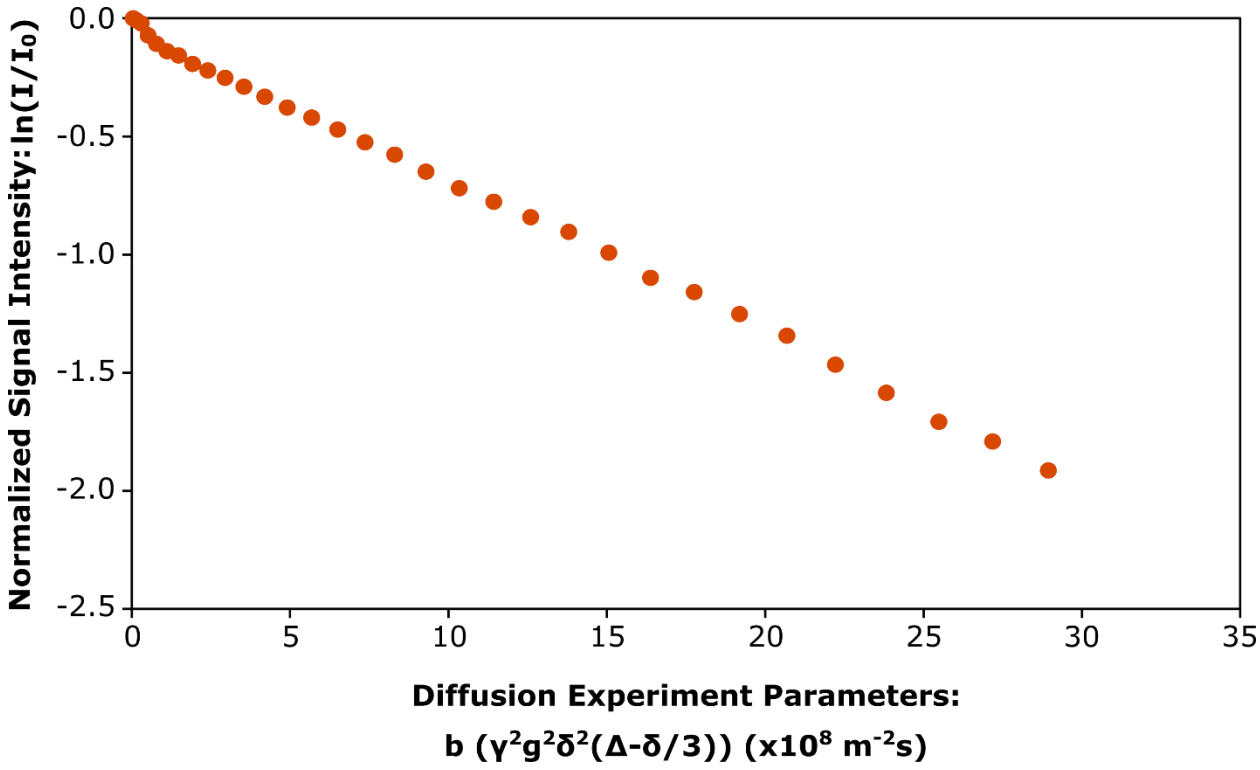

Figure S47. NMR diffusometry signal decay curve of micelle sample from polymer 1f (25% *n*BA) at 15 °C.

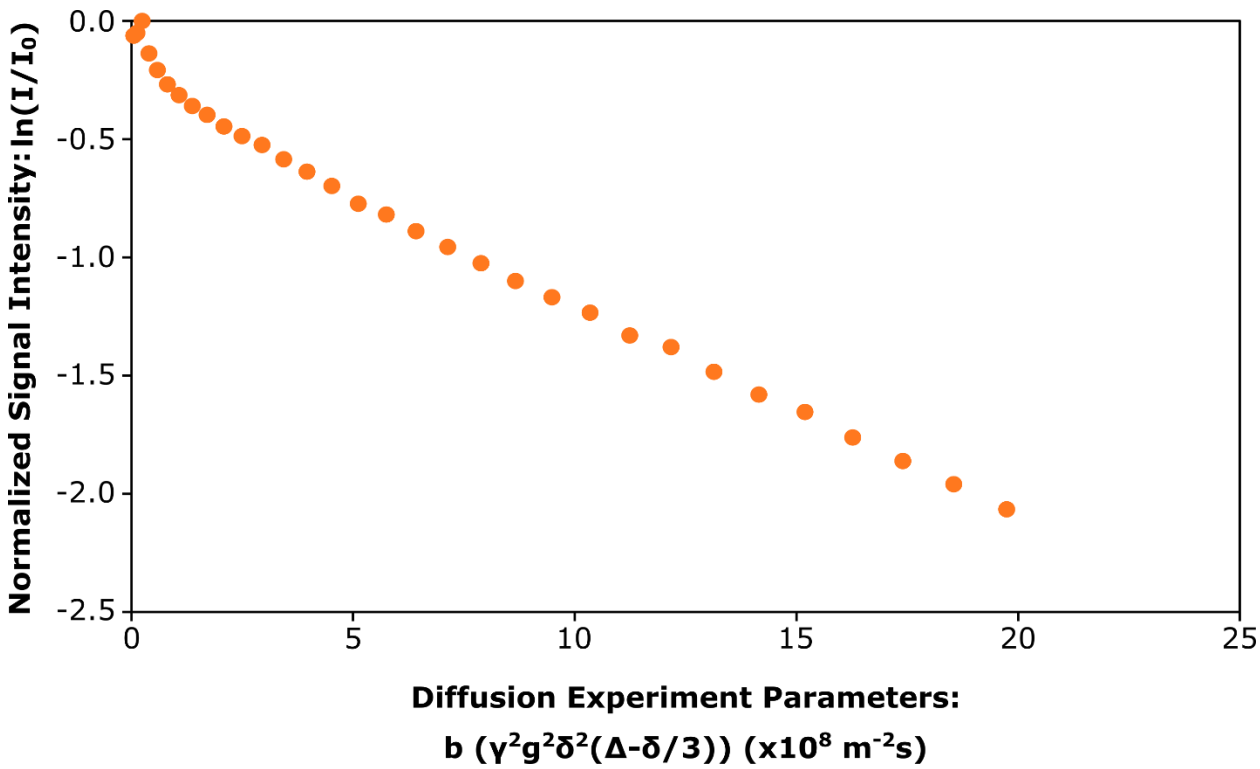

Figure S48. NMR diffusometry signal decay curve of micelle sample from polymer 1f (25% *n*BA) at 35 °C.

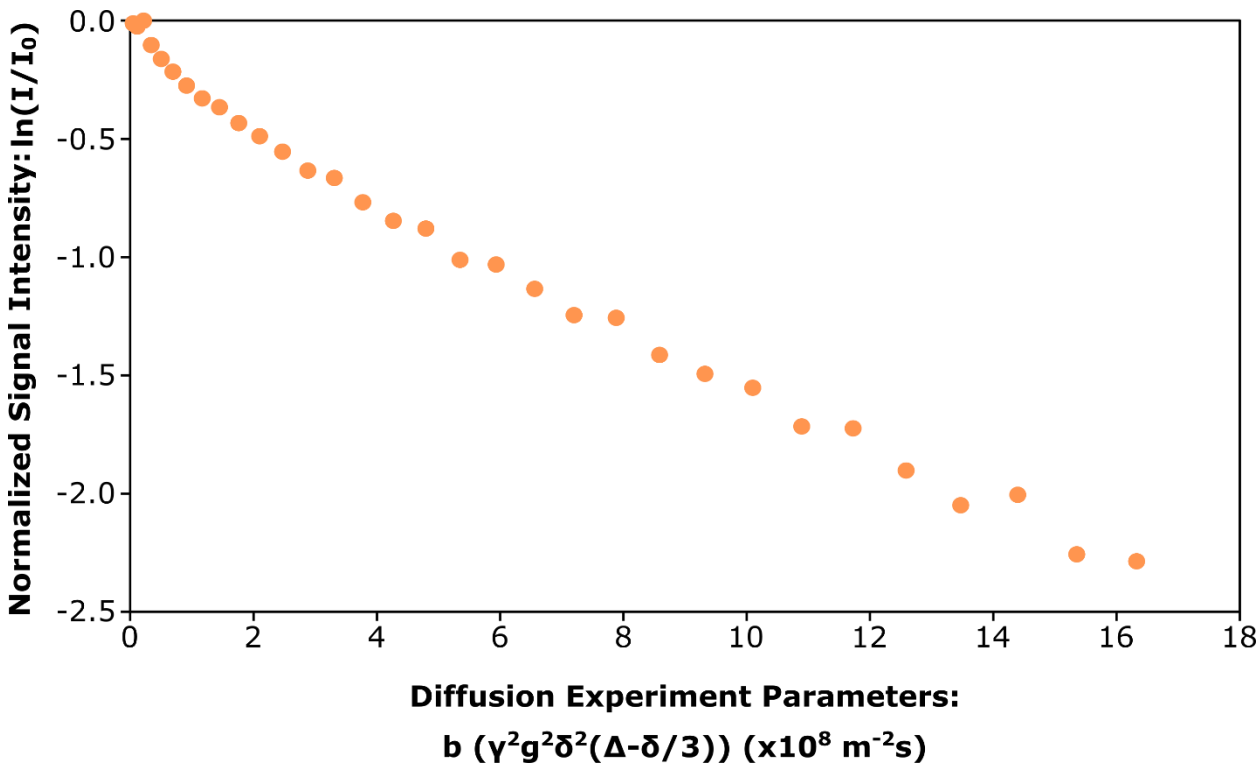

Figure S49. NMR diffusometry signal decay curve of micelle sample from polymer 1f (25% *n*BA) at 45 °C.

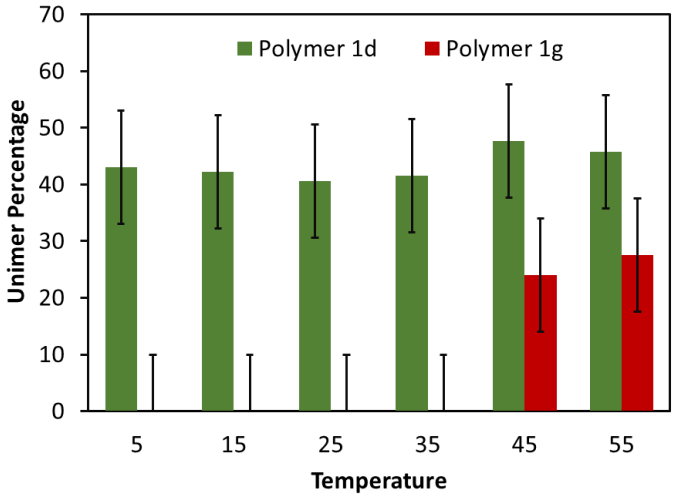

Figure S50. Unimer percentages derived from signal decay curves for 0% *n*BA (red) and 50% nBA (green) micelle solutions as a function of temperature. Error bars are 10% for unimer percentages. The samples, at each temperature, were equilibrated for at least 30 minutes before diffusion experiments were performed.

Detemination of $K_{micellization}$ from unimer concentration

Based on nonionic micelle theory[4-5], we can determine the equilibrium constant of unimer association (Table S2, also known as the micellization constant $K_{micellization}$) from these measurements. Note that we cannot state unambiguously that these systems are at equilibrium, but they are at least in quasi-equilibrium since they are stable for two days or more. Note that we are operating in the high aggregation number regime ($N_{agg} \approx 100$). We use the measured free unimer concentration as the concentration at which the free unimers are in (quasi) equilibrium with the micelles.

Table S2. Determination of $K_{\text{micellization}}$ based on polymer composition.

Mol% *n*BA	M_n (avg of NMR+GPC) (g/mol)	[Polymer] (*M*)	Unimer mole fraction	[Unimer] (*M*)	$K_{\text{micellization}}$ (M^{-1})
100	12100	0.00041	0.55	0.00023	4400
75	12000	0.00042	0.36	0.00015	6700
60	11900	0.00042	0.29	0.00012	8200
50	12700	0.00039	0.37	0.00015	6900
40	11700	0.00043	0.33	0.00014	7100
25	12800	0.00039	0.25	0.00010	10000
0	11700	0.00043	0	0	*

All samples measured at 5 mg/mL concentration. *unimer concentration below measurable limit, so $K_{micellization}$ very large.

Discussion of intermediate region in signal decay curves

There is always an intermediate region of intensity that does not lie on either line in a two-component Stejskal-Tanner plot, regardless of temperature and other experimental parameters. This intermediate region depends on several factors, including (1) the difference between the two *D* values (the closer they are, the broader the intermediate region), (2) the relative magnitudes of the two components, and (3) if there is polydispersity in one or other of the components. This intermediate region is most prominent in the signal decay curve of the 25% *n*BA micelles at 55 °C. It is possible in this case, that there may be some spread in micelle size and there may be aggregates that are not uniform size at this temperature. We have previously seen evidence with diffusometry of micelle size dispersity and/or strong size dependencies near transition temperatures/compositions.[6-7] Note, however, that there is always curvature in the intermediate regime where straight lines do not overlap the signal data points. Straight lines were inserted into Fig. 3E to guide the eye as to the identities of the two separate diffusion coefficients, and these do not represent the actual fit line. Figure S44 below shows an actual fit line that cleanly yields two diffusion coefficients and overlaps the intermediate curved region.

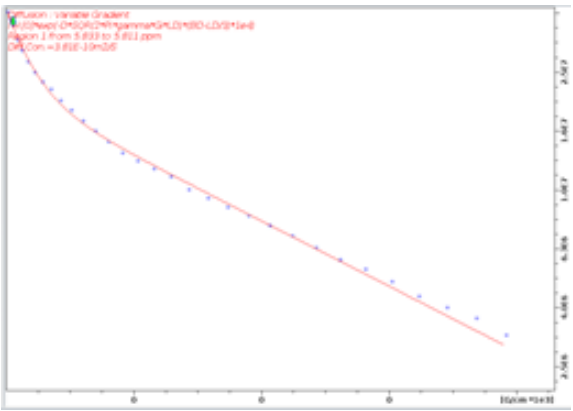

Figure S51. NMR diffusometry signal decay curve and fit line from polymer **1b** at 55 °C. Note that the dashed lines in Figure 3E of the main paper are not fit lines, but are simply to guide the eye to distinguish between single-component vs. two-component NMR signal decay curves.

4.9 Experimental References:

1. Skey, J.; O'Reilly, R. K., *Chem. Comm.* **2008**, (35), 4183-4185.

2. Chong, D.; Tan, J.; Zhang, J.; Zhou, Y.; Wan, X.; Zhang, J., *Chem. Comm.* **2018**, *54* (56), 7838-7841.

3. Callaghan, P. T.; Lelievre, J., *Biopolymers* **1985**, *24* (3), 441-460.

4. H-J Butt, K. G., M. Kappl, *Physics and Chemistry of Interfaces*. Wiley: Weinheim, Germany, 2003; p 373.

5. Phillips, J. N., *Trans. Faraday Soc.* **1955**, *51* (0), 561-569.

6. Kidd, B. E.; Li, X.; Piemonte, R. C.; Cooksey, T. J.; Singh, A.; Robertson, M. L.; Madsen, L. A., *Macromolecules* **2017**, *50* (11), 4335-4343.

7. Li, X.; Cooksey, T. J.; Kidd, B. E.; Robertson, M. L.; Madsen, L. A., *Macromolecules* **2018**, *51* (20), 8127-8135.

Chapter 5: Development of Controlled Polymerization Methods for the Preparation of Poly(Olefin Sulfones)

5.1 Authors

Ryan J. Carrazzone, [§,†,‡] Anna Q. Steele, [§,‡] Kearsley M. Dillon, [§,‡] John B. Matson*[§,‡]

[§]Department of Chemistry, Virginia Tech, Blacksburg, Virginia 24060, United States

[†]Macromolecules Innovation Institute, Virginia Tech, Blacksburg, Virginia 24060, United States

[‡]Virginia Tech Center for Drug Discovery, Virginia Tech, Blacksburg, Virginia 24060, United States

5.2 Abstract

Poly (olefin sulfones) (POSs) are an interesting class of polymers which, to this point, have not been polymerized with control over molecular weight and end group functionality. We have investigated the effectiveness of several reversible deactivation radical polymerization (RDRP) techniques in mediating the polymerization of POSs. We synthesized a library of chain transfer agents with varying compositions suitable for a wide range of monomer activities. We observed more efficient initiation, but similar lack of molecular weight control, from photoiniferter POS polymerizations relative to thermally initiated POS polymerizations. We observed linear growth of molecular weight, but poor rate of initiation, from photo-RAFT polymerizations of POS utilizing a camphorquinone/amine photoinitiating system. Additionally, we observed rapid initiation, but non-linear growth of molecular weight, from photo-RAFT polymerizations of POS utilizing diphenyl(2,4,6-trimethylbenzoyl)phosphine oxide (TPO) as a photoinitiator. This study

represents the first steps towards achieving "living" radical polymerization of POSs, informs future studies seeking to control molecular weight and end group functionality of this class of polymers.

5.3 Introduction

Poly(olefin sulfones) (POSs) are an interesting class of polymers consisting of a backbone containing alkene and sulfur dioxide (SO_2) units in a perfectly alternating manner. These polymers have existed in the literature for nearly a century, being first identified by Seyer and King in 1933 after their accidental synthesis of poly(cyclohexene sulfone).[1] The synthesis of POSs was further explored into the 1950s, where it was shown that various monosubstituted, disubstituted, and cycloalkenes were capable of forming copolymers with SO_2.[2-4] In fact, the study of POSs led to the discovery of the ceiling temperature phenomenon in 1943,[5-6] a critical finding in the history of polymer chemistry. While POSs were an attractive area of research in the early days of polymer chemistry, their synthesis has remained relatively unchanged since these initial reports.

In general, synthesis of POSs consists of dissolving an olefin in condensed SO_2 and performing a free radical copolymerization via addition of a thermal initiator such as *tert*-butyl hydroperoxide.[7-8] These polymerizations are carried out at low temperatures, in the range of -40 to 0 °C, due to the low boiling point of SO_2 and the low ceiling temperature of POSs. As a result of free radical polymerization (FRP), the resultant polymers are synthesized with poor control over molecular weight, molecular weight distribution, and end group functionality. Additionally, since FRP does not maintain living chain ends, it impedes the preparation of POS block copolymers which might be easily synthesized by chain extension.

Despite these limitations, POSs remain interesting for their potential usefulness as depolymerizable polymers, or polymers which unzip into their constituent monomers in response to specific stimuli.[9-11] Several methods for triggered depolymerization of POSs utilizing non-specific chain scission techniques have been described in the literature, including base-triggered[7, 12] and radiation-triggered[13-15] scission. In this manner, POSs have shown promise in applications that benefit from the use of degradable polymers, such as stereolithography,[16] micro-electronics,[17] and photo-detachable adhesives[8]. With triggered-depolymerization in mind, it becomes clear that control over POS end-group functionality would open the door to a wealth of applications relying on precisely triggered head-to-tail unzipping.

With the advent of reversible-deactivation radical polymerization (RDRP) techniques, such as reversible addition-fragmentation chain-transfer (RAFT) and atom transfer radical polymerization (ATRP), control over polymer molecular weight and end-group functionality has become an achievable goal for a wide array of polymer systems.[18-21] In particular, RAFT is an attractive technique for its relatively simple set up and vast functional group tolerability. The RAFT process is also amenable to initiation via light, whether through photo-RAFT polymerization (wherein an external photoinitiator is added) or photoiniferter polymerization (wherein the chain transfer agent acts as a photoinitiator, chain transfer agent, and terminator). In the present work we seek to develop methods for the controlled polymerization of POSs via light-initiated RAFT, allowing for precise control of polymer molecular weight and end-group functionality.

5.4. Results and Discussion

5.4.1. Determining a Polymerization Method for Controlled Synthesis of POSs

Achieving a RAFT polymerization with living characteristics (i.e. low *Đ*, high chain-end fidelity, predictable M_n by [M]/[I] ratio) requires a precise balancing act of various equilibria, many of which can be shifted by careful selection of reaction parameters. For radical polymerizations this requires favoring rapid initiation relative to propagation and minimizing irreversible termination events. In RAFT polymerizations these goals are achieved by utilizing a fast, efficient initiator (k_i>k_p) and a high rate of reversible transfer relative to termination (k_{add}>k_t), as shown in Scheme 5-1.[22-23]

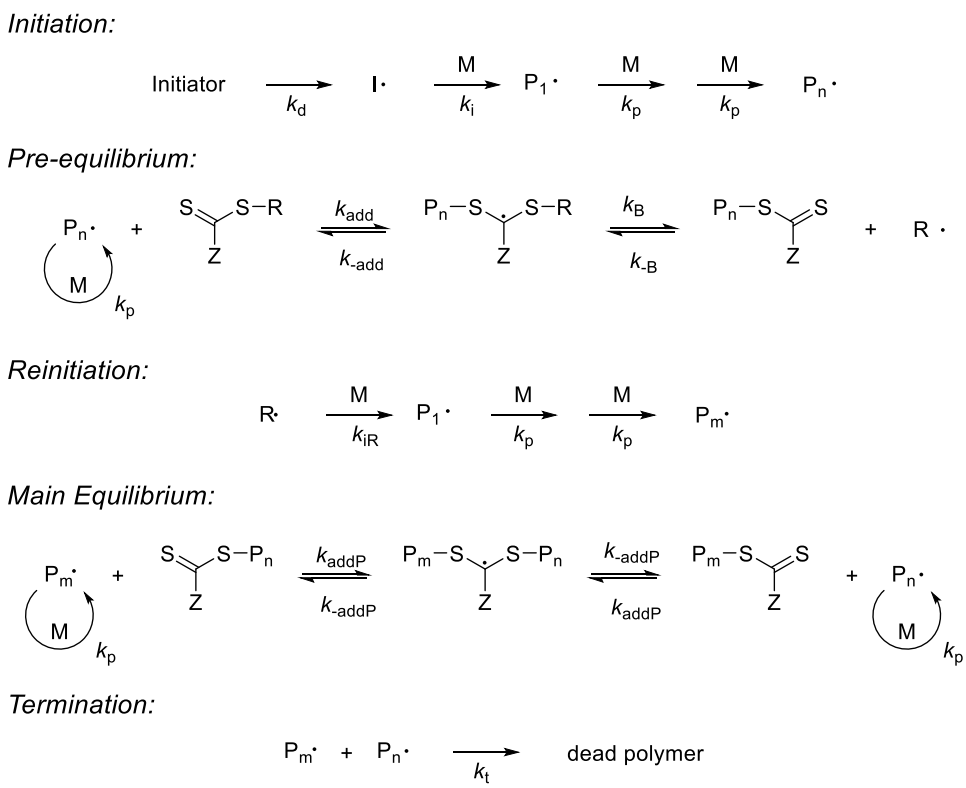

Scheme 5-1. Equilibria of RAFT polymerization. Adapted from Keddie, D. J. *Chem. Soc. Rev.* **2014**. *43*, 496-505.

Optimization of the initiation step in RAFT is done through choice of initiator and temperature. A large majority of RAFT polymerizations are performed using thermally activated initiators. These compounds decompose into initiating radicals at set rates depending upon the temperature of the polymerization. Often, a temperature at which rapid decomposition of the initiator occurs is chosen to ensure that all polymer chains are initiated at relatively the same time. Unfortunately, the low temperature required for POS polymerizations limits the scope of thermal initiators that can be used. The most commonly used thermal initiator for POS polymerizations is *tert*-butyl hydroperoxide (tBuOOH), which decomposes into highly reactive initiating species even at low temperatures. Despite this, tBuOOH has been reported to be stable at 30 °C,[24] signifying that the thermal decomposition at -30 °C would be extremely slow relative to rates of decomposition for thermal initiators in conventional RAFT polymerizations. Because fast initiation is critical in a successful RAFT polymerization, we sought to utilize alternative methods of initiation.

Aside from thermally activated initiators, light activated initiators are also commonly used in RAFT polymerizations.[25-27] Most light-sensitive initiators either decompose or undergo a series of reactions to produce initiating radicals in response to irradiation with the appropriate wavelength of light. Since the generation of initiating radicals from light activated initiator generally does not depend on temperature, we expected they would lead to more efficient initiation than thermally activated initiators for POS polymerizations.

There are several methods to perform RAFT polymerizations mediated by irradiation with light (i.e., photo-RAFT, PET-RAFT, and photoiniferter). In evaluating which of the methods would work best for POS polymerizations we considered the simplicity of the photoiniferter

approach. In photoiniferter polymerizations the chain transfer agent also serves as the initiator and the terminator, as opposed to adding an external photoinitiator (Scheme 5-2). In this regard, photoiniferter is the least complicated of the aforementioned techniques in terms of the experimental setup. Thus, we chose to first employ photoiniferter polymerizations in an effort to achieve controlled polymerization of POSs.

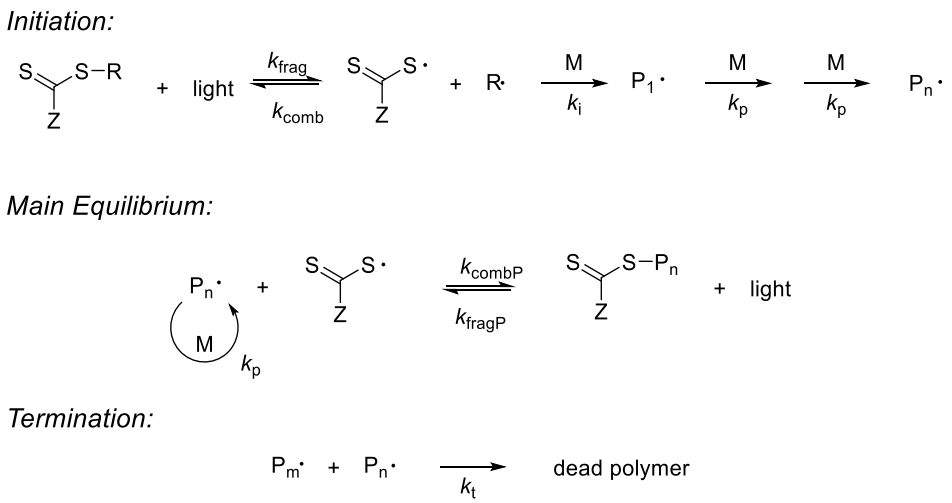

Scheme 5-2. Mechanism of photoiniferter polymerization.

5.4.2 Evaluating Photoiniferter Polymerization in the Controlled Synthesis of POSs

As the controlled polymerization of POSs has not been studied previously, we sought to systematically investigate the photoiniferter system utilizing a wide array of chain transfer agents (CTAs). We designed a library of CTAs with varying Z- and R-groups, and we organized them in relation to their effectiveness towards the controlled polymerization of either less-activated or more-activated monomers (Scheme 5-3). This provided us with a variety of CTA compositions that were suitable for a wide range of monomers. We synthesized the majority of these CTAs, though some were purchased from commercial sources to expedite the process.

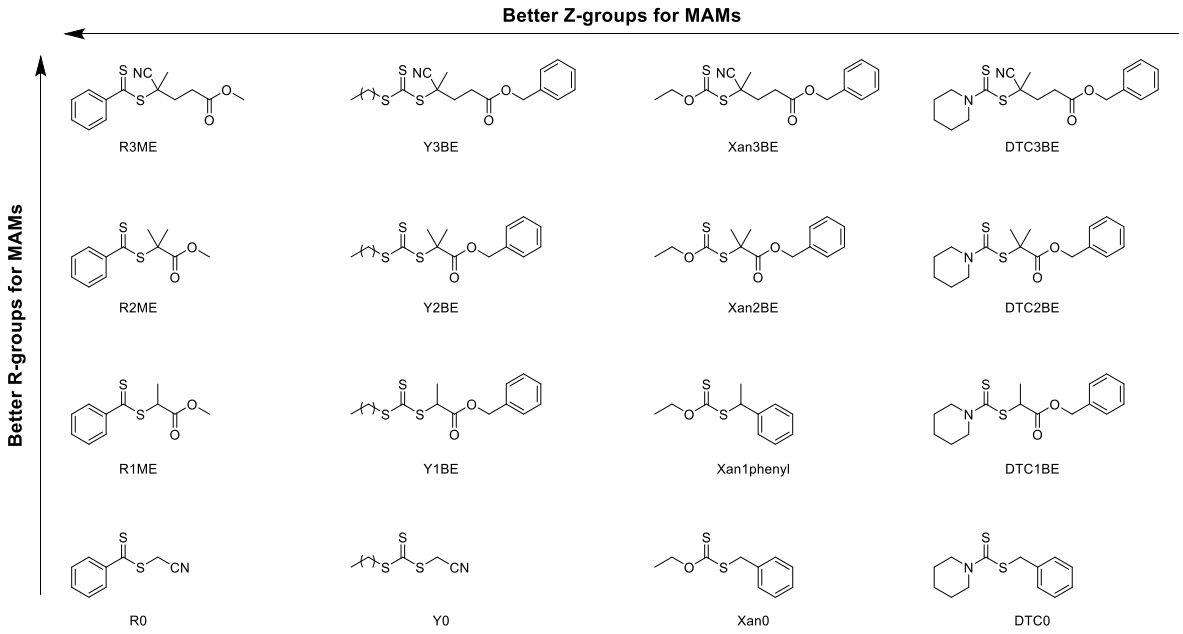

Scheme 5-3. Library of chain transfer agents of varying compositions suitable for a wide range of monomer activities. Labels denote the Z- and R- groups.

With our library of CTAs prepared, we needed to design a reactor capable of performing light-mediated polymerizations of POSs. In designing the reactor there were several criteria it needed to meet: the ability to maintain a reaction temperature of -30 °C for extended periods of time, the ability to incorporate a light source capable of irradiating the reaction mixture, and the ability to withstand pressure buildup from condensed SO_2. Our final reactor design is shown in Figure 5-1 below. We utilize a recirculating chiller set to -40 °C and a copper coil to cool an acetone bath in which we can submerge our reaction flask. This allows us to maintain a temperature around -30 °C in the reaction mixture for extended periods of time. The specialty made glass beaker that holds the chilled acetone has a small indent at the bottom which, with the help of a cork ring, allows us to fit an LED, heatsink, and some desiccant underneath it. Additionally, there are small holes on either side of the cork ring which allow us to flow a constant stream of air

(passed through a column of Drierite) underneath the beaker. The desiccant and constant flow of dry air prevent frost buildup on the bottom side of the beaker, which could interfere with irradiation of the reaction mixture. Finally, we utilize a specialty made thick-walled glass Schlenk tube which is capable of withstanding pressure buildup from the SO_2 in a scenario where we are unable to keep the reaction mixture below -10 °C (the boiling point of SO_2). As an additional precaution, we utilize a spring-loaded pressure relief Kontes screw to cap the polymerization, which enables the reaction flask to vent in the case of large pressure buildup.

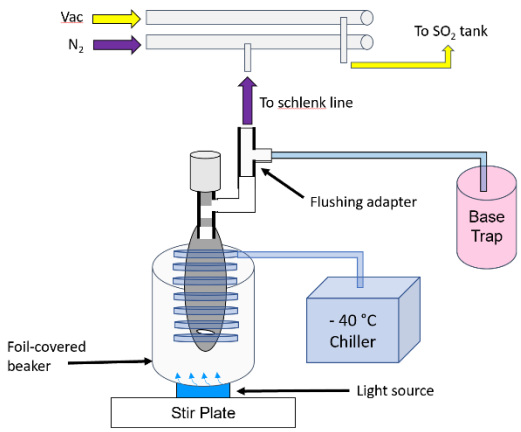

Figure 5-1. Experimental setup for light-mediated POS polymerization.

We then began to evaluate the CTAs effectiveness in controlling photoiniferter polymerization of POS. To accomplish this task, we developed a standard reaction template which could be employed for each of the CTAs, shown in Scheme 5-4. These reactions followed a similar scheme to the polymerizations of POS found in the literature, with approximately 100 equivalents of hexene relative to the CTA and SO_2 acting as monomer and solvent in vast excess with respect to both CTA and 1-hexene. The addition of 4-fluorobenzaldehyde as an internal standard served

in helping determine monomer conversion by NMR. We found that all the CTA types led to the formation of high molecular weight polymer under UV (385 nm) irradiation. Furthermore, the dithioester type CTAs and the trithicarbonate type CTAs led to the formation of high molecular weight polymer under green (520 nm) and blue (450 nm) light irradiation, respectively.

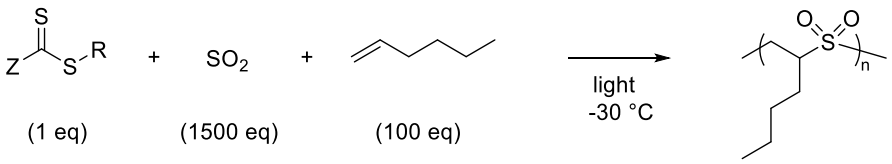

Scheme 5-4. General reaction scheme for photoiniferter polymerization of POS. One equivalent of fluorobenzaldehyde was included as an internal standard for NMR analysis.

We evaluated the livingness of the photoiniferter polymerizations via NMR and SEC analysis of aliquots at various timepoints throughout the reaction. In all of the photoiniferter polymerizations that resulted in the formation of polymer we observed rapid, non-linear conversion of monomer with time, rapid evolution of molecular weight before plateauing, and large molecular weights by SEC relative to the theoretical molecular weight (determined by [M]/[CTA] and monomer conversion). A representative polymerization is shown in Figure 5-2. These characteristics are indicative of free radical polymerization rather than controlled radical polymerization. In fact, the molecular weight evolution and monomer conversion of these polymerizations closely resemble those of thermally initiated free radical polymerizations of POSs, albeit with a lower dispersity achieved (1.45 versus 1.94 for free radical polymerization).

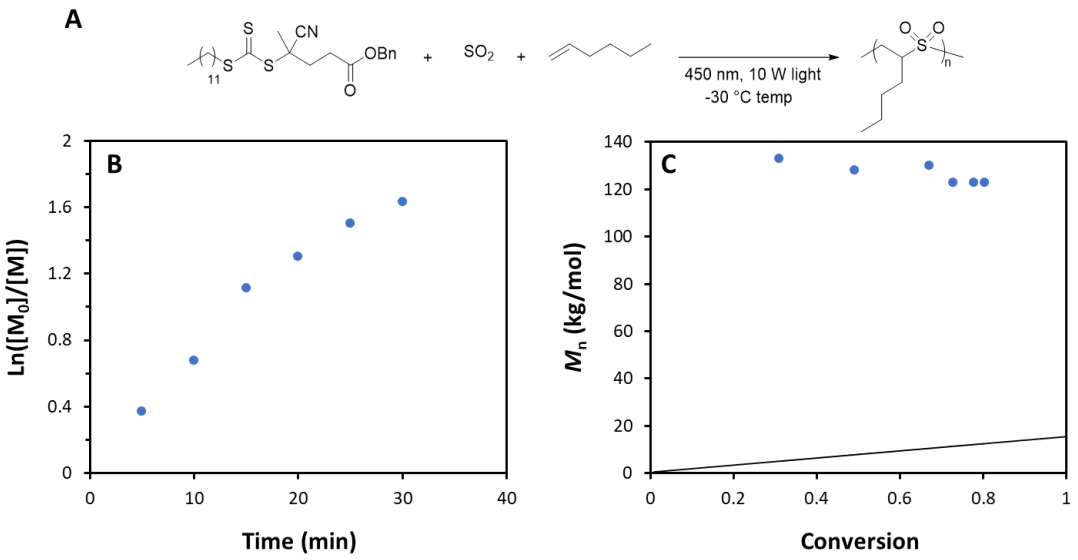

Figure 5-2. A) Reaction scheme of photoiniferter polymerization utilizing Y3BE. B) Semi-logarithmic plot of monomer conversion versus time. C) Plot of $M_{n(SEC)}$ versus monomer conversion. The solid black line represents $M_{n(theo)}$.

One explanation for the free radical like behavior of these photoiniferter polymerizations lies in the equilibrium between CTA and its products after photolysis, as shown in Scheme 5-2. If the chosen CTA absorbs an appreciable amount of light at the wavelength used for polymerization, or if a strong intensity of light is used, the equilibrium is shifted far towards the photolysis products. While this is beneficial for achieving rapid initiation of polymer chains, it may favor the activated/propagating state too heavily, effectively forfeiting control over the polymerization. Additionally, the lower dispersity could be a result of more rapid initiation from CTA-derived radicals relative to initiation from slowly decomposing tBuOOH, further supporting our theory of rapid and complete photolysis of the CTA.

In an effort to attain control over the photoiniferter polymerizations we utilized two strategies for shifting the equilibrium back towards intact CTA. The first strategy we employed involved lowering the intensity of light irradiation. Since photolysis of the CTA is directly dependent on the intensity of irradiating light, lowering the light intensity should shift the equilibrium towards intact CTA. When lowering light intensity from 10 W to 1 W in a photoiniferter polymerization with Y3BE as the CTA, we observed no formation of polymer. Interestingly, when lowering light intensity from 10 W to 1 W in a photoiniferter polymerization using Xan0 as the CTA we observed slower monomer conversion over time, but a similar rapid production of high molecular weight polymer, as shown in Figure 5-3. These results suggest that lowering light intensity slows down the rate of photolysis, but does not sufficiently control the amount of actively propagating polymer chains.

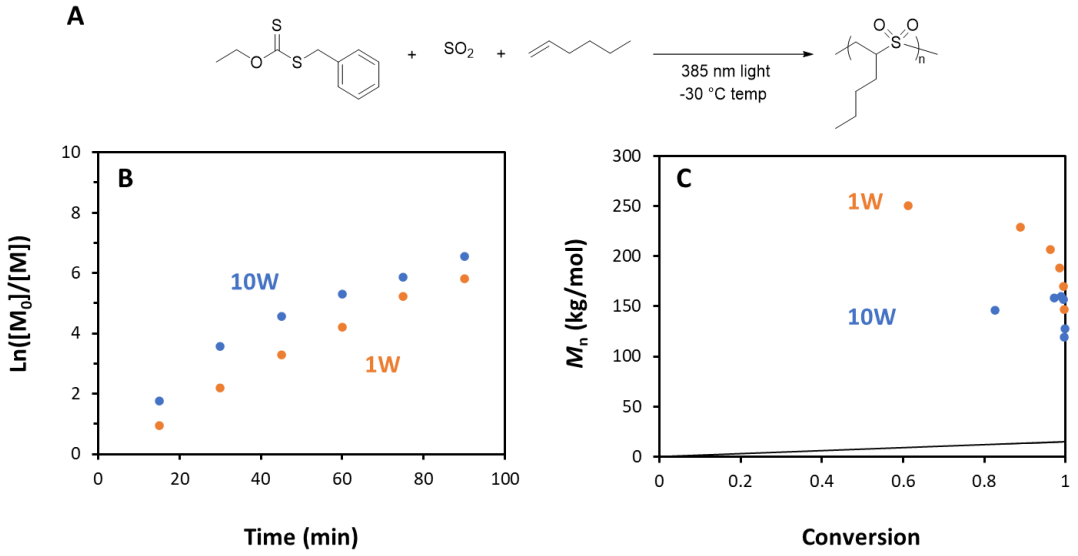

Figure 5-3. A) Reaction scheme of photoiniferter polymerization utilizing Xan0. B) Semi-logarithmic plot of monomer conversion versus time for polymerization with 385 nm light at 10 W (blue circles) and 1 W (orange circles). C) Plot of $M_{n(SEC)}$ versus monomer conversion for

polymerization with 385 nm light at 10 W (blue circles) and 1 W (orange circles). The solid black line represents $M_{n(theo)}$.

The second strategy we employed to achieve controlled photoiniferter polymerizations of POSs involved adding additional CTA to the reaction to increase the rate of deactivation. To avoid increasing the amount of initiating radicals in the polymerization, thus impacting the theoretical molecular weight, we utilized CTA precursors which lacked the initiator-radical-forming R-groups. These disulfide molecules cleave under irradiation with the proper wavelength of light generating two trithiocarbonate radicals, akin to one of the photolysis products of Y3BE. We hypothesized that the incorporation of these additional trithiocarbonate radicals would increase the time polymer chains spent in the deactivated state and lead to more controlled polymerizations.

When adding disulfide to the photoiniferter polymerization using Y3BE we observed an increased rate of monomer conversion, rapid formation of a plateau molecular weight, and a much lower overall molecular weight achieved (Figure 5-4). While the lower molecular weight more closely correlated to $M_{n(theo)}$, the non-linear growth of molecular weight with monomer conversion suggested a free radical type polymerization. Additionally, the polymerization with added disulfide resulted in a large dispersity (2.1 versus 1.48 without disulfide), further reinforcing that the polymerization lacked control. We attributed the lower molecular weight to initiation from thiol radicals, a degradation product of the trithiocarbonate radical after loss of CS_2,[28] and concluded that addition of disulfide did not promote deactivation of propagating chains.

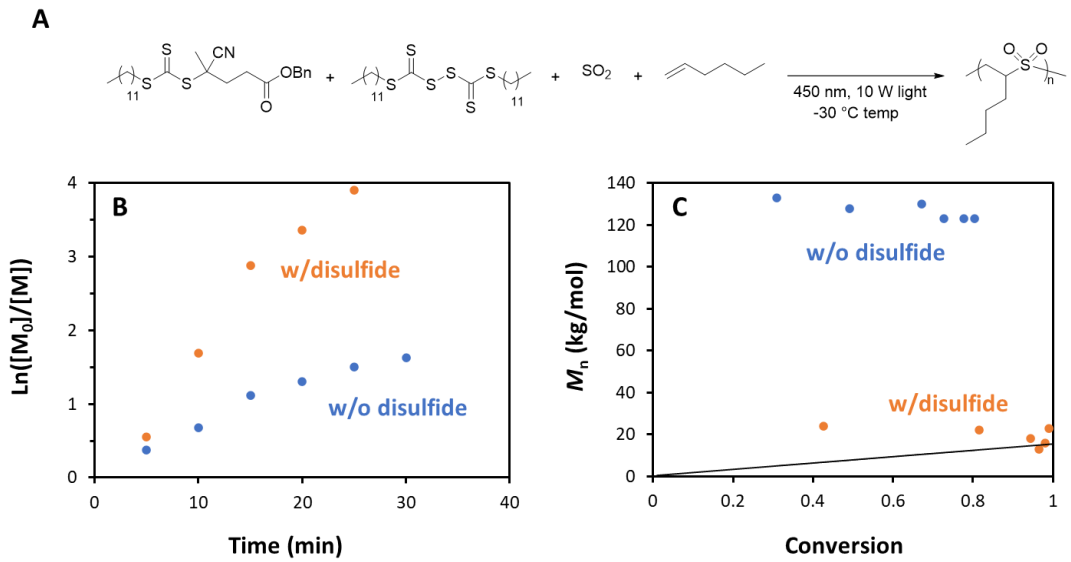

Figure 5-4. A) Reaction scheme of photoiniferter polymerization utilizing Y3BE with added disulfide (conditions for polymerization with added disulfide followed $[SO_2]$:[hexene]:[CTA]:[disulfide] = 1500:100:1:2). B) Semi-logarithmic plot of monomer conversion versus time for polymerization with added disulfide (orange circles) and without (blue circles). C) Plot of $M_{n(SEC)}$ versus monomer conversion for polymerization with added disulfide (orange circles) and without (blue circles). The solid black line represents $M_{n(theo)}$.

5.4.3 Utilizing Photo-RAFT Polymerization for the Controlled Synthesis of POSs

As we could not find reaction conditions that led to controlled photoiniferter polymerzations of POSs, we began to explore alternative methods of polymerization. In photo-RAFT polymerizations a compound which generates initiating radicals in response to light is used as the initiator, as opposed to the thiocarbonylthio species acting as an iniferter. Since the CTA is not subjected to photolysis, the polymerization is controlled through the RAFT equilibria. In this

way, photo-RAFT avoids the need for thiocarbonylthio radicals to deactivate propagating polymer chains. For this reason, we theorized that photo-RAFT might afford control over the polymerization of POSs where photoiniferter polymerizations could not.

Designing a method for photo-RAFT polymerization requires careful choice of initiator and CTA such that the wavelength of irradiating light cleaves only the initiator. We chose to first investigate camphorquinone, a photoinitiator activated by blue light, in photo-RAFT polymerizations of POSs. Photoinitiation by camphorquinone is a bimolecular process where camphorquinone is excited by irradiation to a high energy state and undergoes photo-induced electron transfer with a coinitiator to form initiating radicals.[29-30] We performed polymerizations using a variety of CTAs following the general reaction scheme depicted in scheme 5-5.

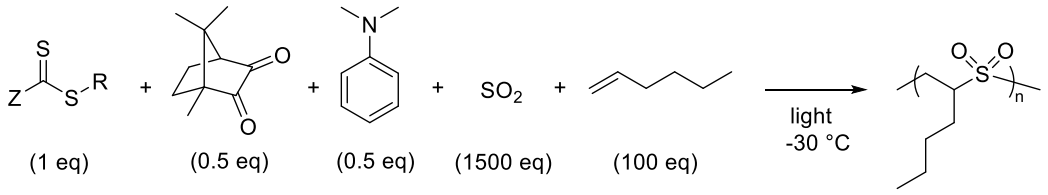

Scheme 5-5. General reaction scheme of photo-RAFT polymerization of POS.

We chose to start with R3ME and Xan0, two significantly different CTAs in terms of the monomers for which they can effectively mediate polymerizations. In evaluating the timepoints of polymerizations using each of these CTAs we observed characteristics that differed significantly from free radical polymerization. When utilizing Xan0 as the CTA we observed a fairly linear conversion of monomer over time, with some negative deviation at later timepoints (Figure 5-5B). Negative deviation in monomer conversion over time is often attributed to termination events,[31] which is strange to see at such low monomer conversions. Importantly, we also observed a linear

growth of $M_{n(SEC)}$ versus monomer conversion (Figure 5-5C), which is in stark contrast to FRP. While these characteristics are clearly a step towards controlled radical polymerization, we still observed a greatly inflated $M_{n(SEC)}$ relative to $M_{n(theo)}$.

When utilizing R3ME as the CTA we observed a fairly linear conversion of monomer over time, with some positive deviation at later timepoints (Figure 5-5E). Positive deviation in monomer conversion over time is often attributed to slow initiation relative to propagation.[31] Similar to the polymerization with Xan0, we also observed a linear growth of $M_{n(SEC)}$ versus monomer conversion and an inflated $M_{n(SEC)}$ relative to $M_{n(theo)}$ (Figure 5-5F). Interestingly, $M_{n(SEC)}$ for the R3ME photo-RAFT polymerization was much closer to $M_{n(theo)}$ than when Xan0 was utilized. We attribute this result to the difference in CTA activity, with the more active dithioester decreasing the rate of polymerization more effectively than the xanthate.

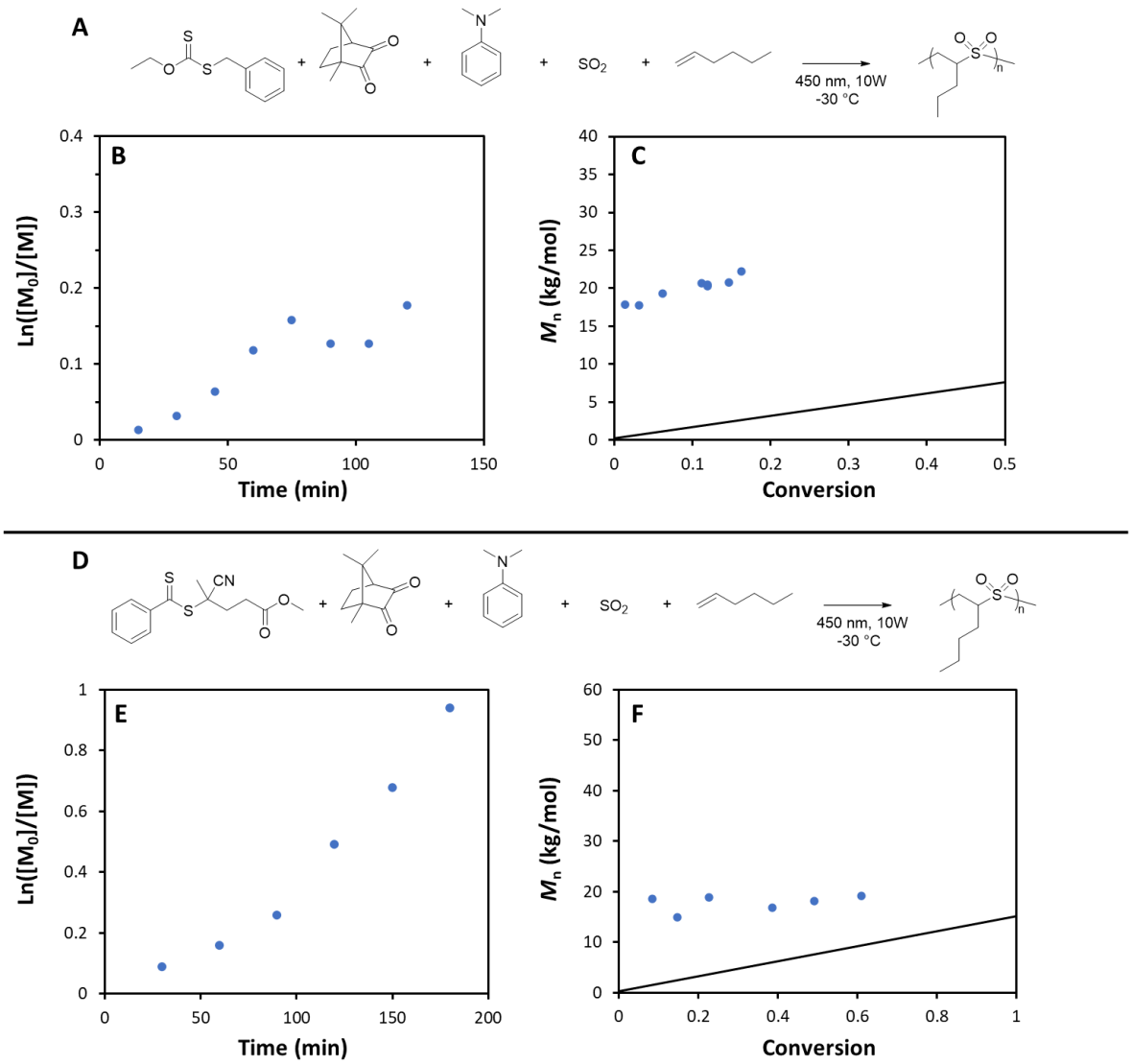

Figure 5-5. A) Reaction scheme of photo-RAFT polymerization utilizing Xan0 and camphorquinone. B) Semi-logarithmic plot of monomer conversion versus time for Xan0 polymerization. C) Plot of $M_{n(SEC)}$ versus monomer conversion for Xan0 polymerization. The solid black line represents $M_{n(theo)}$. D) Reaction scheme of photo-RAFT polymerization utilizing R3ME and camphorquinone. E) Semi-logarithmic plot of monomer conversion versus time for R3ME polymerization. F) Plot of $M_{n(SEC)}$ versus monomer conversion for R3ME polymerization. The solid black line represents $M_{n(theo)}$.

Both Xan0 and R3ME showed promising steps towards effectively controlling the polymerization of POSs when utilizing photo-RAFT, though both lacked strong agreement between $M_{n(SEC)}$ and $M_{n(theo)}$. One explanation for the discrepancy between these values lies in a slow rate of initiation. When rate of initiation is lower than rate of propagation, molecular weights measured by SEC will be greater than theoretical molecular weight based on monomer conversion. This problem prompted our initial departure from thermally activated initiator in favor of light activated initiator to avoid the issue of slow decomposition rate at low temperature. While it is true that low temperature should not slow the activation of the camphorquinone/amine system, the bimolecular electron transfer to generate initiating radicals will be slowed at low temperatures. For this reason, we sought to employ a photoinitiator which does not rely on a bimolecular reaction to increase the rate of initiation.

Alongside camphorquinone, another commonly used and commercially available photoinitiator is diphenyl(2,4,6,-trimethlbenzoyl)phosphine oxide (TPO). TPO readily cleaves in response to long wave UV irradiation[32] and the resulting phosphonyl radical rapidly initiates polymer chains[33], making it an ideal candidate for photo-RAFT polymerization. We expected that the unimolecular nature of radical generation from TPO would translate to faster initiation rates than the camphorquinone/amine system, thus, we began to investigate its effectiveness in photo-RAFT polymerizations of POSs.

We first investigated the rate of TPO photolysis at various wavelengths of light. To accomplish this task we performed photoinitiated free radical polymerizations of POS using TPO. We found that high molecular weight polymer was rapidly formed when irradiating with 385 or 410 nm light, and polymer formation was relatively slower when irradiating with 450 nm light.

Based on these data, we concluded that rapid photolysis of TPO occurs at 385 or 410 nm light, and slow photolysis occurs at 450 nm.

Seeking to leverage the rapid photolysis of TPO at lower wavelengths of light to achieve efficient initiation of polymer chains, we then began investigating which CTAs would be suitable for photo-RAFT polymerization at these wavelengths. Effective photo-RAFT requires that the chosen CTA does not undergo photolysis at the wavelength of light used to activate the photoinitiator. We knew from previous work with photoiniferter polymerizations that all the CTAs underwent photolysis upon irradiation with 385 nm light. As a result, we first investigated the dithioester type CTAs under irradiation with 410 nm light. We found that while R3ME formed high molecular weight polymer, neither R2ME, R1ME, or R0 resulted in the formation of any polymer at this wavelength. Accordingly, we began to investigate these CTAs in photo-RAFT polymerizations using TPO.

When utilizing R0 as the CTA we observed a linear conversion of monomer over time and rapid polymer growth to a plateau molecular weight, as shown in Figure 5-6. These results were similar to what we had achieved previously with R3ME when utilizing the camphorquinone/amine photoinitiating system. In contrast to the previous data, we noted that in the R0/TPO polymerization molecular weight growth did not continue after the initial jump in molecular weight. We attributed this result to a combination of poor chain transfer (k_{add}) during the pre-equilibrium step and a low rate of fragmentation from the R group (k_B). Thus, we suspect that CTAs with R-groups better suited for more-activated monomers (MAMs) will be more effective in controlling the photo-RAFT of POSs and investigations into these CTAs are currently underway in our lab.

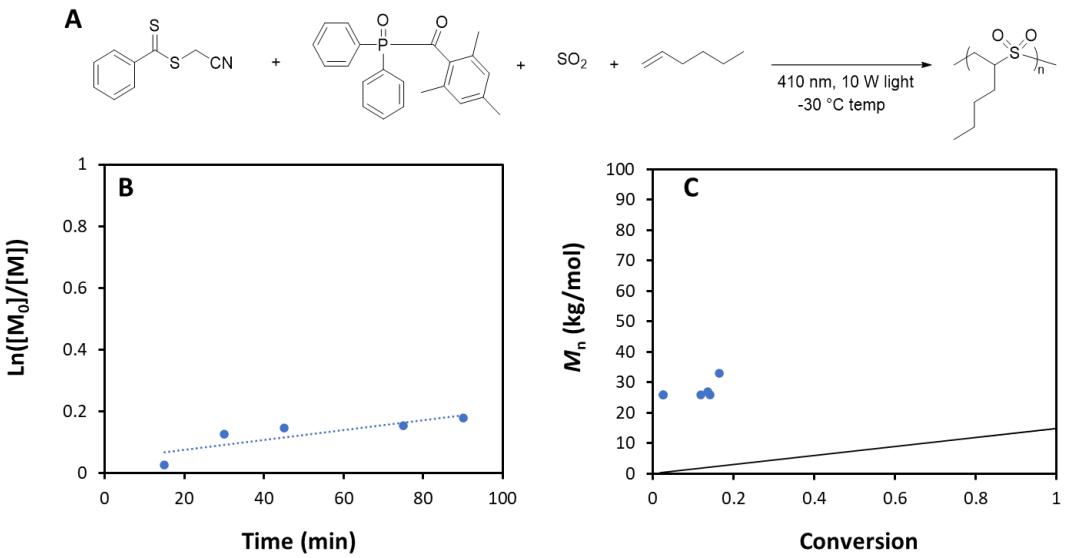

Figure 5-6. A) Reaction scheme of photo-RAFT polymerization utilizing R0 and TPO (conditions for polymerization followed [SO_2]:[hexene]:[CTA]:[TPO] = 1500:100:1:0.1). B) Semi-logarithmic plot of monomer conversion versus time for R0 polymerization. C) Plot of $M_{n(SEC)}$ versus monomer conversion for R0 polymerization. The solid black line represents $M_{n(theo)}$.

5.5 Conclusions and Future Work

In this work, we developed methods for photoiniferter and photo-RAFT polymerization of POSs. Photoiniferter polymerizations with CTAs of varying activity showed faster initiation rates than thermally initiated free radical polymerization of POS, but lacked effective control over the polymerization. We attributed this result to rapid photolysis of the CTAs leading to prolonged periods of activation for the propagating polymer chains. We then employed photo-RAFT polymerization to avoid photolysis of the CTA. Photo-RAFT polymerizations with a camphorquinone/amine photoinitiator system led to more controlled polymerizations but resulted in polymer molecular weights higher than expected values due to slow initiation. We expect that

faster initiation rates from TPO, a unimolecular photoinitiator, will lead to controlled polymerizations of POSs and are currently investigating their effectiveness.

After achieving living polymerization of POSs we aim to synthesize block copolymers via chain extension. We aim to utilize the depolymerization of POSs in the creation of drug delivery systems with precisely triggered release. Furthermore, we expect the high-chain end fidelity afforded from controlled radical polymerizations to allow for simple functionalization of the polymer chain end, and plan to investigate methods for head-to-tail depolymerization of POSs through careful choice of endgroup.

5.6 References

1. Seyer, W. F.; King, E. G., *J. Am. Chem. Soc.* **1933**, *55* (8), 3140-3149.

2. Snow, R. D.; Frey, F. E., *Industrial & Engineering Chemistry* **1938**, *30* (2), 176-182.

3. Frederick, D. S.; Cogan, H. D.; Marvel, C. S., *J. Am. Chem. Soc.* **1934**, *56* (8), 1815-1819.

4. Dainton, F. S.; Ivin, K. J.; Evans, M. G., *Proc. R. Soc. London, Ser. A* **1952**, *212* (1108), 96-112.

5. Snow, R.; Frey, F., *J. Am. Chem. Soc.* **1943**, *65* (12), 2417-2418.

6. Dainton, F.; Ivin, K., *Nature* **1948**, *162* (4122), 705-707.

7. Lobez, J. M.; Swager, T. M., *Macromolecules* **2010**, *43* (24), 10422-10426.

8. Possanza Casey, C. M.; Moore, J. S., *ACS Macro Letters* **2016**, *5* (11), 1257-1260.

9. Phillips, S. T.; DiLauro, A. M., *ACS Macro Letters* **2014**, *3* (4), 298-304.

10. Kaitz, J. A.; Lee, O. P.; Moore, J. S., *MRS Communications* **2015**, *5* (2), 191-204.

11. Yardley, R. E.; Kenaree, A. R.; Gillies, E. R., *Macromolecules* **2019**, *52* (17), 6342-6360.

12. Sasaki, T.; Yaguchi, H., *J. Polym. Sci. A* **2009**, *47* (2), 602-613.

13. Lawrie, K. J.; Blakey, I.; Blinco, J. P.; Cheng, H. H.; Gronheid, R.; Jack, K. S.; Pollentier, I.; Leeson, M. J.; Younkin, T. R.; Whittaker, A. K., *J. Mater. Chem.* **2011**, *21* (15), 5629-5637.

14. Bowmer, T. N.; Odonnell, J. H., *J. Macromol. Sci. Chem.* **1982**, *A17* (2), 243-263.

15. Pacansky, J.; Waltman, R. J.; Pacansky, G., *Chem. Mater.* **1993**, *5* (10), 1526-1532.

16. Sasaki, T.; Kondo, T.; Noro, M.; Saida, K.; Yaguchi, H.; Naka, Y., *J. Polym. Sci. A* **2012**, *50* (8), 1462-1468.

17. Bowden, M. J.; Chandross, E. A., *J. Electrochem. Soc.* **1975**, *122* (10), 1370.

18. Matyjaszewski, K., *Macromolecules* **2012**, *45* (10), 4015-4039.

19. Braunecker, W. A.; Matyjaszewski, K., *Prog. Polym. Sci.* **2007**, *32* (1), 93-146.

20. Moad, G.; Rizzardo, E.; Thang, S. H., *Polymer* **2008**, *49* (5), 1079-1131.

21. Perrier, S.; Takolpuckdee, P., *J. Polym. Sci. Pol. Chem.* **2005**, *43* (22), 5347-5393.

22. Keddie, D. J., *Chem. Soc. Rev.* **2014**, *43* (2), 496-505.

23. Keddie, D. J.; Moad, G.; Rizzardo, E.; Thang, S. H., *Macromolecules* **2012**, *45* (13), 5321-5342.

24. Willms, T.; Kryk, H.; Oertel, J.; Lu, X.; Hampel, U., *J. Therm. Anal. Calorim.* **2017**, *128* (1), 319-333.

25. Chen, M.; Zhong, M. J.; Johnson, J. A., *Chem. Rev.* **2016**, *116* (17), 10167-10211.

26. Tan, J. B.; Bai, Y. H.; Zhang, X. C.; Huang, C. D.; Liu, D. D.; Zhang, L., *Macromol. Rapid Commun.* **2016**, *37* (17), 1434-1440.

27. Tan, J. B.; He, J.; Li, X. L.; Xu, Q.; Huang, C. D.; Liu, D. D.; Zhang, L., *Polym. Chem.* **2017**, *8* (44), 6853-6864.

28. Quinn, J. F.; Barner, L.; Barner-Kowollik, C.; Rizzardo, E.; Davis, T. P., *Macromolecules* **2002**, *35* (20), 7620-7627.

29. Cook, W. D., *Polymer* **1992**, *33* (3), 600-609.

30. Jakubiak, J.; Allonas, X.; Fouassier, J. P.; Sionkowska, A.; Andrzejewska, E.; Linden, L. A.; Rabek, J. F., *Polymer* **2003**, *44* (18), 5219-5226.

31. Matyjaszewski, K., Overview: Fundamentals of Controlled/Living Radical Polymerization. In *Controlled Radical Polymerization*, American Chemical Society: 1998; Vol. 685, pp 2-30.

32. Fouassier, J. P., *Radiation Curing in Polymer Science and Technology*. Springer: Netherlands, 1993; p 563.

33. Gatlik, I.; Rzadek, P.; Gescheidt, G.; Rist, G.; Hellrung, B.; Wirz, J.; Dietliker, K.; Hug, G.; Kunz, M.; Wolf, J.-P., *J. Am. Chem. Soc.* **1999**, *121* (36), 8332-8336.

5.7 Experimental

Materials

All reagents were obtained from commercial vendors and used as received unless otherwise stated. 2,2′-Azobis(2-methylpropionitrile) (AIBN) was recrystallized from methanol prior to use. 1-hexene was purchased from Alfa Aesar and distilled prior to use. Dry solvents were purified by passage through a solvent purification system (MBraun).

Methods

NMR spectra for characterization of molecular structures were measured on an Agilent 400 MHz spectrometer. ^{1}H and ^{13}C NMR chemical shifts are reported in ppm relative to internal solvent resonances. Yields refer to chromatographically and spectroscopically pure compounds unless otherwise stated. Size exclusion chromatography (SEC) was carried out in THF at 1 mL/min at 30 °C on two Agilent PLgel 10 µm MIXED-B columns connected in series with a Wyatt Dawn Heleos 2 multi-angle light scattering detector and a Wyatt Optilab Rex refractive index detector. No calibration standards were used, and d*n*/d*c* values were obtained by offline differential refractive index measurements.

Synthesis of R3 acid

R3 acid was prepared according to a modified procedure from the literature:[1] Bromobenzene (3.00 g, 19.1 mmol) in 5 mL of dry THF was added to a round bottom containing Mg turnings (0.464 g, 19.1 mmol) in 25 mL of dry THF while stirring under nitrogen. After 30 min, the reaction mixture was cooled to 0 °C and carbon disulfide (1.15 mL, 19.1 mmol) was added dropwise via syringe. The reaction mixture was allowed to warm to rt while stirring for 3 h. Grignard reagent was then hydrolyzed by slow addition of water (5 mL). The Mg salts were removed by filtration and washed

with water. The filtrate was then diluted with 1N HCl and extracted with diethyl ether twice. The red ether layer was extracted with 1N NaOH thrice, and the yellow ether layer discarded leaving a dark red solution of the sodium salt of dithiobenzoic acid.

The dithiobenzoic acid salt solution (150 mL) was transferred to a RBF equipped with a stir bar. A solution of KI (1.90 g, 11.5 mmol) and I_2 (2.91 g, 11.5 mmol) in water (20 mL) was added dropwise while stirring. The reaction was allowed to stir for 12 h after complete addition of iodine solution, and disappearance of the dithiobenzoic acid salt was followed by TLC using CH_2Cl_2 as eluent. The solution was then transferred to a separatory funnel and extracted with CH_2Cl_2 (50 mL) twice. The organic layer was then washed with 10% $Na_2S_2O_3$, water, and brine. Silica gel was added to the solution, which was then concentrated via rotary evaporation. The silica gel was dry-loaded onto a silica gel column, and the product was eluted with CH_2Cl_2. Product containing fractions, as determined by TLC (CH_2Cl_2 eluent) were combined and concentrated via rotary evaporation to yield a red solid.

Synthesis of R2 acid

R2 acid was prepared according to a modified literature procedure:[1] Bromobenzene (3.00 g, 19.1 mmol) in 5 mL of dry THF was added to a round bottom containing Mg turnings (0.464 g, 19.1 mmol) in 25 mL of dry THF while stirring under nitrogen. The reaction mixture was allowed to warm to rt while stirring for 3 h. From the reaction mixture, 3.00 mL of THF containing Grignard reagent (0.345 g, 1.9 mmol) was transferred via syringe to a RBF containing Na_2CO_3 (0.500 g, 4.8 mmol) and equipped with a stir bar under nitrogen. The reaction mixture was diluted with acetone (5 mL) and carbon disulfide (120 uL, 2.0 mmol) was added dropwise via syringe while stirring. The reaction mixture was allowed to stir for 90 mins after complete addition of carbon disulfide. A solution of 2-bromo-2-methylpropanoic acid (0.320 g, 1.9 mmol) in acetone (5 mL) was added

via syringe while stirring. Reaction progress was monitored by TLC using CH_2Cl_2 as eluent. Upon complete disappearance of the spot corresponding to dithioester salt, the reaction mixture was transferred to a separatory funnel and diluted with 1N HCl (40 mL). The acidic solution was then extracted with CH_2Cl_2 thrice. The combined organic layer was washed with water, brine, and dried over Na_2SO_4. Silica gel was added to the CH_2Cl_2 solution, which was then concentrated via rotary evaporation. The silica gel was dry-loaded onto a silica gel column, and the product was eluted with CH_2Cl_2. Product containing fractions, as determined by TLC (CH_2Cl_2 eluent), were combined and concentrated via rotary evaporation to yield a red solid. R1 acid was prepared in a similar manner.

Synthesis of R3ME

R3 acid (1.00 g, 3.58 mmol) was added to a RBF containing K_2CO_3 (0.495 g, 3.58 mmol) in DMF (10 mL) while stirring. Iodomethane (670 uL, 10.7 mmol) was then added dropwise via syringe. Reaction progress was monitored by TLC using CH_2Cl_2 as eluent. Upon complete disappearance of the spot corresponding to R3 acid, the reaction mixture was diluted with water (20 mL) and transferred to a separatory funnel. The reaction mixture was then extracted with CH_2Cl_2 thrice. The combined organic layer was washed with water, brine, and dried over Na_2SO_4. Silica gel was added to the CH_2Cl_2 solution, which was then concentrated via rotary evaporation. The silica gel was dry-loaded onto a silica gel column, and the product was eluted with hexanes. Product containing fractions, as determined by TLC (CH_2Cl_2 eluent) were combined and concentrated via rotary evaporation to yield a red oil. R2ME and R1ME were prepared in a similar manner.

Synthesis of Y3 acid

Y3 acid was prepared according to a previously reported procedure:[2] Dodecanethiol (10 mL, 41.7 mmol) was dissolved in hexanes (150 mL) in a round bottom flask. To the flask was added a solution of potassium *tert*-butoxide (4.68 g, 41.7 mmol) in THF (50 mL). The reaction mixture was stirred at rt for 20 min. CS_2 was added (2.7 mL, 44.7 mmol), and the reaction mixture was stirred for an additional 1 h. I_2 was then added in portions until the reaction mixture maintained a persistent dark brown color. The reaction mixture was stirred overnight at rt. The reaction mixture was transferred to a separatory funnel and washed consecutively with 10% $Na_2S_2O_3$, H_2O, and brine. The organic layer was then dried over Na_2SO_4 and concentrated via rotary evaporator.

The resulting viscous yellow oil (22.8 g, 41.1 mmol) was redissolved in EtOAc (100 mL) in a round bottom flask. To the flask was added 4,4′-azobis(4-cyanovaleric acid) (11.6 g, 41.4 mmol). The reaction mixture was heated at reflux overnight. Silica gel was poured into the reaction flask, and the silica slurry was concentrated via rotary evaporator. The silica was then dry-loaded onto a silica gel column, eluting with CH_2Cl_2. The product-containing fractions were combined and concentrated via rotary evaporator to yield the product as a yellow solid. Xan3 acid and DTC3 acid were prepared in a similar manner.

Synthesis of Y2 acid

Y2 acid was prepared according to a previously reported procedure:[3] Dodecanethiol (5.00 mL, 20.9 mmol) was dissolved in acetone (30 mL) in a round bottom flask. To the flask was added tribasic potassium phosphate (8.86 g, 41.7 mmol). The reaction mixture was stirred at rt for 10 min. CS_2 (3.78 mL, 62.6 mmol) was then added dropwise, and the reaction mixture was stirred for an additional 1 h. To the flask a solution of 2-bromo-2-methyl propanoic acid (3.91 g, 23.4 mmol) in 5 mL of acetone was added dropwise. The reaction mixture was stirred overnight at rt. Reaction conversion was monitored by TLC using CH_2Cl_2 as the eluent. The reaction mixture was diluted

with ~100 mL CH_2Cl_2, transferred to a separatory funnel, and washed consecutively with 1N HCl and brine. The organic layer was dried over Na_2SO_4 and concentrated via rotary evaporation. Silica gel was added to the concentrated solution before removing the rest of the solvent via rotary evaporation. The silica gel was dry-loaded onto a silica gel column, and the product was eluted with CH_2Cl_2. Product containing fractions, as determined by TLC, were combined and concentrated via rotary evaporation to yield a yellow solid. The crude product was recrystallized from hexanes to yield yellow crystals. Y1 acid, Xan2 acid, DTC2 acid, and DTC1 acid were prepared in a similar manner.

Synthesis of Y3BE

Y3 acid (1.00 g, 2.5 mmol) was added to a solution of 1-ethyl-3-(3-dimethylaminopropyl)carbodiimide hydrochloride (EDC) (0.522 g, 2.7 mmol) and 4-dimethylaminopyridine (0.030 g, 0.247 mmol) in CH_2Cl_2 (12 mL) while stirring. The reaction mixture was allowed to stir for 15 min. Benzyl alcohol (283 μL, 2.7 mmol) was added dropwise while stirring. Reaction progress was monitored by TLC using CH_2Cl_2 as eluent. Upon complete disappearance of the spot corresponding to Y3 acid, the reaction mixture was diluted with CH_2Cl_2 and transferred to a separatory funnel. The reaction mixture was washed with 1N HCl twice, water, and brine, then dried over Na_2SO_4. Silica gel was added to the CH_2Cl_2 solution, which was then concentrated via rotary evaporation. The silica gel was dry-loaded onto a silica gel column, and the product was eluted with CH_2Cl_2. Product containing fractions, as determined by TLC (CH_2Cl_2 eluent) were combined and concentrated via rotary evaporation to yield a yellow oil. Y2BE, Y1BE, Xan3BE, Xan2BE, DTC3BE, DTC2BE, and DTC1BE were prepared in a similar manner.

Synthesis of Xan0

Potassium *O*-ethyl dithiocarbonodithioate (1.00 g, 6.2 mmol) was added to a RBF equipped with a stir bar and diluted with acetone (15 mL). Benzyl bromide (741 μL, 6.2 mmol) was added dropwise while stirring. Reaction progress was followed by TLC using CH_2Cl_2 as eluent. Upon complete disappearance of the spot corresponding to potassium *O*-ethyl dithiocarbonodithioate, the reaction was diluted with acetone (50 mL). Silica gel was added to the acetone solution, which was then concentrated via rotary evaporation. The silica gel was dry-loaded onto a silica gel column, and the product was eluted with hexanes. Product containing fractions, as determined by TLC (1:1 hexanes:CH_2Cl_2 eluent) were combined and concentrated via rotary evaporation to yield a light yellow oil. DTC0 was prepared in a similar manner.

Thermally initiated polymerization of poly (1-hexene sulfone)

A representative example of a thermally initiated POS polymerization is as follows: To a thick-walled Schlenk tube equipped with a stir bar was added fluorobenzaldehyde (10 mg, 80 μmol) and 1-hexene (1.00 mL, 8 mmol). The reaction mixture was then degassed through 5 freeze/pump/thaw cycles and backfilled with nitrogen. The Schlenk tube was cooled in liquid nitrogen and flowed with SO_2, allowing SO_2 to condense in the reaction vessel. Occasionally the flow of SO_2 was stopped and the Schlenk tube was warmed to rt to check the level of SO_2. This process was repeated until a total volume of approximately 6 mL was reached (5 mL, 120 mmol). The reaction vessel was then placed in the reactor and cooled to -30 °C. After temperature was reached, tBuOOH (1.1 μL, 8 μmol) was added via syringe under nitrogen flow to initiate the polymerization. Aliquots were removed periodically by submerging a pipe cleaner into the reaction mixture under nitrogen flow and subsequently rinsing it with $CDCl_3$. After 30 mins, the reaction mixture was poured into stirring MeOH to precipitate polymer.

Photoiniferter polymerization of poly (1-hexene sulfone)

A representative example of a photoiniferter POS polymerization is as follows: To a thick-walled Schlenk tube equipped with a stir bar was added fluorobenzaldehyde (10 mg, 80 μmol), 1-hexene (1.00 mL, 8 mmol), and Y3BE (40 mg, 80 μmol). The reaction mixture was then degassed through 5 freeze/pump/thaw cycles and backfilled with nitrogen. The Schlenk tube was cooled in liquid nitrogen and flowed with SO_2 allowing SO_2 to condense in the reaction vessel. Occasionally the flow of SO_2 was stopped and the Schlenk tube was warmed to rt to check the level of SO_2. This process was repeated until a total volume of approximately 6 mL was reached (5 mL, 120 mmol). The reaction vessel was then placed in the reactor and cooled to -30 °C. After temperature was reached, the 450 nm LED was turned on and adjusted to 10 W output to initiate polymerization. Aliquots were removed periodically by submerging a pipe cleaner into the reaction mixture under nitrogen flow and subsequently rinsing it with $CDCl_3$. After 30 mins, the reaction mixture was poured into stirring MeOH to precipitate polymer.

Photo-RAFT polymerization of poly (1-hexene sulfone)

A representative example of a photo-RAFT POS polymerization is as follows: To a thick-walled Schlenk tube equipped with a stir bar was added fluorobenzaldehyde (10 mg, 80 μmol), 1-hexene (1.00 mL, 8 mmol), R0 (16 mg, 80 μmol), and diphenyl(2,4,6-trimethylbenzoyl)phosphine oxide (3 mg, 8 μmol). The reaction mixture was then degassed through 5 freeze/pump/thaw cycles and backfilled with nitrogen. The Schlenk tube was cooled in liquid nitrogen and flowed with SO_2 allowing SO_2 to condense in the reaction vessel. Occasionally the flow of SO_2 was stopped and the Schlenk tube was warmed to rt to check the level of SO_2. This process was repeated until a total volume of approximately 6 mL was reached (5 mL, 120 mmol). The reaction vessel was then placed in the reactor and cooled to -30 °C. After temperature was reached, the 410 nm LED was turned on and adjusted to 10 W output to initiate polymerization. Aliquots were removed

periodically by submerging a pipe cleaner into the reaction mixture under nitrogen flow and subsequently rinsing it with $CDCl_3$. After 30 mins, the reaction mixture was poured into stirring MeOH to precipitate polymer.

5.7 Experimental References

1. Vosloo, J. J.; De Wet-Roos, D.; Tonge, M. P.; Sanderson, R. D., *Macromolecules* **2002**, *35* (13), 4894-4902.

2. Foster, J. C.; Carrazzone, R. J.; Spear, N. J.; Radzinski, S. C.; Arrington, K. J.; Matson, J. B., *Macromolecules* **2019**, *52* (3), 1104-1111.

3. Skey, J.; O'Reilly, R. K., *Chem. Commun.* **2008**, (35), 4183-4185.

Chapter 6: Conclusions and Future Perspective

Chapter 2

In this chapter we introduced the concept of tuning H_2S release from polymer micelles by controlling the mobility of chains in the micelle core. We accomplished this goal by synthesizing a series of amphiphilic block copolymers in which the hydrophobic blocks were functionalized to varying degrees with H_2S-releasing *S*-aroylthiooxime (SATO) groups or plasticizing alkyl oxime groups. Using DSC, we showed that the glass transition temperature of the core-forming block could be modified predictably through the ratio of SATO groups versus oxime groups. These differences in chain flexibility translated to the micelle cores of the resultant polymer micelles, resulting in a range of H_2S release rates across the polymer series. We hypothesized that the differences in release rate arose from changes in the rate of diffusion of triggering molecules into the micelle cores. In this regard, the concept of tuning release rate of a small molecule by controlling polymer chain flexibility in the micelle core may be applied more broadly in the design of macromolecular donor systems for other active pharmaceutical ingredients.

This work is expanded upon in chapter 3 to develop another macromolecular H_2S donor system and in chapter 4 to investigate the impact of chain flexibility on the self-assembly of amphiphilic block copolymers. However, the use of SATOs as H_2S donors complicates the utilization of these donor systems in biological settings. The aldehydes that are generated as a by-product of H_2S formation from SATOs may lead to off-target effects. In the future, the concept of controlled H_2S release from polymer micelles via tunable core flexibility should be applied to more biologically relevant donor compounds, like *N*-thiocarboxyanhydrides (NTAs).

It would also be interesting to observe the impact of an external plasticizing agent that could be encapsulated within the micelles on H_2S release rates. This is an idea that has been suggested multiple times but is not something we have explored in depth at this time. The use of an external plasticizing agent would allow us to maintain a constant concentration of SATO groups on our amphiphilic block copolymer. This would be particularly beneficial if small amounts of the external crosslinker could impart large changes in the micelle core mobility, providing an alternate method for controlling H_2S release without needing to severely dilute the donor concentration.

Chapter 3

In this chapter we build upon our previous work by developing a macromolecular H_2S donor system that seeks to control release rate by limiting chain mobility in the micelle core, rather than by increasing it. To accomplish this goal, we synthesized a series of amphiphilic block copolymers and incorporated varying amounts of a crosslinking agent into the core-forming blocks. This allowed the formation of polymer micelles with differing amounts of chain mobility in the micelle cores. As a result, the micelles exhibited varying rates of H_2S release, with higher amounts of crosslinking leading to slower release rates. These results further demonstrated our theory that H_2S release from polymer micelles could be easily controlled by tuning the rate of diffusion of a triggering molecule into the micelle core.

The issues with utilizing SATOs as our H_2S-releasing group are once again apparent in this work. Due to the instability of the SATO group in water, we chose a synthetic route where SATO group formation would be the last step. This led to complications in the crosslinking process, in which we had to devise a method to incorporate crosslinks into the micelle cores whilst still allowing for complete functionalization of the remaining aldehydes. This meant we needed to avoid the formation of highly crosslinked structures and led to our adoption of the modified arm-

first approach in which we first formed lightly crosslinked polymer clusters which we could further functionalize and later assemble into micelles containing crosslinks in the core. This approach resulted in large micelle size distributions and large variance in the H_2S release rate from crosslinked micelles.

It would be interesting to observe the impact of crosslinking on H_2S release without the disparity in micelles size complicating release rates. To accomplish this, we could synthesize amphiphilic block copolymers incorporating a functional comonomer capable of undergoing stimuli responsive crosslinking (i.e., coumarin photodimerization). This would allow for crosslinking after formation of micelles, greatly reducing the distribution of micelle sizes, and likely decreasing the variability in H_2S release rates.

Chapter 4

In this chapter we revisit the concept of varying chain mobility in micelle cores, this time investigating its impact on unimer–micelle coexistence. We synthesized a series of amphiphilic block copolymers with varying amounts of chain flexibility in the core-forming block, but a consistent level of hydrophobicity throughout the series. Using light scattering experiments, we demonstrated that the micelles were consistent in size and aggregation number, verifying that core-forming block mobility did not impact micelle morphology. Using NMR diffusometry experiments we showed that more unimers were present in solution for polymers with greater flexibility in the core-forming block. This was an interesting result in that chain mobility is not considered to impact polymer chain phase behavior based on current micellar theory.

It would be interesting to observe if the impact of core-forming block mobility on unimer–micelle coexistence held true for other amphiphilic block copolymer architectures. For example,

we could easily synthesize ABA block copolymers from a difunctional PEGylated macro-CTA utilizing similar hydrophobic block compositions to our previous work. Observing the relationship between unimer populations and core-forming block mobility from different amphiphilic block copolymer architectures might tell us more about how core chain mobility is impacting the polymer chain phase behavior.

Chapter 5

In this chapter we investigated RDRP techniques to achieve polymerizations of POSs with control over molecular weight and end groups. We synthesized a library of CTAs suitable for RAFT polymerization of a wide range of monomers. We evaluated these CTAs in photoiniferter and photo-RAFT polymerizations of POSs. By monitoring monomer conversion and molecular weight throughout the polymerizations we demonstrated that light mediated POS polymerizations exhibit more efficient initiation than thermally initiated POS polymerizations. Additionally, we demonstrated that photo-RAFT polymerizations of POSs with proper choice of CTA exhibit linear molecular weight growth, though further investigation is needed to achieve "living" polymerization.

It would be interesting to observe the effectiveness of more exotic CTAs towards controlling the molecular weight and end group functionality of POS polymerizations. For example, by functionalizing the phenyl ring of the dithioester type CTAs with substituents such as F- or CF_3- we could access CTAs with higher chain transfer constants, which may help reduce the initial jump in molecular weight. As such, we expect that with careful tuning of the CTA, photo-RAFT will lead to "living" polymerizations of POS.

It would be interesting to see the impact of end group functionality on the depolymerization of POSs. With “living” radical polymerization, chain end fidelity should be high and end group functionality could be selected through composition of the CTA. In this manner, we could prepare a series of POSs with varying end groups based on the CTA used for polymerization. Additionally, we could investigate head-to-tail depolymerization of these polymers through photolysis of the thiocarbonylthio end groups. This would provide an entirely new method for depolymerization of POSs.

Furthermore, after achieving “living” polymerization of POSs, it would be interesting to investigate the preparation of block copolymers through chain extension. For example, amphiphilic POSs could be made by chain extension of a POS with a hydrophilic monomer, such as oligo ethylene glycol acrylate. This would allow us to harness the potential of POS depolymerization in polymer nanostructures, such as micelles or liposomes, and open up applications for triggered delivery of molecules.